Vibration and Control in Structures under Single and Multiple Hazards

Lead Guest Editor: Aly M. Aly
Guest Editors: Elena Dragomirescu, Jiming Xie, and Mohammad Amin Hariri-Ardebili
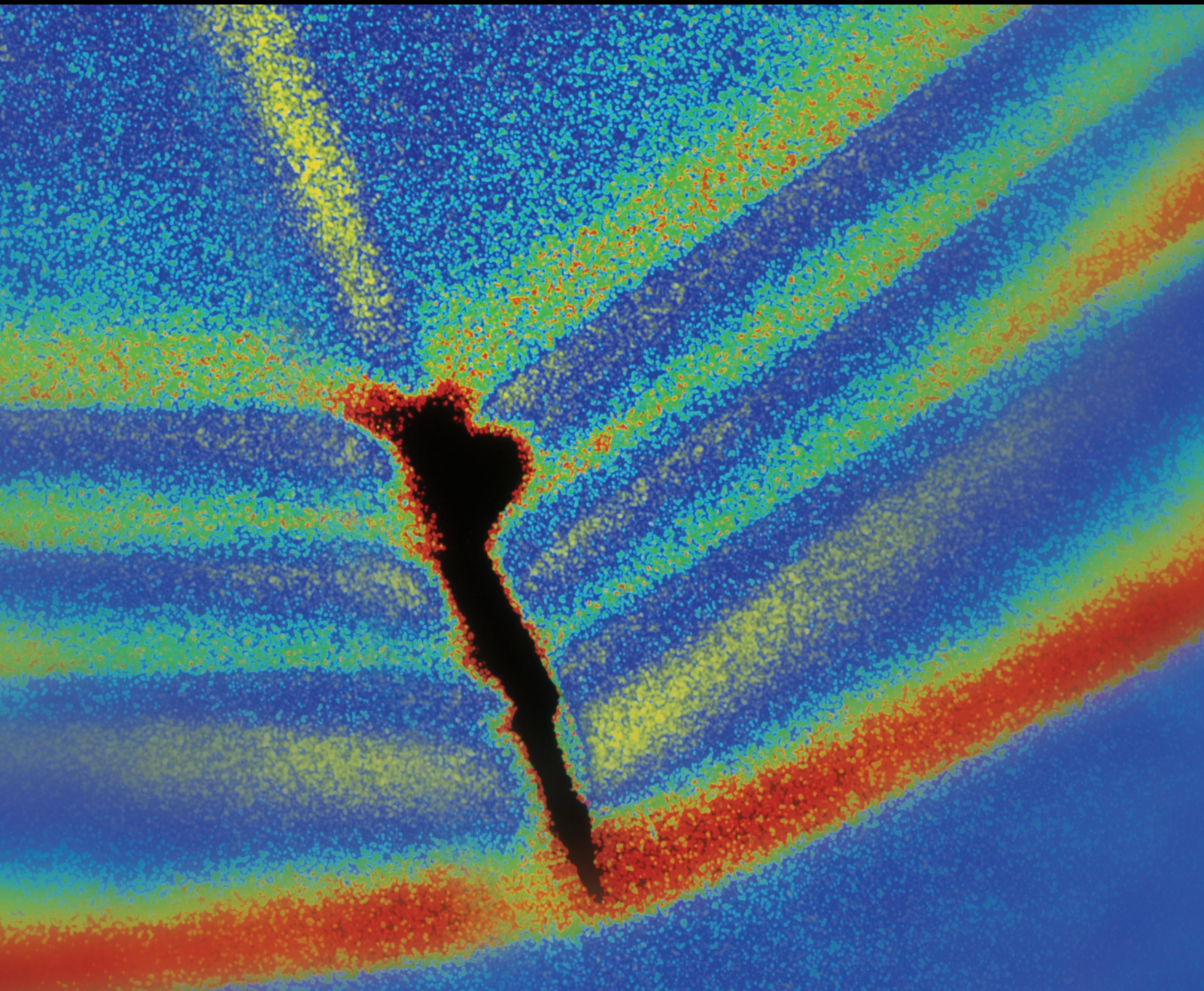
Vibration and Control in Structures under Single and Multiple Hazards

Vibration and Control in Structures under Single and Multiple Hazards

Lead Guest Editor: Aly M. Aly
Guest Editors: Elena Dragomirescu, Jiming Xie, and Mohammad Amin Hariri-Ardebili

Editorial Board

Contents

Editorial

Vibration and Control in Structures under Single and Multiple Hazards

Aly Mousaad Aly,[1] Elena Dragomirescu,[2] Jiming Xie,[3] and M. A. Hariri-Ardebili[4]

[1]*Louisiana State University, Baton Rouge, LA 70803, USA*
[2]*University of Ottawa, Ottawa, ON, Canada*
[3]*Zhejiang University, Hangzhou, Zhejiang Province 310058, China*
[4]*University of Colorado Boulder, Boulder, CO 80309, USA*

Correspondence should be addressed to Aly Mousaad Aly; aly@lsu.edu

Vibrations in civil engineering structures and mechanical systems arise from different sources of excitations including natural hazards induced loadings of structures, machineries and devices, rotating unbalance, and fault bearings. The field of vibration and control is developed into a multidisciplinary thematic which encompasses knowledge from structural dynamics, modelling, modal analysis, electrical engineering, computer sciences, and control theory, crucial for the understanding and treatment of the issues raised from occurrence of excessive vibrations.

Wind and seismic loads in civil engineering structures, and mechanical unbalance in machines, pose the potential for damage and, if not properly addressed, they can result in loss of life and property. Single and multiple hazards induced forces can wreak catastrophic failure and damage to machines, buildings, and critical infrastructure in general. Consequently, advanced research on vibration analysis and control of structures is vital for the safety and serviceability of the infrastructure under single and multiple hazard loads. Thus, recently, several vibration analysis methods and control techniques are developed and employed in civil and mechanical engineering.

The articles presented in this special issue focus on the state-of-the-art techniques and methods employed in the analysis and control of structures under different types of hazards. This issue comprises analytical methods and experimental investigations and brings vibration and structural control to real world engineering applications.

Unbalanced vibration of the spindle rotor system in high-speed cutting processes seriously affects the surface quality of the machined products. Also, it can greatly reduce the service life of the electric spindle. The contribution "Active Control for Multinode Unbalanced Vibration of Flexible Spindle Rotor System with Active Magnetic Bearing" by X. Qiao and G. Hu proposes an optimal influence coefficient control method with weights for multinode unbalanced vibration of flexible electric spindle rotors.

The active mass dampers are very effective control devices for high-rise buildings, to suppress vibrations under strong winds. In the paper "An Observer-Based Controller with a LMI-Based Filter against Wind-Induced Motion for High-Rise Buildings" by C.-J. Chen et al., the authors show that the negative influence of noise in sensors impedes the application of active mass dampers in practice.

The flexibility-based method for modeling shear wall finite element and multi-vertical-line element (SFI-MVLEM) with the method of deleting failure component elements is potential for the understanding of the structural behavior under seismic excitations. The paper "The Performance of Resistance Progressive Collapse Analysis for High-Rise Frame-Shear Structure Based on OpenSees" by Q. Zhang and Y. Li analyzes a frame-shear structure using OpenSees program, based on the nonlinear flexibility theory and multi-vertical-line theory that considered bending-shear coupling, and its progressive collapse resistance under abnormal conditions.

Vibration control and energy harvesting can be realized by integrating geometrical and material nonlinear energy sink (NES) with a piezoelectric-based vibration energy harvester under shock excitation. In the work by Y.-W. Zhang et al. entitled "Integration of Geometrical and Material Nonlinear Energy Sink with Piezoelectric Material Energy Harvester," the authors showed that the nonlinear spring and hysteresis behavior of the NES could reflect geometrical and material nonlinearity, respectively.

Despite the fact that most weather-related failures of high-voltage transmission lines (HVTLs) are attributed to downbursts accompanied by heavy rainfall, research works are mainly focused on the behavior of the transmission tower-line structures under dry downburst winds. The paper by C. Zhou et al. entitled "Characteristics of Rainfall in Wind Field of a Downburst and Its Effects on Motion of High-Voltage Transmission Line" presents a preliminary study to discuss the characteristics of rainfall in the downbursts and their effects on vibration of HVTLs.

The multiple cardan gyroscope has two rotational degrees of freedom, which can generate strong moments to constrain the two horizontal orthogonal deflections if the rotor operates in high speeds, so the structural dynamic responses can be decreased. The work by H. He et al. entitled "Vibration Control of Tower Structure with Multiple Cardan Gyroscopes" proposes a novel method for the control of tower structures under wind and earthquake loads by using multiple cardan gyroscopes as dampers.

The squeeze film damper (SFD) can enhance the system stability under the bearing fault but the enhancement decreases with the increasing speed. In their paper "Dynamic Analysis of a Rotor-Bearing-SFD System with the Bearing Inner Race Defect," J. Zhang et al. investigate the dynamic behavior of a rotor-bearing-SFD system with the inner race defect of bearing. Their results show that the speed and defect width have different influences on the distribution and amplitude of frequency and the beneficial effect of the SFD varies according to the mounted position in the rotor system.

Structural and damping solutions, including (1) height reduction, (2) steel belts, (3) tuned mass damper, (4) viscous dampers, and (5) orientation change, can be very effective in reducing wind-induced vibrations. In the paper by N. Longarini et al. entitled "Structural Improvements for Tall Buildings under Wind Loads: Comparative Study," the authors investigated the behavior of a very slender building under wind loads, to satisfy both strength and serviceability (comfort) design criteria. The study shows the potential of damping enhancement in slender buildings to mitigate vibrations, reduce design loads, and hence provide an optimal balance among resilience, serviceability, and sustainability requirements.

We hope that this special issue would shed light on recent advances and developments in the area of structural vibration and control for single and multiple hazards and attract attention of the scientific community to pursue further research and studies leading to the rapid implementation of the control devices and methods to create smart, resilient, and sustainable infrastructures which is very important as per current climate change and population growth.

Acknowledgments

Aly Mousaad Aly
Elena Dragomirescu
Jiming Xie
M. A. Hariri-Ardebili

Research Article

Structural Improvements for Tall Buildings under Wind Loads: Comparative Study

Nicola Longarini,[1] Luigi Cabras,[2] Marco Zucca,[1] Suvash Chapain,[3] and Aly Mousaad Aly[3]

[1]*Politecnico di Milano, Milan, Italy*
[2]*University of Trento, Trento, Italy*
[3]*Louisiana State University, Baton Rouge, LA, USA*

Correspondence should be addressed to Aly Mousaad Aly; aly@lsu.edu

The behavior of a very slender building is investigated under wind loads, to satisfy both strength and serviceability (comfort) design criteria. To evaluate the wind effects, wind tunnel testing and structural analysis were conducted, by two different procedures: (i) Pressure Integration Method (PIM), with finite element modeling, and (ii) High Frequency Force Balance (HFFB) technique. The results from both approaches are compared with those obtained from Eurocode 1 and the Italian design codes, emphasizing the need to further deepen the understanding of problems related to wind actions on such type of structure with high geometrical slenderness. In order to reduce wind induced effects, structural and damping solutions are proposed and discussed in a comparative study. These solutions include (1) height reduction, (2) steel belts, (3) tuned mass damper, (4) viscous dampers, and (5) orientation change. Each solution is studied in detail, along with its advantages and limitations, and the reductions in the design loads and structural displacements and acceleration are quantified. The study shows the potential of damping enhancement in the building to mitigate vibrations and reduce design loads and hence provide an optimal balance among resilience, serviceability, and sustainability requirements.

1. Introduction

1.1. Background. The increased population in urban societies and the constant pressure of limited land area with expensive prices have caused the evolution of high-rise buildings. High-rise buildings may be considered as a symbol of development and civilization. From structural point of view, these are buildings of which height will be affected by lateral forces resulting from earthquake and wind loads to the extent that such forces will play a major role in the design process [1]. High-rise building construction is a challenging project undertaken by experts and engineers. To build a tall building, one should think of a construction project whose design depends totally on analytical analysis and scaled modeling.

As high-rise buildings are receiving more global eminence, their impact on society and economy has become pronounced worldwide. Over time, new frontiers in high-rise construction complement emerging needs for performance,

efficacy, and economic design. Designers are concerned about choosing structural systems that can carry lateral loads as well as ascertained serviceability and occupant comfort requirements. The economic viability of tall buildings depends strongly upon serviceability and occupant comfort as prerequisites. In general, tall buildings are built to sustain extreme wind loads within an expected long lifespan. The probability of catastrophic failure is small; however, studies on wind induced motion and effects on high-rise buildings are essential from a serviceability and economic point of view. The design of buildings with a slenderness ratio (aspect ratio = height/width) greater than five is usually governed by serviceability more than safety [2]. The serviceability of tall buildings under wind is typically measured by the amount of lateral displacements and acceleration. Excessive lateral displacements can cause structural and nonstructural damage, while excessive acceleration can lead to unpleasantness to the building occupants [3].

An additional challenge is the uncertainty in the amount of structural damping early in the planning phase [4]. To alleviate this issue, structural control is a potential method for structural tuning and damping enhancement. The purpose of structural control in civil engineering structures is to reduce vibrations produced by external stressors such as earthquake and wind loads, by different techniques such as modifying stiffness, mass, damping, or shape. Structural control methods are typically classified as active, passive, and semiactive techniques. Passive systems use supplemental devices, which respond to the vibrations of the structure by dissipating the energy triggered by strong dynamic loads, without the need for an external energy supply. A variety of passive control mechanisms have been suggested by researchers and engineers, including tuned mass dampers, viscous dampers, friction dampers, and tuned water dampers.

An external power source is needed for an active control system to control actuators that apply prescribed forces to a structure/building, to inject/dissipate energy and hence minimize certain optimization objectives. The command signals to the actuator depend on the measured system response (feed-back control). However, active control systems can be unstable, and they need bulky power transformers and consume significant amount of energy, which may not be available, especially immediately after natural disasters, such as earthquakes and high winds. For this purpose, passive control systems remain the most reliable and practical technique for structural control. Some passive control systems are presented as follows.

1.2. Tuned Mass Dampers (TMDs). A vibration absorber or a TMD consists of spring, mass, and a damping device installed on a primary system to lessen the dynamic response. The main concept in the TMD is that the frequency of the damper is tuned to resonate out of phase with the vibration of the primary structure, leading to significant energy dissipation. Numerous studies are focused on the performance of the TMD and its capability to suppress vibrations, especially due to wind loads. The concept of vibration suppression by a TMD dates back to 1909, when the vibration absorber was invented by Farham, making it as one of the earliest control devices [5]. Following this invention, numerous studies were conducted to validate the application, as well as to enhance the performance of the device with different structural configurations. The concept of using a robust TMD was proposed recently, in which an approach was developed to determine the optimal parameters under structural uncertainties. Significant reductions in the response can be realized by the optimum selection of the mass ratio and tuning frequency ratio [6]. In high-rise buildings, when the inherent sutural damping is low, the TMD is proved to be very effective in reducing the responses [7]. TMDs are used as controlling devices in high-rise buildings in Japan, Hong Kong, United States, Australia, and some other countries. The Hancock Tower in Boston 244 m, as mentioned in [8], has two TMDs installed at the opposite ends of the 58th floor with each unit weighting 300 tons. However, there are several limitations on the practical application of TMDS; for example, being tuned to a single vibrational mode is limited

to narrow band of operation frequencies [9]. The limitations of the TMD can be significant when dealing with buildings excited at higher modes of vibration, for example, under earthquake loads. Also, TMDs are sensitive to uncertainties in the structural parameters. Structural parameters may change due to damage, material degradation, or even environmental variations. Such changes can lead to a detuned TMD, with reduced effectiveness [10].

1.3. Tuned Liquid Dampers. Tuned liquid dampers (TLDs) gained increased popularity due to their effectiveness in absorbing low-frequency vibrations induced by wind, being cost effective, requiring less maintenance, and being easily implementable [11]. TLDs are energy dissipation devices, suggested for vibration suppression under different dynamic loads. A typical TLD consists of a container with liquid/water to reduce vibrations of a primary structure. This allows significant energy dissipation and hence reduced structural responses [12]. The fundamental principle of vibration control in structures using TLDs is based on sloshing and wave breaking for energy dissipation [11]. For efficient energy dissipation, the fundamental frequency of liquid in a TLD should be close to that of the primary structure. Several research studies have been conducted on TLDs in the past few decades. The research conducted by Bauer in 1984 [13] proposed a damping device to control vibrations, where a rectangular container filled with two immiscible liquids was utilized, in which the interface motion dissipated the energy effectively. Recently, TLDs have been shown to be effective in lateral vibration control of high-rise buildings. The Hobert Tower in Tasmania (Australia) with a height of 105 m is equipped with 80 TLDs. Similarly, in Kagawa (Japan) 16 units of TLDs are installed in the Gold Tower which has a height of 158 m. The installation of TLDs is found to suppress vibrations of buildings under wind loads by one-third to half of the original responses [8].

1.4. Viscous Dampers. Damping is an important mechanism that dissipates energy and hence permits a structure to achieve high performance under dynamic loads such as earthquake, strong wind, or blast. Numerous fluid damping devices with practical applications have been proposed over the past few decades. The use of damping devices filled with viscoelastic liquid to dissipate energy was studied extensively, both analytically and experimentally [14]. When a VD is subjected to an external load, friction forces develop among different elements. Friction forces are developed among the molecules of the damping medium, shaft and medium, piston and medium, and so on. All these actions combine together to form a damping force which acts 90 degree out of phase with the displacement driven force in a primary structure [15, 16]. Previous uses of viscous dampers (VDs) in military applications include the attenuation of weapon grade shock, aircraft, ship vibration, and underwater detonation.

Viscous dampers that were used in military applications during the cold war have been adopted for civil engineering structural applications [17]. A number of countries are practicing the use of VDs in tall building including Hong Kong, China, Japan, and United States. The Sato Building (1992)

and Shimura Dormitory (1993) in Japan are vivid examples of application [8]. These devices are of a prime interest in civil engineering because they possess certain characteristics such as (1) compactness; (2) temperature insensitivity; and (3) linear viscous response over a range of frequencies [15]. In 1991 a cooperative effort between NCEER and Taylor Devices, Inc., began to adopt this defense technology for hazard mitigation in buildings [18].

Various theoretical and experimental works are conducted on the effective usage of VDs in high-rise buildings. A study conducted on a 39-story building shows that the application of VDs reduced the wind induced acceleration of the building by 35% [19]. The imperial building in India (10 story) was studied, two-thirds of the energy induced by wind and small earthquakes realized to be dissipated by VDs [20]. A super tall 62-story building (Xiamen city of southeast China) with 245.75 m height was studied for wind induced response reduction by VDs; there was a significant reduction in displacement and acceleration [21].

1.5. Belt Trusses and Outriggers. In general, moment resisting frames and shear walls are efficient and economical structural systems for low- and medium-rise buildings. But when the height of a building goes up, these systems may not be sufficient enough to resist load induced by the wind and earthquakes. Belt truss systems are effectively used to control excessive drift due to lateral loads and also to enhance the stiffness of tall buildings [22]. The outrigger and belt truss systems are dynamic load resisting systems in tall buildings where external columns control core walls with very stiff structural/mechanical elements, at one or more levels. The functional difference between belt trusses and outriggers is that belt trusses tie the peripheral columns of a building, while the later engages them with the central core. Externally induced moments are resisted by the core and axial internal loads developed in outer columns that are connected to an outrigger [23]. Belt trusses are used as "virtual outriggers" because they can transfer the load without the need for a connection between an outrigger system and the core [24]. The Plaza Rakyat Tower (located in Kuala Lumpur) employs "virtual outrigger" systems consisting of belt walls (reinforced concrete building) [8]. The challenges associated with this type of mitigation include the loss of space in buildings, in addition to accompanying structural complexities [25].

1.6. Paper Layout. The current study addresses the application of different response lessening mechanisms in a tall building subjected to wind loads. Five independent response reduction methods are employed to control vibrations under wind loads. Section 2 presents the design criteria set by standard codes for buildings with high slenderness ratios, concerning both strength and serviceability requirements. In Section 3, the building characteristics, wind loads, and wind tunnel experiments are presented. In Sections 4 and 5, the wind induced responses (base moments, base shear, drift, and acceleration) are evaluated using wind tunnel test data and finite element model (FEM). Specifically, Section 4 presents

the pressure integration method, whereas Section 5 introduces the high frequency force balance method. Section 6 focuses on the comparison of the wind induced responses obtained in Sections 4 and 5 with the design limits provided in standard codes (the Eurocode 1 (EC1) [26] and the Italian CNR DT207/2008 (CNR) code [27]). Since the response values evaluated exceeded the design limits provided by standard codes, there was a need to propose structural improvements. Five different solutions (improvements) are presented in detail to bring those values under the prescribed limits. The improvements explained in Section 7 are height reduction, use of belt trusses, installation of dampers, and orientation change. In the first improvement, about 12.5% of the total height of the building was reduced to check its sensitivity to wind. In the second improvement, internal belt trusses are introduced at different levels, for two and four alignments along the horizontal x axis. Again, as third and fourth improvements, installation of a TMD at the top and VDs up to the 20th floors are considered separately to investigate their effectiveness. Rotation of the building to an optimum angle for reduced wind effects is the fifth improvement. All the improvements mentioned above are studied separately, independent of each other. Finally, the conclusions drawn are summarized in Section 8.

2. Design Criteria

2.1. Resistance and Comfort Criteria. An accurate analysis of the structural system is necessary to build a high-rise building that can withstand the complex wind loads. There are two important design criteria that should be considered while designing high-rise building, the first one is Ultimate Limit State (ULS) which deals with strength requirements of structure and the second is Serviceability Limit State (SLS) that deals with comfort of occupants in the building. The ULS criteria are employed to guarantee that the building will not fail under maximum design loads. Similarly, the SLS criteria are used to ascertain that the building will remain operational and functional by satisfying serviceability (usually comfort) conditions. Purpose of SLS requirements is to address the response of people and objects to the behavior of the structure under the load. These criteria have to be fulfilled, to yield adequate structural robustness, as well as to provide required comfort satisfaction to occupants. The comfort criterion can be fulfilled by limiting peak floor acceleration to predefined values provided in standard codes [28–32]. Moreover, considering the SLS design criterion, it is fundamental to investigate the serviceability behavior (in terms of interstory displacements) of the secondary building elements like finishes and system elements [33, 34]. Generally, the response effects of the structure (also called the stress effects) have to be evaluated and compared with the resistant effects; the stress effects are the actions on the structural elements (in terms of shear, bending, axial, and torsional stresses), in addition to the response (displacement and acceleration) of the structural primary and secondary elements. All stress effects can be evaluated by an appropriate FEM. The following are the notations that will be used in FEM model for stress effects, E_{Sd} for the actions, δ_{Sd} for the

TABLE 1: Reference values of the acceleration.

| Building usage | Design values | | Notes |
	[m/s²]	[g/1000]	
Residential	0.039~0.082	4.03~8.43	Up to 0.049 m/s², the motion is imperceptible
Office	0.196~0.245	20~25	The motion is perceptible and irksomeness is subjective; up to 0.5 m/s² serious physical problems

TABLE 2: Resistant displacements (δ_{Sd} is top displacements, δ_{Sid} is inter-story displacements, H is building height, and h_i is inter-story height).

δ_{Rd} values	δ_{Rid} values
$H/600 \leq \delta_{Sd} \leq H/500$	$\delta_{Sid} \leq h_i/600$

displacements, and a_{Sd} for the acceleration. Similarly, E_{Rd}, δ_{Rd}, and a_{Rd} are symbols for the actions, displacements, and acceleration for the resistant effects, respectively.

The resistance effects in building can be determined by using standard codes. The international codes can be consulted to determine the resistant shear, the resistant bending moment, and the resistant axial load for the ULS. However, resistant displacements δ_{Rd} and the resistant acceleration a_{Rd} in many cases are not specified in the codes and their values may change either for the characteristics of the finishes or for the use of the building. In most of cases, the resistant displacements δ_{Rd} and in particular the resistant acceleration a_{Rd} are not specified in standard codes and their values may change depending on the use of the building. Thus, the valued stress effects and the resistant effects must satisfy the following relations:

$$E_{Sd} \leq E_{Rd},$$
$$a_{Sd} \leq a_{Rd}, \tag{1}$$
$$\delta_{Sd} \leq \delta_{Rd}.$$

The acceleration in (1) refers to the response (acceleration) of the building at its top, to satisfy the serviceability requirements (SLS), for 10-year return period ($T_R = 10$ years). Comfort limits, a_{Rd}, shown in Table 1, are set to avoid health problems like vertigos, sickness, and so on in the occupants. Moreover, the top displacements (δ_{Sd}) and the interstory displacements (δ_{Sid}), calculated for the SLS, can be compared to the resistant values (δ_{Rd} and δ_{Rid}) shown in Table 2.

2.2. Slenderness Ratio. The aspect ratio or the slenderness ratio can significantly govern the behavior of high-rise buildings under wind. As the building grows taller, response level to the dynamic load changes. Therefore, proportions of height and length need to be considered carefully. The wind analysis has to be even more accurate if the tall building is characterized by an unusual shape or by large geometrical slenderness ($\lambda = H/l$), defined by its aspect ratio (building height (H)/shortest side of its plan (L)). Usually up to $\lambda \geq 8$–11

some comfort problems could exist [27], if the structure does not have enough stiffness or it is not equipped with damping devices. In fact, problems affect the comforts in everyday use in some tall buildings and numerous skyscrapers; all the levels cannot be exploited for the same intended use of the lower floors. Very often, for the presence of spire or for very spindly parts at the top, the total height reduction (Δh_{tot}) is observed in many constructions. The reduction of height is the difference between the top height (H) and the height of the ultimate occupied floor (H_f) having the same intended use of the lower floors. Some examples are Burj Khalifa in Dubai $\Delta h_{tot} = 244.5$ m ($H = 829$ m, $H_f = 584.5$ m), for Willis tower in Chicago $\Delta h_{tot} = 114$ m ($H = 527$ m, $H_f = 413$ m), for Taipei 101 in Taiwan $\Delta h_{tot} = 70$ m ($H = 508$ m, $H_f = 438$ m), for Trump tower in Chicago $\Delta h_{tot} = 82$ m ($H = 423$ m, $H_f = 341$ m), and for Unicredit tower in Milan $\Delta h_{tot} = 82$ m ($H = 231$ m, $H_f = 144$ m).

Nevertheless, in order to reach symbolic constructions fame, many tall buildings have a value of λ around the mentioned limit as these are characterized by streamlined shapes with a spire at the top [35]. Among these are the St. Gilus Circus in London ($H = 136.10$ m, $l = 28.05$ m, $\lambda = 7.50$), the Pirelli building in Milan ($H = 125$ m, $l = 18.70$ m, $\lambda = 6.68$), the Marina City buildings in Chicago ($H = 180$ m, $l = 33.32$ m, $\lambda = 5.40$), the Standard Bank building in Johannesburg ($H = 139$ m, $l = 14.17$ m, $\lambda = 9.81$), the Trump Tower in NY ($H = 202$ m, $l = 35.04$ m, $\lambda = 5.76$), and the Bond Center in Hong Kong ($H = 191.50$ m, $l = 32.70$ m, $\lambda = 5.85$).

Furthermore, λ close to 8 represents a border between a very slender tall building and a stubby chimney (some examples of stubby chimneys in Italy are the Enel chimney in Porto Tolle ($H = 243.80$ m, $l = 26.01$ m, $\lambda = 9.34$) and the Enel chimney in "Torre Valdaliga" ($H = 243$ m, $l = 28.70$ m, $\lambda = 8.47$)).

In case of high geometrical slenderness λ [36], the classic problems due to the wind load could add up to those caused by dynamic effects, like the galloping due to the vortex shedding. In tall buildings, these effects are particularly dangerous since they concern the resistance of both the main structural elements and the elements supported by the main structure (e.g., the steel connections of the facades).

3. Structural and Wind Load Modeling

3.1. Characteristics of the Building. The tall building studied in this paper is located in north Italy and is optimized for office use. The building is characterized by a high value of slenderness λ. The main features of the structure are as follows:

(i) Total height $H = 225$ m and rectangular floor plan (Figure 1) has sides $l_1 \cong 64$ m in x-direction (along wind) and $l_2 \cong 23$ m in y-direction (across wind); the geometric slenderness ratio is $\lambda \cong 10$;

(ii) Circular columns and cores of the building are made with High Strength Concrete (HSC, with $R_{ck} \cong 75$ MPa), but floor deck is made with Normal Strength
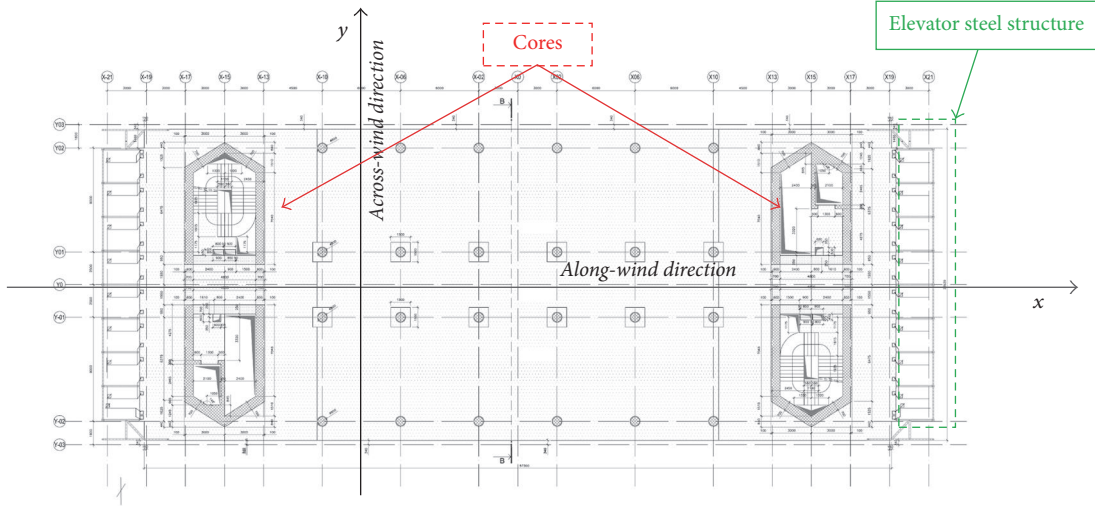
FIGURE 1: Typical floor plan.

$f_1 = 0.14\,\text{Hz}$ $f_2 = 0.15\,\text{Hz}$ $f_3 = 0.26\,\text{Hz}$
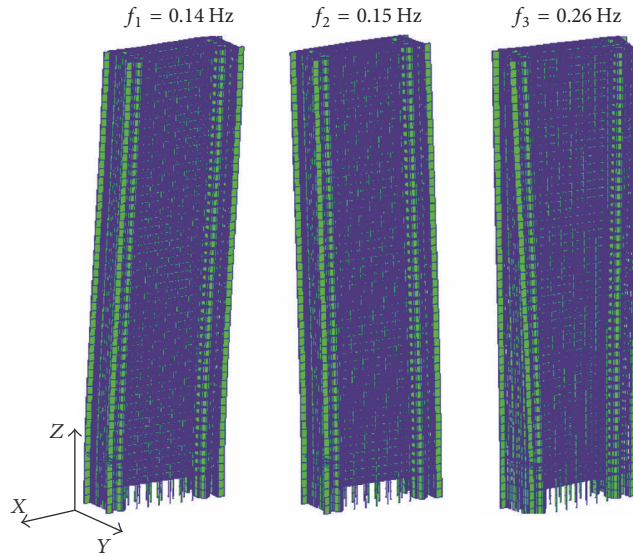
FIGURE 2: First, second, and third mode shapes of the building.

Concrete (NSC, with $R_{ck} \cong 45\,\text{MPa}$); slab is posttension reinforced in the two main directions;

(iii) Slab foundation is in NSC with normal and posttension reinforcement in the two main directions.

The wind resistant structural elements, cores of the building, are located at the opposite sides of the typical floor plan. The thickness of their walls is tapered along the vertical development of the building. Thickness, in the basement, is 1.20 m, from the ground level to the fifth floor is 1.00 m, from the fifth to the twenty-seventh floor is 0.70 m, and from the twenty-seventh to the top of the building is 0.50 m. The inner layout, optimized for the office use, shows four lines of circular columns along the longest side, two of which are located along the facades and the other two are close to the central horizontal axis of the floor plan. The structures of the elevators are made of S355 steel and structural glass; these are

joined to the main concrete structure and do not contribute with the bracing system. Figure 1 shows the floor plan.

In the FEM, the columns and the beams are represented by beam elements; the cores and the decks are represented by plates. The eigenvalue analysis is carried out to calculate the natural frequencies for the first three modes. Frequencies for I, II, and III vibration modes are $f_I = 0.14\,\text{Hz}$ (bending in x-axis direction), $f_{II} = 0.15\,\text{Hz}$ (bending in y-axis direction), and $f_{III} = 0.26\,\text{Hz}$ (torsional around z-axis). Figure 2 shows the mode shapes along with the dominant structural frequencies.

3.2. Aerodynamic Loads. High-rise buildings are wind sensitive structures so lateral wind load imposed on building is a governing factor in their structural design. Situation becomes even more complicated if the frequency of oncoming wind resonates with natural frequency of building which depends
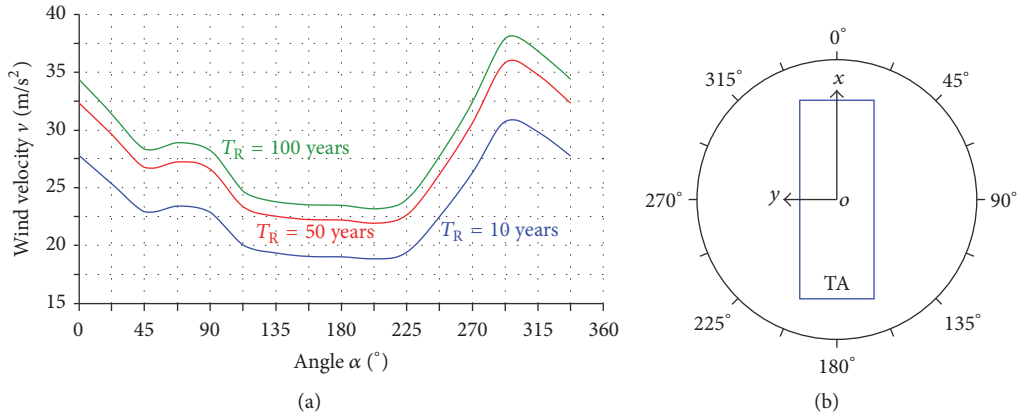
FIGURE 3: (a) Wind velocity as a function of the direction angle α. (b) Angle α relative to the position of the building.

on structural properties of building. Pattern in which wind flows around the building is distorted by flow separation and wakes developments. Combination of these affects results in aerodynamic pressures on the structural system that imposes fluctuating forces, and the building tends to respond in the lateral directions, as well as in torsion [37].

The response in the along-wind consists of fluctuating and mean components, and the average wind speed is usually used to directly evaluate mean load and responses based on pressure and load coefficients. The fluctuating component of response and loads depend dominantly on (1) turbulence intensity; (2) size reduction effects; and (3) dynamic amplification (resonance). The "gust factor" approach can be employed to predicted the along-wind response with a reasonable accuracy when the interference effects are not significant [37].

Crosswind oscillations can be excessive, if building has low damping. Cross wind excitation is closely related to "vortex shedding" [38]. The building acts as bluff body that separates the flow from surface of structure causing asymmetric pressure distribution around the cross-section of structure. There can be a situation of resonance, if vortex shedding frequency and natural frequency of building coincide, causing excessive oscillation in transverse direction or even failure.

Possible aerodynamic coupling in various degrees of freedom is responsible for torsional motion of building. If the resultant wind load coincides with center of mass at each floor, an eccentric loading can be expected, which excites the torsional mode of vibration. Torsional responses are sensitive to ratio of transverse to torsional frequencies [39]. Thus, it is fundamental to perform the wind tunnel test for precise evaluation of along-wind, crosswind, and torsional responses in this tall building.

3.3. Wind Tunnel Testing. It is critical to determine the wind loads for the specific mean recurrence interval and uncertainties associated with these loads. Wind loads and loads factors are prescribed by analytical method given in codes for ordinary building. But in case of tall buildings, these methods lack precision and may not accurately account for important phenomena such as cross wind loads, aerodynamic

instability, vortex shedding, and aerodynamic interaction between adjacent building [40]. Thus, to get more precise, project specific information regarding wind loads and building motion, wind tunnel simulation of a scaled model is required.

For the present case, in this tall building, the wind tunnel tests are fundamental to investigate the effects of the wind, like vortex shedding phenomenon (in relation to the dangerous structural behaviors like the galloping). For the aerodynamic tests, it is essential to obtain wind velocities in the site of construction. There are different approaches for the definition of the wind speed, which are described as follows.

Approach 1. Directional velocities values are considered based on estimated wind speed in the site.

Approach 2. Directional velocities values are considered only when these values are higher than the velocities prescribed in the codes; otherwise velocity prescribed in the codes is considered.

Approach 3. The values are set by the codes with relation to the buildings plan; these values are the same in the two main directions.

Particularly, in this case, "Approach 1" is followed and the site directional velocities come out from an in-depth study of the location site [41]. The different velocities are reproduced in the wind tunnel on a rigid scale models (1 : 100) [36, 42]. The tests have investigated two different layouts, with urban contest and without the urban contest. The present analysis refers to the layout "building with the urban contest," which has given higher stress values. The maximum wind velocity comes from the north-west direction ($270°$–$300°$ in Figure 3). For return period $T_R = 100$ years, the maximum velocity is $v_{max} = 38$ m/s; this value is higher than the nondirectional value $v_{code} = 33$ m/s, indicated in the Italian code (DM 2008) for the same T_R. Wind velocities as a function of the direction, identified by the angle α, are shown in Figure 3.

The forces F and the moments M at the base of the scale models, during the wind tests for each of the 16 wind

directions, are recorded as a function of the time. These are expressed by the following dimensionless coefficients:

$$C_{FX} = \frac{F_X}{qBH},$$

$$C_{FY} = \frac{F_Y}{qBH},$$

$$C_{FZ} = \frac{F_Z}{qBH},$$

$$C_{MX} = \frac{M_X}{qBH^2}, \tag{2}$$

$$C_{MY} = \frac{M_Y}{qBH^2},$$

$$C_{MZ} = \frac{M_Z}{qBH^2},$$

where $q = 0.5 \cdot \rho \cdot v_{ref}^2$ is the dynamic pressure, ρ is air density, $v_{ref} = v(z_{ref})$ refers to the average wind speed at a reference point $z_{ref} = 100$ m, and B represents the longest side (top view), of a building with the height H. Time histories of pressures on the surface of the models are measured, in about 400 pressure meters ("TAPs"), for the same 16 wind directions.

4. Pressure Integration Method (PIM)

In this method, finite element model of the full scale structure was employed to predict the behavior of the real building. This method has the great potential to estimate the wind loads because it can address the limitations of the conventional force balance technique while maintaining the advantage of that technique [43]. 400 TAPs were distributed on the outer surfaces (for the wind tunnel experiment). The distribution of TAPs is such that number of TAPs per unit area is increasing as it goes upward as shown in Figure 4. Pressure value on each TAP of the model is calculated as

$$p_{TAP}(t, z_{ref}) = c_p(t) \, qV(z_{ref}), \tag{3}$$

where $c_p(t)$ is dimensionless time history of pressure coefficient and q is dynamic pressure. Once the time history of pressure on surface is determined, external force acting on each TAP surface can be calculated as

$$f_{TAP}(t, z_{ref}) = p_{TAP} A_{TAP}, \tag{4}$$

where A_{TAP} is the area of each TAP which is evaluated by Thiessen polygon method. In order to estimate forces F and moments M at floor levels, the part of f_{TAP} corresponding to each floor has been identified. For each k-floor the surfaces A_k are identified; the generic A_k is given by the space between two floors (product of the horizontal length of the floor and the interstory distance), as shown in Figure 5(a). Then the surfaces A_{ki} (Figure 5(c)) are considered by the intersection of the "area of influence" of the k-floor A_k (Figure 5(a)) and the area of influence of the i-TAP, A_{TAPi} (Figure 5(b)).

For each wind direction α, the generic wind force F_k and moment M_k in the generic k-floor implemented in the FEM are given by

$$F_k = \left[\frac{(p_{TAP1}A_{k1} + p_{TAP2}A_{k2} + \cdots + p_{TAPn}A_{kn})}{(A_{k1} + A_{k2} + \cdots + A_{kn})} \right],$$

$$M_k \tag{5}$$

$$= (p_{TAP1}A_{k1}l_{k1} + p_{TAP2}A_{k2}l_{k2} + \cdots + p_{TAPn}A_{kn}l_{kn}),$$

where l_{ki} ($i = 1, \ldots, n$) represents the eccentricity between center of gravity and the centroid of the area A_{ki}. The corresponding F_k and M_k were applied in the barycenter of each FEM's k-floor.

By the linear time history analysis (Figure 6), considering the first 10 mode shapes and different coefficients of structural damping ($\xi = 1\%$–4%), the acceleration at the top of the building (a_{Sd}) was obtained. All acceleration is calculated by combing the two translational values (x- and y-directions) with the torsional value (around z-axis). For $\xi = 1\%$ the value of a_{Sd} at top of building is 0.45 m/s^2 (Figure 6) which is higher than the comfort limit value $a_{Rd} = 0.20$ m/s^2 in Table 1. However, when the damping in the building is increased up to 4%, the maximum acceleration is about 0.25 m/s^2, which is still higher than the comfort limit value. It implies that damping should be increased beyond 4% to get the desired value of acceleration (i.e., below 0.20 m/s^2). This value of damping in the structure can be achieved by installing damping devices (TMD or VDs), which is studied in the subsequent sections.

5. High Frequency Force Balance Method (HFFB)

The HFFB technique is widely used to measure wind forces on buildings, by wind tunnel testing, replicating the full scale scenario. High accuracy force sensors are employed to measure wind induced loads at the base. The generalized loads are correlated to measured loads, if the building has uncoupled linear translational and uniform mode shapes [44].

HFFB procedure defines the global wind stress action on the building as the summation of the static and dynamic contributions [45–48]. The dynamic contribution is characterized by the background and the resonant part. Thus, the generic action, for example, the total moment $\widehat{M}_{tot}$ at the base of the building, is given by

$$\widehat{M}_{tot} = \overline{M} + M_{dyn} = \overline{M} + g_B \cdot \sigma_{MB} + g_R \cdot \sigma_{MR}, \tag{6}$$

where

(i) $\widehat{M}_{tot}$ is total stress moment (static and dynamic contributions);

(ii) $\overline{M}$ is static contribution of the stress moment;

(iii) M_{dyn} is dynamic contribution of the stress moment;

(iv) $g_B \cdot \sigma_{MB}$ is background part of the dynamic contribution;

(v) $g_R \cdot \sigma_{MR}$ is resonant part of the dynamic contribution.
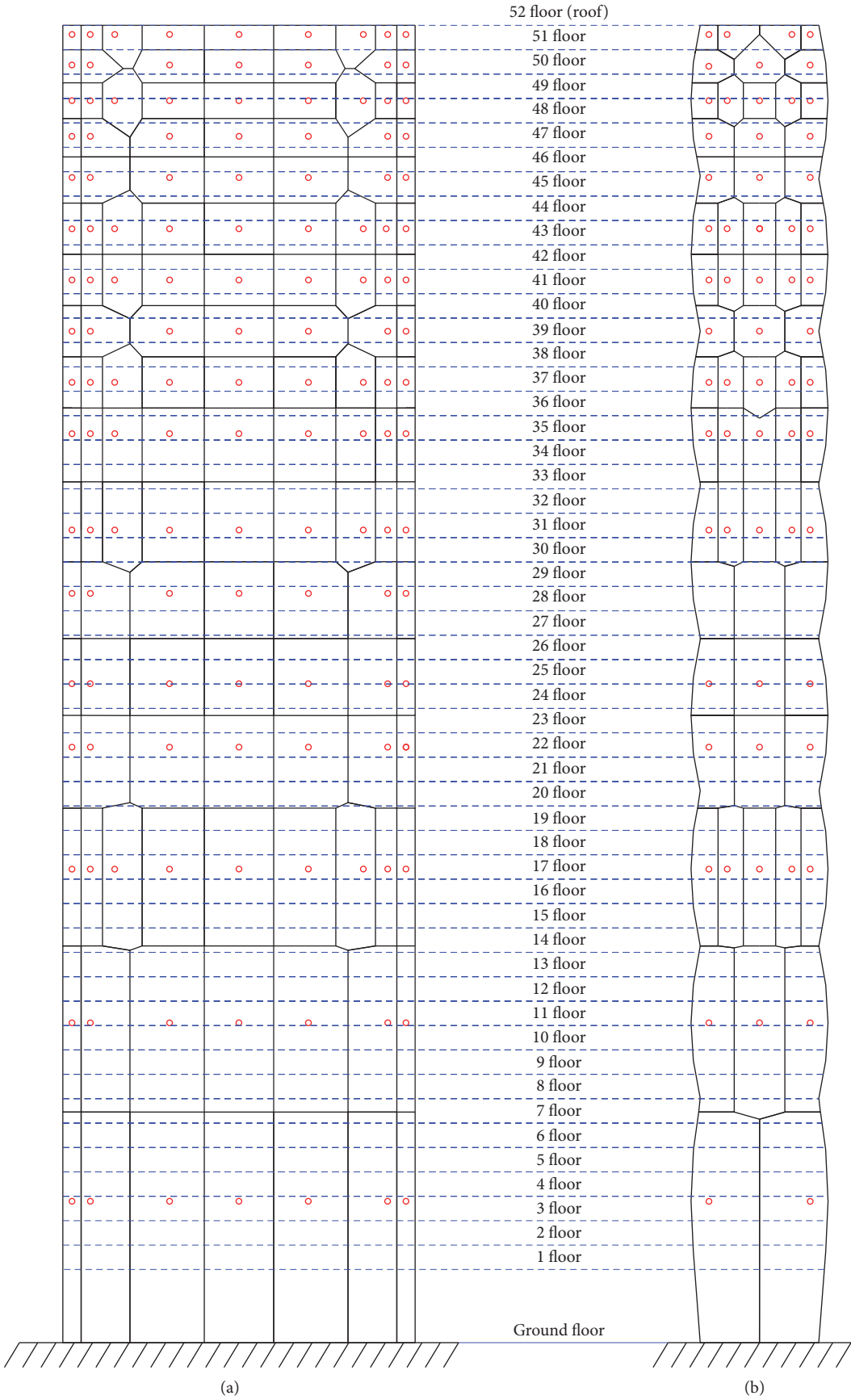
FIGURE 4: Pressure tap layout (a) facade East and (b) facade North.
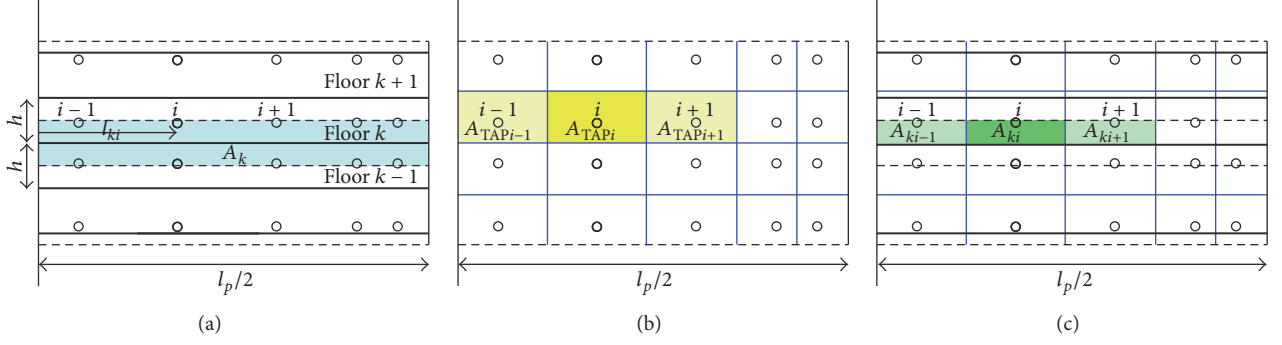
FIGURE 5: (a) Area of influence of the k-floor A_k. (b) Area of influence of the i-TAP $A_{\text{TAP}i}$. (c) Area A_{ki} obtained by the intersection of A_k and $A_{\text{TAP}i}$.
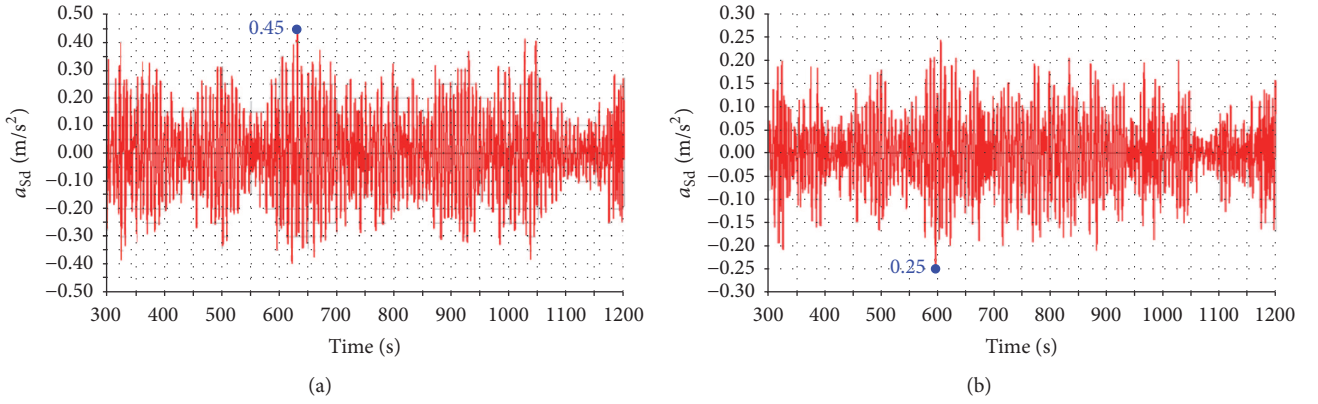
FIGURE 6: Time history of the acceleration (in y-direction): (a) for $\xi = 1\%$ and (b) for $\xi = 4.0\%$.

In (6) it is possible to distinguish

(i) the extreme Gumbel value

$$\widehat{M} = \overline{M} + g_B \cdot \sigma_{MB} \qquad (7)$$

(ii) the resonant value:

$$\widehat{M}_{\text{dyn},R} = g_R \cdot \sigma_{MR}$$

$$= \left(\sqrt{2 \ln (f_i \cdot T)} + \frac{0.5772}{\sqrt{2 \ln (f_i \cdot T)}} \right) \qquad (8)$$

$$\cdot \sqrt{\frac{\pi}{4 \cdot \xi} f_i \cdot S_M (f)}$$

in which

(i) T refers to the time period (for the evaluation of the maximum value of the stress action (600 s));

(ii) f_i is the building natural frequency associated with the direction in which the moment is valued (in

this case, the first, the second, and the third natural frequencies are considered, by a modal analysis using FEM)

(iii) $S_M(f)$ refers to the PSD (power spectral density) of the base moments (measured by a dynamometric balance);

(iv) ξ is the structural damping.

The Gumbel forces and moments coefficients values (for each time history and for all the wind directions) are obtained starting from the Fisher Tippet II probability density function [49] and the fully probabilistic method [50], ensuring the probabilities of occurrence related to the Gumbel coefficients values and the wind velocities are the same. The resonant part of the dynamic contribution is used to evaluate the forces $F_{\text{eq}}(z)$ and the resonant moment $M_{\text{eq}}(z)$.

$$F_{\text{eq}} (z) = \widehat{M}_{\text{dyn},R} \frac{m (z) \, \varphi_i (z)}{\int_o^H \varphi_i (z) \, z m (z) \, dz},$$

$$M_{\text{eq}} (z) = \widehat{M}_{\text{dyn},R} \frac{\phi_i (z) \, I (z)}{\int_o^H \phi_i (z) \, I (z) \, z \, dz} \qquad (9)$$
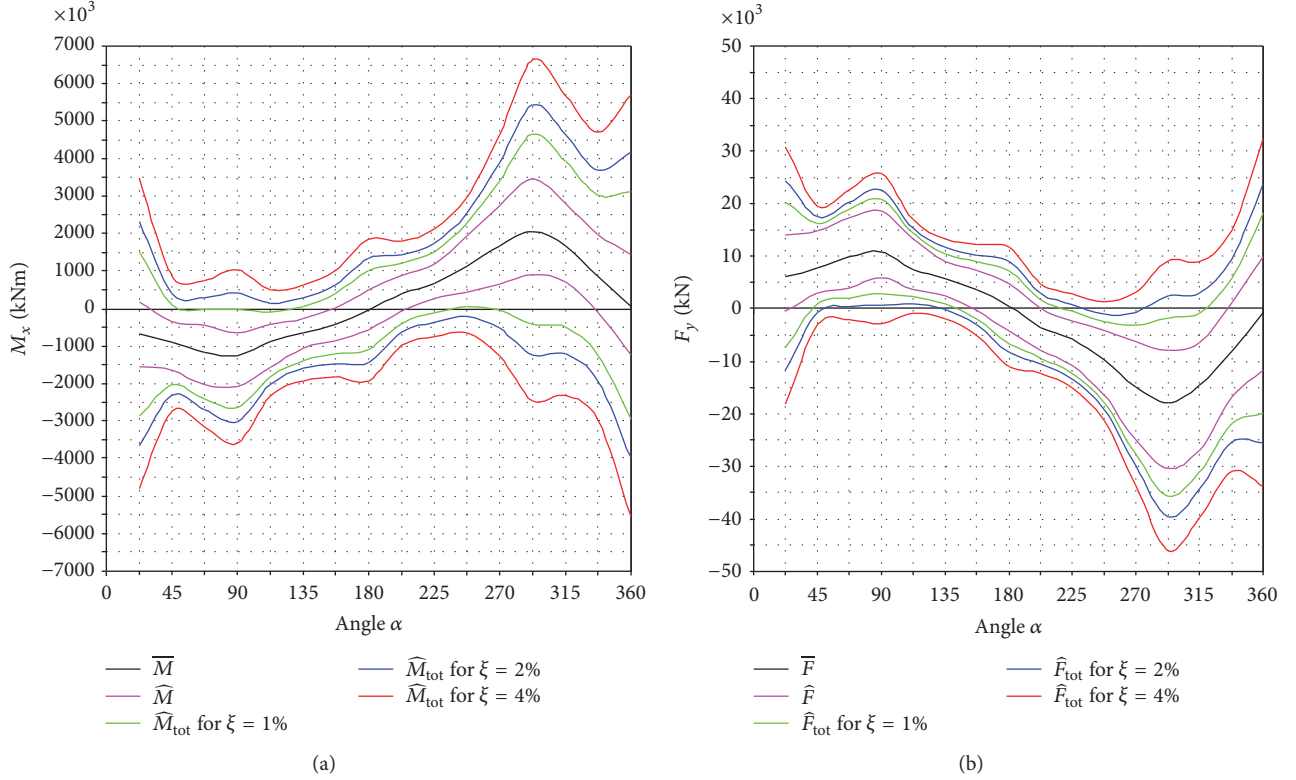
FIGURE 7: Base loads: (a) base moment in x direction (M_x) and (b) base shear in y-direction.

in which $m(z)$ designates the distributed mass of the tower and $I(z)$ refers to the second moment of area, while $\phi_i(z)$ refers to the first eigenvector associated with the direction in which the force is valued. From $F_{eq}(z)$ and $M_{eq}(z)$ the translational and rotational acceleration are calculated in

$$a_x(z) = \frac{\int_o^H \varphi_I(z) F_{eq}(z)\,dz}{\int_o^H \varphi_I^2(z) m(z)\,dz} \varphi_I(z);$$

$$a_z(z) = \frac{\int_o^H M_{eq}(z) \varphi_{III}(z)\,dz}{\int_o^H \varphi_{III}^2(z) M(z)\,dz} \varphi_{III}(z); \qquad (10)$$

$$a_y(z) = \frac{\int_o^H F_{eq}(z) \varphi_{II}(z)\,dz}{\int_o^H \varphi_{II}^2(z) m(z)\,dz} \varphi_{II}(z).$$

To take the effect of nonsimultaneousness into account, the contributions in x-, y-, and z-directions have to be combined by specific coefficients [29]. With the HFFB procedure, it is possible to point out the dynamic effects. Base shear, bending moment, and the acceleration response are calculated as function of the direction angle α, for several damping ratios ξ (1.0%; 2.0%; and 4.0%) (Figures 7 and 8). For each wind direction α, it is possible to see the static and dynamic contribution of the wind effects, particularly for the sector around 292° there are maximum values of the actions. The

differences between the static part and the dynamic part are underlined. The acceleration is calculated at the corner of the building, combing acceleration a_x and a_y, respectively, with the contribution of the torsional acceleration a_z. In Figure 9, point P represents a generic point on the building floor; d_x and d_y are the distances of P from the centroid in x- and y-direction, respectively. The maximum design acceleration at point P is given by $a_{Sdx} = a_x + d_y a_z$ and $a_{Sdy} = a_y + d_x a_z$.

6. Design Limits

The stress forces and the acceleration, calculated by the PIM and the HFFB procedures, show the dynamic effects due to the geometrical slenderness and shape of the building. The value of shear force (F) and the moment (M) at the base of building and top acceleration (a_{Sd}) are evaluated by two procedures described above which are different from those prescribed in the international codes. The codes used for the comparisons are the Eurocode 1 (EC1) and the Italian CNR DT207/2008 (CNR) indicated in the Italian code (DM 2008).

For the stress forces, comparison is carried out considering the base shear force for $T_R = 100$ years (ULS). In the codes (EC1, DM 2008, and CNR), the base shear force along-wind direction (design value) is very similar to that evaluated by the HFFB, but it is different for the across-wind direction. Using the wind velocities estimated for the site [41], the base shear force (F_0) is shown in Table 3.

(a)

(b)
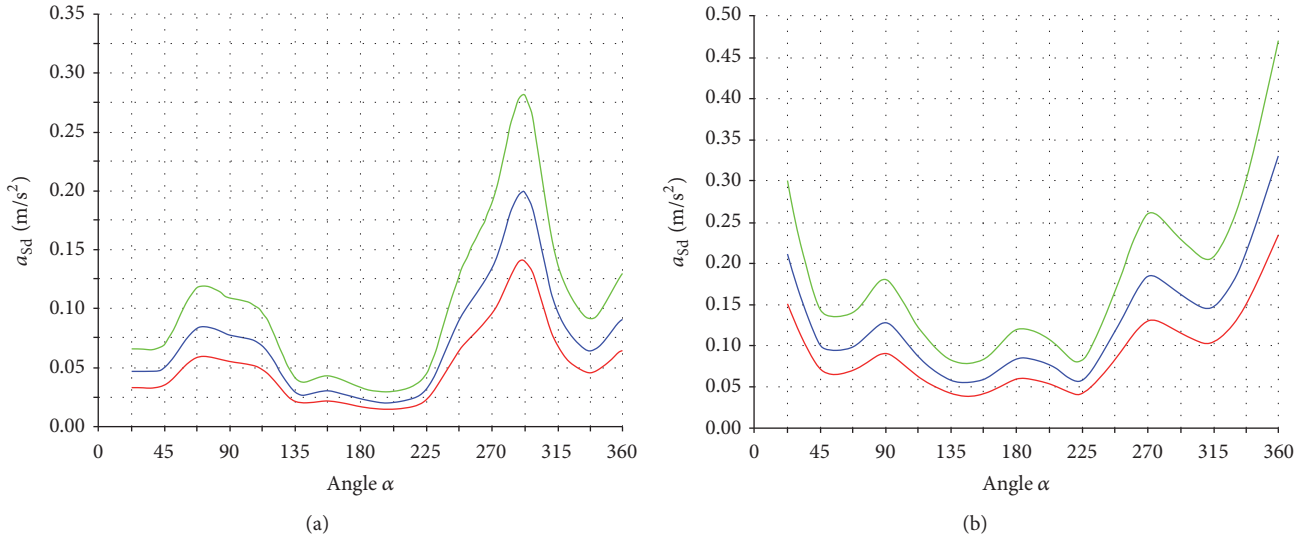
FIGURE 8: Acceleration response for different damping ratios ξ: (a) in x-direction and (b) in y-direction (the torsional component is considered).
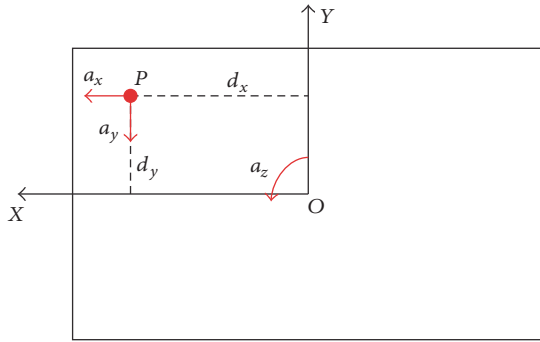
FIGURE 9: Representation of a point P for acceleration estimation.

Among the applicable codes in Italy, the across-wind effects can be evaluated only by the CNR, but, in their evaluation, the CNR does not consider the maximum wind velocity (38 m/s for $\alpha = 292.5°$), since it takes in account only the wind speed in correspondence to the main axes of the building. Using the CNR, the structure does not appear afflicted by the vortex shedding, actually realized in wind tunnel testing, which causes high value of stress effects in across-wind direction. From the codes, evaluating the vortex shedding critical velocity v_{cr} and comparing it with the reference velocity v_{ref}, it results that the vortex shedding does not exist in the present building case. In fact, for $v_{cr} = 50$ m/s ($T_R = 10$ years) the following relations are satisfied:

$$v_{cr} < 1.25 v_{ref} \longrightarrow 50 \, \text{m/s} < 39.68 \, \text{m/s} \, (= 1.25 \cdot 31.75 \, \text{m/s}), \quad \text{(valid for EC1)},$$

$$v_{cr} < v_{ref} \longrightarrow 50 \, \text{m/s} < 31.90 \, \text{m/s}, \quad \text{(valid for CNR)}. \tag{11}$$

In the estimation of v_{cr}, structural damping is not naturally set, but in case of reinforced concrete structure it ranges between $\xi = 0.8$ and 2% (for the SLS, it would be more advantageous to use an high values of ξ). In this building, natural structural damping is taken as 1%. The comparison in terms of acceleration in y-direction is shown in the Table 4 for $T_R = 10$ years (SLS) and for two different damping ratios ($\xi = 1\%$ and $\xi = 4\%$).

From Table 4 one can see that, in the CNR code, the dynamic effects of the wind are taken into account, even if these are overestimated. In Table 5, the displacements obtained by wind tunnel tests, as well as with PIM, are listed.

7. Improvements

From above two procedures applied in wind tunnel test (HFFB and APTH), wind induced responses in the building are determined. In order to reduce those responses up to the acceptable limit prescribed in standard code, there needs to be some improvements in the building. The improvements in the building are analyzed in terms of (i) reduction of height, (ii) changing internal structural configuration by putting belt truss in different level, (iii) installation of damping devices (TMD and VD), and (iv) changing the orientation of building. Before analyzing those improvements, it is necessary to clarify some questions about the wind velocity (Section 7.1).

TABLE 3: Shear design value at the base of the building.

Wind direction	v_{ref} [m/s]	Shear direction	F_0 [kN], CNR (EC1)	F_0 [kN], HFFB
0°–180°	34,4	Along-wind	12211 (10392)	10816
		Across-wind	10079	33863
90°–270°	32,5	Along-wind	31881 (31000)	33597
		Across-wind	13322	15499
292.5°	38	x	—	27955
		y	—	46052

TABLE 4: Stress design acceleration.

	PIM	HFFB	CNR	EC1
a_{max} ($\xi = 1\%$ - $T_R = 10$ years) [m/s^2]	0.45	0.47	0.53	0.19
a_{max} ($\xi = 4\%$ - $T_R = 10$ years) [m/s^2]	0.25	0.24	—	—

TABLE 5: Stress design displacements.

	Wind tunnel tests	PIM
δ_{max} ($\xi = 1\%$ - $T = 10$ anni) [m]	0.45	0.41
δ_{max} ($\xi = 4\%$ - $T_R = 10$ anni) [m]	0.25	0.22

7.1. Wind Velocity and the Building Orientation.

To determine the site wind velocity, it is necessary to take in account two coefficients: the missing data correction coefficient c_1 [51] and the directional coefficient c_2 [52]. If c_2 was estimated by Kasperski in place of Cook [53] referring to [51], the maximum value of the site wind velocity could be decreased. For the north-west sector (270°–360°) the wind site study sets the reference velocity v_{ref} = 28.5 m/s (for T_R = 100 years and quote z = 100 m). Tacking in account the missing data coefficient c_1 = 1.14 and the directional correction coefficient c_2 = 1.15 (by Cook), the reference velocity increases to the new value of v_{ref} = 37.3 m/s. As mentioned before, considering Kasperski [52] c_2 decreases to c_2 = 1.11 obtaining a new value v_{ref} = 36.06 m/s. This last value is lower than the first one but always higher than the code no-directional velocity estimated by the Italian regulation v_{ref} = 33.25 m/s (T_R = 100 years, at 100 m). Keeping in mind the fact that the wind velocity is changed with the direction, one can find an optimal ordination for the building that can result in minimized overall loads and responses. The effect of wind directionality on the responses will be investigated later in this study (Section 7.5).

7.2. Height Reduction.

It is obvious that higher the building, the higher the flexibility, for the same footage. Here the study focuses on how sensitive the wind induced responses are to change in the building height. In the first design phase, the building height was 225 m; a reduction in the height in the order of 12.5% was considered to check the response sensitivity. The reduction in the height was considered to

TABLE 6: Percentages of increase in the dominant frequencies.

Vibrational mode shape	Δf [%]
I (flexural along x)	19
II (flexural along y)	18
III (torsional around z)	19

understand its effect as an alternative to installing a TMD, or modifying the layout of the building, by creating belt internal trusses.

The reduction in the height was achieved by eliminating the top five floors. Apparently, the reduction involves the loss of five floors, but if we consider the fact that the structure supporting the TMD needs three floors, the reduction of height actually leads to a loss of two floors, saving costs and execution time. Consequently, the slenderness decreases to $\lambda \cong 8.50$ leading to (i) a reduction of the displacement at the top; (ii) a reduction of base forces and moments; and (iii) an increase in the structural stiffness, with rigidity improvement. If we consider a simplified cantilever beam model, for the same bending stiffness (EI) of the cross-section and the same distributed load (p), along the height (H), the initial displacement (δ_i) and the reduced displacement (δ_r) are given by (per unit load)

$$\delta_i = \frac{\left(pH_i^4\right)}{(8EI)},$$

$$\delta_r = \frac{\left(pH_r^4\right)}{(8EI)} = 0.59 \times \frac{\left(pH_r^4\right)}{(8EI)}. \tag{12}$$

Thus, the reduction in the displacement at the top is about $\Delta\delta \cong 41\%$. Considering that the base shear is proportional to the height of the building, and the base moment is a quadratic function of the building height (under the same load p), the reduction in the base shear is $\Delta F \cong 12.5\%$ and the reduction in the bending moment is $\Delta M \cong 23\%$. The initial stiffness of the building k_i = 8EI/H_i^3 is increased to k_r = 8EI/H_r^3 = $1.49 \times$ 8EI/H_i^3 under the same load. Thus, the increment is about $\Delta k \cong 49\%$. An estimate of the main frequencies could be obtained by the following simplified relation:

$$f = \frac{(k/m)^{1/2}}{2\pi}, \tag{13}$$

where k is estimated stiffness and m is mass. Due to reduction in height, total mass of building is decreased by (Δm = 5.55%) which ultimately increased the natural frequencies (Δf) as listed in Table 6 (about 20% increase). Combining the reduction in both wind speed and building height, improvements in terms of base shear reduction (ΔF_y), moment (ΔM_x) and top floor acceleration (Δa_{max}) reductions are listed in Table 7. All the improvements are verified by the HFFB method.

While Table 7 lists the combined effects of the reduction in the building height and the wind speed, the sole reduction in the responses due to the reduced building height is significant. The reductions in the base shear force are in the order of 13%, the reduction in the base bending moment is about 26%, and the reduction in the acceleration is about 21%.

TABLE 7: Structural improvements for different velocities and heights: reductions in the base shear and bending moments and the acceleration response of the top floor.

Configuration	H [m]	v [m/s]	ΔF_y [%]	ΔM_x [%]	Δa_{max} [%]
Initial	225	38 (Directional velocity)	—	—	—
Initial	225	33 (Directional velocity)	19.8	18.6	9.0
Initial	225	33 (No-directional velocity)	17.4	11	7.7
Proposed	199	38 (Directional velocity)	13	26	21
Proposed	199	36 (Directional velocity)	19.5	38.4	22
Proposed	199	33 (Directional velocity)	32.6	40.6	29.4
Proposed	199	33 (No-directional velocity)	28.2	38.3	15.3

7.3. Structural Configuration. To save the internal layout of the structure from significant changes that could result from increase of thickness, different structural configurations are considered. Introduction of an internal belt truss system or a beam-wall increases the stiffness of structure. This system consists of main cores linked with outer columns by stiff members which can be about one or more story depth. Under lateral wind loads, the internal moments are resisted by both core and tension/compression developed in outer columns. Thus the effectiveness of the building to carry bending is enhanced [23]. The configurations are characterized by beams height one or two interstory distance. It is possible to realize the beams in concrete (beam-wall case) or in S355 steel (belt truss case).

In both cases, the belt truss could span along two or four horizontal alignment with a depth of one or more stories as shown in Figure 10. In case of two alignments the belt truss can be placed either along the central axes or along the facades.

The analysis discussed in this paragraph is related to the building with a height of 225 m. The beam-wall or belt truss elements work as a stiffening bracing system along the axis x. The response reduction was investigated by using a belt truss system in the building at different levels. Three different cases are studied and configurations of each case are explained below.

Case 1. Two horizontal alignments of belt trusses with four interstory depths are considered. The configurations of the proposed bracing system for Case 1 over the building's height are (i) at 1/2 and top; (ii) at 1/2 and 3/4; (iii) at 1/4 and 1/2; (iv) at 1/2; and (v) at top as shown in Figure 11 (see also Table 8).

Case 2. Four horizontal alignments of the belt trusses with two interstory depth are considered, where the belt trusses are located (i) at 1/2 and (ii) at the top of the building (see Table 9).

Case 3. Four horizontal alignments of the belt truss with one interstory height are considered and belt trusses are introduced at 1/4, 1/2, and 3/4 of building height (see Table 10).

The comparisons between the original and the modified configurations are carried out in terms of decrease in base moment, ΔM_y [%]; increase in the first vibrational mode (along the axis x), Δf_1 [%]; and decrease of the top

TABLE 8: Comparisons between the original building and the solution proposed in Case 1, n. 4 interstories in height and n. 2 lines in horizontal length: Case 1.

Belt trusses quotes	ΔM_y	$\Delta \delta$	Δf_1	Note
1/2 and top	15.8%	45.8%	25.7%	Number 2 belt trusses – height: number 2 interstory
1/2 and 3/4	21.0%	50.0%	28.9%	Number 2 belt trusses – height: number 2 interstory
1/4 and 1/2	28.9%	47.9%	26.9%	Number 2 belt trusses – height: number 2 interstory
1/2	19.0%	43.7%	24.4%	Number 2 belt trusses – height: number 4 interstory
Top	6.0%	27.1%	13.6%	Number 2 belt trusses – height: number 4 interstory

TABLE 9: Comparison between the original building and the solution proposed in Case 2, n. 2 interstory in height and n. 4 lines in horizontal length: Case 2.

Belt trusses quotes	ΔM_y	$\Delta \delta$	Δf_1	Note
at 1/2	18.8%	45.8%	25.7%	Number 4 belt trusses – height: number 2 interstories
Top	5.8%	27%	12.9%	Number 4 belt trusses – height: number 2 interstories

displacement in x-direction, $\Delta \delta$ [%]. The improvements for all the cases are shown in Tables 8–10. If one looks at the general pattern from Tables 8, 9, and 10, it can be observed that the best solution to improve the structural behavior under wind load is to place the belt trusses at half height of the building rather than at the top, as confirmed in Table 11. Although there is maximum reduction of displacement ($\Delta \delta = 50\%$) in Case 1 when the belt trusses are at 1/2 and 3/4, the reduction in base moment is small as compared to the other configurations (1/4 and 1/2). Thus, among all configurations and best improvements in the base moment ($\Delta M_y = 28.9\%$),

(a)

(b)
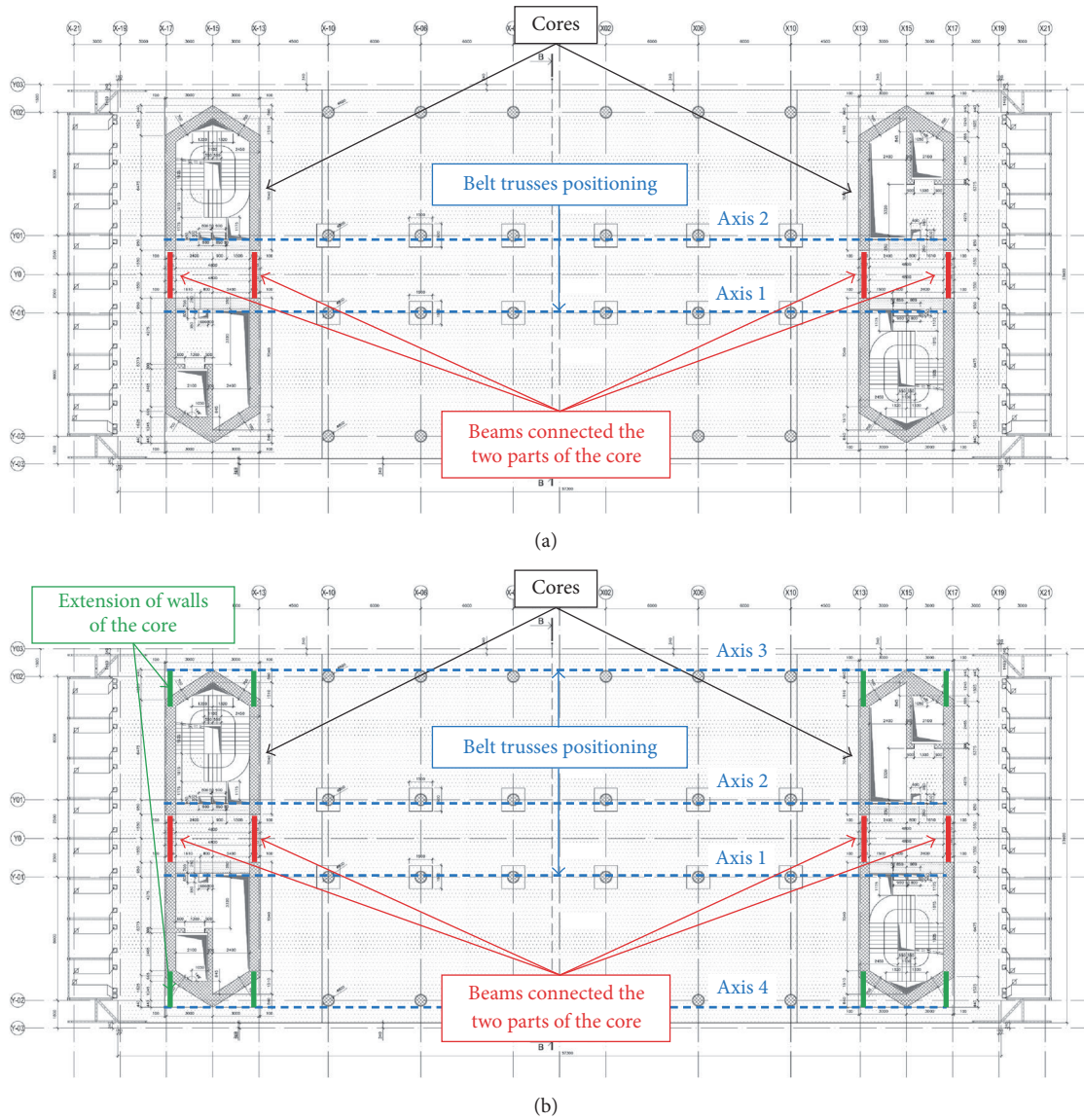
FIGURE 10: Schematic representation of the location of the built trusses in the top view: (a) two alignments and (b) four alignments.

TABLE 10: Percentages of response reduction achieved by the solution proposed in Case 3, n. 1 interstory in height and n. 4 lines in horizontal length: Case 3.

Belt trusses quotes	ΔM_y	$\Delta \delta$	Δf_1	Note
1/2, 1/4 and 3/4	18.4%	35.4%	19.8%	Number 3 belt trusses – height: number 1 interstory

TABLE 11: Effects of belt-truss location of the response.

Belt trusses quotes	ΔM_y	$\Delta \delta$	Δf_1	Note
top	4.2%	20.2%	9.4%	Number 2 belt trusses – height: number 2 interstories
1/2	14.0%	32.6%	18.6%	Number 2 belt trusses – height: number 2 interstories

the displacement ($\Delta \delta$ = 47.9%) and the natural frequency (Δf_1 = 26.9%) are achieved in Case 1, when the belt trusses are at 1/4 and 1/2 (Table 8).

The significant improvement in terms of natural frequency (Δf_1 = 28.9%, this value determines some dynamic effects related to the wind action) is represented by two belt

trusses with two interstory height located at 1/2 and 3/4, but the base moment is reduced significantly when belt trusses are at 1/4 and 1/2. Clearly, the solution with belt trusses with four interstory heights is more invasive for the layout of the building.

(a) 1/2 and top   (b) 1/2 and 3/4   (c) 1/4 and 1/2   (d) 1/2 (double)   (e) Top (double)

FIGURE 11: Schematic representation of the position of the belt trusses for Case 1: see Table 8.

Therefore, structural improvements related to some different structural configurations are illustrated. Each configuration is characterized by the insertion of concrete beam-wall or steel belt truss to increase the stiffness of the building. The concrete beam-wall seems easier to realize in comparison to the belt truss but the presence of the necessary openings in the longitudinal beam-walls is negative for the strut and tie behavior (thus, only f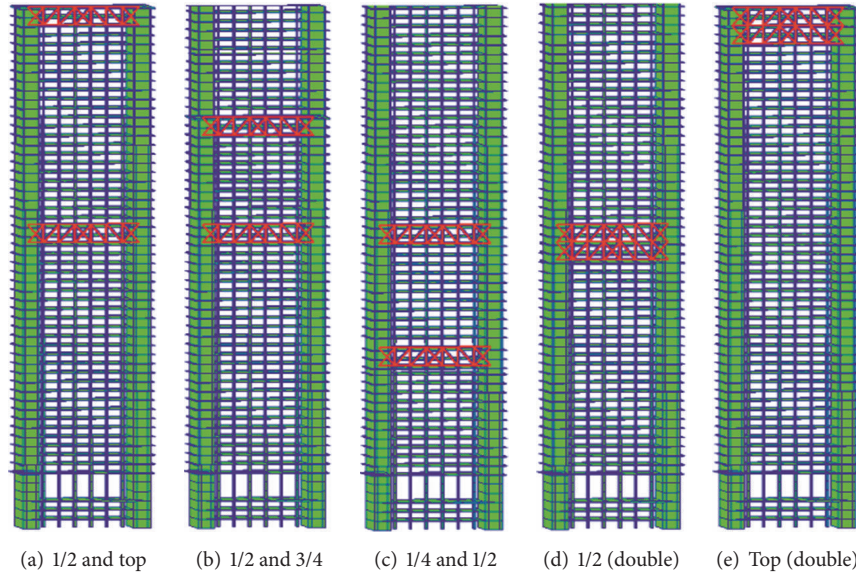ew openings could be realized). Conversely, the configurations with steel belt trusses guarantee the strut and tie behavior but their positioning could be painstaking.

7.4. Installation of Dampers. To improve the structural behavior some active or passive mass dumpers solutions could be considered [6, 54–56]. In the present case, a solution represented by TMD is taken into account. The damper is represented by a nodal mass linked to center of gravity of top floor, by a linear spring-damper element. The mass damper is implemented in the FEM of building, as well as the HFFB procedure. The TMD stiffness ratio and the coefficient of damping are evaluated according to [55]. The TMD was assumed to be installed at top of the tower, making use of the top three stories, which has increased the structural damping from 1% to 4%. Response reduction is analyzed in terms of reduction in base shear for different wind direction angles. Significant reduction in base shear is achieved by installation of TMD as listed on Table 12. It can be observed from Table 12 that the base shear is considerably reduced in each wind direction angle; however, the highest reduction ($\Delta F = 43.46\%$) is obtained along the x-axis at a damping ratio ξ of 4.0%, when the wind angle is 292.5°.

Another solution, represented by VDs, is implemented in the FE model as shown in Figure 12. The dampers are installed transversely in the cores from the base up to the 20th floor. The installation includes problems due to the openings in the walls of the cores to pass from the elevator areas to the inner

TABLE 12: Improvements by the TMD.

Wind direction	Base shear direction	F_0 [kN], HFFB $- v_{\text{site}}$, $\xi = 1.0\%$	F_0 [kN], HFFB $- v_{\text{site}}$ $\xi = 4.0\%$
0°–180°	Along-wind	10816	8338
	Across-wind	33863	19847
90°–270°	Along-wind	33597	27718
	Across-wind	15499	10875
292.5°	x-axis	27955	15803
	y-axis	46052	35697

areas. By installing viscous dampers base shear is reduced by $\Delta T_0 = 45\%$ (at ULS), peak acceleration in x-direction is reduced by $\Delta a_x = 25\%$ (at SLS), and displacement at the top of building is reduced by $\Delta\delta = 33\%$ (at ULS). Although viscous dampers are effective in reducing displacement and base shear, they are not that effective in reducing peak acceleration of building. Despite the installation of viscous dampers, the peak acceleration obtained is 0.32 m/s², which is greater than the comfort limit of 0.2 m/s² (for office usage). In order to get compatible value of acceleration (smaller than 0.20 m/s²) installation of viscous damper should be extended up to 35th story.

7.5. Global Layout. The wind direction angle and interference effects are two important factors that should be carefully studied early in the design phase. Wind loads and responses in high-rise buildings depend on wind direction angle and interference of existing building in that area. Since the approaching wind flow may have different mean wind speeds when it reaches the building from different directions, and considering the fact that along-wind and the cross wind responses are different, it is feasible to rotate original building
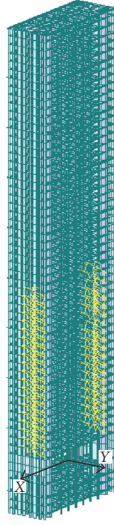
FIGURE 12: FEM with the viscous dampers implemented in the cores.

FIGURE 13: Representation of the orientation change.

TABLE 13: Percentages of response reduction for two proposed orientations.

TA rotation	$\Delta a_{\mathrm{Sd},y}$	$\Delta \delta_{\mathrm{Sd},y}$
45°	13%	11%
65°	28%	24%

layout in such a way that the wind induced responses are reduced [57].

From the dynamic procedures and the tests in the wind tunnel, it is possible to understand the most correct layout for building, especially if other tall buildings will rise up nearby [58]. The decrease of the stress effects in y-direction is obtained by 45° clockwise rotation of building from the initial layout (Figure 13). When the building is rotated by 45° there was only slight reduction of responses, but in case of 65° clockwise rotation the highest reductions of acceleration and the displacement at the top are obtained (Table 13 where symbol of acceleration is $a_{\mathrm{Sd},y}$, and the displacement is $\delta_{\mathrm{Sd},y}$).

Acceleration in y-direction is decreased by 27.27% ($a_{\mathrm{Sd},y}$ is reduced: from $0.88 \, \mathrm{m/s}^2$ to $0.64 \, \mathrm{m/s}^2$) and displacement in y-direction is also reduced by 25% ($\delta_{\mathrm{Sd},y}$ is decreased from 1.20 m to 0.90 m). Despite the mentioned improvements in y-direction, the 65° clockwise rotation of building from the original layout has increased the acceleration ($a_{\mathrm{Sd},x}$) and the displacement ($\delta_{\mathrm{Sd},x}$) in x-direction. In the x-direction, acceleration is increased by 9% and displacement is increased by 3.5% ($a_{\mathrm{Sd}x}$ is changed from $0.53 \, \mathrm{m/s}^2$ to $0.58 \, \mathrm{m/s}^2$ and $\delta_{\mathrm{Sd},x}$ is changed from 0.85 m to 0.88 m). Since wind effects in the x-direction are low, compared to y-direction, slight increase of responses in x-direction could be acceptable, as compared to large reduction of responses in y-direction.

This reduction in responses is achieved without adding any structural element or component in the primary building, hence no additional cost on the building. This confirms the
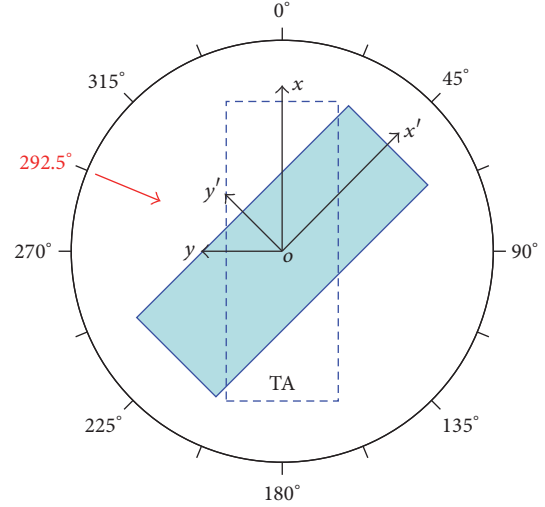
advantage of rotating the building to the suggested orientation. It also explores the significance of response prediction in high-rise building during preliminary design stage.

8. Conclusions

In this paper, some limits of available design standards (Eurocode 1 & the Italian design code) to evaluate wind actions on high-rise buildings (displacements and acceleration responses) are presented, pointing them out in a comparison to a more sophisticated methods (i.e., the use of the PIM with FEM of the building, and the HFFB technique). These limits are highlighted by the fact that the detailed analysis method resulted in higher base shear and moment values than those provided by the design standards, and that was strongly influenced by the high aspect ratio of the building. In fact, vortex shedding effects were realized in the current study in both results obtained by the PIM and the HFFB methods, and such phenomenon was greatly dependent on the building geometry which is not fully addressed in the codes.

Structural improvements are proposed which resulted in considerable response reductions, without significantly alerting the architectural shape of the original building. These solutions include (i) height reduction, (ii) steel belts, (iii) tuned mass damper, (iv) viscous dampers, and (v) orientation change. A reduction in the apparent height in the order of 12.5% was considered to check the response sensitivity. The reduction in the height was considered to understand its effect as an alternative to installing a TMD. The reduction in the height was achieved by eliminating the top five floors. Apparently, the reduction involves the loss of five floors, but if we consider that the structure supporting the TMD needs three floors, the reduction of height actually leads to a loss of only two floors. This height lessening led to reduced base shear force, in the order of 13%, reduced base bending moment (26%), and reduced acceleration (21%).

Belt truss systems with different structural configurations are studied and compared in terms of their capability to

bring reduction to the base bending moment, reduction of displacement at the top, and the increase of natural frequencies. The optimal numbers and location of belt trusses are determined by comparing three different cases for the maximum reduction of wind induced responses. In each case, it is observed that the performance of the belt truss systems is at its maximum level when they are placed at half height of the building rather than at the top. It can also be concluded that two horizontal alignments of belt trusses along the major axis of the building are more effective than four alignments, considering same number of belt trusses. Nevertheless, two horizontal alignments of belt trusses with two interstory depths located at 1/4 and 1/2 the height of the building (Case 1) are efficient in reducing the responses, where the displacement at the top is reduced by about 48% and the bending moment is reduced by 29%.

Vibration suppression by the installation of a TMD is evaluated by reductions in the base shear and bending moments, as well as displacement and acceleration. Results show considerable reduction in base shear in each wind direction angle; however a maximum reduction in base shear (43.5%) is achieved by an equivalent damping ratio of 4.0%, when the wind direction angle is 292.5°. The TMD appears to be a valid technical solution but, in order to implement it, the loss of the top three floors has to be considered, which is necessary to build the structure supporting the TMD.

Another improvement is presented by viscous dampers, where the dampers are installed transversely in the cores from the base up to the 20th floor. VDs were installed to examine their potential to reducing the base loads, peak acceleration, and the maximum displacement. Substantial improvements are achieved using viscous dampers: base shear is reduced by 45%, peak acceleration is lessened by 25%, and the displacement is reduced by 33%. Although the installation of viscous dampers up to the 20th floor is effective in reducing displacement and base shear, it is not enough to reduce the peak acceleration to the prescribed limits. Thus, the installation of VDs up to the 35th floor was suggested.

Finally, the importance of the global positioning of the building (orientation change) was examined, considering its rotation with respect to an original layout. The rotation of the building by 65° from the initial layout resulted in the highest reduction in displacement and acceleration. The reduction in the acceleration is 27% whereas the displacement is reduced by 25%. This reduction in responses is achieved without adding any structural elements or components to the primary building, hence no additional cost. This reveals the advantage of rotating the building to the suggested orientation and highlights the significance of response prediction in high-rise buildings during the preliminary design stage.

Conflicts of Interest

The authors declare that there are no conflicts of interest regarding the publication of this paper.

Acknowledgments

References

[1] A. Farouk, *High Rise Buildings and How They Affect Countries Progression*, Department of Architecture Engineering, Cairo University, 2011, https://www.g-casa.com/conferences/zagreb/papers/Akram1-HighRise.pdf.

[2] H. Y. O. S. Park and C. L. I. M. Park, "Drift control of high-rise buildings with unit load method," vol. 6, pp. 23–35, 1997.

[3] H. S. Park, H. G. Sohn, I. S. Kim, and J. H. Park, "Application of GPS to monitoring of wind-induced responses of high-rise buildings," *The Structural Design of Tall and Special Buildings*, vol. 17, no. 1, pp. 117–132, 2008.

[4] T. Kijewski, "Full-scale study of the behavior of tall buildings under winds," *Proc. SPIE*, vol. 4337, no. 219, pp. 441–450, 2001.

[5] R. Rana and T. T. Soong, "Parametric study and simplified design of tuned mass dampers," *Engineering Structures*, vol. 20, no. 3, pp. 193–204, 1998.

[6] A. M. Aly, "Vibration control of high-rise buildings for wind: A robust passive and active tuned mass damper," *Smart Structures and Systems*, vol. 13, no. 3, pp. 473–500, 2014.

[7] Y.-M. Kim, K.-P. You, and H.-Y. Kim, "Wind-induced excitation control of a tall building with tuned mass dampers," *The Structural Design of Tall and Special Buildings*, vol. 17, no. 3, pp. 669–682, 2008.

[8] A. Kareem, T. Kijewski, and Y. Tamura, "Mitigation of Motion of Tall Buildings with Specific Examples of Recent Applications," *Wind Struct*, vol. 2, no. 3, pp. 201–251, 2007.

[9] K. A. O'Connor, J. D. Johnson, S. E. Hammack et al., "Inescapable shock induces resistance to the effects of dexamethasone," *Psychoneuroendocrinology*, vol. 28, no. 4, pp. 481–500, 2003.

[10] S. Nagarajaiah and B. Basu, "Output only modal identification and structural damage detection using time frequency wavelet techniques," *Earthquake Engineering and Engineering Vibration*, vol. 8, no. 4, pp. 583–605, 2009.

[11] Y. Fujino, L. Sun, B. M. Pacheco, and P. Chaiseri, "Tuned liquid damper (TLD) for suppressing horizontal motion of structures," *Journal of Engineering Mechanics*, vol. 118, no. 10, pp. 2017–2030, 1992.

[12] M. J. F. Silva and A. C. Costa, "Experimental Studies On The Characteristics Of Tuned Liquid Dampers For Reducing Vibration In Structures," in *Proceedings of the 14th World Conference Earthquake*, China, 2008.

[13] H. F. Bauer, "Oscillations of immiscible liquids in a rectangular container: A new damper for excited structures," *Journal of Sound and Vibration*, vol. 93, no. 1, pp. 117–133, 1984.

[14] N. Makris, M. C. Constantinou, and G. F. Dargush, "Analytical model of viscoelastic fluid dampers," *Journal of Structural Engineering*, vol. 119, no. 11, pp. 3310–3325, 1994.

[15] M. C. Constantinou and M. D. Symans, "Seismic response of structures with supplemental damping," *The Structural Design of Tall and Special Buildings*, vol. 2, no. 2, pp. 77–92, 1993.

[16] C. Prabha and L. Mathew, "Effect of Fluid Viscous Dampers in Multi-Storeyed Buildings," *International Journal of Research in Engineering and Technology*, vol. 2, no. 9, pp. 59–64, 2014.

[17] D. P. Taylor, *Using Modern Technology for the Reduction of Earthquake Damage in Buildings*, Taylor Devices Inc, North Tonawanda, NY, USA, 2012, http://taylordevices.com/pdf/2013-dampers/Change%2012.pdf.

[18] M. Constantinou, "Application of fluid viscous dampers to earthquake resistant design," in *Report on Research Accomplishments 1986–1994*, pp. 73–80, National Center for Earthquake Engineering and Research, Buffalo, NY, USA, 1994, http://cidbimena.desastres.hn/pdf/eng/doc8169/doc8169-contenido.pdf.

[19] R. J. McNamara, D. P. Taylor, and P. Duflot, "Fluid Viscous Dampers to Reduce Wind-Induced Vibrations in Tall Buildings," Tech. Rep., Taylor Devices Europe, Brussels, 2005, http://www.taylordevices.eu/pdfs/tall-building_1.pdf.

[20] P. S. Kumar, M. V. Naidu, S. M. Mohan, and S. S. Reddy, "Application of Fluid Viscous Dampers In Multi-Story Buildings," *Application of Fluid Viscous Dampers In Multi-Story Buildings*, pp. 17064–17069, 2016.

[21] K. Ding, X. Zhao, Y. Yang, and L. Ye, "Application of viscous dampers for super tall residential buildings in high-wind strong-seismic area," in *Proceedings of the 2016 World Congress on Advances in Civil, Environmental, and Materials Research (ACEM16)*, Jeju Island, South Korea, August 2016.

[22] A. Khanorkar, S. V. Denge, and S. P. Raut, "Belt truss as lateral load resisting structural system for tall building: a review," *IJSTE - International Journal of Science Technology & Engineering*, vol. 2, no. 10, pp. 658–662, 2016.

[23] B. M. Simantini and M. Manjunath, "An analysis of outrigger belt truss system in high-rise buildings," *IUP Journal of Structural Engineering*, vol. 8, no. 3, pp. 16–25, 2015.

[24] R. S. Nair, "Belt Trusses and Basements as "Virtual" Outriggers for Tall Buildings," *Engineering Journal*, vol. 35, no. 4, pp. 140–146, 1998.

[25] P. S. Kian, "The use of outrigger and belt truss system for high-rise concrete buildings," *Civil Engineering Dimension*, vol. 3, no. 1, pp. 36–41, 2001.

[26] Eurocode., "Eurocode 1: Actions on Structures Part 1-4: General Actions Wind actions," *prEN 1991-1-4, European Standard*, 2004.

[27] CNR., "Istruzioni per la valutazione delle azioni e degli effetti del vento sulle costruzioni," in *Proceedings of the CNR – Commissione di studio per la predisposizione e l'analisi di norme tecniche relative alle costruzioni, CNR-DT 207/2008*, 2009 (Italian), http://people.dicea.unifi.it/gianni.bartoli/normative/CNR_DT207_2008.pdf.

[28] R. McNamara, A. Kareem, and T. Kijewski, "Ask the experts. Perception of motion criteria for tall buildings subjected to wind: a panel discussion," in *Proceedings of the 2002 Structures Congress*, Reston, Va, USA, 2002.

[29] K. C. S. Kwok, P. A. Hitchcock, and M. D. Burton, "Perception of vibration and occupant comfort in wind-excited tall buildings," *Journal of Wind Engineering & Industrial Aerodynamics*, vol. 97, no. 7-8, pp. 368–380, 2009.

[30] M. D. Burton, K. C. S. Kwok, and A. Abdelrazaq, "Wind-Induced Motion of Tall Buildings: Designing for Occupant Comfort," *The International Journal of High-Rise Buildings*, vol. 4, no. 1, pp. 1–8, 2015.

[31] A. W. Irwin, "Human response to dynamic motion of structures," *Structural Engineering*, vol. 56, no. 9, 1978.

[32] T. Goto, T. Ohkuma, Y. Tamura, and O. Nakamura, "Guidelines for the evaluation of habitability to building vibration. Part II: AIJ recommendations," in *Proceedings of the Structures Congress' 92*, vol. 92, pp. 484–487, 1991.

[33] L. G. Griffis, "Serviceability limit states under wind load," *Engineering Journal*, vol. 30, no. 1, pp. 1–16, 1993.

[34] M. Huang, C. Chan, and K. C. Kwok, "Occupant comfort evaluation and wind-induced serviceability design optimization of tall buildings," *Wind and Structures An International Journal*, vol. 14, no. 6, pp. 559–582, 2011.

[35] M. Belloli, L. Rosa, and A. Zasso, "Wind loads on a high slender tower: Numerical and experimental comparison," *Engineering Structures*, vol. 68, pp. 24–32, 2014.

[36] L. Rosa, G. Tomasini, A. Zasso, and A. M. Aly, "Wind-induced dynamics and loads in a prismatic slender building: A modal approach based on unsteady pressure measurements," *Journal of Wind Engineering & Industrial Aerodynamics*, vol. 107-108, pp. 118–130, 2012.

[37] P. Mendis, T. Ngo, N. Haritos, A. Hira, B. Samali, and J. Cheung, "Wind loading on tall buildings," *EJSE Special Issue: Loading on Structures*, vol. 3, pp. 41–54, 2007.

[38] S. O. Hansen, "Vortex-induced vibrations of structures," in *Proceedings of the Structural Engineers World Congress*, Bangalore, India, November 2007, http://citeseerx.ist.psu.edu/viewdoc/download?doi=10.1.1.547.4368&rep=rep1&type=pdf.

[39] A. Kareem, "Wind induced torsional loads on structures," *Engineering Structures*, vol. 3, no. 2, pp. 85-86, 1981.

[40] P. Irwin, R. Denoon, and D. Scott, *Wind Tunnel Testing of High-Rise Buildings: An output of the CTBUH Wind Engineering Working Group*, Council on Tall Buildings and Urban Habitat, Chicago, USA, 2013, https://store.ctbuh.org/PDF_Previews/Books/2013_WindTunnelGuide_Preview.pdf.

[41] M. P. Repetto, G. Solari, F. Tubino, and A. Freda, "Analisi del vento di progetto presso il quartiere storico dellarea della Fiera di Milano," *SGS_PRE_VEN_SPC_002(B) Genova*, 2006.

[42] A. Zasso, A. M. Aly, L. Rosa, and G. Tomasini, "Wind induced dynamics of a prismatic slender building with 1: 3 rectangular section," in *Proceedings of the VI International Colloquium on Bluff Bodies Aerodynamics Applications*, Milan, Italy, 2008.

[43] A. M. Aly, "Pressure integration technique for predicting wind-induced response in high-rise buildings," *Alexandria Engineering Journal*, vol. 52, no. 4, pp. 717–731, 2013.

[44] M. F. Huang, Q. Li, and W. Lou, "Uncertainty quantifications in HFFB dynamic analyses of a complex tall building," in *Proceedings of the 2016 World Congress on Advances in Civil, Environmental, and Materials Research (ACEM16)*, Jeju Island, South Korea, August 2016.

[45] X. Chen and A. Kareem, "Validity of wind load distribution based on high frequency force balance measurements," *Journal of Structural Engineering*, vol. 131, no. 6, pp. 984–987, 2005.

[46] T. Tschanz and A. G. Davenport, "The base balance technique for the determination of dynamic wind loads," *Journal of Wind Engineering and Industrial Aerodynamics*, vol. 13, no. 1, pp. 429–439, 1983.

[47] N. Lin, C. Letchford, Y. Tamura, B. Liang, and O. Nakamura, "Characteristics of wind forces acting on tall buildings," *Journal of Wind Engineering & Industrial Aerodynamics*, vol. 93, no. 3, pp. 217–242, 2005.

[48] S. Pasto, L. Facchini, L. Procino, and P. Spinelli, "Equivalent static wind loads on tall buildings," in *Proceedings of the VI International Colloquium on Bluff Bodies Aerodynamics Applications*, pp. 20–24, Milan, Italy, 2008.

[49] J. A. Peterka and J. E. Cermak, "Wind pressures on buildings-probability densities," *Journal of the Structural Division*, vol. 101, no. 6, pp. 1255–1267, 1975.

[50] N. J. Cook, "Calibration of the quasi-static and peak-factor approaches to the assessment of wind loads against the method of Cook and Mayne," *Journal of Wind Engineering & Industrial Aerodynamics*, vol. 10, no. 3, pp. 315–341, 1982.

[51] M. P. Repetto, G. Solari, and M. Tizzi, "Il ruolo dei dati mancanti nella statistica dei venti estremi," *in XI Convegno Nazionale di Ingegneria*, 2010.

[52] M. Kasperski, "Design wind loads for a low-rise building taking into account directional effects," *Journal of Wind Engineering & Industrial Aerodynamics*, vol. 95, no. 9-11, pp. 1125–1144, 2007.

[53] N. J. Cook, "Note on directional and seasonal assessment of extreme winds for design," *Journal of Wind Engineering & Industrial Aerodynamics*, vol. 12, no. 3, pp. 365–372, 1983.

[54] S. M. Zahrai and S. Abbasi, "Study on Possibility of Using Tuned Liquid Dampers (TLD) in High Frequency Structures," in *International Conference on Technological advancements in Civil engineering (ICTACE 2012)*, 2012.

[55] T. T. Soong and M. C. Costantinou, *Passive and active structural vibration control in civil engineering*, vol. 345, Springer, 2014.

[56] A. M. Aly Sayed Ahmed, A. Zasso, and F. Resta, "Proposed configurations for the use of smart dampers with bracings in tall buildings," *Smart Materials Research*, vol. 2012, Article ID 251543, 16 pages, 2012.

[57] A. M. Aly and S. Abburu, "On the design of high-rise buildings for multihazard: fundamental differences between wind and earthquake demand," *Shock and Vibration*, vol. 2015, Article ID 148681, 22 pages, 2015.

[58] A. M. Aly, "Influence of turbulence, orientation, and site configuration on the response of buildings to extreme wind," *The Scientific World Journal*, vol. 2014, Article ID 178465, 2014.

Research Article

Active Control for Multinode Unbalanced Vibration of Flexible Spindle Rotor System with Active Magnetic Bearing

Xiaoli Qiao and Guojun Hu

Shaoxing University Yuanpei College, Shaoxing 312000, China

Correspondence should be addressed to Guojun Hu; 514914515@qq.com

The unbalanced vibration of the spindle rotor system in high-speed cutting processes not only seriously affects the surface quality of the machined products, but also greatly reduces the service life of the electric spindle. However, since the unbalanced vibration is often distributed on different node positions, the multinode unbalanced vibration greatly exacerbates the difficulty of vibration control. Based on the traditional influence coefficient method for controlling the vibration of a flexible rotor, the optimal influence coefficient control method with weights for multinode unbalanced vibration of flexible electric spindle rotors is proposed. The unbalanced vibration of all nodes on the whole spindle rotor is used as the control objective function to achieve optimal control. The simulation results show that the method has an obvious control effect on multinode unbalanced vibration.

1. Introductions

Maglev support technology is one of the world's most recognized high-tech innovations. It can be used as a support technology for high-speed machine electric spindles in high-end CNC machine tools. With the increase of the spindle rotational speed, the spindle will show flexibility characteristics when the speed of the spindle rotor exceeds its critical speed. When a flexible spindle rotor is running at the first or higher critical speed, the different vibration mode determines the response characteristics of the spindle. Therefore, a real-time active control technique is required for the unbalanced vibration control of the flexible spindle rotor system. According to the vibration mode characteristics of the flexible spindle rotor, the control force is changed in real time, so that the vibration suppression of the rotor is optimized.

The conventional flexible rotor unbalanced vibration control method can be divided into two categories: modal method and influence coefficient method [1]. The biggest advantage of the coefficient method is that it does not depend on the mathematical model of the control object, which is independent of the modal characteristics of the rotor, and directly achieves vibration control based on the

relationships between the correction force and rotor node displacement. So, the influence coefficient method is one of the most promising methods in the field of unbalanced vibration control of flexible rotors. There are many studies on vibration control by use of the influence coefficient method. Tseng et al. [2] proposed a real-time dynamic balance scheme by the influence coefficient method. Li et al. [3] used the influence coefficient method to carry out the first two-order flexible modes of the rotor, respectively. Kim and Lee [4] recognized the sensor runout with the influence coefficient method without applying additional sensors and equipment and applied the influence coefficient method to the harmonic vibration suppression of the flexible rotor. Kang et al. [5] used an automatic balance method based on the influence coefficient method. The influence coefficient balancing equations, with suitable constraints on the level of the residual vibrations and the magnitude of correction weights, were cast in linear matrix inequality (LMI) forms and solved with the numerical algorithms developed in convex optimization theory by Untaroiu et al. [6]. Yu et al. [7] used the active magnetic bearing as the actuator, which detected the transfer function model to obtain the influence coefficient matrix to achieve the vibration suppression of the flexible spindle rotor. Knospe [8] proposed a flexible rotor unbalance control
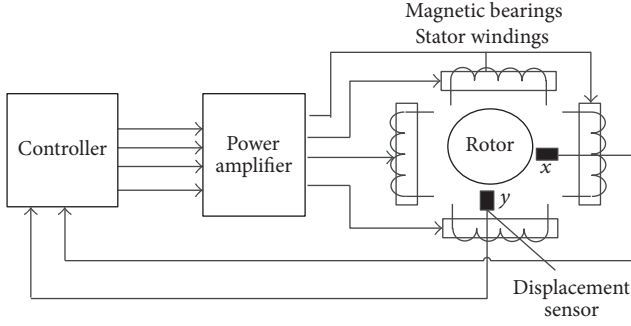
FIGURE 1: The working principle of an active magnetic bearing.

method based on the influence coefficient method. Lee et al. [9] proposed an active balancing method for rotating machinery using the influence coefficient method. Kang et al. [10] studied the optimal balancing of flexible rotors by minimizing the condition number of influence coefficients, and so on.

The flexible spindle vibration control method with active magnetic bearing is characterized in real time and online. According to the real-time situation of the flexible spindle vibration, the active magnetic bearing can adjust the electromagnetic correction force online to make the vibration control for the flexible spindle rotor achieve the best effect. So, the influence coefficient method with active magnetic bearing is the most widely used method for unbalanced control in flexible spindle rotors.

The traditional influence coefficient method for controlling flexible spindle rotor vibration needs to calculate the electromagnetic force by solving the multivariate system, which causes the number of vibration suppression nodes to be not more than the number of excitation nodes of the active magnetic bearing. In order to solve the above problem, the paper puts forward the optimal influence coefficient control method with weights for multinode unbalanced vibrations of flexible electric spindle rotors, which uses all the unbalanced vibration nodes of the whole spindle as the control objective function to achieve the optimal control of multinode unbalanced vibration.

2. Principle of Active Magnetic Bearing

A simplified active magnetic bearing control schematic diagram is shown in Figure 1; the rotor is free to be suspended in (x_0, y_0), which is at the center of the active magnetic bearing. The deviation of the rotor between the actual position (x, y) and the set (x_0, y_0) is detected by a noncontact position sensor, which is fed back to the control device. The control objective is to maintain the rotor near the expected value (x_0, y_0). In this way, according to the deviation between the actual position (x, y) and the set position (x_0, y_0), a position adjustment command signal is produced by the controller, which is converted into a current by a power amplifier. The current is inputted to the bearing electromagnet coil to produce the desired electromagnetic control force $(F_{m,x}, F_{m,y})$, which makes rotor stability suspension [11].

3. Dynamic Model of the Flexible Spindle Cutting System Supported by Active Magnetic Bearings

3.1. Finite Element Model of Magnetic Bearing-Flexible Spindle Cutting System. The simplified structure of the flexible electric spindle with an active magnetic bearing is shown in Figure 2(a). The active magnetic bearing-flexible spindle cutting system mainly includes a high-speed motor rotor, different sizes of elastic spindle sections, active magnetic bearings, cutter holder, cutter, and other components. When the finite element model of the flexible magnetic spindle machining system is established, the following is simplified: the rotor, cutter holder, and cutter of the motor are equivalent to isotropic materials in order to reduce the computer's calculation time. The simplified electric spindle rotor system is divided into shafts of different sizes, magnetic bearings, cutters, and other units along the central axis of the spindle, and the units are connected to each other at the nodes. The finite element model of the spindle rotor system is shown in Figure 2(b). $n1, n2, n3, n4, n5, n6, n7,$ and $n8$ are nodes in the motorized spindle rotor.
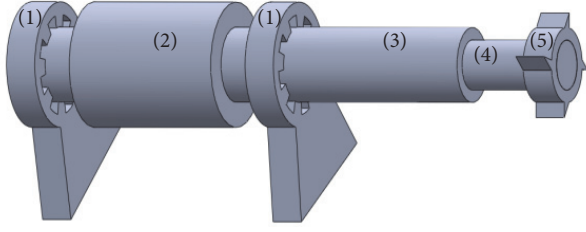
The finite element model of the spindle rotor system is established according to the rotor dynamics theory. Among them, the magnetic bearing characteristics, in the form of electromagnetic force, are applied to the corresponding spindle node. The dynamic cutting process is also a dynamic cutting force, which is applied to the cutter node.

The center axis of the spindle is defined as the z-axis, and the plane perpendicular to the z-axis is the X-Y plane to establish the $OXYZ$ coordinate system. So, the spindle position can be represented by the coordinates of the x- and y-axis and cross section of the deflection angles θ_x and θ_y in any section. The finite element model of the flexible magnetic spindle machining system is [12, 13]

$$M_s \ddot{U} + (D_s + \Omega_s G_s) \dot{U} + K_s U = F_{am} + F_{um}, \qquad (1)$$

where M_s represents the mass matrix, K_s represents the stiffness matrix, D_s represents the damping matrix, G_s represents the gyro matrix, Ω_s represents the steady-state working speed of the electric spindle, F_{um} represents the unbalanced force of all the nodes on the electric spindle rotor, F_{am} is the radial electromagnetic control force of the active magnetic bearing, and n represents the total number of unit nodes. The subscripts x and y represent the direction of the coordinate axes, respectively. The stiffness and damping in (1) mainly refer to the equivalent stiffness and damping generated by the active magnetic bearing and the controller, the stiffness and structural damping of the spindle, and the stiffness and damping in the dynamic cutting process.

3.2. Equivalent Electromagnetic Force Model of Active Magnetic Bearings. The equivalent electromagnetic force model of the active magnetic bearing has been deduced in detail in the relevant books and literature, and the process is not deduced here. This paper still adopts the differential

(a) The simplified structure of the flexible motorized spindle with the active magnetic bearing. (1) Active magnetic bearing (AMB), (2) rotor, (3) motorized spindle, (4) cutter holder, and (5) cutter
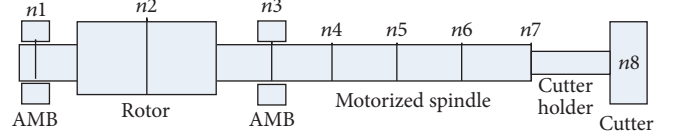
(b) The finite element model of the spindle rotor system

FIGURE 2: The flexible motorized spindle with the active magnetic bearing.

electromagnetic structure to carry on the active electromagnetic force model establishment [14]. The differential control structure of the active magnetic bearing is shown in Figure 3.

The two opposing magnetic poles in the same coordinate axis direction apply electromagnetic force to the electric spindle rotor at the same time, but the bias current I_0 of the two poles is the same and the control current Δi is opposite. Therefore, the equivalent electromagnetic force in the direction of the two opposing C-type magnetic poles is

$$
\begin{aligned}
F_{m,x} &= \frac{4\mu_0 A N_c^2 I_0 \cos\alpha}{\delta_0^2}\Delta i - \frac{4\mu_0 A N_c^2 I_0^2 \cos^2\alpha}{\delta_0^3}\Delta x \\
&= C_i \Delta i + C_x \Delta x \\
F_{m,y} &= \frac{4\mu_0 A N_c^2 I_0 \cos\alpha}{\delta_0^2}\Delta i - \frac{4\mu_0 A N_c^2 I_0^2 \cos^2\alpha}{\delta_0^3}\Delta y \\
&= C_i \Delta i + C_y \Delta y,
\end{aligned} \tag{2}
$$

where

$$
\begin{aligned}
C_i &= \frac{4\mu_0 A N_c^2 I_0 \cos\alpha}{\delta_0^2}; \\
C_x &= C_y = \frac{4\mu_0 A N_c^2 I_0^2 \cos^2\alpha}{\delta_0^3},
\end{aligned} \tag{3}
$$

where C_i represents the equivalent current stiffness coefficient of the magnetic bearing and C_x and C_y represent the equivalent displacement stiffness coefficient in the x-direction and y-direction of the magnetic bearing. When the active magnetic bearing is running in the linear region near the operating point, the current stiffness coefficient and the displacement stiffness coefficient can be equivalent to a constant.

4. Unbalanced Vibration Controls for the Multinode Flexible Spindle Rotor System

4.1. Traditional Influence Coefficient Method. According to the finite element method, when there are the unbalanced masses of em2, em5, em7, and em8 in the n2, n5, n7, and n8 nodes of the flexible electric spindle rotor, the differential

equation of motion of the flexible electric spindle rotor system is

$$
M_s \ddot{U} + (D_s + \Omega_s G_s)\dot{U} + K_s U
$$

$$
= \begin{bmatrix}
\cdots \\
\mathrm{em}_2\omega^2\cos(\omega t + \varphi) & 2n_2 - 1 \\
\cdots \\
\mathrm{em}_5\omega^2\cos(\omega t + \varphi) & 2n_5 - 1 \\
\cdots \\
\mathrm{em}_7\omega^2\cos(\omega t + \varphi) & 2n_7 - 1 \\
\cdots \\
\mathrm{em}_8\omega^2\cos(\omega t + \varphi) & 2n_8 - 1 \\
\cdots \\
\mathrm{em}_2\omega^2\sin(\omega t + \varphi) & 2N + 2n_2 - 1 \\
\cdots \\
\mathrm{em}_5\omega^2\sin(\omega t + \varphi) & 2N + 2n_5 - 1 \\
\cdots \\
\mathrm{em}_7\omega^2\sin(\omega t + \varphi) & 2N + 2n_7 - 1 \\
\cdots \\
\mathrm{em}_8\omega^2\sin(\omega t + \varphi) & 2N + 2n_8 - 1 \\
\cdots
\end{bmatrix}. \tag{4}
$$

If the flexible electric spindle rotor system is in the linear range, the relationship between response and the external excitation force of each node's own degree can always be expressed as the following [15]:

$$
\begin{bmatrix}
v_{R1} \\
v_{R2} \\
\vdots \\
v_{Rn}
\end{bmatrix} = \begin{bmatrix}
c_{11} & c_{12} & \cdots & c_{1m} \\
c_{21} & & & \\
\vdots & & \ddots & \vdots \\
c_{n1} & & \cdots & c_{nm}
\end{bmatrix}\begin{bmatrix}
f_{c1} \\
f_{c2} \\
\vdots \\
f_{cn}
\end{bmatrix} + \begin{bmatrix}
v_{i1} \\
v_{i2} \\
\vdots \\
v_{in}
\end{bmatrix},
$$

$$
V_R = CF_c + V_i, \tag{5}
$$

where n is the number of nodes. The node to which the correction force is applied is called the excitation node, and m
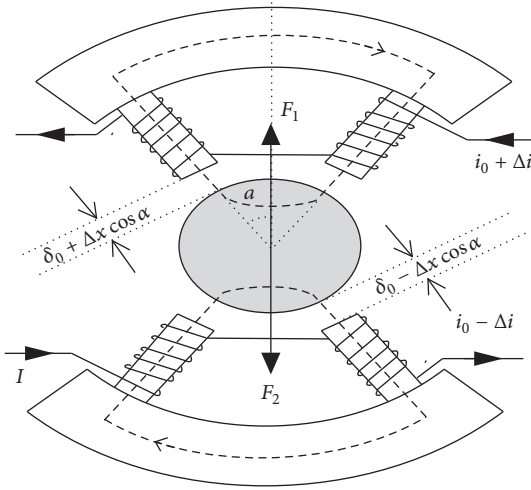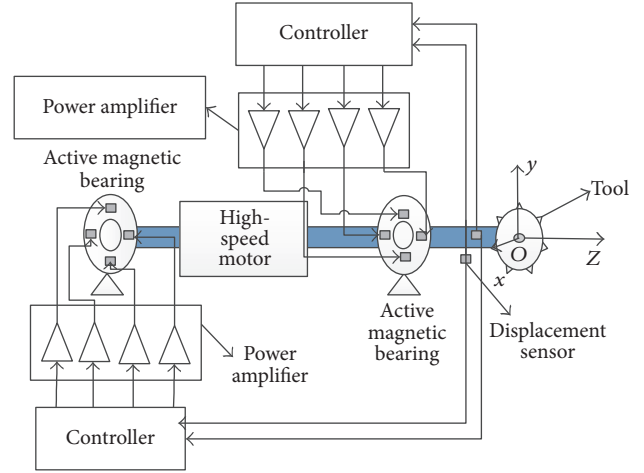
FIGURE 3: Active magnetic bearing differential structure.

FIGURE 4: Active control for multinode unbalanced vibration in cutting base on active magnetic bearings.

is the number of the excitation nodes. V_i indicates the original vibration of the node, as the $n \times 1$ dimension vector. V_R is the residual vibration of the node after the unbalanced correction force, which is the $n \times 1$ dimension vector. F_c represents the unbalanced correction force vector, which is the $m \times 1$ dimension vector. C is known as the coefficient of influence matrix, the $n \times m$ complex matrix, which can be calculated by a theoretical or an experimental test method. The purpose of the flexible spindle vibration control is to suppress the vibration of the unbalanced vibration nodes, that is, make the residual vibration V_R be zero vectors or be minimal.

The influence coefficient matrix is composed of an influence coefficient c_{ij}, and each influence coefficient indicates that the vibration change detected at the ith node after the jth excitation node is applied to the unit correction force. The influence coefficient reflects the transfer function relationship between the excitation force of the excitation node and the node response at a given speed. In the linear range, the influence coefficient matrix elements are only functions of the speed. Only in the constant speed condition is the influence coefficient matrix the constant matrix.

c_{ij} can be obtained by the following equation:

$$c_{ij} = \frac{(v_i)_{\text{fin}} - (v_i)_{\text{ini}}}{\left(f_{c,j}\right)_{\text{fin}} - \left(f_{c,j}\right)_{\text{ini}}} = \frac{\Delta v_i}{\Delta f_{c,j}}, \quad (6)$$

where the subscript ini represents the initial value before the correction and the subscript fin represents the final value after correction.

Assume that the target node response is $V_{R,k}$ under the effect of $F_{c,k}$; the incentive is changed to $F_{c,k+1}$; the target node response becomes $V_{R,k+1}$. Then,

$$V_{R,k} = CF_{c,k} + V_i,$$
$$V_{R,k+1} = CF_{c,k+1} + V_i. \quad (7)$$

In order for the excitation $F_{c,k+1}$ to completely suppress the vibration of the target node, that is, $V_{R,k+1} = 0$, the following can be solved:

$$F_{c,k+1} = F_{c,k} - C^{-1}V_{R,k}. \quad (8)$$

Equation (8) shows that if the influence coefficient matrix C is known, the corrected force $F_{c,k+1}$ can be accurately obtained by a single operation to make rotor vibration $V_{R,k+1}$ zero.

Based on the finite element software developed by Matlab, the multinode unbalanced vibration of the flexible electric spindle rotor system supported by the active magnetic bearing is studied. The spindle parameters are the spindle length $l = 1430$ mm, core length $l_e = 200$ mm, rotor outer diameter $D_{r,\text{out}} = 100$ mm, and rotor inner diameter $D_{r,\text{in}} = 50$ mm. Under the active magnetic bearing with the equivalent stiffness of 1×10^6 N/m, the unbalance is given as 1 g·mm, which is applied to rotor nodes 2, 5, 7, and 8. The phases of the unbalance in $n2$, $n5$, $n7$, and $n8$ are x-direction, y-direction, $-x$-direction, and $-y$-direction, respectively. The control scheme is shown in Figure 4. According to the vibration displacement of the cutter in the cutting process, the equivalent stiffness and equivalent damping of the active magnetic bearing are adjusted in real time to control the multinode unbalanced vibration of the rotating spindle rotor system. The vibration displacement is inputted to the controller (the traditional influence coefficient method) to produce the required control force. The required control force is amplified by the power amplifier and converted to control current required by the active magnetic bearing. And so, the multinode unbalanced vibration of the cutting spindle system in the cutting process is controlled. The influence coefficient is obtained by using the offline measurement in order to eliminate the interference of inaccurate problems, which is obtained by a look-up table in the simulation.

The original vibration amplitudes of electric spindle rotor nodes 1, 2, 3, 5, 7, and 8 in the range of 1 to 500 rad/s are shown in Figure 5. The rotor has two vibration peaks at critical speed
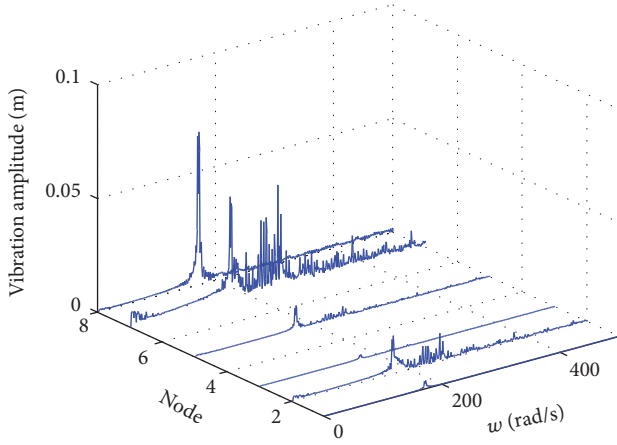
Figure 5: Original vibration of 1, 2, 3, 5, 7, and 8 nodes of the rotor.
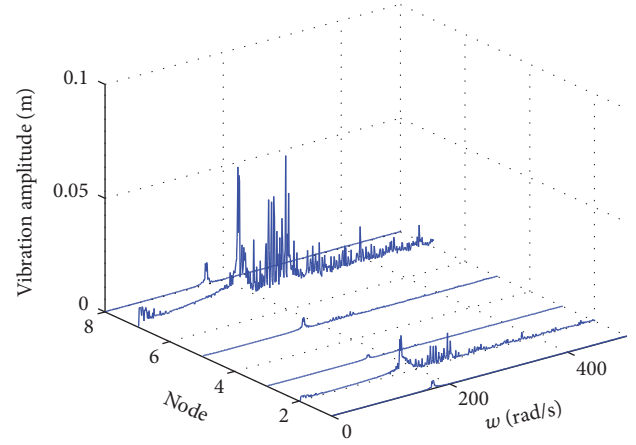

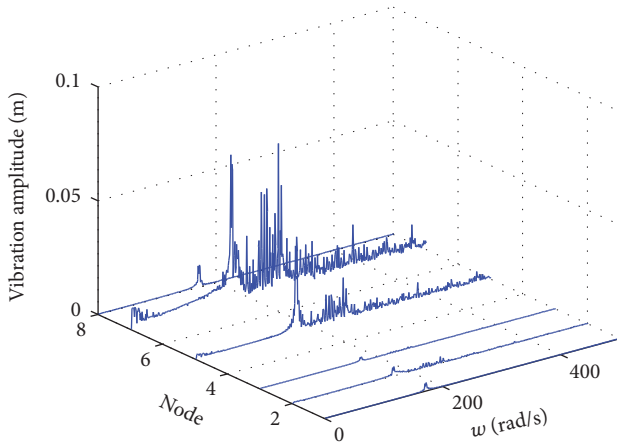Figure 7: Nodes 5 and 8 vibrations controlled.

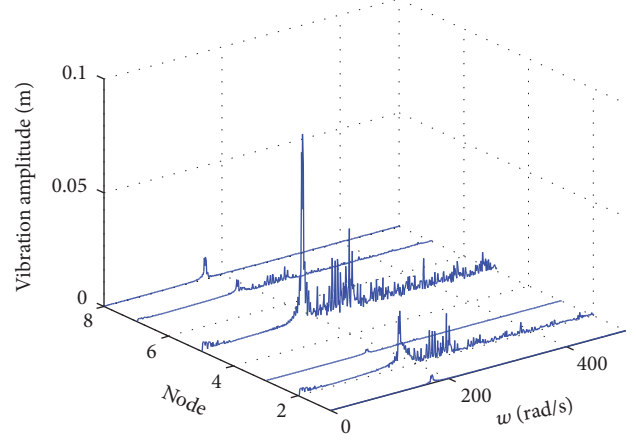Figure 6: Nodes 2 and 8 vibrations controlled.

Figure 8: Nodes 7 and 8 vibrations controlled.

positions 183.8 and 224.6 rad/s, respectively. Among them, the vibration of the first-order bending critical speed is larger. The vibration amplitudes of nodes 2, 5, 7, and 8 are about 25 mm, 42 mm, 40 mm, and 70 mm.

According to (8), the correcting electromagnetic force required for double nodes vibration controlled with double excitation nodes can be calculated in real time. When the active magnetic bearing nodes 1 and 3 are used as the excitation nodes, the vibration amplitudes of the rotor nodes 2 and 8 are shown in Figure 6. The vibration amplitudes of the rotor nodes 5 and 8 are shown in Figure 7. The vibration amplitudes of the rotor nodes 2 and 8 are shown in Figure 8.

Figures 6 to 8 show that the vibration control of the specified nodes is very effective, and the amplitude of vibration is reduced greatly. As can be clearly seen from Figures 6 to 8, since the only control target of vibration control is to eliminate the vibration of the specific nodes, the vibration of the other nodes is not taken into account. In the first-order bending critical speed, only the vibrations of the specific nodes are suppressed, while the other nonspecific nodes vibrations are aggravated by different degrees.

At this point, the real-time vibration control for the flexible motor spindle rotor system in the entire speed range is

needed to consider the following issues: in some known speed points, such as critical speed, the applied electromagnetic force may cause excessive vibration on other nonspecified nodes by the above traditional influence coefficient control method to simply eliminate the vibration of the specified node.

The solution to the above problem is to require the vibration control method for multinode unbalanced vibrations of the flexible spindle rotor system which has the ability to take into account multinode unbalanced vibrations and even control the vibration of all nodes in the rotor system at the same time.

4.2. Weighted Optimization of the Influence Coefficient Method. Equation (5) is a multivariate system. When the number of unbalanced vibration nodes and the number of stimulating nodes are equal ($n = m$), the vibrations of all nodes are corrected to zero by a single solution of unbalanced correction force vectors. When $n < m$, there is a set of solutions for completely suppressing the unbalanced vibration nodes. When $n > m$, all the unbalanced vibration nodes cannot be corrected to zero at the same time. In general, the rotor is usually supported by two active magnetic

bearings ($m = 2$). According to the above analysis, only the two unbalanced vibration nodes can be precisely controlled by two active magnetic bearings.

On the other hand, the correction force for the vibration control of the flexible spindle rotor system can be calculated by (8).

In the case of $n \neq m$, since C is not a square matrix, its inverse matrix does not exist, and the correction force of (8) cannot be used. In fact, when $n > m$, (5) cannot be solved by the multivariate system. This leads to the problem that the number of unbalanced vibration nodes cannot be more than the number of the excitations in vibration controlling for the flexible electric spindle rotor. A method of suppressing the vibration of the flexible rotor is proposed [15], which can avoid the nonsquare matrix inversion problem in the multivariate system. The unbalanced vibrations of all nodes in the whole rotor can be used as the objective function to realize the optimal control.

In the evaluation of the vibration of the flexible spindle rotor system, it is not equally important for vibration of all the nodes. In order to reasonably weigh the vibration of each node position, you can determine the evaluation of the vibration of each node position. The vibration evaluation weight matrix W is defined as an $n \times n$ diagonal matrix:

$$W = \begin{bmatrix} w_1 & & & 0 \\ & w_2 & & \\ & & \ddots & \\ 0 & & & w_n \end{bmatrix}. \tag{9}$$

The element w_i in the weight matrix W defines the weight of the vibration at the ith node position.

Weighted square and minimization of vibration amplitude is the objective function, which is the most commonly used in optimal control of rotor vibration; that is,

$$J = \frac{1}{2} V_{R,k}{}^* W V_{R,k}, \tag{10}$$

where J is the instantaneous value of the objective function. The superscript $*$ represents the Hermitian transform of the matrix. According to (10), the optimal control problem of rotor vibration suppression becomes a problem of how to minimize the objective function J.

Assuming that the original unbalanced vibration V_i remains constant during being controlled, the current rotor vibration can be expressed by the amount of change of rotor vibration and correction force for the previous iteration period; that is,

$$V_{R,k+1} = C \left(F_{c,k+1} - F_{c,k} \right) + V_{R,k}. \tag{11}$$

Substituting (9)-(10) into (11), we can get the relationship between the objective function J, the rotor vibration, and the correction force of the last iteration period:

$$\begin{aligned} J = & \frac{1}{2} \left(C \left(F_{c,k+1} - F_{c,k} \right) + V_{R,k} \right)^* \\ & \cdot W \left(C \left(F_{c,k+1} - F_{c,k} \right) + V_{R,k} \right), \end{aligned} \tag{12}$$

where $C, F_{c,k}$, and $V_{R,k}$ are known in (12). In order to make the objective function J the minimum extremum by the correction force at time $k + 1$, it can be obtained by the partial derivative of J; that is,

$$\frac{\partial J}{\partial F_{c,k+1}} = 0. \tag{13}$$

It is necessary that the quadratic function of J is $F_{c,k+1}$ to ensure the minimum value of the partial derivative of the objective function J. The condition is that the vibration evaluation weight matrix W is positive definite matrix and must be full rank. In order to make the influence factor matrix satisfy the full-rank condition, according to the literature [15], the selected active magnetic bearing excitation position follows two principles:

(1) Avoid setting the active magnetic bearing excitation position on the node of the vibration mode.

(2) Make sure that the effect of the correction force from each excitation node on the vibration vectors of the rotor system is independent; that is, the correction forces of each excitation node are not coupled to each other.

The partial derivation of J is obtained:

$$\frac{\partial J}{\partial F_{c,k+1}} = C^* W \left(C \left(F_{c,k+1} - F_{c,k} \right) + V_{R,k} \right). \tag{14}$$

According to (13) and (14), the minimum value $F_{c,\min}$ of the objective function J can be obtained:

$$\begin{aligned} F_{c,\min} &= \left[C^* W C \right]^{-1} \left[C^* W C F_{c,k} - C^* W V_{R,k} \right] \\ &= \left[C^* W C \right]^{-1} \left[C^* W \left[C F_{c,k} - V_{R,k} \right] \right] \\ &= - \left[C^* W C \right]^{-1} C^* W V_i. \end{aligned} \tag{15}$$

Of course, because the actual C and V_i are unknown, $F_{c,\min}$ can gradually approach the estimate of the influence coefficient and the robustness of the iterative convergence, as follows:

$$F_{c,k+1} = \left[C^* W C \right]^{-1} \left[C^* W \left[C F_{c,k} - V_{R,k} \right] \right]. \tag{16}$$

We can see that (16) is exactly equivalent to (8) if C is square matrix and W is unit matrix. The greatest contribution of (16) is to avoid the direct inversion problem when the coefficient matrix is not a square matrix. Equation (16) can control the vibrations of an unlimited number of nodes according to the rules of weights.

When the objective function J is the minimum extreme value, the residual vibrations of the rotor nodes can be solved by substituting (16) into (8):

$$\begin{aligned} V_{R,\min} &= C \left[- \left[C^* W C \right]^{-1} C^* W V_i \right] + V_i \\ &= \left[I_{n \times n} - C \left[C^* W C \right]^{-1} C^* W \right] V_i, \end{aligned} \tag{17}$$

where $I_{n \times n}$ represents the $n \times n$ unit matrix.

(a) Vibration of nodes without being controlled

(b) Vibration of nodes with control (W_1)
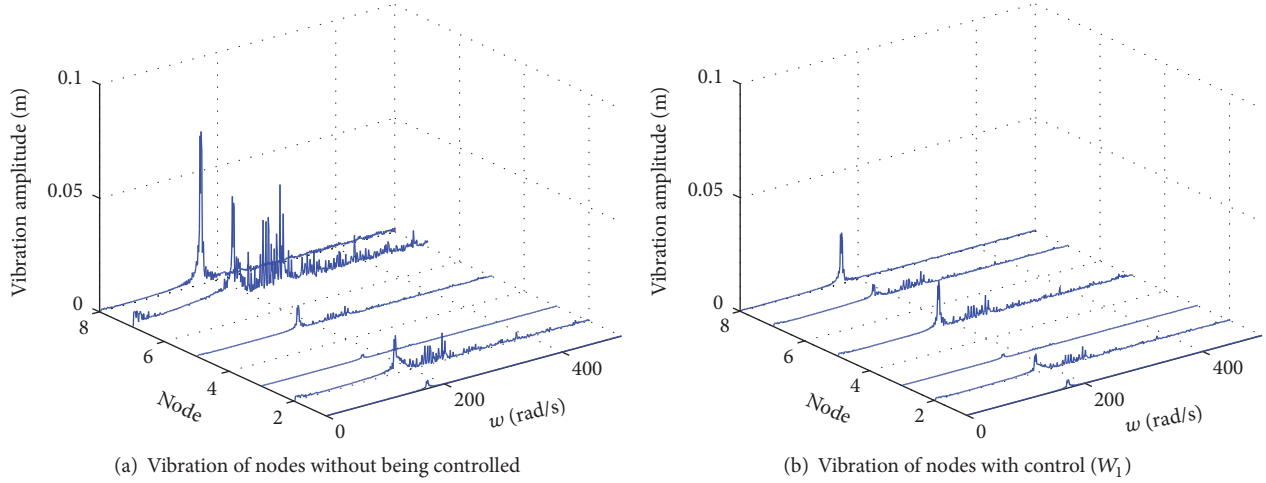
FIGURE 9: Vibration weighted optimal control effect of nodes 1, 2, 3, 5, 7, and 8.

(a) Vibration of nodes controlled (W)

(b) Vibration of nodes controlled (w_2 and w_8 are adjusted)
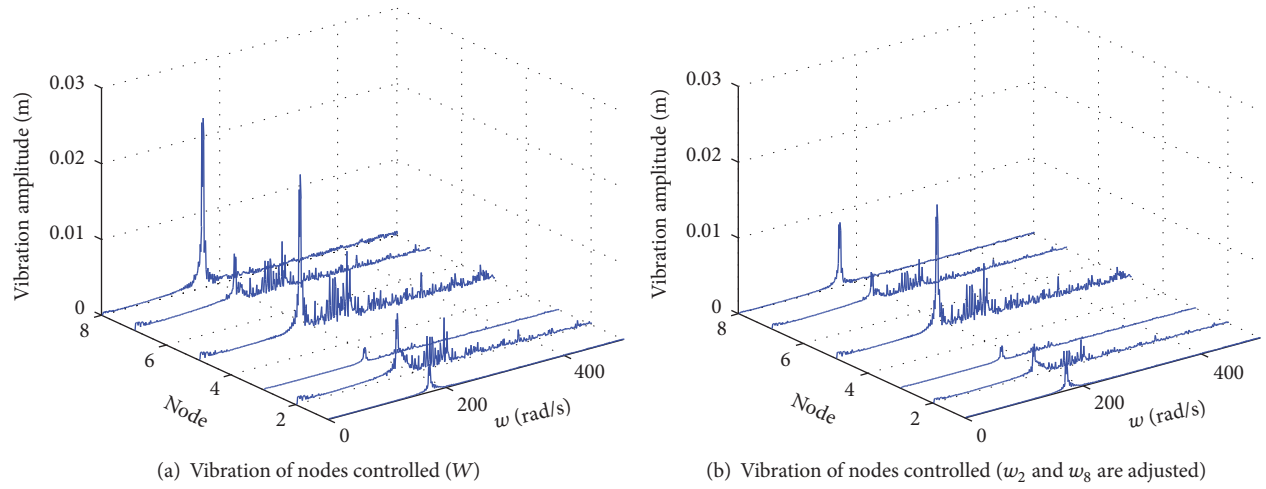
FIGURE 10: Weighted optimal control for nodes 2 and 8 vibration by adjusting weights w_2 and w_8.

In order to verify the control effect of the vibration of multinode unbalanced vibration by using weighted optimization of the influence coefficient method, the simulation is carried out in Matlab. The control scheme is the same as the one in Figure 4. The controller is replaced with weighted optimization of the influence coefficient method. The influence coefficient matrix of the rotor is also determined by the offline method, which is obtained by looking up the table according to the rotor speed in real-time control. In simulation, the active magnetic bearing nodes 1 and 3 are taken as the excitation nodes, and nodes 2, 5, 7, and 8 are taken as the unbalanced vibration nodes. All the vibration weights of nodes are equal; that is, W is the unit matrix. Figure 9 shows the vibration control effect in the range of 1 to 500 rad/s. When the weights w_2 and w_8 in W are changed, the control effects of nodes 2, 5, 7, and 8 are shown in Figure 10. As a comparison, Figure 11 shows the comparison of the vibration response of node 2 with the different weight. Figure 12 shows the comparison of the vibration response of node 5 with the different weight. Figure 13 shows the comparison of

the vibration response of node 7 with the different weight. Figure 14 shows the comparison of the vibration response of node 8 with the different weight. In Figures 11 to 14, the blue solid line is the vibration control of nodes 2, 5, 7, and 8 with the unit matrix W, and the red dotted line is the vibration control effect of nodes 2 and 8 after the adjusted weights w_2 and w_8 in W to pursue the perfect minimization vibrations of nodes 2 and 8.

As can be seen from Figures 11 to 14, the vibration of nodes 2 and 8 is lower than the previous one by the adjusted weight, but there is little suppression for the vibration of node 5 and node 7. As long as the appropriate weight is selected, you can control unbalanced vibrations of all the nodes on the spindle rotor.

It can be seen that, under the control strategy of multinode weighted vibration objective function J, it is very effective to reduce the multinode unbalanced vibration of the flexible spindle rotor system. When weights are adjusted, some nodes have better control. So, the right weight W will directly determine the vibration control effect of multiple unbalanced
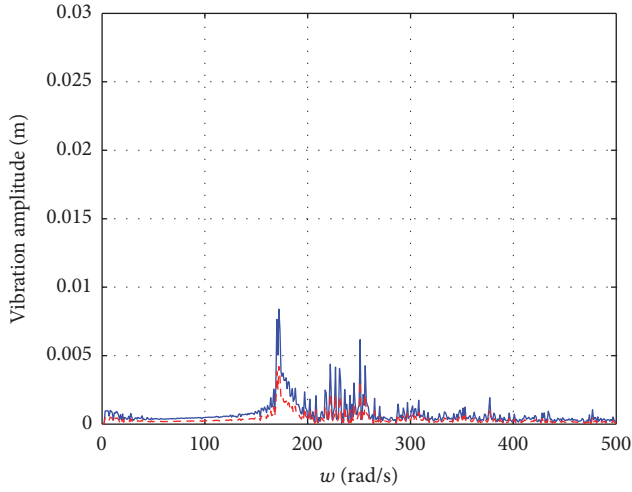
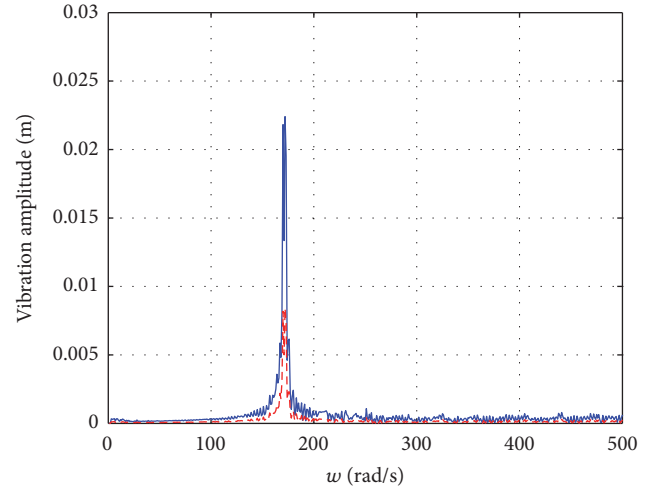Figure 11: Comparison of two control effects (node 2).

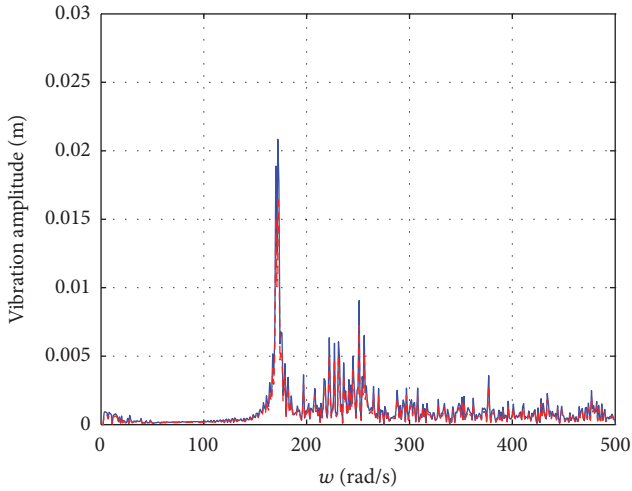Figure 14: Comparison of two control effects (node 8).
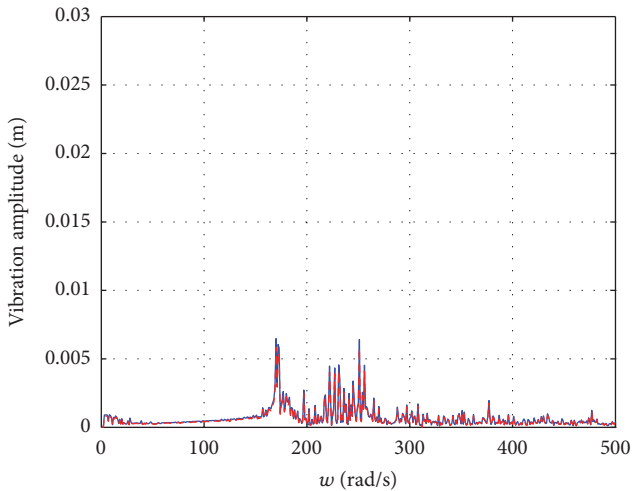

Figure 12: Comparison of two control effects (node 5).

Figure 13: Comparison of two control effects (node 7).

vibration nodes on the whole rotor. In particular, the multinode weighted objective function J takes into account the vibration of each node and does not cause the vibration peak at other unknown nodes.

5. Conclusions

It is necessary to solve the multivariate equations to calculate the required electromagnetic force based on the traditional influence coefficient method for the vibration suppression of the flexible electric spindle rotor, which led to the number of vibration suppression nodes being not more than the number of excitation nodes of the active magnetic bearing. In order to avoid solving the nonsquare matrix inverse problem of multivariate equations, the optimal influence coefficient control method with weights for multinode unbalanced vibration of flexible electric spindle rotors is proposed on the basis of the traditional influence coefficient method, which can use all the unbalanced vibration of nodes as the objective function to achieve the optimal control, and the control effect is proved by the comparison simulation. The simulation results show that the optimal control method of the flexible electric spindle rotor system with mixed weight objective function has a good effect of suppressing the multinode unbalanced vibration of the rotor system.

Conflicts of Interest

The authors declare that they have no conflicts of interest regarding the publication of this paper.

Acknowledgments

References

[1] Y. Zhong, Y. Z. He, and Z. Wang, *Rotor Dynamics*, Tsinghua University Press, 1987.

[2] C.-Y. Tseng, T.-W. Shih, and J.-T. Lin, "A Kalman filter-based automatic rotor dynamic balancing scheme for electric motor mass production," *Materials Science Forum*, vol. 505-507, no. 2, pp. 997–1002, 2006.

[3] H. W. Li, Y. Xu, and H. D. Gu, "Field dynamic balancing method in AMB flexible rotor system," *China Mechanical Engineering*, vol. 19, no. 12, pp. 1419–1428, 2008.

[4] C.-S. Kim and C.-W. Lee, "In situ runout identification in active magnetic bearing system by extended influence coefficient method," *IEEE/ASME Transactions on Mechatronics*, vol. 2, no. 1, pp. 51–57, 1997.

[5] Y. Kang, T. Lin, and M. Chu, "Design and simulation of a neural-PD controller for automatic balancing of rotor," in *Proceedings of the 3rd International Symposium on Neural Networks*, pp. 1104–1109, Chengdu, China, 2006.

[6] C. D. Untaroiu, P. E. Allaire, and W. C. Foiles, "Balancing of flexible rotors using convex optimization techniques: optimum min-max LMI influence coefficient balancing," *Journal of Vibration and Acoustics*, vol. 130, no. 2, Article ID 021006, 2008.

[7] Z. Yu, L. T. Meng, and L. M. King, "Electromagnetic bearing actuator for active vibration control of a flexible rotor," *Proceedings of the Institution of Mechanical Engineers Part C*, vol. 212, no. 8, pp. 705–716, 1998.

[8] C. Knospe, "Robustness of adaptive unbalance control of rotors with magnetic bearings," *Journal of Vibration and Control*, vol. 2, no. 1, pp. 33–52, 1996.

[9] S.-H. Lee, B.-S. Kim, J.-D. Moon et al., "A study on active balancing for rotating machinery using influence coefficient method," in *Proceedings of the IEEE International Symposium on Computational Intelligence in Robotics and Automation (CIRA '05)*, pp. 659–664, IEEE, Espoo, Finland, June 2005.

[10] Y. Kang, T.-W. Lin, Y.-J. Chang, Y.-P. Chang, and C.-C. Wang, "Optimal balancing of flexible rotors by minimizing the condition number of influence coefficients," *Mechanism and Machine Theory*, vol. 43, no. 7, pp. 891–908, 2008.

[11] G. Schweitzer, Eric, and H. Maslen, *Magnetic Bearings: Theory, Design And Application to Rotating Machinery*, China machine press, 2012.

[12] X. Qiao and C. Zhu, "Active control of milling chatter based on the built-in force actuator," *Journal of Mechanical Engineering*, vol. 48, no. 1, pp. 185–192, 2012.

[13] X. L. Qiao and C. S. Zhu, "The active vibration attenuation of a built-in motorized milling spindle," *Journal of Vibration and Control*, vol. 20, no. 13, pp. 1934–1945, 2014.

[14] X. L. Qiao, C. S. Zhu, and Z. X. Zhong, "Stability and control for chatter in cutting based on active magnetic bearings," *China Mechanical Engineering*, vol. 12, no. 27, pp. 1632–1637, 2016.

[15] W. Stephen, *Adaptive optimal control of active balancing systems for high-speed rotating machinery [Ph.D. thesis]*, The University of Michigan, Ann Arbor, Mich, USA, 1999.

Research Article

An Observer-Based Controller with a LMI-Based Filter against Wind-Induced Motion for High-Rise Buildings

Chao-Jun Chen,[1] Zuo-Hua Li,[1] Jun Teng,[1] Wei-Hua Hu,[1] and Ying Wang[2]

[1]*School of Civil and Environment Engineering, Shenzhen Graduate School, Harbin Institute of Technology, Shenzhen 518055, China*
[2]*Department of Civil and Environmental Engineering, University of Surrey, Guildford GU2 7XH, UK*

Correspondence should be addressed to Zuo-Hua Li; lizuohua@hit.edu.cn

Active mass damper (AMD) control system is proposed for high-rise buildings to resist a strong wind. However, negative influence of noise in sensors impedes the application of AMD systems in practice. To reduce the adverse influence of noise on AMD systems, a Kalman filter and a linear matrix inequality- (LMI-) based filter are designed. Firstly, a ten-year return period fluctuating wind load is simulated by mixed autoregressive-moving average (MARMA) method, and its reliability is tested by wind speed power spectrum and correlation analysis. Secondly, a designed state observer with different filters uses wind-induced acceleration responses of a high-rise building as the feedback signal that includes noise to calculate control force in this paper. Finally, these methods are applied to a numerical example of a high-rise building and an experiment of a single span four-storey steel frame. Both numerical and experimental results are presented to verify that both Kalman filter and LMI-based filter can effectively suppress noise, but only the latter can guarantee the stability of AMD parameters.

1. Introduction

Active mass damper (AMD) is used to control the dynamic response of highly flexible buildings horizontally under environmental loadings such as strong wind [1–5]. Generally, a vector composition of displacement and velocity in the horizontal direction is used as a feedback signal for AMD control system [6, 7], but the whole displacements and velocities of each floor are too difficult to be measured directly. Therefore, a state observer design method is of great importance to the implementation of AMD control system in high-rise structures. The references showed the state observers can solve the problem for linear uncertain systems [8–10] and nonlinear systems [11–15]. Compared with displacement and velocity, [16] shows that the acceleration signal is easier to be measured and control system based on acceleration feedback is more robust. Unfortunately, the problem in the design process of an observer is that accelerometers may lead to a large estimation error that is regarded as noise. Therefore, filters for noise have to be considered.

At present, such filter process is often based on Kalman filter. In [17], a Kalman filter technique was used to estimate effective signal to noise ratio (SNR) in wireless sensor network (WSN) systems. Based on a maximum-likelihood criterion, Kalman filter for discrete-time systems was presented in [18]. In addition, an optimization-based adaptive Kalman filtering method was proposed in [19]. Moreover, a hybrid Kalman filter was established to denoise fiber optic gyroscope (FOG) sensors signal for discrete-time system in [20]. By unscented Kalman filter (UKF), extended Kalman filter (EKF), or particle filter (PF), the interacting multiple sensor filter (IMSF) had been presented in [21]. Similarly, based on H_∞ filter and particle filter (PF), mixture Kalman filter (MKF) was built for conditionally linear dynamic systems in unknown non-Gaussian noises by [22]. A robust cubature Kalman filter (CKF) was designed for multisensors discrete-time systems with uncertain noise variances in [23]. Generally, Kalman filter, considering the disturbance as the observation input, can be used to estimate the system state by output data and is often applied in linear, discrete-time and finite dimensional systems [24–27]. Normal Kalman filter cannot consider input excitation during state estimation. The state derivative of a general AMD control system includes the

velocity and acceleration responses, which are closely related to the external excitation. As a result, it leads to a large estimation error when neglecting the influence of external excitation. Furthermore, since the Kalman filter is strongly dependent on the statistical properties of noise and the selected Kalman filter gain is not a global optimal solution, the problem of control forces and strokes that are oversized output in an AMD system with Kalman filter should be considered. Therefore, a new real-time filter with optimal Kalman filter gain that considers external excitation can be designed for high-rise buildings based on linear matrix inequality (LMI) approach [28].

In this paper, a state observer design method based on structural acceleration is proposed for high-rise buildings under strong wind firstly. For comparative analysis, a Kalman filter and a LMI-based filter that consider input excitation are presented to reduce the adverse influence of noise on AMD control systems. Specifically, based on variable substitution method [29, 30], the design problem of the LMI-based filter can be transformed into a group of nonlinear matrix inequalities, which can be turned into a group of convex and easily solved linear matrix inequalities. Finally, a numerical example of a high-rise building and an experiment of a single span four-storey steel frame are presented to verify the efficiency of the proposed filters. The result shows that only the control system with a LMI-based filter can guarantee the stability of the AMD parameters and effectively filter out noise.

2. An Observer-Based Controller with a Filter and Numerical Verification

2.1. An Observer-Based Controller Design. The force equilibrium of a multi-degree-of-freedom (MDOF) system is

$$M\ddot{X}(t) + C\dot{X}(t) + KX(t) = B_w w(t) + B_s u(t), \quad (1)$$

where M, C, and K are the mass, damping, and stiffness matrix of the system, respectively. u is the control force. B_s and B_w are the location matrices of control force and strong wind, respectively. And $\ddot{X}$, $\dot{X}$, and X are the acceleration, velocity, and displacement of the system, respectively.

System state Z includes displacement and velocity. Then, (1) can be expressed into the state-space equation as

$$\dot{Z}(t) = AZ(t) + B_1 w(t) + B_2 u(t)$$
$$Y(t) = CZ(t) + D_1 w(t) + D_2 u(t), \quad (2)$$

where u and w are the control force and the input excitation, respectively. A, B_1, and B_2 are the state matrix, the excitation matrix, and the control matrix, and C, D_1, and D_2 are the state output matrix and the direct transmission matrix of excitation and control force, which can be expressed as

$$A = \begin{bmatrix} 0 & I \\ -M^{-1}K & -M^{-1}C \end{bmatrix},$$

$$B_1 = \begin{bmatrix} 0 \\ -M^{-1}B_w \end{bmatrix},$$

$$B_2 = \begin{bmatrix} 0 \\ -M^{-1}B_s \end{bmatrix},$$

$$C = \begin{bmatrix} I & 0 \\ 0 & I \\ -M^{-1}K & -M^{-1}C \\ 0 & 0 \end{bmatrix},$$

$$D_1 = \begin{bmatrix} 0 \\ 0 \\ -M^{-1}B_w \\ 0 \end{bmatrix},$$

$$D_2 = \begin{bmatrix} 0 \\ 0 \\ -M^{-1}B_s \\ 1 \end{bmatrix}. \quad (3)$$

The control force of the system is

$$u(t) = -G \cdot Z. \quad (4)$$

Substituting (4) into (2) leads to

$$\dot{Z} = (A - B_2 G) Z + B_1 w(t)$$
$$Y = (C - D_2 G) Z + D_1 w(t), \quad (5)$$

where $\overline{A} = A - B_2 G$, $\overline{B} = B_1$, $\overline{C} = C - D_2 G$, and $\overline{D} = D_1$. A brief form of (5) is

$$\dot{Z} = \overline{A}Z + \overline{B}w$$
$$Y = \overline{C}Z + \overline{D}w. \quad (6)$$

The second equation of (6) can be written in the form of a partitioned matrix.

$$\left\{ \begin{matrix} Y_1 \\ Y_2 \end{matrix} \right\} = \begin{bmatrix} \overline{C}_1 \\ \overline{C}_2 \end{bmatrix} \cdot Z + \begin{bmatrix} \overline{D}_1 \\ \overline{D}_2 \end{bmatrix} \cdot w, \quad (7)$$

where Y_1 is a vector of displacement and velocity of the structure and its AMD and Y_2 is a vector of acceleration, respectively. According to (7), the external excitation vector can be written as

$$w = \overline{D}_2^{-1} \cdot (Y_2 - \overline{C}_2 Z). \quad (8)$$

Substituting (8) into (6) and (7) leads to

$$\dot{Z} = \left(\overline{A} - \overline{B}\,\overline{D}_2^{-1}\overline{C}_2 \right) Z + \overline{B}\,\overline{D}_2^{-1} Y_2$$
$$Y_1 = \left(\overline{C}_1 - \overline{D}_1 \overline{D}_2^{-1}\overline{C}_2 \right) Z + \overline{D}_1 \overline{D}_2^{-1} Y_2, \quad (9)$$

where $\widetilde{A} = \overline{A} - \overline{B}\,\overline{D}_2^{-1}\overline{C}_2$, $\widetilde{B} = \overline{B}\,\overline{D}_2^{-1}$, $\widetilde{C} = \overline{C}_1 - \overline{D}_1\overline{D}_2^{-1}\overline{C}_2$, and $\widetilde{D} = \overline{D}_1\overline{D}_2^{-1}$.
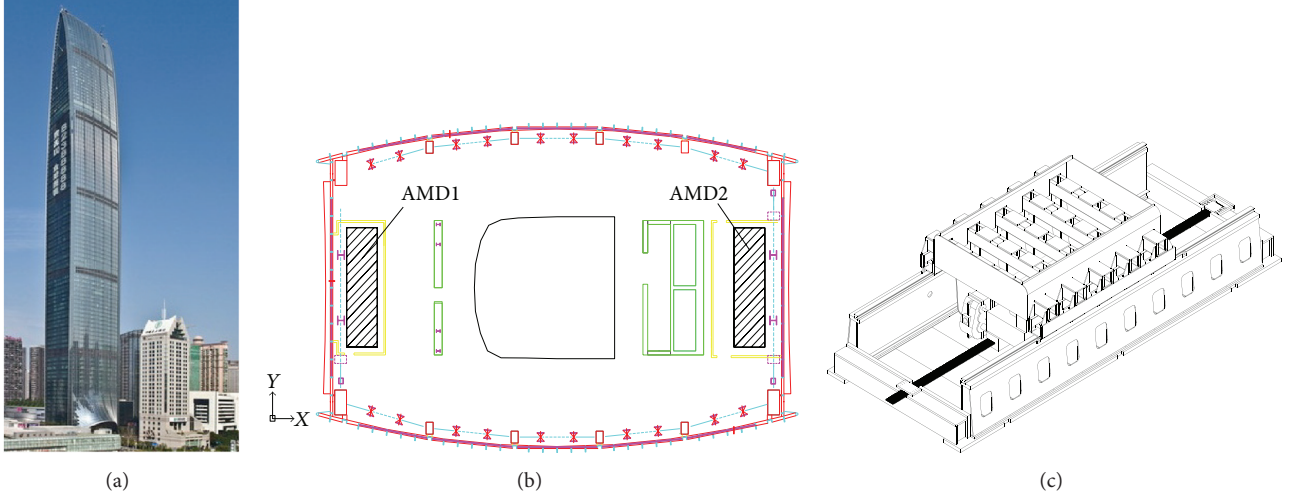
FIGURE 1: KK100 and its AMD systems: (a) picture of the building; (b) locations of the AMD systems; (c) an AMD system.

Equation (9) can be written as

$$\dot{Z} = \widetilde{A}Z + \widetilde{B}Y_2$$
$$Y_1 = \widetilde{C}Z + \widetilde{D}Y_2. \tag{10}$$

The state observer is

$$\dot{Z} = \widetilde{A}Z + \widetilde{B}Y_2 + G_o\left(Y_1 - \widetilde{Y}_1\right)$$
$$\widetilde{Y}_1 = \widetilde{C}Z + \widetilde{D}Y_2. \tag{11}$$

Substituting the second equation of (11) into the first equation leads to

$$\dot{Z} = \left(\widetilde{A} - G_o\widetilde{C}\right)Z + \left(\widetilde{B} - G_o\widetilde{D}\right)Y_2 + G_oY_1$$
$$\widetilde{Y}_1 = \widetilde{C}Z + \widetilde{D}Y_2, \tag{12}$$

where G_o is the feedback gain of the observer. Y_2 and Z can be used to estimate the estimated states $\widetilde{Y}_1$ of the structure and its AMD. $\widetilde{Y}_1$ is then used to calculate the control force.

2.2. The Simulation of Wind-Induced Motions of a High-Rise Building.

In this paper, a high-rise building called KingKey Financial Center (KK100) shown in Figure 1(a) has a height of 441.8 m, and its slenderness ratio is 10.2. Its structural periods and frequencies are listed in Table 1. Moreover, the lumped mass method is used for establishing the mass matrix of KK100 whose total mass is 5.79×10^5 tons. Its stiffness matrix that has taken into account structural flexural and shear deformations is built based on unit-displacement method, and its structural damping ratio is 0.015. The first four natural mode shapes of KK100 along the minor-axis are given in Figure 2.

Its AMD control system shown in Figures 1(b) and 1(c) includes two sets of synchronous AMD devices, which are located on both sides of the 91st floor, mainly used for the controlling wind-induced motion along the minor-axis. The parameters of the control system are listed in Table 2.

TABLE 1: The periods and frequencies of KK100.

Vibration mode	Periods (s)	Frequencies (Hz)
1	7.1522	0.1398
2	1.9490	0.5131
3	0.9525	1.0499
4	0.6445	1.5516

TABLE 2: Key parameters of the AMD system.

Index	AMD
Auxiliary mass (t)	250×2
Effective stroke (m)	± 2.2
Peak power (kW)	300×2
Maximum driving force (kN)	275×2

KK100 is located in Caiwuwei Financial Center, Luohu District, Shenzhen, China. According to the Chinese loads code on buildings, the roughness category of the area is C and the basic wind pressure of ten-year return period is $0.45\,\text{kN/m}^2$. Based on Davenport spectrum, a fluctuating wind speed can be generated. The power spectral density of fluctuating wind speed is decreased as the following equation.

$$S_u\left(f\right) = 4k\overline{V}^2\left(10\right)\frac{x^2}{f\left(1 + x^2\right)^{4/3}}$$
$$x = 1200\frac{f}{\overline{V}\left(10\right)}, \tag{13}$$

where $\overline{V}(10)$ is the average wind speed at a height of 10 m above ground level and f is the frequency of the fluctuating wind, respectively. k is the coefficient related to ground roughness and can be expressed as

$$k = \frac{1}{6 \times 8.8^2} \times 35^{3.6(\alpha-0.16)}, \tag{14}$$

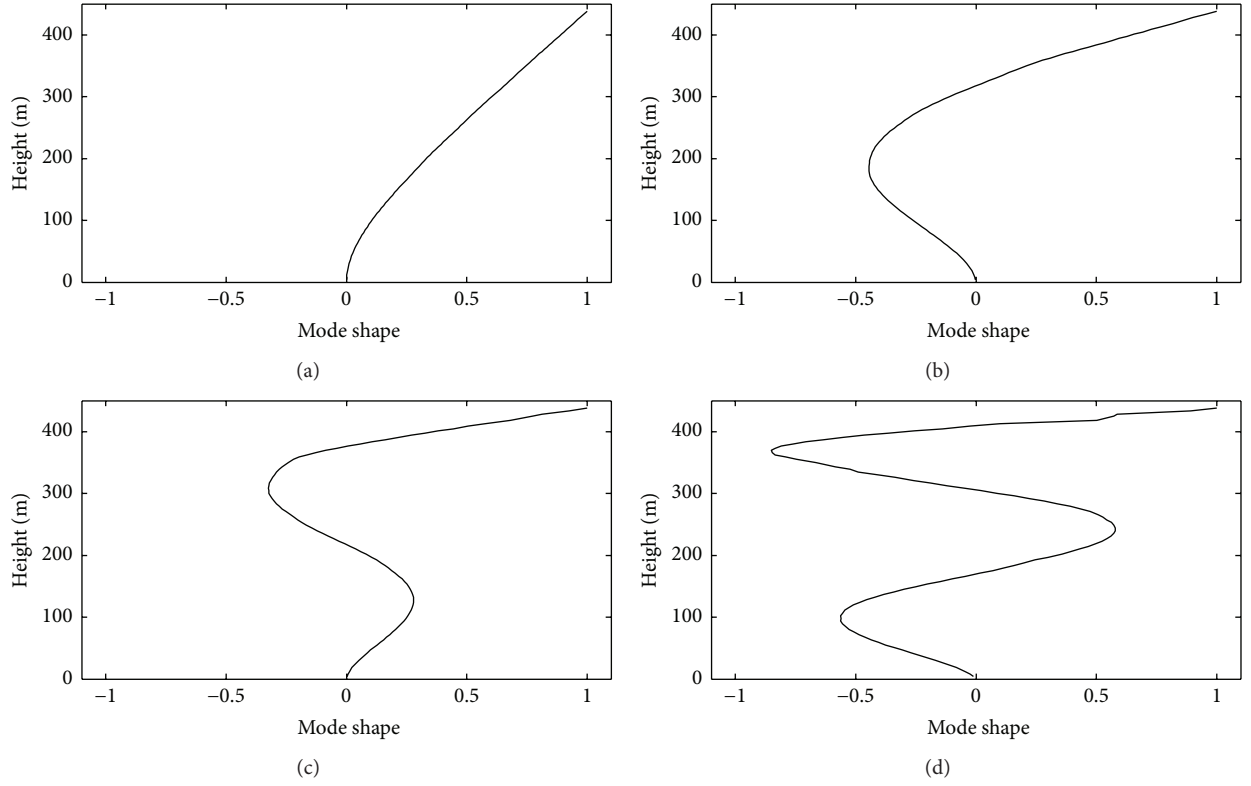where $\alpha = 0.22$ is the C category ground roughness exponent.

Figure 2: Mode shapes of KK100: (a) Mode 1; (b) Mode 2; (c) Mode 3; (d) Mode 4.

The spatial correlation of fluctuating wind in time domain is mainly related to transverse and vertical correlation and is represented by correlation function. In frequency domain, the coherence function is used to describe the spatial correlation. Compared with the vertical dimension of KK100, the lateral dimension is relatively small. Therefore, the vertical correlation of fluctuating wind load is only considered. The coherence coefficient of fluctuating wind pressure in vertical direction is

$$\rho_z\left(z_1, z_2\right) = e^{\left(-|z_1 - z_2|/L_z\right)}, \tag{15}$$

where $|z_1 - z_2|$ is the distance between two floors in vertical direction and $L_z = 60$ m according to Chinese loads code on buildings.

Mixed autoregressive-moving average (MARMA) model [31] is proposed to simulate the stochastic process. A stochastic wind speed time series can be generated as

$$[U(t)] = \left[u_1(t), u_2(t), \ldots, u_m(t)\right]^T$$
$$= \sum_{k=1}^{p} \left[\Psi_k\right] \left[U(t - k\Delta t)\right] + N(t), \tag{16}$$

where

$$[U(t - k\Delta t)]$$
$$= \left[u_1(t - k\Delta t), u_2(t - k\Delta t), \ldots, u_m(t - k\Delta t)\right]^T \quad (17)$$

$$N(t) = \left[N_1(t), N_2(t), \ldots, N_m(t)\right]^T,$$

where $u_i(t - k\Delta t)$ is the wind speed of the ith random wind speed time series at time $(t - k\Delta t)$ and p is the order of autoregressive model. $N_i(t)$ is a zero mean random number series that obeys normal distribution with a given covariance R_u, respectively. The relationship between power spectral density and covariance satisfies Wiener-Khintchine approach that can be described as

$$R_u^i\left(k\Delta t\right) = \int_0^{\infty} S_u^i\left(f\right) \cos\left(2\pi k\Delta t f\right) df. \tag{18}$$

R_u can be obtained by (18), and $[\Psi_k]$ is a regression coefficient matrix based on R_u. Equation (16) can be separated by time Δt, and the recursive matrix is expressed as

$$\begin{bmatrix} u_1(j\Delta t) \\ \vdots \\ u_m(j\Delta t) \end{bmatrix} = \sum_{k=1}^{p} \left[\Psi_k\right] \begin{bmatrix} u_1\left[(j - k)\Delta t\right] \\ \vdots \\ u_m\left[(j - k)\Delta t\right] \end{bmatrix}$$
$$+ \begin{bmatrix} N_1(j\Delta t) \\ \vdots \\ N_m(j\Delta t) \end{bmatrix}, \begin{bmatrix} j\Delta t = 0, \ldots, T \\ k \le j \end{bmatrix}. \tag{19}$$

Discrete fluctuating wind speed vectors with a time-interval Δt can be derived from (19). In order to test the reliability of the simulation results, the Fourier transformation is applied to finish wind speed power spectrum and
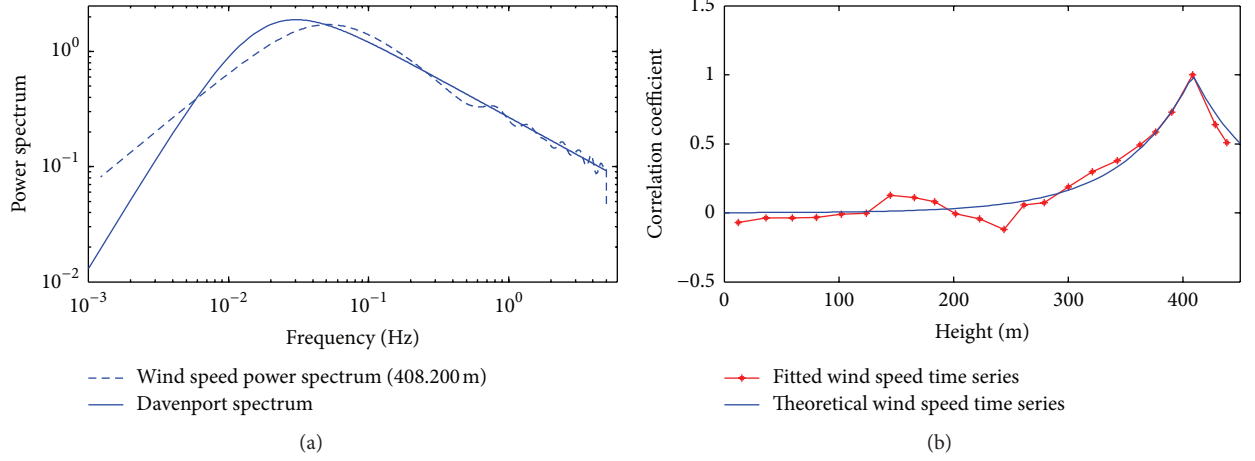
(a)

(b)

FIGURE 3: Tests of the fluctuating wind speed time series on 92nd floor (408.200 m): (a) wind speed power spectrum test; (b) correlation test.
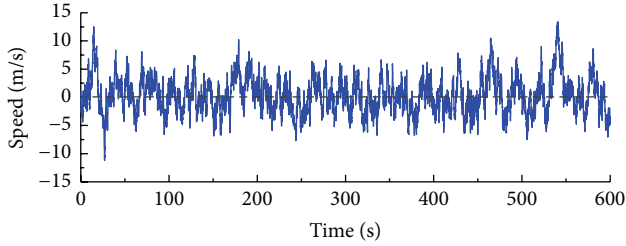

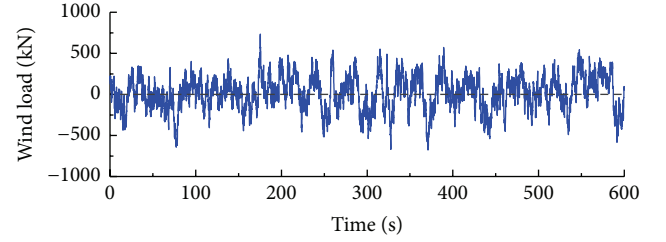FIGURE 4: A ten-year return period fluctuating wind speed time series on 92nd floor (408.200 m).

FIGURE 5: A ten-year return period fluctuating wind load on 92nd floor (408.200 m).

correlation tests shown in Figure 3. Figure 3(a) shows that spectrum analysis of the simulated fluctuating wind speed based on MARMA method is similar to Davenport spectrum in a wide frequency band ($f \geqslant 10^{-2}$ Hz). It covers the natural frequency of high-rise buildings. Figure 3(b) indicates the vertical correlation of two kinds of fluctuating wind speed time series is high goodness-of-fit.

Following these above steps, the fluctuating wind speed time series of each floor can be generated along the height of KK100. Time-history curve of the fluctuating wind speed on 92nd floor (at 408.200 m above ground) is shown in Figure 4. As the fluctuating wind speed and structural information have been given, the simulated fluctuating wind load on each floor of KK100 can be calculated by (20). Time-history curve of the ten-year return period simulated fluctuating wind load on 92nd floor is shown in Figure 5. The simulated wind load is only used for numerical analysis in the paper, and it cannot represent the realistic wind load of KK100.

$$P_i = \rho \overline{V}(z) u_i(z, t) \mu_s S, \tag{20}$$

where P_i is the fluctuating wind load at ith floor and ρ is the air density. $\overline{V}(z)$ is the average wind speed at ith floor. u_i is the fluctuating wind speed that is associated with height and time. μ_s and S are the shape factor of a building and the area of windward side, respectively.

An observer-based controller shown in Figure 6(a) and *an original controller* shown in Figure 6(b) are designed to suppress the wind-induced motions of KK100. The structural acceleration of the 87th floor under uncontrolled and controlled scenarios is shown in Figure 7, and AMD parameters of different systems are shown in Figure 8. Table 3 presents the control effects and values of AMD parameters. In this paper, *control effect* is quantified as the ratio between structural response reduction and the structural response without control, and *AMD parameters* include control force and stroke. From Figures 7 and 8, the original controller and the observer-based controller can obviously reduce the wind vibration response. The frequencies of KK100 in different vibration modes are obtained and nicely consistent with its theoretical values listed in Table 1. For example, its natural frequency shown in Figure 7(d) is 0.1399 Hz in line with its theoretical value (0.1398 Hz). Moreover, the maximum variations of the displacement and acceleration control effects between two different systems are only 0.0012% and 0.0712%, and the AMD parameters of the state observer increase by −7.6087 kN and 0.0001 m. In a word, the observer-based controller is used instead of the original controller, in order to overcome the difficulty in direct measurement of the state vector that includes both structural displacements and velocities in the horizontal direction of KK100.

(a)   (b)
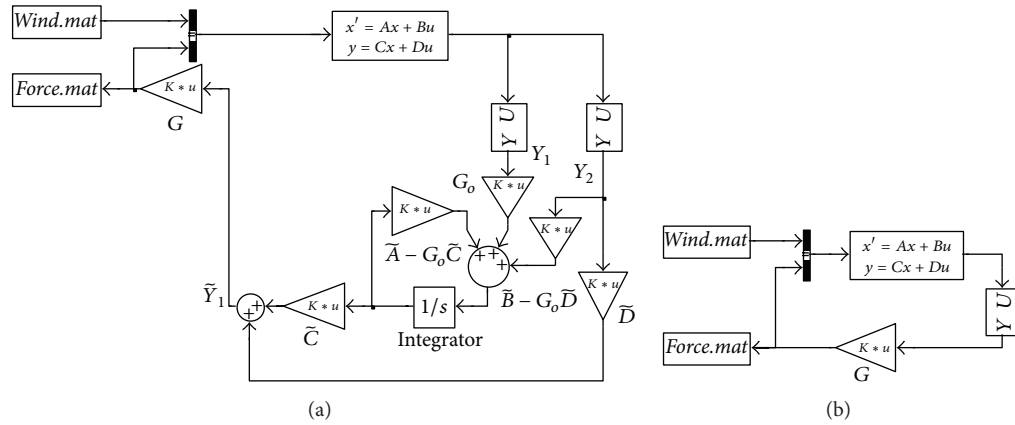
FIGURE 6: Simulink module of the control systems: (a) an observer-based controller; (b) an original controller.
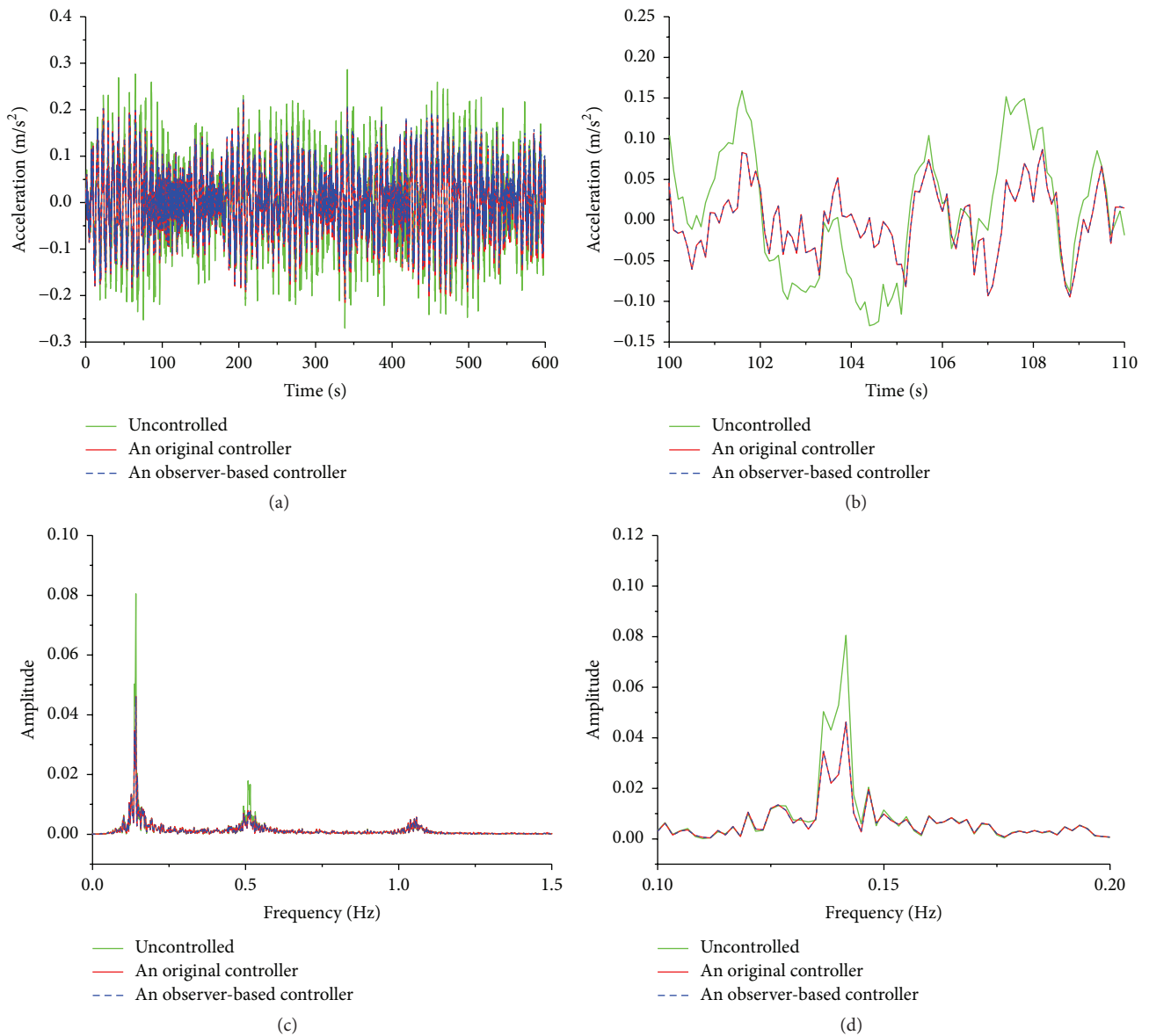

FIGURE 7: Comparison of structural acceleration in 87th floor under uncontrolled and controlled scenarios: (a) and (b) time domain; (c) and (d) frequency domain.
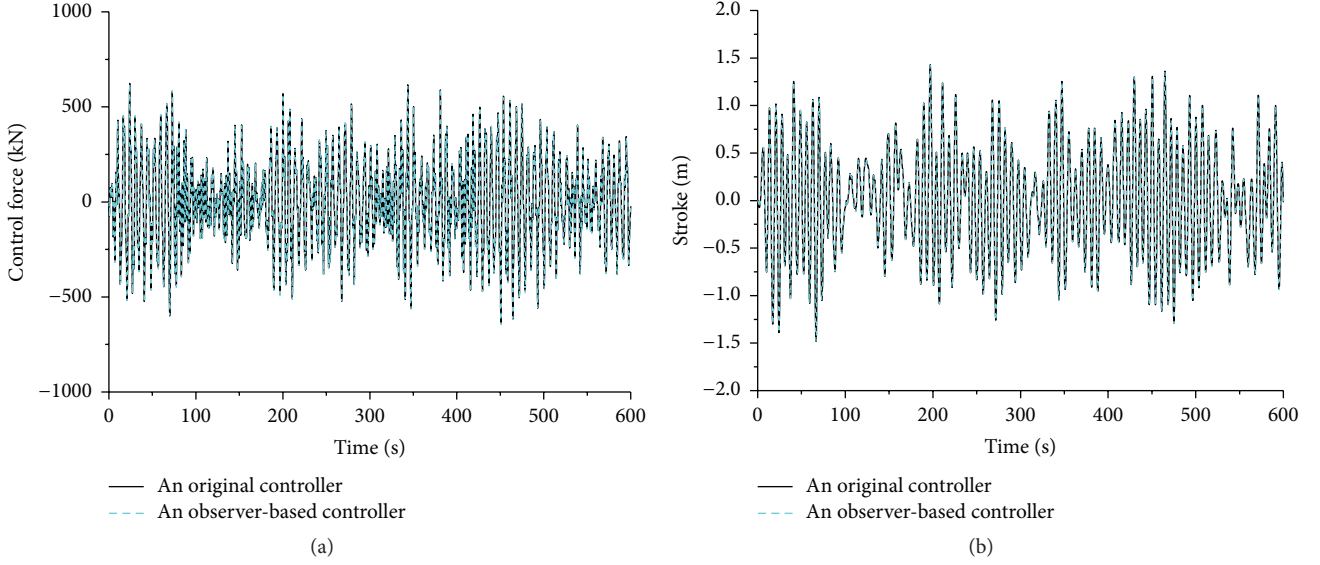
FIGURE 8: Comparison of AMD parameters: (a) AMD control forces; (b) AMD strokes.

TABLE 3: Control effectiveness of structural responses.

Index		An original controller	An observer-based controller	Error
Displacement control effect (%)	87th floor	28.1909	28.1897	0.0012
	91st floor	28.2056	28.2044	0.0012
Acceleration control effect (%)	87th floor	28.7039	28.6327	0.0712
	91st floor	27.5019	27.4487	0.0532
AMD control forces (kN)		638.2055	645.8142	−7.6087
AMD strokes (m)		1.4769	1.4768	0.0001

2.3. A Kalman Filter Design.

When the external excitation is not taken into account, the state-space equation of a MDOF control system with noise can be described as

$$\dot{Z}(t) = AZ(t) + B_2 u(t) + w_1(t)$$
$$Y(t) = CZ(t) + D_2 u(t) + w_2(t), \tag{21}$$

where w_1 and w_2 are random process noise and measurement noise, respectively, and are assumed to be independent. Covariance matrices [18] of these Gaussian noises are

$$Q = E\left[w_1(t) \cdot w_1(t)^T\right],$$
$$R = E\left[w_2(t) \cdot w_2(t)^T\right], \tag{22}$$

where $E(\cdot)$ is the expectation value of $(\cdot)$.

The control force is

$$u(t) = -GZ(t). \tag{23}$$

Substituting (23) into (21) leads to

$$\dot{Z}(t) = (A - B_2 G) Z(t) + w_1(t)$$
$$Y(t) = (C - D_2 G) Z(t) + w_2(t). \tag{24}$$

A Kalman filter [32] for control systems can be constructed as

$$\dot{\widehat{Z}}(t) = (A - B_2 G) \widehat{Z}(t) + G_f\left(Y - \widehat{Y}\right)$$
$$\widehat{Y}(t) = (C - D_2 G) \widehat{Z}(t), \tag{25}$$

where G_f is the Kalman filter gain, $\widehat{Z}$ is the optimal estimation of the state, and $\widehat{Y}$ is the observation, respectively. According to [33], the Kalman filter gain can be written as

$$G_f = P_e (C - D_2 G)^T R^{-1}, \tag{26}$$

where P_e is the model state error covariance matrix and can be solved by the following Riccati equation

$$P_e A^T + A P_e - P_e (C - D_2 G_c)^T R^{-1} (C - D_2 G_c) P_e$$
$$+ Q = 0. \tag{27}$$

Note that the Kalman filter shown by (25) ignores the influence of external excitation during the system state estimation. However, the derivative of state vectors of a general

AMD control system includes the velocity and acceleration responses, which are closely related to the external excitation. Therefore, it leads to a large estimation error when neglecting the influence of external excitation. In order to ensure that the Kalman filter can effectively correct the system state estimation values, the output of the filter includes displacement and velocity responses.

The rebuilt state-space equation of the control system is

$$\dot{Z}(t) = (A - B_2 G) Z(t) + B_1 w(t) + w_1(t)$$
$$Y(t) = Z(t) + w_2(t). \tag{28}$$

In a linear system, the relationship between external excitation w and state vector Z is

$$w = HZ, \tag{29}$$

where H is an unknown transfer function matrix.

Substituting (29) into (28) leads to

$$\dot{Z}(t) = (A - B_2 G + B_1 H) Z(t) + w_1(t)$$
$$Y(t) = Z(t) + w_2(t). \tag{30}$$

Equation (30) is transformed into a discrete system.

$$Z(k + 1) = e^{\varepsilon(A - B_2 G + B_1 H)} Z(k) + w_1(k + 1)$$
$$Y(k + 1) = Z(k + 1) + w_2(k + 1), \tag{31}$$

where ε is a time-step.

According to [34], a Kalman filter of discrete systems is

$$\widehat{Z}(k + 1) = \widetilde{Z}(k + 1) + G_{fk+1} \left[Y(k + 1) - \widehat{Y}(k + 1) \right]$$

$$\widetilde{Z}(k + 1) = \Phi(k) \widehat{Z}(k)$$

$$\Phi(k) = e^{\varepsilon(A - BG + B_1 H)}$$

$$\widehat{Y}(k + 1) = \widetilde{Z}(k + 1)$$

$$Y(k + 1) = \widehat{Y}(k) \tag{32}$$

$$G_{fk+1} = \widetilde{P}_{k+1} \left[\widetilde{P}_{k+1} + R \right]^{-1}$$

$$\widetilde{P}_{k+1} = \Phi(k) \widehat{P}_k \left[\Phi(k) \right]^T + Q_k$$

$$\widehat{P}_{k+1} = \left[I - G_{fk+1} \right] \widetilde{P}_{k+1} \left[I - G_{fk+1} \right]^T$$
$$+ G_{fk+1} R G_{fk+1}^T,$$

where $\Phi(k)$ is the state transition matrix. $\widetilde{Z}(k)$ and $\widehat{Z}(k)$ are the estimates of the state $Z(k)$ before and after correction. $\widetilde{P}_k$ and $\widehat{P}_k$ are the estimates of model state error covariance matrix before and after correction.

Since the discrete filter shown (32) contains an uncertain coefficient matrix H, it still cannot be used in practice. In general, ε is sufficiently short and $\|H\| < \infty$; thus

$$\lim_{\delta \to 0} [\Phi(k)] = \lim_{\Delta t \to 0} e^{\varepsilon(A - B_2 G + B_1 H)} = e^0 = I. \tag{33}$$

The discrete filter shown (32) can be written as

$$\widehat{Z}(k + 1) = \widehat{Z}(k) + G_{fk+1} \left[Y(k + 1) - \widehat{Y}(k + 1) \right]$$

$$\widehat{Y}(k + 1) = \widehat{Z}(k + 1)$$

$$G_{fk+1} = \widetilde{P}_{k+1} \left(\widetilde{P}_{k+1} + R \right)^{-1}$$

$$\widetilde{P}_{k+1} = \widehat{P}_k + Q_k \tag{34}$$

$$\widehat{P}_{k+1} = \left(I - G_{fk+1} \right) \widetilde{P}_{k+1} \left(I - G_{fk+1} \right)^T$$
$$+ G_{fk+1} R G_{fk+1}^T.$$

A Simulink block diagram of the rebuilding control system with a Kalman filter shown in Figure 9 is designed to filter noise. The state observer is depicted by the dashed box, and the symbol inside the solid box represents the Kalman filter.

In this paper, a measured acceleration signal in 87th floor has been collected by the health monitoring system of KK100. This signal includes noise and is processed by wavelet transformation to acquire the actual part of the structural acceleration. Thus, the characteristics of a special noise can be understood. Based on the measured and the actual acceleration signal, the estimate of the state can be obtained by the state observer, and the difference between the actual state Z and the estimated state $\widehat{Z}$ is defined as the measurement noise w_2 of the system. Therefore, covariance matrix of the measurement noise R can be solved. Additionally, since the output of the Kalman filter is the system state, $Q = R$ is set up.

Based on the above obtained covariance matrices Q and R, under a ten-year return period wind load, three systems can be established for KK100. System 1 does not contain noise, systems 2 and 3 include noise, and system 3 with a Kalman filter should be considered. The structural acceleration of different control systems is shown in Figure 10, and the corresponding control effects are listed in Table 4. Figure 10 indicates the control system with noise that does not take any measure is to diverge, and the acceleration control effects of different floors are negative. Compared with the control system without noise, the control system with filtering noise can also obviously reduce the acceleration response of the structure. From Table 4, the maximum variations of the control effects between System 1 and System 3 are only 0.8150% and 1.0505%, meaning the control effects are equivalent to the former. The fact can prove the effectiveness of the Kalman filter.

According to (26) and (27), a Kalman filter gain of linear continuous-time systems should be solved by a model state error covariance matrix P_e, covariance matrices of random process noise, and measurement noises Q and R. Based on the above statistics, P_e is used to calculate the Kalman gain
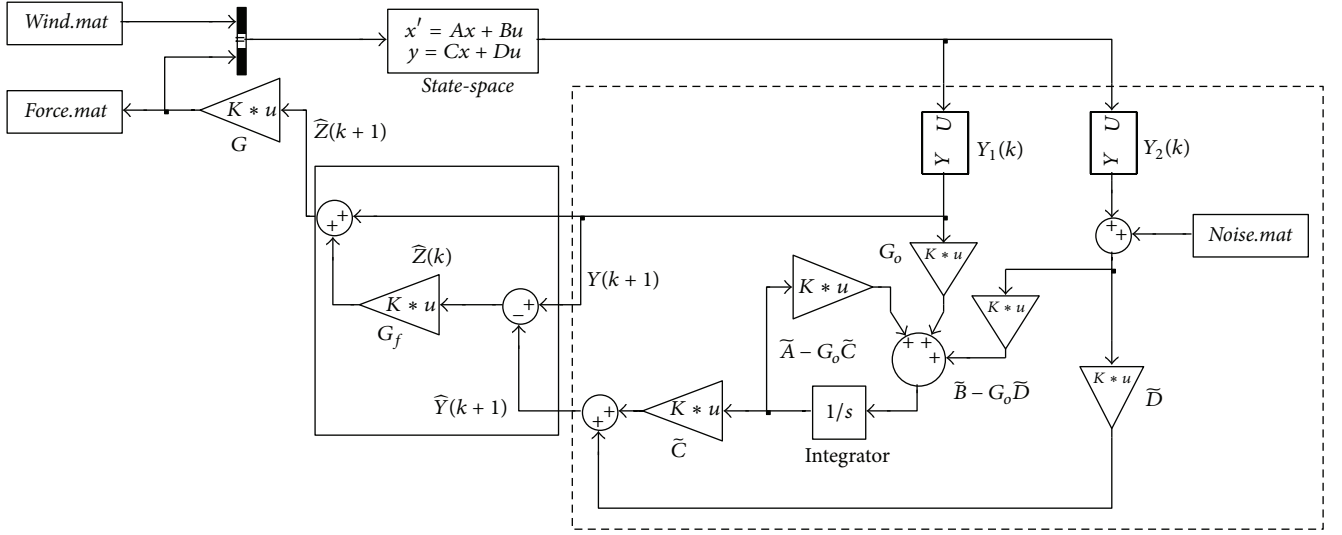
FIGURE 9: Simulink block diagram of the system with a Kalman filter.

TABLE 4: Comparison of the acceleration control effects (%).

Floor	System 1	System 2	System 3 (Kalman filter)
87th	29.4691	−24.5848	28.6541
91st	28.2815	−12.5420	27.2310

of discrete systems; this process has been shown by (34). These above methods do not contain selection process for an optimal gain. Since the selected Kalman filter gain is not a global optimal solution, the observed control force and stroke of system 3 display in Figure 11 are diverging as time goes on. When the absolute value of the AMD stroke is maximum (−3.07 m), its AMD speed is up to (−0.90 m/s). Obviously, a real-time robust filter with optimal gain needs to be designed based on LMI approach to solve this problem.

2.4. A LMI-Based Filter Design.

When the output contains displacement and velocity responses, the state-space equation of the Kalman filter can be written as

$$\dot{\widehat{Z}}(t) = (A - B_2 G)\widehat{Z}(t) + G_f (Y - \widehat{Y})$$
$$\widehat{Y}(t) = \widehat{Z}(t). \tag{35}$$

Subtracting the first equation in (28) from the first equation in (35), the residue equation is then defined as

$$\Delta\dot{Z}(t) = \left[(A - B_2 G) - G_f\right]\Delta Z(t) + B_1 w(t)$$
$$+ \left[w_1(t) - G_f w_2(t)\right], \tag{36}$$

where $\Delta Z(t)$ is the state of the residue equation and $\Delta Z(t) = Z(t) - \widehat{Z}(t)$.

Define

$$\widehat{A} = A - B_2 G - G_f$$
$$\widehat{B} = \begin{bmatrix} B_1, I, -G_f \end{bmatrix} \tag{37}$$
$$\xi(t) = \begin{bmatrix} w(t)^T, w_1(t)^T, w_2(t)^T \end{bmatrix}^T.$$

From (37), the residue equation is

$$\Delta\dot{Z}(t) = \widehat{A}\Delta Z(t) + \widehat{B}\xi(t)$$
$$Y(t) = \Delta Z(t). \tag{38}$$

γ is a given positive constant. In [35], if and only if there exists a symmetric positive-definite matrix X_1 such that the following inequality holds, then the control system shown as (38) has a H_∞ state feedback filter.

$$\begin{bmatrix} \widehat{A}X_1 + X_1\widehat{A}^T & \widehat{B} & X_1 \\ \widehat{B}^T & -\gamma I & 0 \\ X_1 & 0 & -\gamma I \end{bmatrix} < 0. \tag{39}$$

η is a given positive constant. In [29], if and only if there exists symmetric positive-definite matrices X_2 and Q such that the following inequalities hold, then the control system shown as (38) has a H_2 state feedback filter.

$$\widehat{A}X_2 + X_2\widehat{A}^T + \widehat{B}\widehat{B}^T < 0,$$
$$\begin{bmatrix} -Q & X_2 \\ X_2 & -X_2 \end{bmatrix} < 0, \tag{40}$$
$$\text{trace}(Q) < \eta^2.$$

The first inequality of inequalities (40) can be satisfied by inequality (39). The variables X_1, X_2, Q, and G_f are
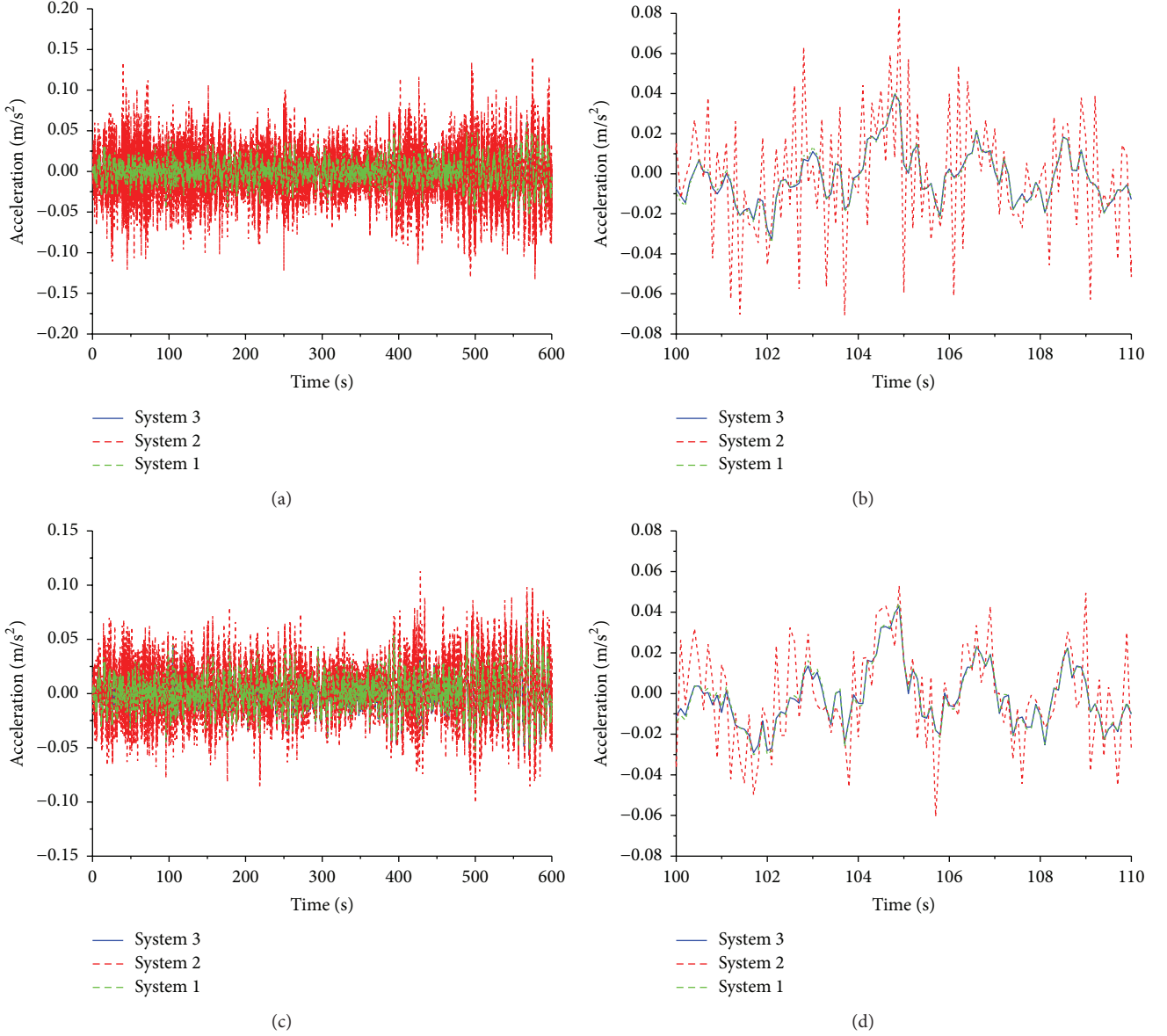
(a)

(b)

(c)

(d)

FIGURE 10: Comparison of structural acceleration in 87th and 91st floors of KK100: (a) and (c) 0–600 s; (b) and (d) 100–110 s.

nonconvex and difficult to be solved due to the filter gain matrix G_f coupling with the different matrices of X_1, X_2. Therefore, variable substitution method cannot be used to linearize these constraints. A public Lyapunov matrix can be found to handle the problem [29].

$$X = X_1 = X_2. \tag{41}$$

The optimization problems from inequalities (39) to (40) can be summarized as

$$\min \quad \eta$$
$$\text{s.t.} \quad (1)\,\text{Inequality }(39)\,;\ (2)\,\text{Inequalities }(40)\,. \tag{42}$$

Both sides of the first inequality of inequalities (42) are pre- and postmultiplying diag$\{X^{-1}, I, I\}$, defining $P = X^{-1}$, and then the matrix inequalities (42) are

$$\min \quad \eta$$

$$\text{s.t.} \quad \begin{bmatrix} P\widehat{A} + \widehat{A}^T P & P\widehat{B} & I \\ \widehat{B}^T P & -\gamma I & 0 \\ I & 0 & -\gamma I \end{bmatrix} < 0,$$

$$\begin{bmatrix} -Q & P^{-1} \\ P^{-1} & -P^{-1} \end{bmatrix} < 0, \tag{43}$$
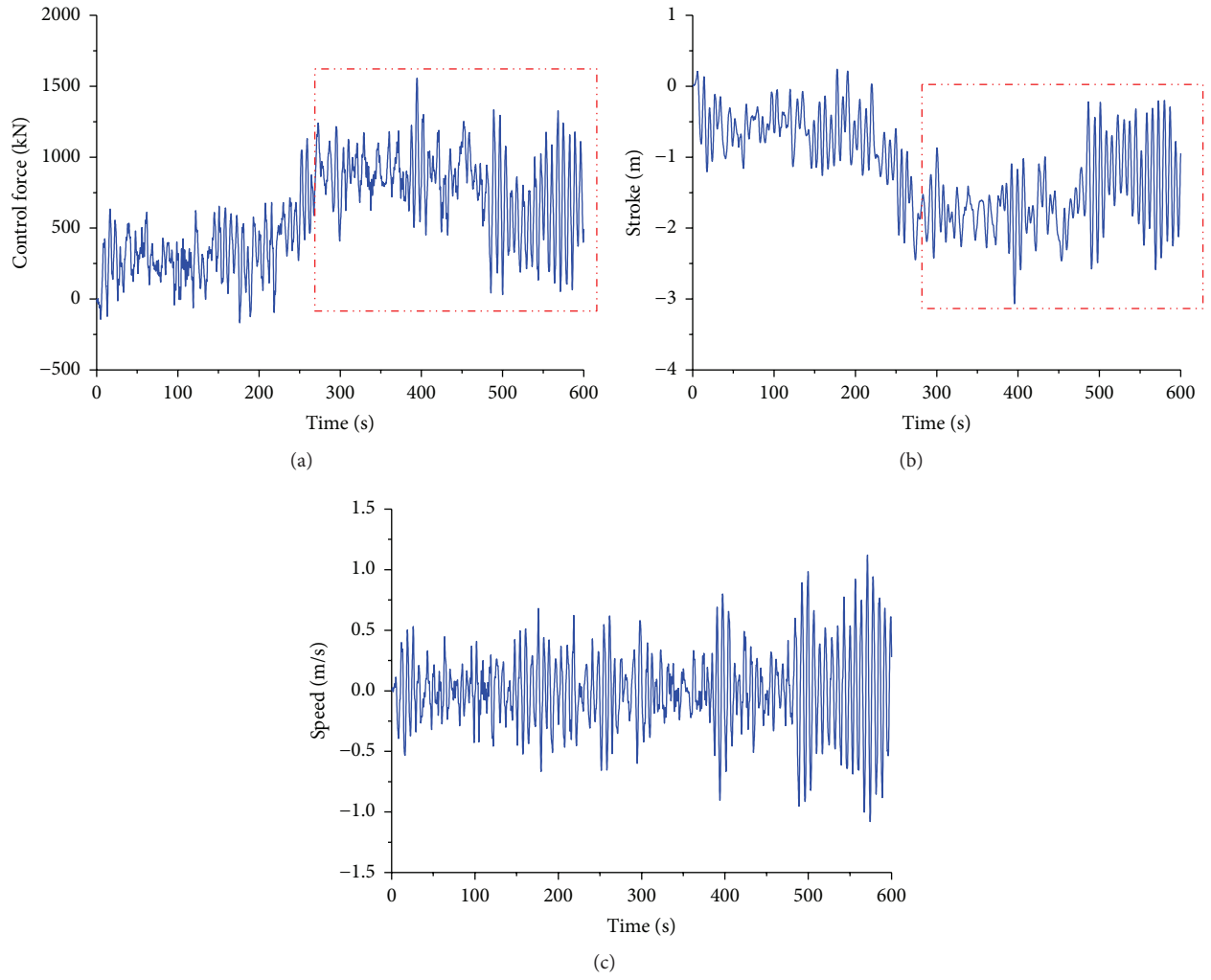
$$\text{trace}\,(Q) < \eta^2.$$

FIGURE 11: AMD parameters of the system with a Kalman filter: (a) AMD control forces, (b) AMD strokes, and (c) AMD speeds.

Substituting (37) into inequalities (43) leads to

$$
\begin{aligned}
&\min \quad \eta \\
&\text{s.t.} \quad
\begin{bmatrix}
(A - BG)^T P + P(A - BG) - \left(PG_f\right) - \left(PG_f\right)^T & P\left[B_1, I, -G_f\right] & I \\
\left[B_1, I, -G_f\right]^T P & -\gamma I & 0 \\
I & 0 & -\gamma I
\end{bmatrix} < 0, \\
&\begin{bmatrix}
-Q & P^{-1} \\
P^{-1} & -P^{-1}
\end{bmatrix} < 0, \\
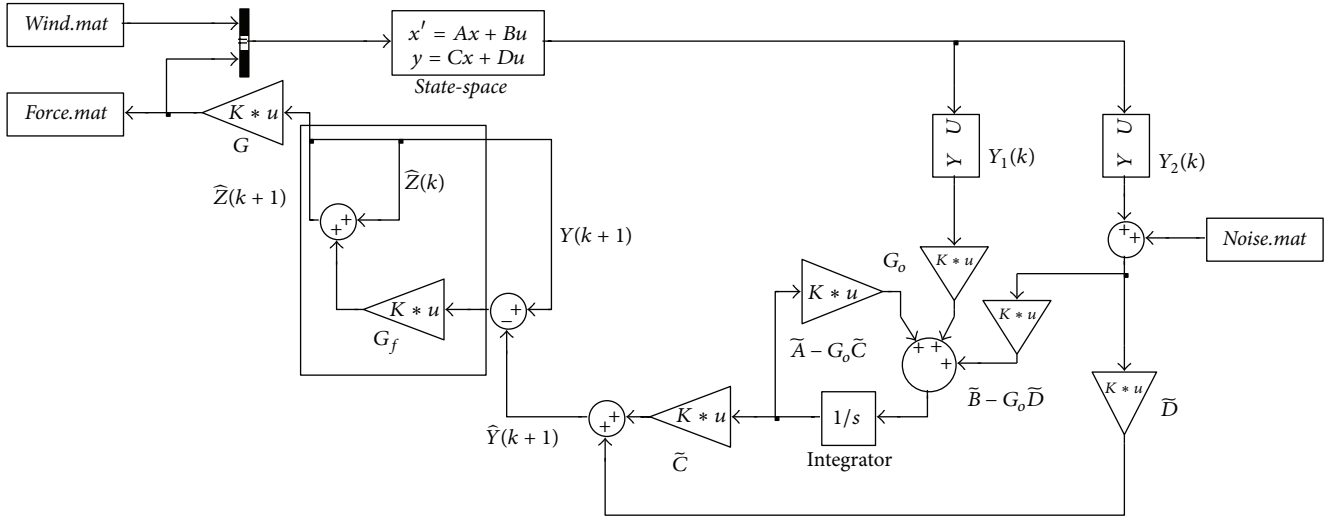&\text{trace}\,(Q) < \eta^2.
\end{aligned}
\tag{44}
$$

FIGURE 12: Simulink block diagram of the system with a LMI-based filter.

Define $N = PG_f$; then the constraint condition for solving the optimization problem (42) can be described as the following inequalities:

$$\begin{bmatrix} (A-BG)^T P + P(A-BG) - N - N^T & [PB_1, P, -N] & I \\ [PB_1, P, -N]^T & -\gamma I & 0 \\ I & 0 & -\gamma I \end{bmatrix}$$
$$< 0, \tag{45}$$

$$\begin{bmatrix} -Q & P^{-1} \\ P^{-1} & -P^{-1} \end{bmatrix} < 0,$$

$$\text{trace}(Q) < \eta^2.$$

The optimal solutions of W, N, and X are obtained through the solver MINCX of LMI toolbox of Matlab, respectively. Then the matrices of optimal feedback gain of the controller and filter are

$$G_f = P^{-1}N. \tag{46}$$

The state-space equation of the LMI-based filter is

$$\dot{\widehat{Z}}(t) = (A - BG)\widehat{Z}(t) + G_f\left(Y - \widehat{Y}\right)$$

$$\widehat{Y}(t) = \widehat{Z}(t) \tag{47}$$

$$G_f = P^{-1}N.$$

A LMI-based filter of discrete systems can be written as

$$\widehat{Z}(k+1) = \widehat{Z}(k) + G_f\left[Y(k+1) - \widehat{Y}(k+1)\right]$$

$$\widehat{Y}(k+1) = \widehat{Z}(k+1)$$

$$Y(k+1) = \widehat{Y}(k) \tag{48}$$

$$G_f = P^{-1}N.$$

A Simulink block diagram of the rebuilding control system with a LMI-based filter shown in Figure 12 is designed to consider the negative influence of noise, but it does not depend on statistical properties of noise. The symbol inside the solid box in Figure 12 represents the LMI-based filter. Its gain G_f is different with the Kalman filter gain. In LMI-based filter, since the discrete-time step is short, the actual state $Y(k+1)$ can be replaced by the estimated state $\widehat{Y}(k)$ [36].

The LMI-based filter shown as (48) is designed by ensuring that H_2 norm (η) of the input and output transfer function of the residue equation shown as (38) is minimum. H_∞ norm (γ) is taken as 1×10^{-9}. A numerical example of KK100 is presented to verify the effectiveness of the LMI-based filter. Systems 1 and 2 are the same as Section 2.3. System 3 with a LMI-based filter has been established. The structural acceleration and the AMD parameters of different control systems are shown in Figures 13–15, and the corresponding control effects are listed in Table 5. Moreover, a shorter return period wind has a more significant effect on noise signal. Therefore, a one-year return period simulated fluctuating wind load that acts on KK100 is also provided to illustrate the effectiveness of the proposed LMI-based filter.

Figures 13 and 14 give a comparison of the system without noise and the system with filtering noise under ten-year and one-year return period simulated fluctuating wind loads. The system with a LMI-based filter can obviously reduce the acceleration response of the structure. From Table 5, when ten-year return period wind load is considered, the maximum variations of the control effects between System 1 and System 3 are only 0.4264% and 0.5695%. This fact can prove the effectiveness of the LMI-based filter. Since the gain is a global optimal solution, the observed control force and stroke of system 3 displayed in Figure 15 are stable as time goes on. Obviously, compared with the Kalman filter, the system with a LMI-based filter can filter out noise in the feedback signals and guarantee the stability of the AMD parameters. As one-year
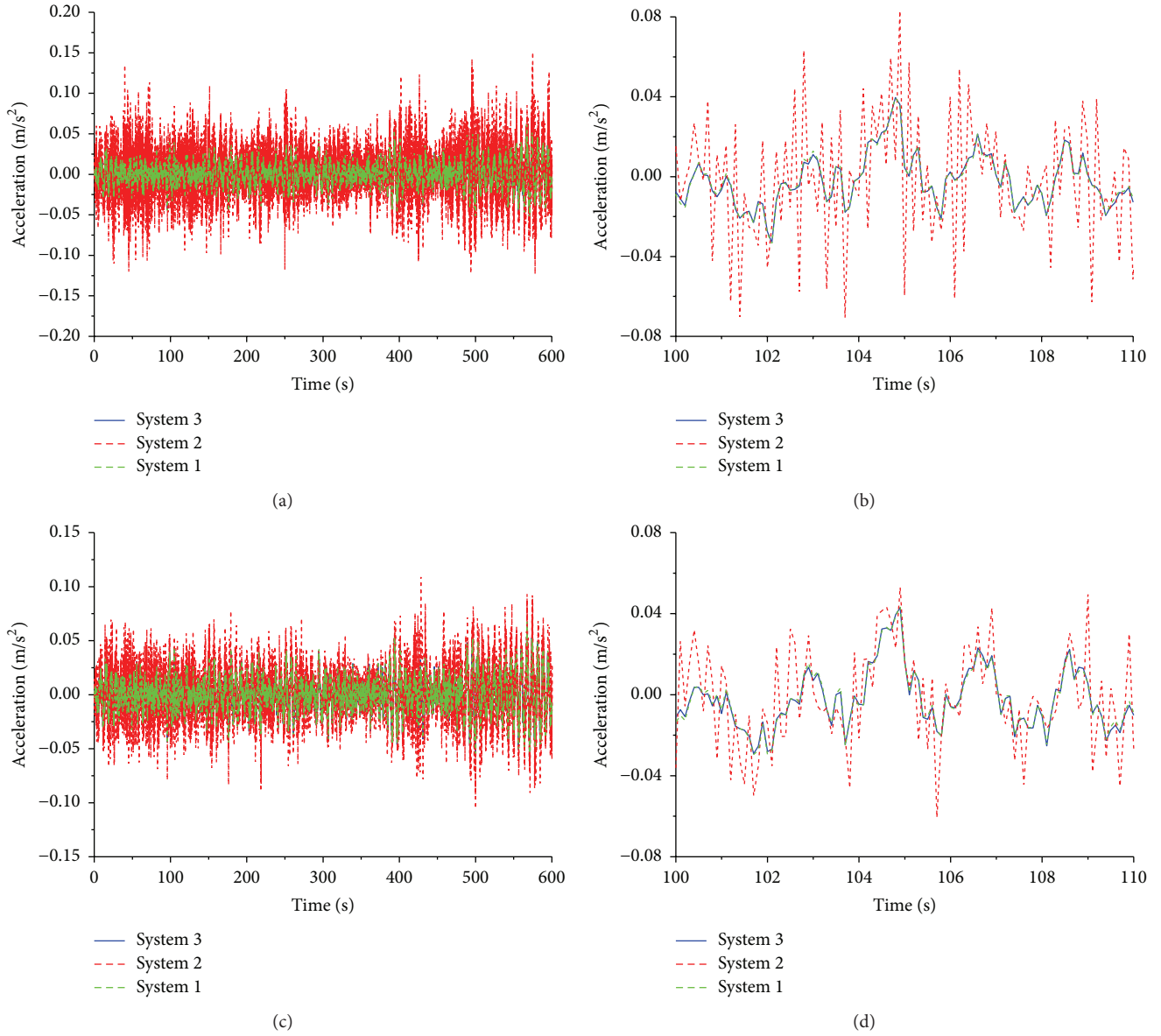
(a)

(b)

(c)

(d)

Figure 13: Comparison of structural acceleration in 87th and 91st floors of KK100 under ten-year return period wind load: (a) and (c) 0–600 s; (b) and (d) 100–110 s.

Table 5: Comparison of the acceleration control effects (%).

Floor	Ten-year return period wind load			One-year return period wind load		
	System 1	System 2	System 3 (LMI-based filter)	System 1	System 2	System 3 (LMI-based filter)
87th	29.4691	−24.5848	29.0427	30.6599	−22.3591	29.9219
91st	28.2815	−12.5420	27.7120	29.9043	−10.3111	28.8975

return period wind load is taken into account, the same results can be acquired.

3. Experimental Verification

This experimental system shown in Figure 16 consists of a four-storey steel frame made of steel and an AMD control device installed on the fourth floor [7]. Specifically, the AMD system mainly consisted of a servo motor, servo controller, an EtherCAT bus system, a dSPACE with a type of DS1103, and a computer. The loading system is composed of a reducer, an inverter, and an eccentric mass. The measurement system utilizes GT02 force balance accelerometers and Micro-Epsilon laser displacement sensors to measure the horizontal acceleration and displacement of the structure along the minor-axis. Acceleration signals are collected by a controller and used as
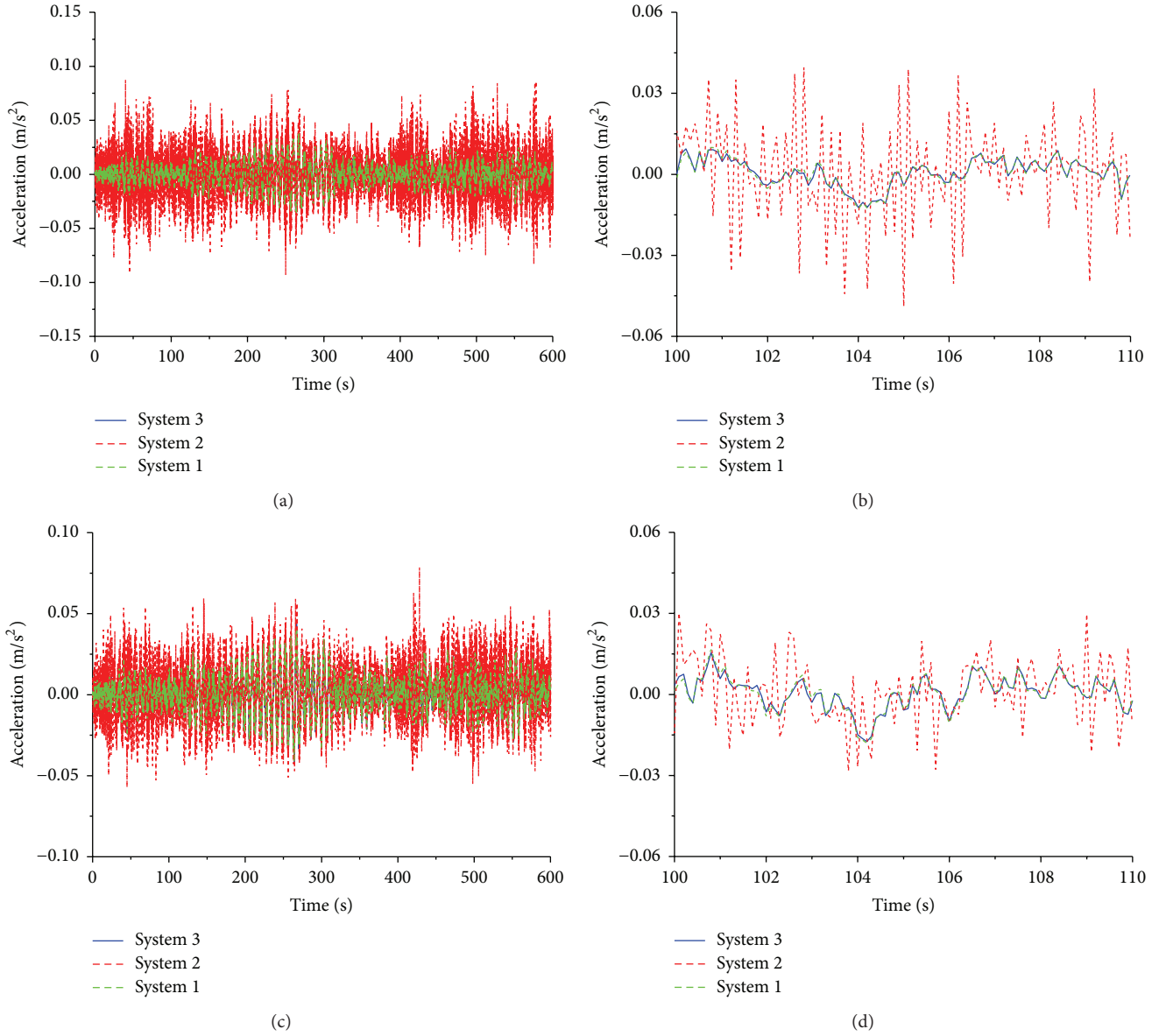
(a)

(b)

(c)

(d)

FIGURE 14: Comparison of structural acceleration in 87th and 91st floors of KK100 under one-year return period wind load: (a) and (c) 0–600 s; (b) and (d) 100–110 s.

the feedback signal to calculate the real-time control forces through a designed observer. An EtherCAT bus system can be used to transmit the forces to the servo motor. The displacement signals of the second, third, and fourth floors are used to verify the control effectiveness.

Signal obtained from GT02 force balance accelerometer includes noise and is processed by wavelet transformation to acquire the actual part in this experiment. Based on the measured and the actual signal, the estimate of the state can be obtained by the state observer, and the difference between the actual state and the estimated state is defined as the measurement noise w_2 of the system. Thus, covariance matrix of the measurement noise R can be solved. Additionally, since the output of the Kalman filter is assumed as the system state, so $Q = R$ is set up. Then, the characteristics of noise

in this accelerometer can be understood. A Kalman filter can be designed to the experimental system based on the above statistics. Meanwhile, a presented LMI-based filter is also designed to the system. A Simulink block diagram of the observer-based experimental control system with different filters shown in Figure 17 is established.

The structural responses and AMD parameters of different control systems with or without noise are shown in Figures 18 and 19. The duration of each scenario is 300 s, and the figures only give data in 30 s. Table 6 presents the corresponding control effects and the values of AMD parameters. The results show that AMD control system without a filter increases the structural response and play a negative role. The displacement and acceleration control effects of the system are all negative. Therefore, it is important to design filters to
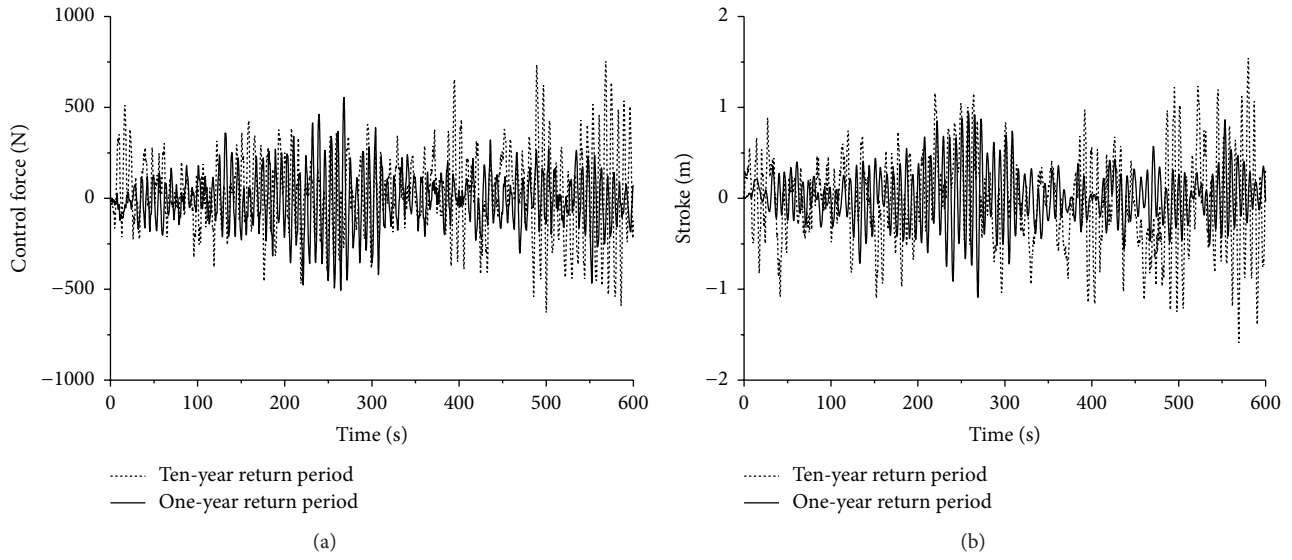
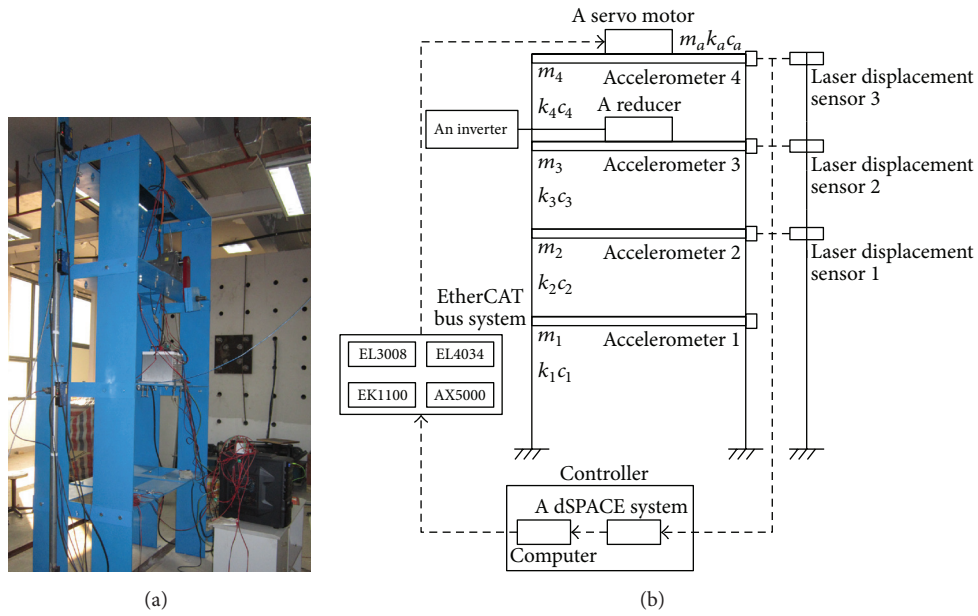FIGURE 15: AMD parameters of the system with a LMI-based filter: (a) AMD control forces; (b) AMD strokes.

FIGURE 16: Pictures of the steel frame structure: (a) practicality; (b) exhibition.

TABLE 6: Control effectiveness of structural responses.

| Index		Without a filter		A Kalman filter		A LMI-based filter	
		Displacement	Acceleration	Displacement	Acceleration	Displacement	Acceleration
Control effect (%)	2nd floor	−13.5934	−12.2130	20.4993	64.2662	19.0997	66.0015
	3rd floor	−13.0100	−4.0517	20.3007	38.2187	19.2022	42.8605
	4th floor	−12.0078	−11.3704	21.7973	62.4459	20.4427	69.2452
Control forces (N)		19.3319		20.3221		16.1615	
Strokes (m)		0.1671		0.1694		0.1059	
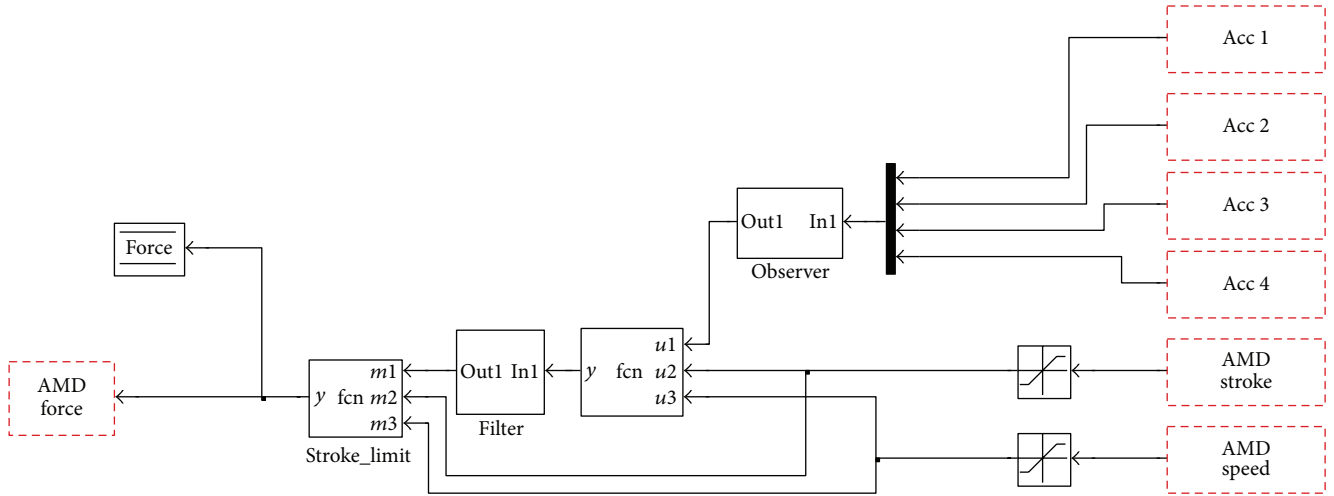
FIGURE 17: Simulink block diagram of the experimental system.
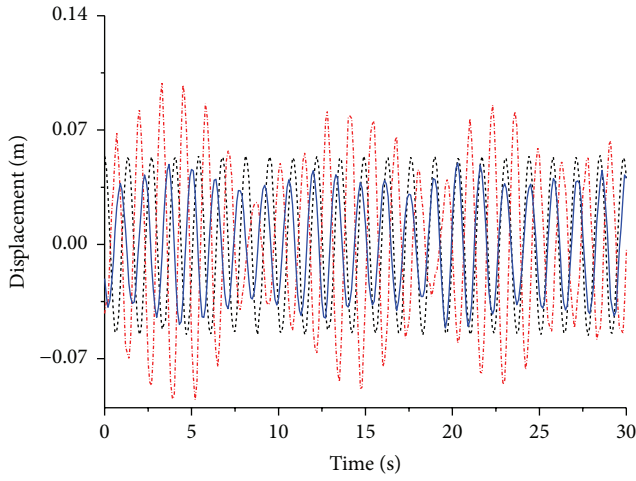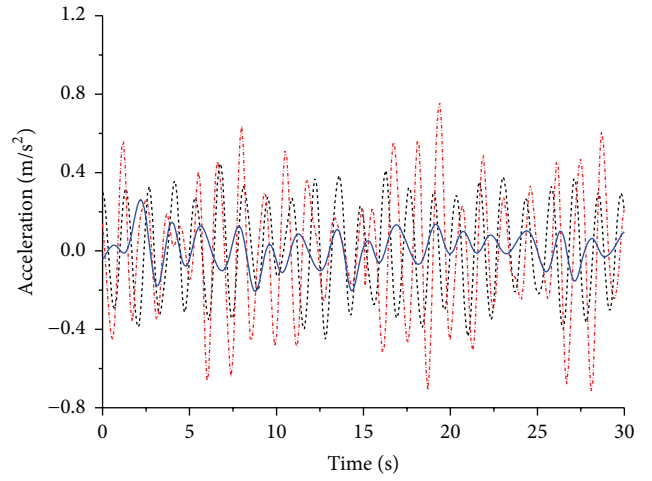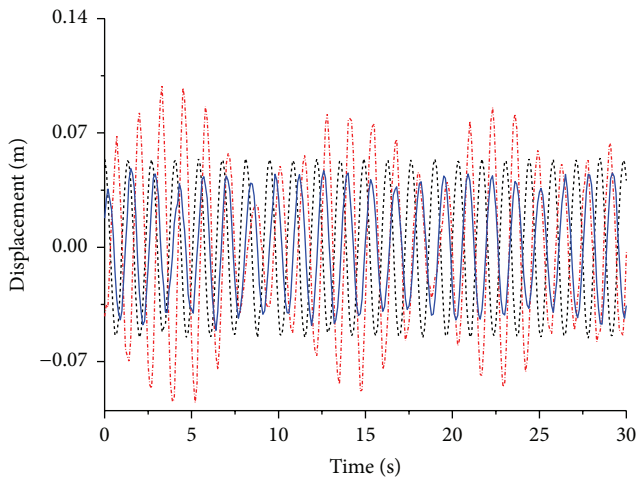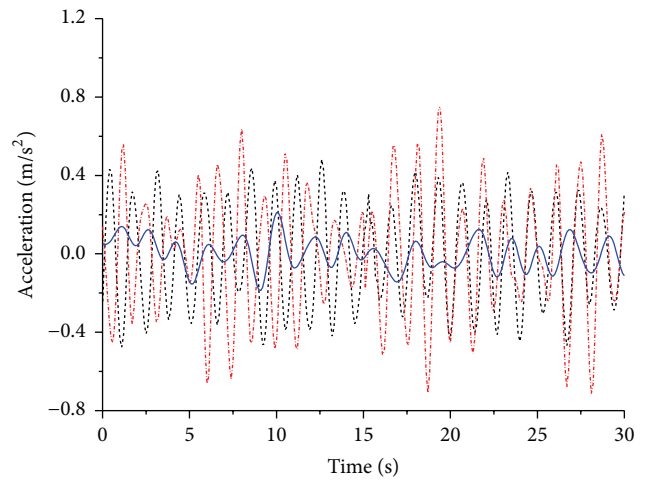
FIGURE 18: Comparison of structural responses in 4th floor of the experimental system: (a) and (c) displacement; (b) and (d) acceleration.
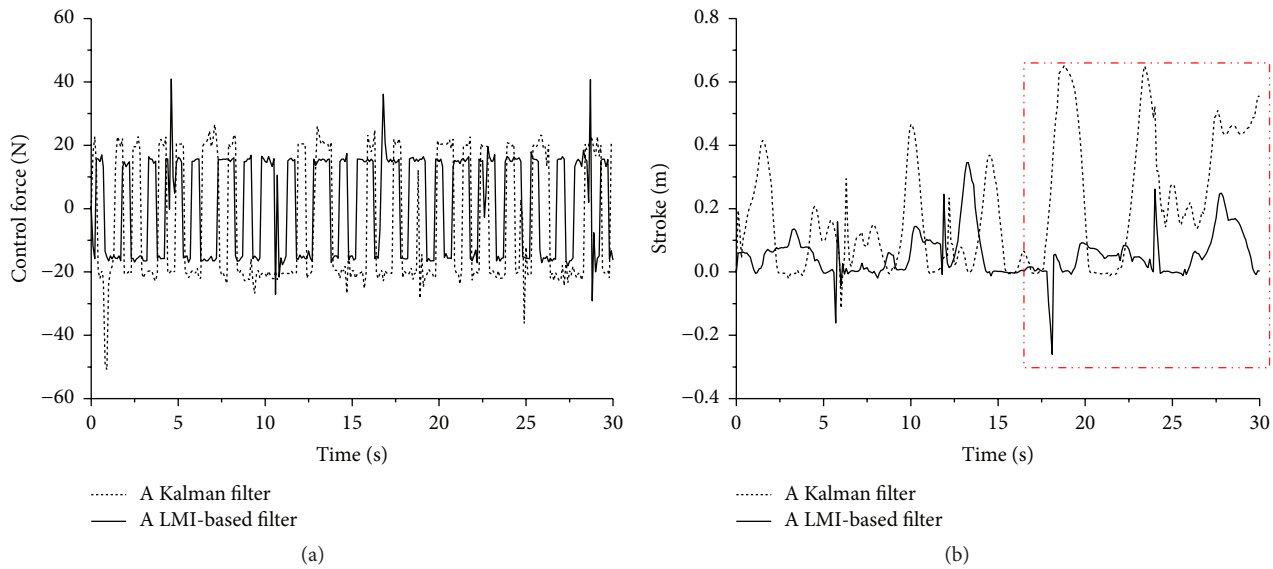
Figure 19: Comparison of AMD parameters of the experimental system: (a) AMD control forces. (b) AMD strokes.

isolate noise. The control effects of the systems with two different filters are all obviously consistent with each other, and these systems can obviously restrain the structural responses. However, the LMI-based filter maintains the AMD parameters in an appropriate range compared with the Kalman filter, and the AMD parameters decrease by 4.1406 N and 0.0635 m.

Because of the interaction between the AMD system and the structure and the coupling between the horizontal and vertical vibrations of the structure, the structural responses do not completely obey the sine law under a sinusoidal load. Since the acceleration control needs high frequency control force that stimulates the structural high-order modes and AMD device is placed on the fourth floor of the structure, the control effect of the third floor has an opposite high-order phase with the second and fourth floor and is significantly less than the control effects of other floors.

4. Conclusions

The paper mainly discusses how to reduce the adverse influence of noise on high-rise buildings with AMD systems. A Kalman filter and a LMI-based filter are all presented for AMD systems with noise. Finally, a numerical example and an experiment are presented to verify the effectiveness of the proposed method. The main conclusions are as follows.

(1) MARMA method is successfully used to simulate a fluctuating wind load, whose wind speed power spectrum is similar to Davenport spectrum in a suitable frequency band.

(2) The original controller and the observer-based controller can obviously reduce the wind-induced acceleration responses. And the observer-based control system has the same control effects and stable AMD parameters as the former.

(3) A Kalman filter and a LMI-based filter are all designed in this paper. The control system with these above filters is consistent with the control system without noise, which indicates that these filters are effective.

(4) However, the control system with a Kalman filter is strongly dependent on the statistical properties of noise, and its selected Kalman filter gain is not a global optimal solution. As a result, its AMD parameters lose stability.

(5) Optimization of filter gain is accomplished based on LMI approach. Therefore, the control system with a LMI-based filter can guarantee the stability of its AMD parameters.

Conflicts of Interest

The authors declare that there are no conflicts of interest regarding the publication of this paper.

Acknowledgments

References

[1] H. Cao, A. M. Reinhorn, and T. T. Soong, "Design of an active mass damper for a tall TV tower in Nanjing, China," *Engineering Structures*, vol. 20, no. 3, pp. 134–143, 1998.

[2] M. Yamamoto, S. Aizawa, M. Higashino, and K. Toyama, "Practical applications of active mass dampers with hydraulic actuator," *Earthquake Engineering and Structural Dynamics*, vol. 30, no. 11, pp. 1697–1717, 2001.

[3] F. Ricciardelli, A. D. Pizzimenti, and M. Mattei, "Passive and active mass damper control of the response of tall buildings to wind gustiness," *Engineering Structures*, vol. 25, no. 9, pp. 1199–1209, 2003.

[4] Y. Ikeda, K. Sasaki, M. Sakamoto, and T. Kobori, "Active mass driver system as the first application of active structural control,"

Earthquake Engineering and Structural Dynamics, vol. 30, no. 11, pp. 1575–1595, 2001.

[5] B. Basu, O. S. Bursi, F. Casciati et al., "A European association for the control of structures joint perspective. recent studies in civil structural control accross europe," *Structural Control and Health Monitoring*, vol. 21, no. 12, pp. 1414–1436, 2014.

[6] J. Teng, H. B. Xing, Y. Q. Xiao, C. Y. Liu, H. Li, and J. P. Ou, "Design and implementation of AMD system for response control in tall buildings," *Smart Structures and Systems*, vol. 13, no. 2, pp. 235–255, 2014.

[7] J. Teng, H. B. Xing, W. Lu, Z. H. Li, and C. J. Chen, "Influence analysis of time delay to active mass damper control system using pole assignment method," *Mechanical Systems and Signal Processing*, vol. 80, pp. 99–116, 2016.

[8] H. Kheloufi, A. Zemouche, F. Bedouhene, and M. Boutayeb, "A new observer-based stabilization method for linear systems with uncertain parameters," in *Proceedings of the European Control Conference (ECC '13)*, pp. 1120–1125, Zurich, Switzerland, July 2013.

[9] H. R. Karimi and M. Chadli, "Robust observer design for takagi-sugeno fuzzy systems with mixed neutral and discrete delays and unknown inputs," *Mathematical Problems in Engineering*, vol. 2012, Article ID 635709, 13 pages, 2012.

[10] A. Golabi, M. T. Beheshti, and M. H. Asemani, "Dynamic observer-based controllers for linear uncertain systems," *Journal of Control Theory and Applications*, vol. 11, no. 2, pp. 193–199, 2013.

[11] M. Farza, M. M'Saad, T. Maatoug, and M. Kamoun, "Adaptive observers for nonlinearly parameterized class of nonlinear systems," *Automatica. A Journal of IFAC, the International Federation of Automatic Control*, vol. 45, no. 10, pp. 2292–2299, 2009.

[12] D. Saoudi, M. Chadli, C. Mechmeche, and N. Benhadj Braiek, "Unknown input observer design for fuzzy bilinear system: an LMI approach," *Mathematical Problems in Engineering*, vol. 2012, Article ID 794581, 21 pages, 2012.

[13] D. Krokavec and A. Filasová, "A reduced-order TS fuzzy observer scheme with application to actuator faults reconstruction," *Mathematical Problems in Engineering*, vol. 2012, Article ID 951953, 25 pages, 2012.

[14] D. Liu, Y. Huang, D. Wang, and Q. Wei, "Neural-network-observer-based optimal control for unknown nonlinear systems using adaptive dynamic programming," *International Journal of Control*, vol. 86, no. 9, pp. 1554–1566, 2013.

[15] N. Boizot, E. Busvelle, and J.-P. Gauthier, "An adaptive high-gain observer for nonlinear systems," *Automatica. A Journal of IFAC, the International Federation of Automatic Control*, vol. 46, no. 9, pp. 1483–1488, 2010.

[16] S. Jeon and M. Tomizuka, "Benefits of acceleration measurement in velocity estimation and motion control," *Control Engineering Practice*, vol. 15, no. 3, pp. 325–332, 2007.

[17] F. Qin, X. Dai, and J. E. Mitchell, "Effective-SNR estimation for wireless sensor network using Kalman filter," *Ad Hoc Networks*, vol. 11, no. 3, pp. 944–958, 2013.

[18] A. Alessandri, M. Baglietto, and G. Battistelli, "A maximum-likelihood Kalman filter for switching discrete-time linear systems," *Automatica. A Journal of IFAC, the International Federation of Automatic Control*, vol. 46, no. 11, pp. 1870–1876, 2010.

[19] M. Karasalo and X. Hu, "An optimization approach to adaptive Kalman filtering," *Automatica. A Journal of IFAC, the International Federation of Automatic Control*, vol. 47, no. 8, pp. 1785–1793, 2011.

[20] R. Peesapati, S. L. Sabat, K. P. Karthik, J. Nayak, and N. Giribabu, "Efficient hybrid Kalman filter for denoising fiber optic gyroscope signal," *Optik*, vol. 124, no. 20, pp. 4549–4556, 2013.

[21] Z. Liu, J. Wang, and Y. Xue, "Interacting multiple sensor filter," *Signal Processing*, vol. 92, no. 9, pp. 2180–2186, 2012.

[22] Y. H. Yu, "Combining H_∞ filter and cost-reference particle filter for conditionally linear dynamic systems in unknown non-Gaussian noises," *Signal Processing*, vol. 93, no. 7, pp. 1871–1878, 2013.

[23] W. J. Qi, P. Zhang, and Z. L. Deng, "Robust weighted fusion Kalman filters for multisensor time-varying systems with uncertain noise variances," *Signal Processing*, vol. 99, no. 1, pp. 185–200, 2014.

[24] B. Fridholm, T. Wik, and M. Nilsson, "Kalman filter for adaptive learning of look-up tables with application to automotive battery resistance estimation," *Control Engineering Practice*, vol. 48, pp. 78–86, 2016.

[25] F. Alonge, F. D'Ippolito, A. Fagiolini, and A. Sferlazza, "Extended complex Kalman filter for sensorless control of an induction motor," *Control Engineering Practice*, vol. 27, no. 1, pp. 1–10, 2014.

[26] O. Rosén, A. Medvedev, and T. Wigren, "Parallelization of the Kalman filter on multicore computational platforms," *Control Engineering Practice*, vol. 21, no. 9, pp. 1188–1194, 2013.

[27] S. W. Pan, H. Y. Su, J. Chu, and H. Wang, "Applying a novel extended Kalman filter to missile-target interception with APN guidance law: A benchmark case study," *Control Engineering Practice*, vol. 18, no. 2, pp. 159–167, 2010.

[28] S. Boyd, L. E. Ghaoui, E. Feron, and V. Balakrishnan, *Linear matrix inequalities in system and control theory*, vol. 15 of *SIAM Studies in Applied Mathematics*, Society for Industrial and Applied Mathematics (SIAM), Philadelphia, Pa, USA, 1994.

[29] L. Yu, *Robust Control-Linear Matrix Inequalities Approach*, Tsinghua University Press, China, 2002.

[30] C. X. Qu, L. S. Huo, and H. N. Li, "Fault tolerant control for civil structures based on LMI approach," *Mathematical Problems in Engineering*, vol. 2013, Article ID 762385, 8 pages, 2013.

[31] E. J. Hannan, "The identification of vector mixed autoregressive-moving average system," *Biometrika*, vol. 56, pp. 223–225, 1969.

[32] J. P. Ou, *Active, Semi-Active and Intelligent Control in Civil Engineering Structure*, Science Press, 2003.

[33] G. Burgers, P. J. van Leeuwen, and G. Evensen, "Analysis scheme in the ensemble Kalman filter," *Monthly Weather Review*, vol. 126, no. 6, pp. 1719–1724, 1998.

[34] R. F. Souto and J. Y. Ishihara, "Robust kalman filter for discrete-time systems with correlated noises," in *Proceedings od the Mediterranean Conference on Control and Automation, (MED '08)*, pp. 1658–1662, fra, June 2008.

[35] J.-H. Ge, P. M. Frank, and C.-F. Lin, "Robust H_∞ state feedback control for linear systems with state delay and parameter uncertainty," *Automatica*, vol. 32, no. 8, pp. 1183–1185, 1996.

[36] R. Panigrahi and B. Subudhi, "Performance enhancement of shunt active power filter using a Kalman filter based H_∞ control strategy," *IEEE Transactions on Power Electronics*, pp. 1–9, 2016.

Research Article

The Performance of Resistance Progressive Collapse Analysis for High-Rise Frame-Shear Structure Based on OpenSees

Qiang Zhang and Yaozhuang Li

Institute of Disaster Prevention Science and Safety Technology, Central South University, Changsha 410128, China

Correspondence should be addressed to Yaozhuang Li; 441894855@qq.com

A finite element model (FEM) of frame-shear structure was constructed using OpenSees program based on the nonlinear flexibility theory and multi-vertical-line theory that considered bending-shear coupling, and its progressive collapse resistance under abnormal conditions was analyzed. Flexibility-based method for modeling shear wall finite element and multi-vertical-line element (SFI-MVLEM) was proposed. Method of deleting failure component elements was presented, as well as the model solving algorithm. The FEM was validated by the completed structure test. On these bases, 3 groups of typical frame-shear structure systems were designed to perform nonlinear dynamic collapse analysis under different initial failure conditions, in order to study the impact of the number of floors and earthquake resistant design on the progressive collapse resistance of frame-shear structures. Analysis results showed that, at initial failure of frame column, the residual shear wall element can well complete the internal force redistribution of structure to provide alternative force transmission path, thereby forming antiprogressive collapse force. In the case of initial failure of shear wall, C-shaped shear wall can form alternative path to diminish the vertical deformation of frame-shear structures. Final comparison shows that the structural seismic design can effectively improve their anticollapse performance.

1. Introduction

Progressive collapse of building structures refers to the horizontal and vertical sequential damage of structures led by local failure caused by explosion, terrorist attacks, and other accidents, which results in collapse of overall structures or large-scale collapse that is disproportionate to the initial damage [1]. Progressive collapse of structures severely harms the public safety and people's lives and property. Internationally, research on the progressive collapse of structures began with the British Ronan Point apartment collapse in 1968 initiated by gas explosion. In 2001, the US World Trade Center collapsed as a result of "911" terrorist attack, which drew the attention of engineering and academic circles [2, 3]. After years of scientific research and exploration, various countries have developed comprehensive antiprogressive collapse design codes. Representative ones are the US GSA and DoD guidelines. Meanwhile, China also officially released the collapse resistance code in 2015, the *Code for Anticollapse Design of Building Structures*. Taking a general view of the codes of

various countries, the antiprogressive collapse design of high-rise structure focuses mainly on enhancing the reinforcement within beams, increasing the bending capacity of beam ends, and strengthening the role of beam mechanism, while exerting the axial tensile catenary action of rebar, in order to enhance the overall structural stability. For now, in terms of analytical methods, the most commonly used method of analyzing progressive collapse resistance is the linear static alternate path method, while the most accurate method is the nonlinear dynamic alternate path method [3–7].

Aside from the research findings in design codes and progressive collapse resistance guidelines, scholars from various countries have also made some progressive collapse in structural testing and numerical simulation in recent years. For example, with respect to collapse testing, Yi et al. [8] conducted a collapse test on a plane frame through quasistatic demolition test to determine the stress process of the test frame and the stress transformation mechanism. On this basis, Li et al. [9] carried out a collapse test on a plane frame infill wall to determine the contribution of infill wall within

the frame to the collapse resistance and collapse process of frame infill wall. With respect to spatial structure testing, Wang et al. [10] used a quasistatic approach to complete a series of progressive collapse tests on dual-layer bidirectional RC frame. They analyzed the transformation and stress mechanisms in each collapse stage of the space frame and put forward the lateral deformation calculating method as well as structural damage model. In terms of numerical calculation, Zhang and Liu [11] proposed several major challenges in solving the progressive collapse of structures: large geometric displacement and deformation, discontinuous displacement field, and collision effect between collapsed elements. Based on the energy balance algorithm, Vlassis et al. [12] constructed a theoretical framework for analyzing the progressive collapse resistance of RC frame structures. On this basis, Li et al. [13] derived the demand relationship between linear and nonlinear resistance of beam and catenary mechanisms in the collapse process of frame structures. Regarding the finite element programming computation, Wang et al. [14] built a 12-story frame structure based on the ABAQUS FEA software for the nonlinear analysis of progressive collapse. In summary, despite many existing antiprogressive collapse theoretical systems and finite element programming computation methods for structures, most of them are for RC frame structures. Few studies have investigated the contribution of shear wall to the antiprogressive collapse in the RC frame-shear wall structures. In addition, there is little research on the effect of seismic design on anticollapse performance of structures despite the widespread concern about antiprogressive collapse capability of high-rise structures. In view of this, this paper discusses the effect of seismic design.

A typical frame-shear building structure (6-degree seismic design) is designed herein according to the *Chinese Code for Design of Concrete Structures* (GB 50010-2010) based on OpenSees finite element program. Using the designed structure, an analysis is made on the effect of number of stories on progressive collapse resistance of frame-shear structure. To consider the effect of seismic design on the structural antiprogressive collapse performance, the frame-shear structure is subjected to 8-degree seismic design in accordance with the *Code for Seismic Design of Buildings* (GB 50011-2010), as well as to progressive collapse analysis. Meanwhile, finite element model is constructed with flexibility method-based fiber beam elements and novel multi-vertical-line shear wall elements that consider bending-shear coupling. Modeling method of the frame structure is presented and verified by an example. On these bases, alternate path method is employed to perform nonlinear dynamic analysis on the RC frame-shear wall structure model. The relevant modeling method and calculation results can provide some references for the antiprogressive collapse analysis of frame-shear structures.

2. Design Information

A 15-story RC frame-shear wall structure is designed according to the *Code for Design of Concrete Structures* (GB 50010-2010) and the *Code for Seismic Design of Structures* (GB 50011-2010) with reference to the structural layout of an actual
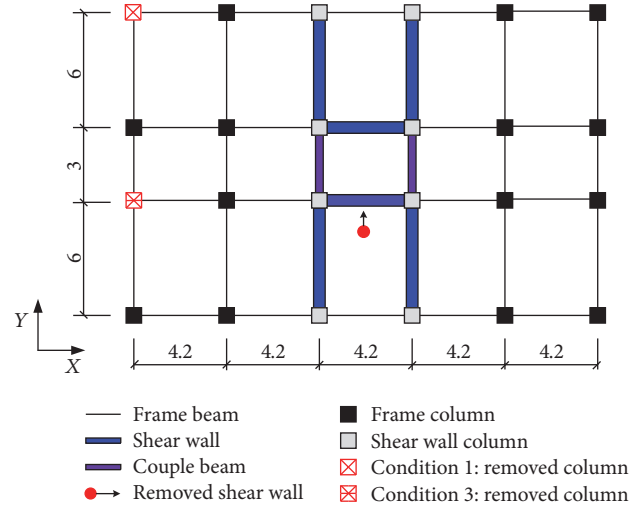

FIGURE 1: Floor plan of the building models (unit: m).

project [15, 16]. The relevant design information is as follows:

(1) Figure 1 presents the planar layout of the structure. The first story is 4.2 m high, while the remaining stories are 3.6 m high. Columns have a cross section size of 650 mm × 650 mm, while those for transverse beams (X direction) and longitudinal beams (Y direction) are 300 mm × 500 mm and 350 mm × 700 mm, respectively. Floor thickness is 120 mm, while column feet are assumed to be fixed to the floor. In terms of materials, concrete used for shear walls and columns has a strength grade of C40, while that used for plates and beams has a strength grade of C30. Longitudinal rebar pieces of constraint elements at the edge of shear walls are the same in grade as those of columns, which are HRB400. Besides, type of longitudinal rebar of beams is selected as HRB335, whereas type of stirrup material is HPB235. Table 1 displays the material parameters of the structural members in these buildings.

(2) Load information: floor dead load is 5.0 kN/m^2 and live load 2.0 kN/m^2. Roof dead load is 7.5 kN/m^2 and live load 0.5 kN/m^2, while surface roughness is set as category C.

(3) Seismic design information: type of soil in the construction site is set as type II. Besides, seismic fortification intensity is 6 degrees, and seismic grade of shear walls and frames is grade 2. To consider the effect of seismic design on the structural antiprogressive collapse, the frame-shear structure is subjected to 8-degree seismic design, while other design information remains unchanged. The corresponding design peak ground acceleration (PGA) with a 10% probability of exceedance in 50 years equals 0.05 and 0.20 g, in which g is the acceleration of gravity. Note that because of different requirements of the maximum axial force ratios specified in the Chinese seismic

TABLE 1: Parameters of structural material.

Item name	Beams	Columns	Shear walls
Concrete	C30 (f_c = 20 MPa)	C40 (f_c = 26.8 MPa)	C40 (f_c = 26.8 MPa)
Longitudinal reinforcing steel	HRB335 (f_y = 335 MPa)	HRB400 (f_y = 400 MPa)	
Hoop reinforcing steel		HPB235 (f_y = 235 MPa)	

TABLE 2: Dynamic properties of the structure.

Item name		6-degree	8-degree
Vibration periods (s)	T_1 (1st-order translation in X direction)	1.5	1.05
	T_2 (1st-order translation in Y direction)	1.5	1.05
	T_3 (1st-order torsion)	1.24	0.88
Self-weight (t)		3250	3480

design code, the steel quantity in 8-degree seismic design is large than that in 6-degree seismic design. Specifically, the maximum axial force ratio for the design intensity of 6-degree is 0.9, whereas that for the design intensity of 8-degree is 0.75. And steel dosage also results in different self-weights in these buildings. The basic dynamic properties of the frame-shear wall structures are given in Table 2.

To consider the effects of different number of stories on the progressive collapse resistance of frame-shear structure and to simplify the collapse analysis process, in this paper, 10-story and 15-story RC frame-shear models are built for separate antiprogressive collapse analyses. To consider the effect of seismic design on the structural anticollapse performance, the frame-shear structure is subjected to 8-degree seismic design and modeling for progressive collapse analysis, followed by comparative analysis of collapse models. In accordance with the provisions of GSA2010 and DoD2010, demolition analysis on key components is needed. To comprehensively analyze the antiprogressive collapse performance of frame-shear structure, the following demolition conditions are designed herein. Regarding the demolition of key columns, corner columns and the short edge column are chosen for removal. Regarding the demolition of shear walls, in accordance with the DoD2010 provisions, load-bearing walls with height greater than twice the story height should be removed in steps, while for those with height less than twice the story height, shear walls can be removed as a whole for the progressive collapse analysis. According to the design information, shear walls of this paper are lower than twice the story height, so shear walls in the center of first floor are chosen for holistic removal. Relevant demolition sites are marked in Figure 1.

In accordance with the DoD2010 provisions, the judging mechanism for progressive collapse failure of structure in this paper is as follows: when the top displacement of removed member exceeds 1/5 of the vertical relative displacement of beam connected to it, the structure is judged as failure, which enters an irreversible collapse process. The frame-shear structure in this paper is symmetrical. Nonlinear dynamic alternate path method is used to analyze the frame-shear model,

in order to ensure the accuracy of antiprogressive collapse analysis.

3. Finite Element Model

3.1. SFI-MVLEM Element Model for Shear Walls. Multi-vertical-line shear wall element considering bending-shear coupling is developed on the basis of three-vertical-line-element theory. Initially proposed by Japanese scholars [17], the three-vertical-line-element model utilizes the axial stiffness by the two external elements and adds a horizontal spring at the position of central line element to simulate the shear response on the RC wall by shifting the neutral axis of wall member. But the defects are that consistent deformation between local springs and central line element is difficult and the height of central line element can hardly be determined, which easily lead to computational difficulty. On this basis, researchers have developed a multi-vertical-line-element theory, where multiple vertical springs are introduced to simulate the axial and bending stiffness of shear walls, and horizontal springs are used at the position of central line element to simulate the shear stiffness, thereby solving the problem of difficulty in consistent deformation. However, shear action cannot be considered for vertical springs, and the contribution of RC material to shear force is neglected, so its use in simulation may lead to computational deviation. Eventually, a multi-vertical-line element theory considering bending-shear coupling was developed [18], which is based on the fixed-strut-angle-model (FSAM) and where a novel RC element is used to replace the vertical fiber element. Bending-shear action and material constitution can directly be considered for a single RC element in the model, and separate stress analysis is possible. Furthermore, interlock behavior of concrete aggregate and dowel action of rebar are modified to improve the computation accuracy of the model. The theoretical schematic diagram is shown Figure 2.

3.2. Flexibility-Based Fiber Line Element for Beam and Column. In the geometric nonlinear analysis of structure's progressive collapse, the actual and assumed displacement fields of line elements like beams and columns differ greatly. So fine
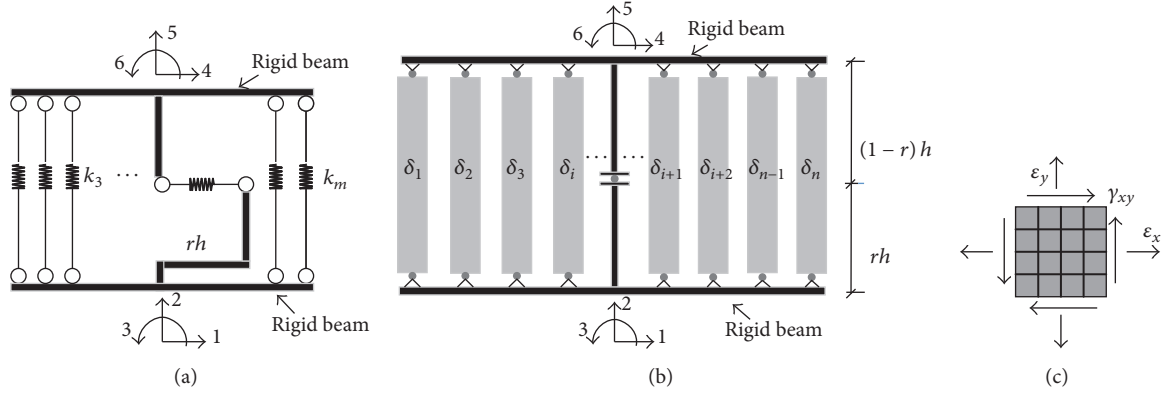
FIGURE 2: Element models: (a) MVLEM element; (b) SFI-MVLEM element; (c) RC panel element.

(a) Initial phase   (b) Static internal force stage   (c) Collapse stage
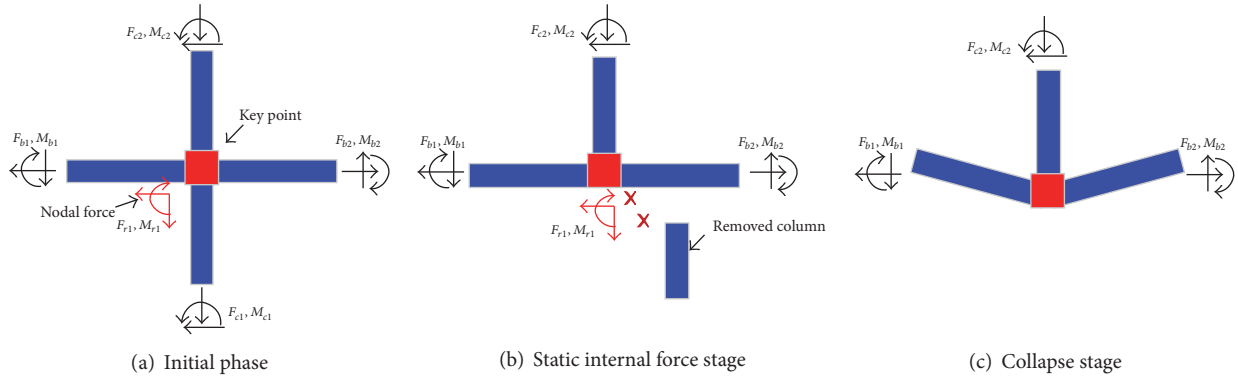
FIGURE 3: Element-deletion method.

division of line elements is needed to approximate the real displacement field, in order to improve the solution accuracy. The fine division of elements will increase the number of elements, which will affect the solution efficiency. To ensure the accuracy and efficiency of solution, flexibility-based fiber line element is used in this paper [19]. Sectional resistance and tangent stiffness of the flexibility-based beam-column elements are calculated by force function interpolation. Calculation is possible as long as the number of elements and the number of integration points are determined according to the dimensions of line members without the need to refine displacement field. In the nonlinear calculation process, good results can be obtained, and convergence is overall favorable.

Since the OpenSees program is different from the commercial finite element programs, if nonlinear dynamic analysis is performed by simply killing the predesigned key members applying "birth-death element" technology, the degree of freedom of the overall structure will undergo changes. Moreover, the instantaneous removal of elements leads to great dynamic effect on the structure, which is likely to result in interruption or nonconvergence of calculation process. In this paper, to achieve precise calculation, first of all, the overall calculation was conducted on the model, and the static internal force and counterforce of failure node were obtained. Then, the key components were removed and the static internal force and counterforce before the components were

removed were exerted on the components at the same time so as to make the structure equal to the overall structure before the components were removed. Finally, to obtain the transient oscillation effect of the structure, the static internal force and counterforce on the key nodes were instantaneously removed, and the time was returned to zero at the same time for nonlinear dynamic calculation [20]. The schematic diagram of analytical procedure is shown in Figure 3.

Regarding iterative integration and solution, this paper employs Krylov-Newton algorithm to facilitate the convergence of program computation. Transformation method is used for boundary condition processing, while SparseSYM is utilized for solving dynamic analysis equations [21].

The SFI-MVLEM element is used as the shear wall element to calculate the elastoplastic behaviors of RC wall corresponding zones by taking into consideration the concrete confinement effect in the confinement zone of wall-edge members and the reinforcement assignment in the nonconfined zone of wall plates. Rebar is set according to the sectional design of members. Figure 4(a) shows the division of shear wall member elements, where the central joints and SFI-MVLEM elements are divided according to the shear wall height. In the figure, the modified ConcreteCM constitutive model is used for the concrete material, while the modified SteelMPF constitutive model is employed for the rebar material. The shear coefficient of element, dowel stiffness of rebar,

(a) Analysis model of shear wall
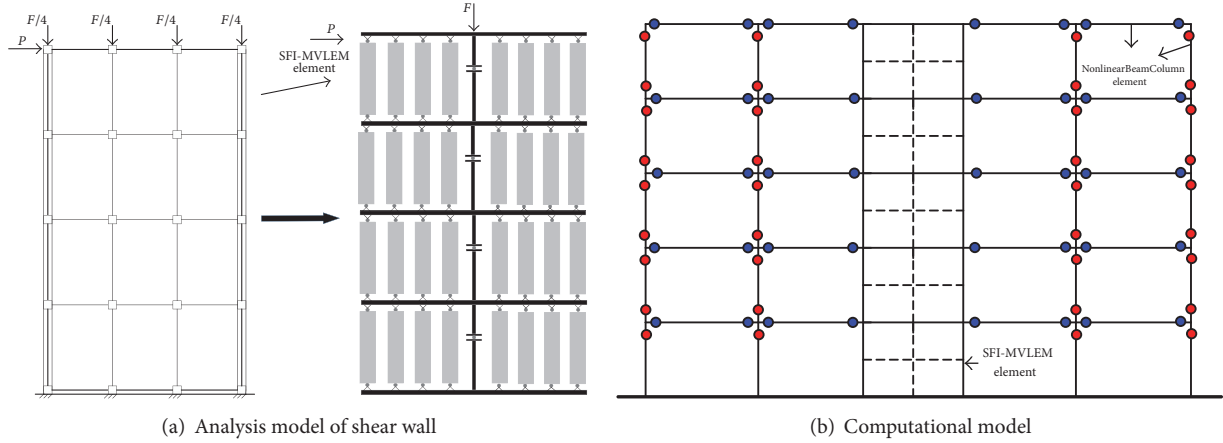
(b) Computational model

Figure 4: Finite element model.

and reinforcement ratio of members are calculated by applying the FSAM theory. The constitutive relations between concrete and rebar are integrated into a FSAM material constitutive model to perform the elastoplastic analysis of shear wall members. Finite elements of flexibility-based line system are modeled with the NonlinearBeamColumn element. Concrete is modeled using the Mander model, while rebar is modeled using the Giuffre-Gotto-Pinto model. For the models in this paper, two sets of shear wall elements are set up for each story taking the 5-story planar frame-shear wall structure as an example. Relevant schematic diagram is shown in Figure 4(b).

3.3. Validation of the Model with a Series of Test Results. Due to space constraints, four sets of shear wall specimens are selected in this paper for calculation with SFI-MVLEM shear wall elements, and the results are compared with the experimental data. The specific procedure is shown in Figure 5. Figure 5(a) [22] presents the linear shear wall with a design shear height ratio of 2.0. Experimental process is dominated by bending failure. Clearly, the calculated results of SFI-MVLEM element are in good agreement with the experimental findings. Figure 5(b) presents the shear wall test with displacement ratio as the loading condition [23]. It can be concluded from the comparison results that the calculations in this paper are also applicable to shear walls controlled by this type of loads. Figure 5(c) shows the large-scale of shear wall specimen, where cracks spread through the wall plate area, and rebar at the bottom yield [24]. Comparison data demonstrates that the SFI-MVLEM element can well calculate the elastic-plastic behavior of such shear walls. Figure 5(d) shows the high-strength concrete shear wall member, whose concrete strength is up to 102 MPa [25]. The model in this paper allows accurate calculation of such shear wall members. It can thus be concluded that the SFI-MVLEM shear wall element has a good accuracy and is simple to model, which is suitable for various kinds of complex shear wall members.

Ren et al. [26] from the Tsinghua University conducted a series of progressive collapse tests on beam-slab structure to consider the antiprogressive collapse performance of beam-slab structure after failure of frame columns. During the tests, they analyzed the failure mechanism and resistance mechanism of floor system in the collapsing process of columns and discussed the contribution of floor slabs to the progressive collapse resistance of frame structure. Progressive collapse tests are simulated using the elements and modeling method presented in this paper. The calculation results are in good agreement with the experimental results, which well predict the experimental curves in the beam mechanism stage and the transition stage between beam and catenary mechanisms. Figure 6 presents the reinforcement drawing in the tests. The calculation results and the contrast data are shown in Figure 7.

In order to study the differences of the full-size experiment and reduced scale experiment of frame-shear wall structure in earthquake disaster, Japan and the United States cooperated a series of structural dynamic time history experiments. The full-scale structure was tested at the Large-Scale Testing Facility at the Building Research Institute (BRI) in Tsukuba, Japan. Then, Wolfgram [27] conducted three groups of reduced scale experiments. In the paper, one frame-shear wall structure experiment was selected for simulation. The calculation results are consistent with the displacement time history curve of the structure experiment test and can satisfy the needs of the research (Figure 8).

4. Nonlinear Dynamic Analysis of Frame-Shear Wall Structure

4.1. Demolition of Bottom Corner Columns. Figure 9 shows the comparisons of vertical displacement time histories between nodes of structure stories after corner column failure. By comparing with the analysis results of various frame-shear structures in this paper, we find that all the three structures have not undergone collapse behavior after demolition of bottom short-side corner column. Besides, vertical displacements at the short-side frame beam are small, all of which reached the free vibration within 1 s into a steady state.

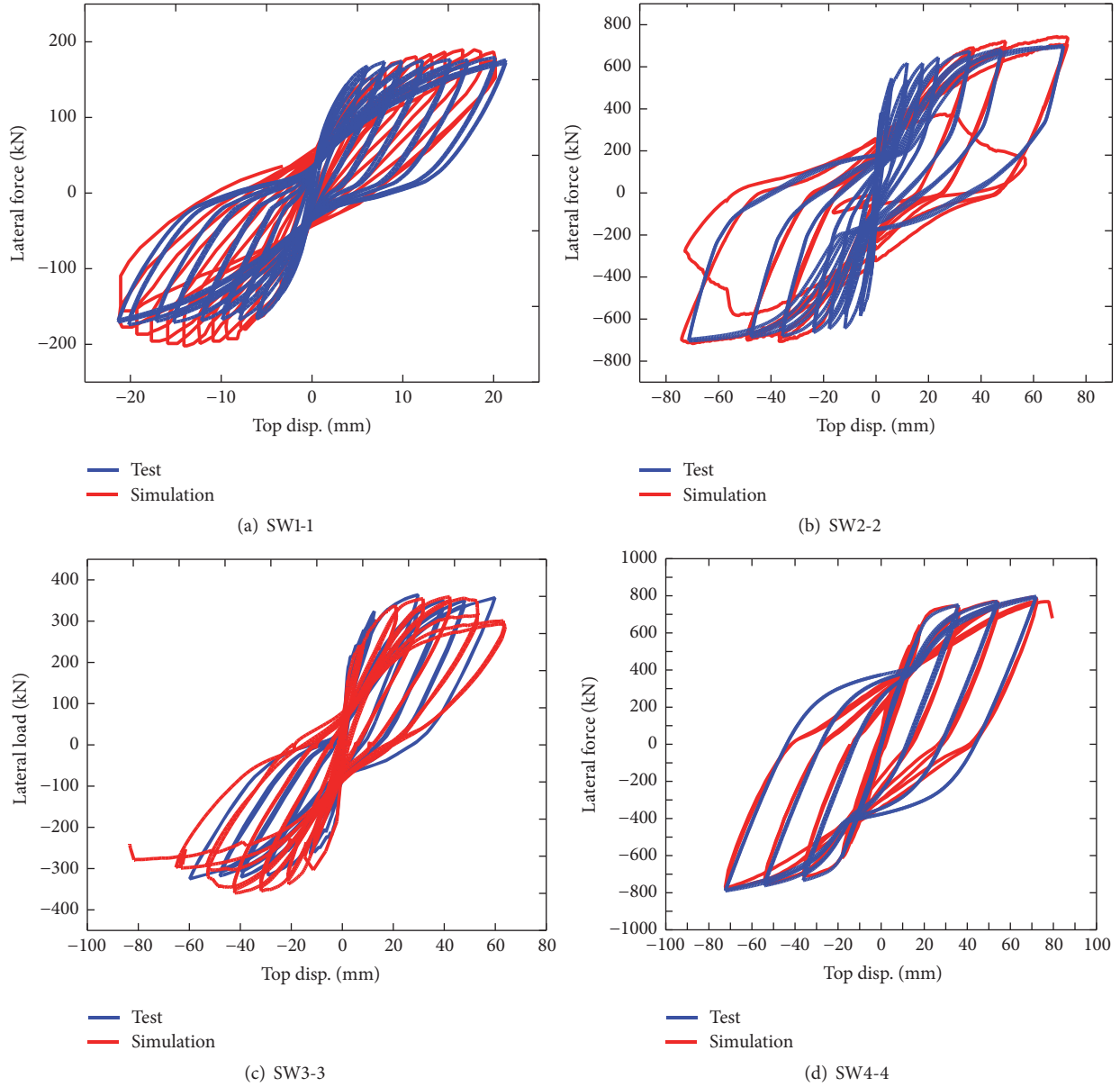(a) SW1-1

(b) SW2-2


(c) SW3-3

(d) SW4-4

FIGURE 5: Top force versus displacement hysteretic curve of specimens.

Comparison of the displacement time history curves between various structures reveals that after demolition of corner column the top displacement at demolition site of 10-story frame-shear structure is at the highest level, which is about 1/100 of the span of the long-side frame beam. The vertical displacement at the first story apex of 15-story structure is slightly smaller, which also does not satisfy the displacement judgment about structural progressive collapse. The 10-story frame-shear structure with seismic design exhibits the lowest displacement level. Its top displacement at demolition site is about 7.1 mm lower than the ordinary 10-story structure. This is because, for the case of demolition of short-side corner column, the side frame originally supported by corner column turns into a cantilever beam, and the upper loads of structure gather towards the failure corner region. By strengthening the

seismic design of structure, the seismic performance level is elevated compared to the ordinary structure. According to "strong column weak beam" design requirements in China, we can enhance the horizontal restraints at the structural beam ends and improve the stiffness and bearing capacity of nodes, while increasing the integrity of structure, thereby enhancing the ductility of high-level structure, so that the collapse resistance at the failure corner region maintains high level [28]. Thus, the vertical displacement at its failure apex is rather small. In addition, for the 15-story structure, the upper frame beam at the corner region creates a hollow rod effect after failure of bottom column, which generates new bending moment at beam ends in the form of gravity equiaxial pressure to dissipate the unbalanced work of superstructure. It can be seen by comparing the top displacement that the higher
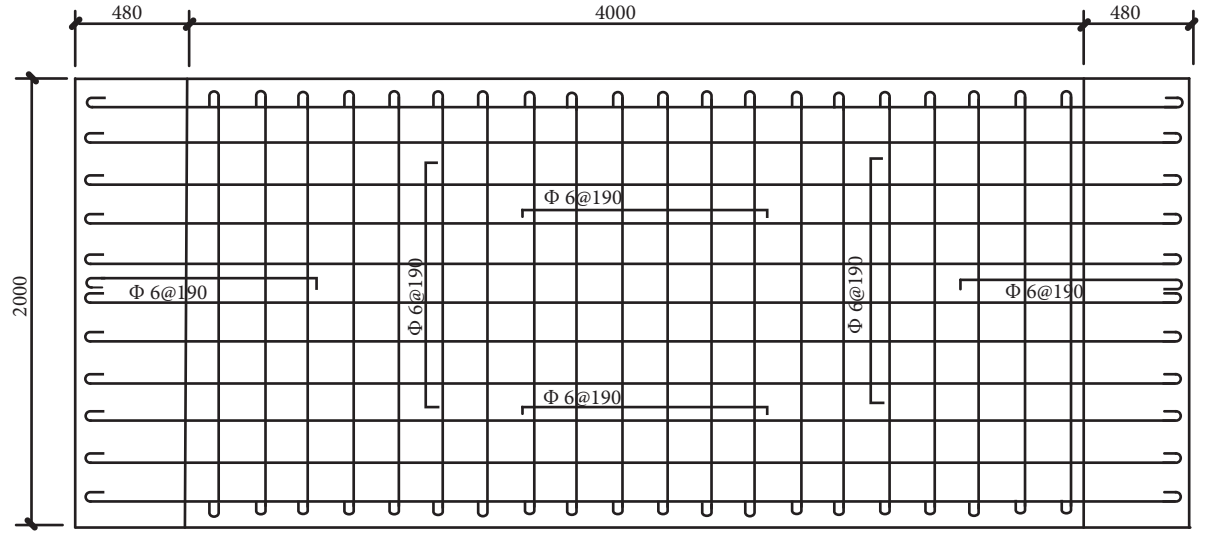
(a) Plate fitted with reinforcing bars
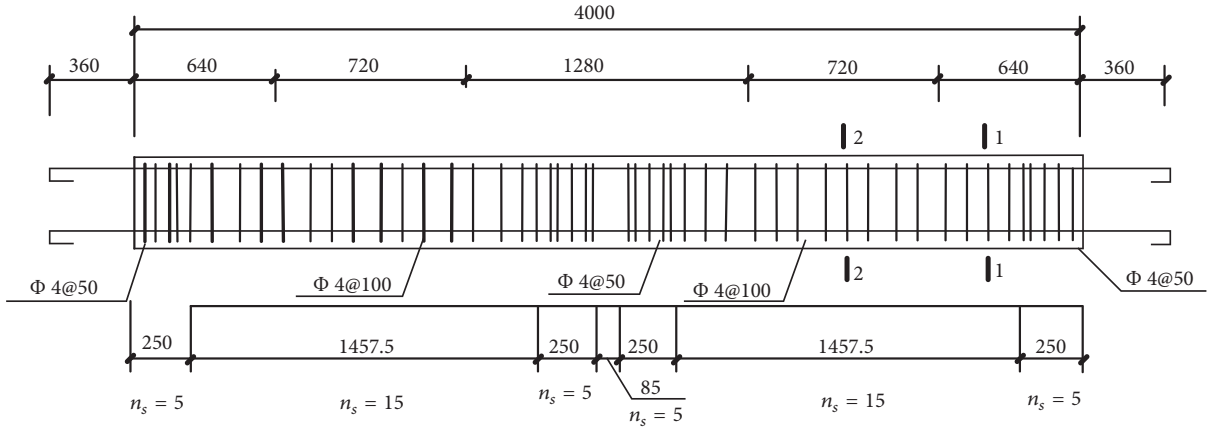
(b) X direction cross section
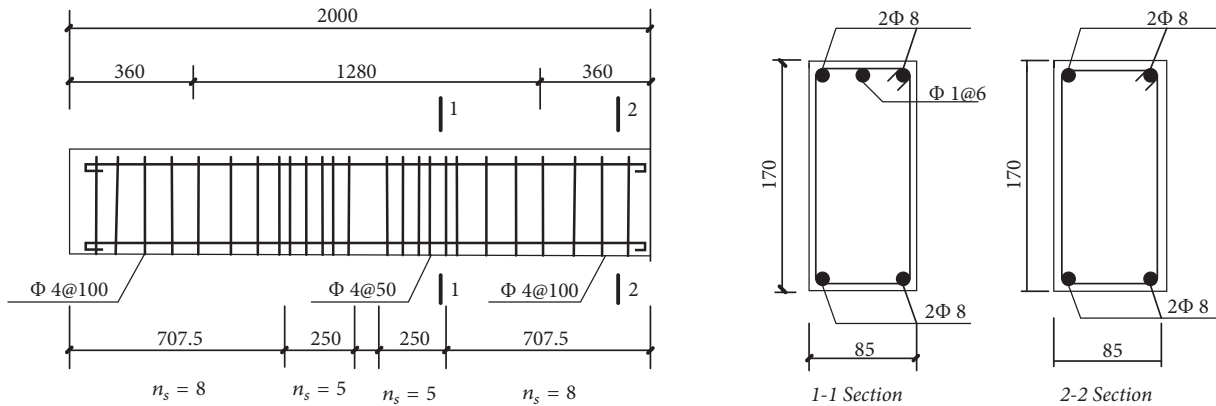
(c) Y direction cross section

FIGURE 6: Reinforce details of the RC frames.

the structure story, the better the hollow rod effect, but the smaller the contribution to collapse resistance. Meanwhile, in terms of top displacement, the time history curve of 15-story structure tends to flatten out and is less oscillatory.

4.2. Demolition of Central Shear Wall. Figure 10 presents the comparisons of time histories between nodes of structure stories after shear wall failure. After the failure of central shear wall, the C-shaped shear wall undergoes a slight deformation,
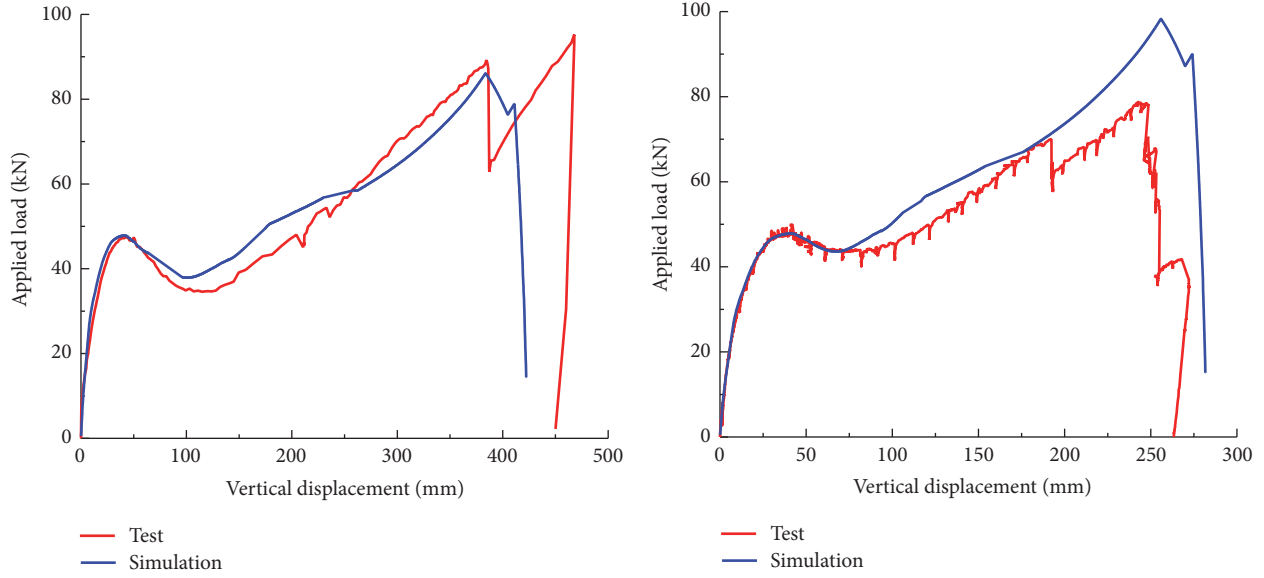
FIGURE 7: Comparisons between the numerical simulations and the test results.
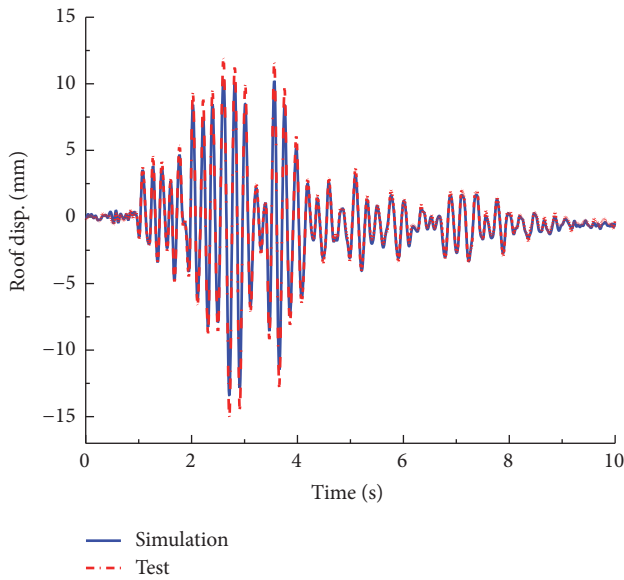

FIGURE 8: Comparisons between the numerical simulations and the test results.

and the structure basically has no risk of progressive collapse. By comparing the displacement time histories between various model nodes, we find that the first story node displacement of the 10-story frame-shear structure is at the highest level after failure of lateral shear wall. Its maximum vertical deformation is only 15.44 mm. Meanwhile, no significant difference is found in the vertical displacement of nodes at the first story failure site between three models. Although the self-weight and bearing capacity of shear wall elements are higher than the frame columns and beams, the three shear walls form a C-shaped tube structure in this paper. When the central shear wall fails, the lateral and side shear walls

can bear the unbalanced load of superstructure to become an effective alternative path. Meanwhile, the frame beam-column structure at the side of failed shear wall can provide the beam-end-beam mechanism collapse resistance contribution and the catenary mechanism anticollapse contribution of rebar tensile force within cross section to dissipate the unbalanced work within the structure, thereby improving the progressive collapse resistance [29, 30]. As for the top story nodes, the apex of 15-story structure enters into the free vibration stabilization period within 1.5 s. The vertical displacements of apexes are similar between the 10-story structures with or without seismic design. Finally, it can be seen that the structure of several floors (10, 15 layers) and structure seismic design of 8 degrees (6 degrees) had slight effect on center shear wall failure in three sets of computing models due to the center position of shear wall and mechanical properties.

4.3. Demolition of Short Edge Columns Near the Center. Figure 11 shows the time history comparisons between nodes of structure stories after failure of short-side middle column. In contrast to the demolition of corner column, the demolition of short-side middle column causes the frame beams on three sides of column ends to become cantilever beams. From the comparison of vertical displacement curves between two cases, it is clear that the vertical displacements of nodes for the case of demolition of middle column frame-shear wall structure are generally smaller than the demolition of corner column. Among them, the maximum bottom node displacement of 10-story structure is reduced by about 26%, while the maximum bottom displacement of 15-story structure is reduced by about 28%. This is caused by the lack of effective horizontal restraint protection for the frame beams at both vertical ends in the corner region after failure of corner support columns. The support column on the other side of frame beam can provide structural horizontal restraints, so
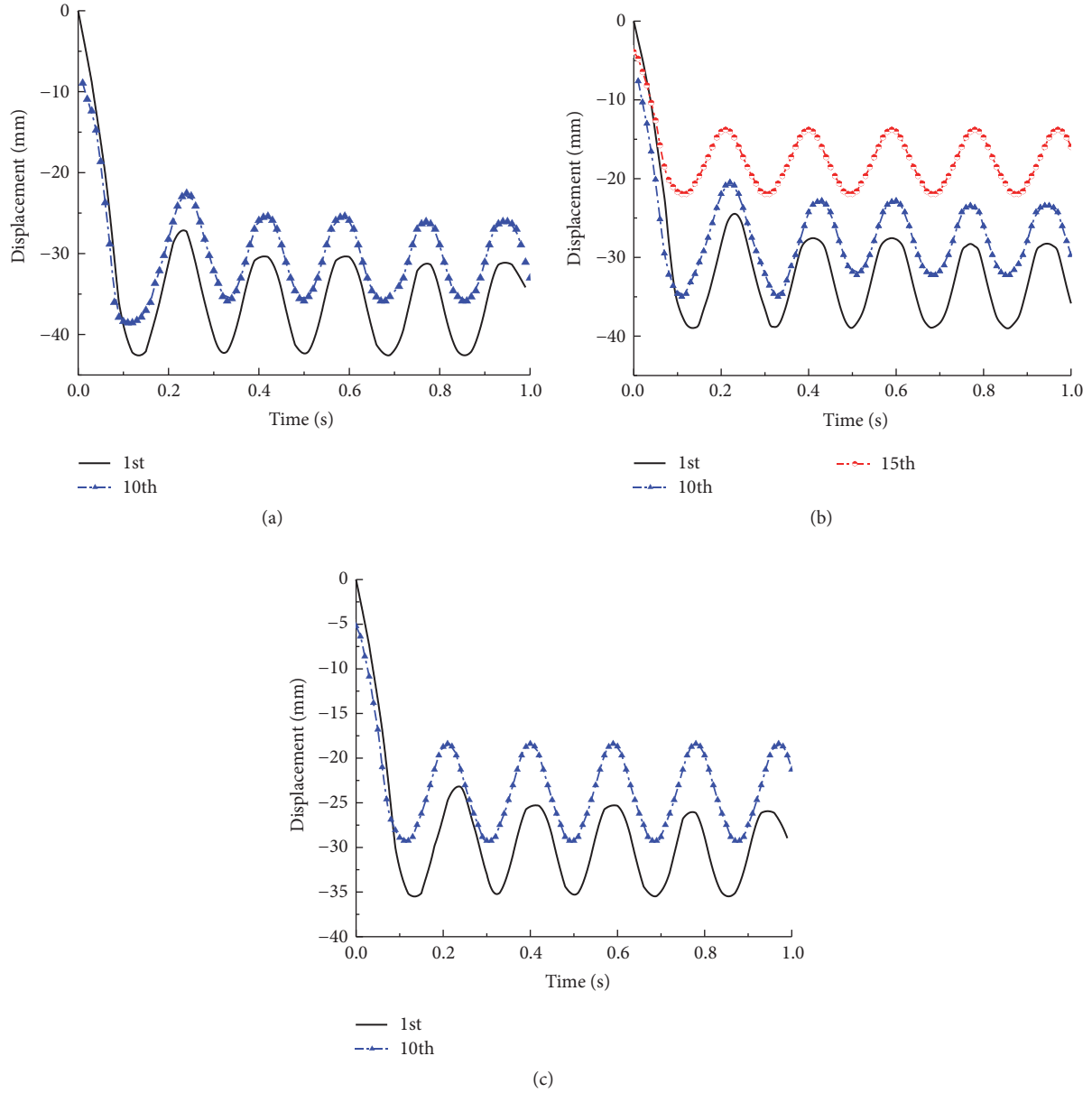
(a)

(b)

(c)

FIGURE 9: Removal of the corner columns in building: (a) 10-story model; (b) 15-story model; (c) 10-story model of the 8-degree seismic design; (a)–(c) vertical displacement of the joint at the top of the removed column on the xth-story.

that pressure arch effect emerges within the beam to form the beam mechanism, which provides progressive collapse resistance in a manner that the ends of vertical two-way frame beams are subjected to bending loads. In the case of demolition of short-side middle column, horizontal restraints are provided by the support columns at frame beam ends after failure of middle column. The ends of three side frame beams form a beam mechanism to resist the collapse force by the end bending moments. Meanwhile, the Y-direction through frame beam in the periphery of structure can provide effective horizontal constraints, so that the beam can play a role of intrabeam rebar tensile force under large deformation to form catenary effect and to provide progressive collapse resistance. Thus, node deformations are generally small after failure of middle column. In addition, in the case of short-side middle column failure, the vertical deformations of bottom nodes for the 10-story frame structure with 8-degree seismic design are small, whose maximum node displacement is reduced by 23% compared to the ordinary 10-story structure. This large vertical deformation is manifested basically the same as the case of corner column failure, indicating that the seismic design can effectively enhance the progressive collapse resistance of high-rise structures and improve the structural safety. Finally, it can be seen that in the case of short-side middle column failure, the structure with higher stories has little effect on the progressive collapse resistance under hollow rod effect.
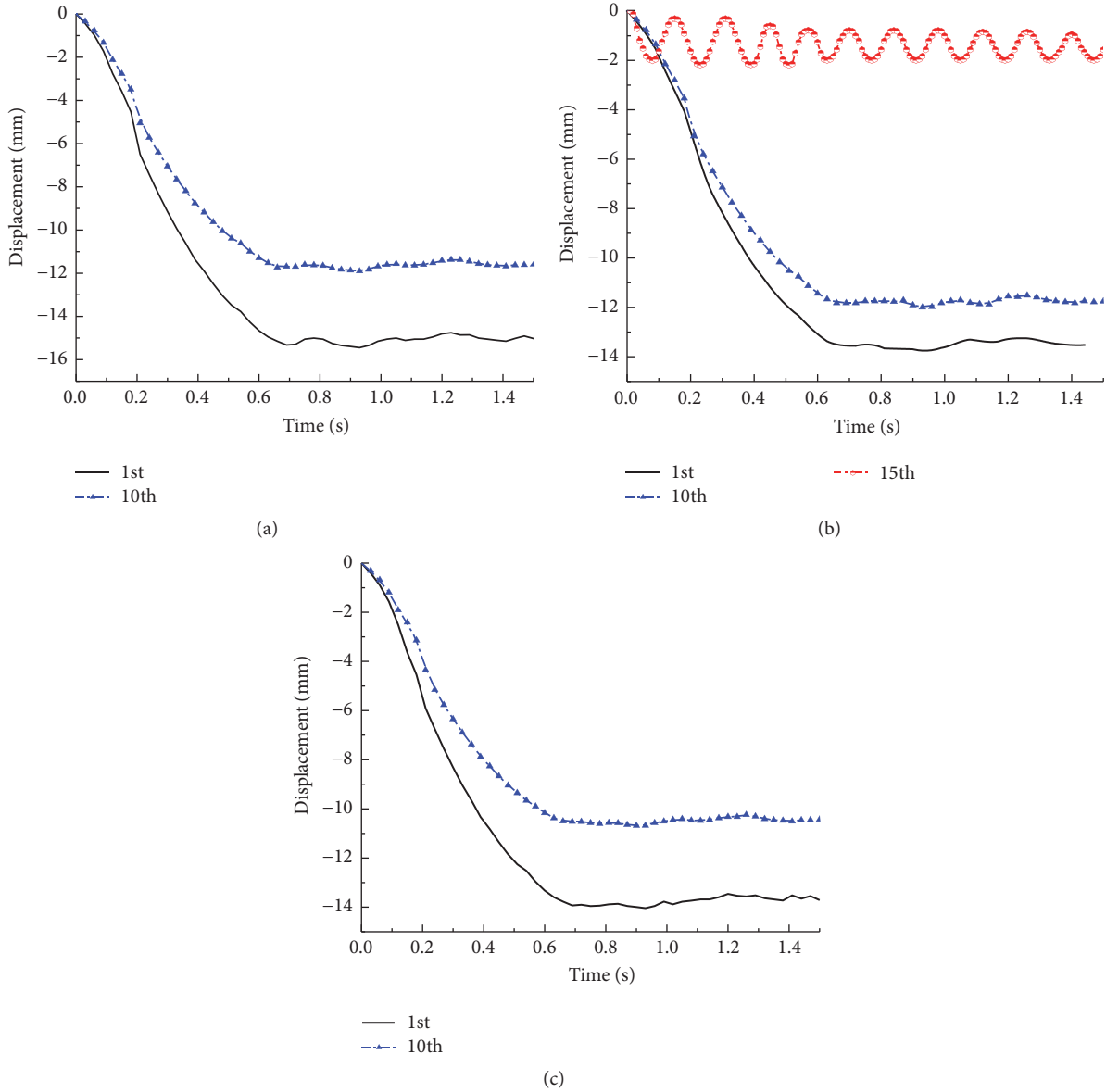
FIGURE 10: Removal of central shear wall in building: (a) 10-story model; (b) 15-story model; (c) 10-story model of the 8-degree seismic design; (a)–(c) vertical displacement of the joint at the top of the removed column on the xth-story.

5. Discussion on Anticollapse Design of Structures

With the development of economy, high-rise structures continue to spring up; progressive collapse resistance design of high-rise structures has been gaining increasing attention. Anticollapse designs are made abroad mainly in accordance with the US GSA2010 and DoD2010 design guidelines. In China, the primary references are the *Code for Design of Concrete Structures* and the *Technical Specification for Concrete Structures of High-Rise Buildings* before 2015. In 2015, the *Code for Anticollapse Design of Building Structures* is officially promulgated, which presents the member tying method, alternate path method, local reinforcement method, and relevant theoretical calculation methods. Moreover, methods of

calculating beam mechanism and rebar catenary mechanism are also supplemented based on the research findings in recent years. In view of the complexity of collapse, the existing specifications and design criteria have not formed a complete technical standard system yet. Further research is needed to perfect the theoretical calculation method, failure judging criteria, collapse judgment, and design parameters.

(1) In recent years, the engineering community's understanding of the design of structural antiprogressive collapse lies in the mere anticollapse design of important buildings in accordance with the codes, while ignoring the influences of anticollapse design on the earthquake, fire, and other disaster resistance of structures. This does not meet the requirements on the establishment of multihazard prevention system.
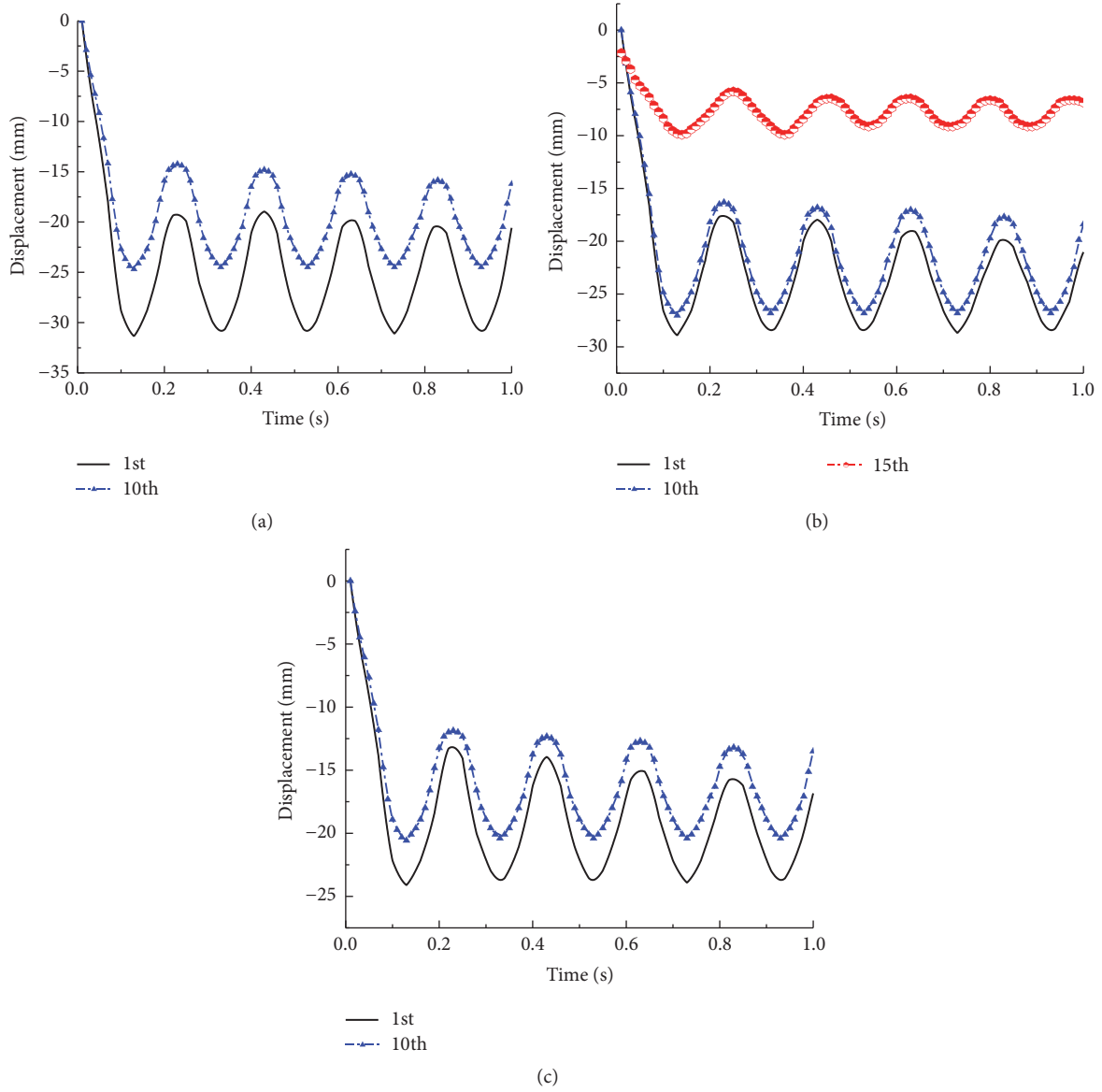
FIGURE 11: Removal of short-side middle column in building: (a) 10-story model; (b) 15-story model; (c) 10-story model of the 8-degree seismic design; (a)–(c) vertical displacement of the joint at the top of the removed column on the xth-story.

For example, addition of intrabeam longitudinal reinforcement layout after the anticollapse design may result in "strong beam weak column" damage of the structure during the earthquake. In addition, with the increase of structural rebar, the impact on rebar increases under fire scenario, which may pose threats to the stability of high-rise structures. Therefore, for safety consideration, a secondary seismic or fire-resistance design may be required after the anticollapse design. This means repeated design, which may result in increased material consumption and aggravated designer's responsibility. This paper attempts to discuss and analyze the structural progressive collapse using influencing factors such as seismic design and story number. We find that the direct seismic design

of structure without collapse design can effectively improve its progressive collapse resistance. However, further in-depth study is needed, and design method suitable for seismic, fire, and progressive collapse resistance of high-rise structures needs to be put forward.

(2) Existing methods for anticollapse analysis of building structures mainly include the linear static alternate path method, nonlinear static alternate path method, linear dynamic alternate path method, and nonlinear dynamic alternate path method, of which the nonlinear dynamic alternate path method is the most accurate method for antiprogressive collapse analysis. Its analytical procedure is as follows: firstly, nonlinear numerical model of structure is constructed; key

members are removed from top to bottom story-by-story, and nonlinear dynamic analysis is performed; if the structure undergoes progressive collapse and rebar in the collapse subarea is increased, then the demolition analysis cycle is continued until the structure no longer collapses. The method is computationally difficult to be widely used. Lu et al. [30, 31] modified the method by using a dynamic amplification factor (DAF) to correct the linear static resistance demand to approximate the true nonlinear dynamic resistance demand. They introduced dynamic method coefficient for considering dynamic response to calculate the dynamic internal force and to determine the design value of load effect and the nonlinear dynamic resistance requirements, so that the designers can choose within this range. Its significance is that it simplifies the cyclic procedure and calculation difficulty of the nonlinear dynamic analysis. Although the analytical results are not as accurate as the nonlinear dynamic method, it still meets the actual needs, so that ordinary designers can also perform the nonlinear design of anticontinuous structural collapse. More simplification attempts and innovative approaches are needed regarding the antiprogressive collapse analysis methods for building structures.

(3) Linear static alternate path method in GSA2010 mostly uses the internal force reduction coefficient and dynamic magnification factor to consider the dynamic response problem of structures. However, in practical engineering, nonlinear and dynamic factors will simultaneously produce effects on structure, which may lead to large computational error. Thus, progressive collapse specifications need to be further perfected and supplemented [32, 33].

(4) Parameter settings in the codes for progressive collapse resistance design are mostly based on the previous collapse disaster data, which are highly occasional. Besides, testing of large-scale structures is costly, demanding in terms of test platform, data collection, and testing personnel, and makes verification of design parameters difficult. In additions, the current structural theory and building material performance are all significantly better than the past, which will thus lead to certain errors in the calculation of parameters.

6. Conclusion

Through the above nonlinear progressive collapse analysis of high-rise frame-shear structures, we can draw the following conclusions:

(1) Nonlinear finite element model of high-rise frame-shear structure is built by using the novel shear wall element SFI-MVLEM and the flexible line fiber element. The feasibility of simulating progressive structural collapse with SFI-MVLEM and line flexibility

elements is verified via collapse tests on substructures comprising four shear wall members and two frame sets as an example. Meanwhile, the use of progressive collapse analysis method and the integral iteration and solution methods proposed in this paper can well obtain the progressive collapse analysis data of structures. This indicates that the finite element program OpenSees can be applied to the seismic and progressive collapse analyses of large-scale high-rise structures.

(2) Considering the effects of story number and seismic design on the structural progressive collapse resistance in the high-rise frame-shear structures, three typical cases are designed for the nonlinear collapse analysis of high-rise structures. The results show that the frame-shear structure has a fairly complete transmission path upon initial failure of the corner column to prevent collapse behavior. When the shear wall produced initial damage, shear wall edge frame beams formed anticollapse strength at end bending moment; the reinforcing steel bar in the beam provided catenary mechanism in the form of tension, formed anticollapse strength and connected with the wall around the ones where shear failed, and could effectively alter force transferring path, so it could effectively resist continuity of collapse, and frame-shear wall structure had small deformation. In the case of short-side middle column failure, the structural vertical deformation is smaller than the corner column failure. Finally, anticollapse performance of high-rise structures is well improved after 8-degree seismic design.

Conflicts of Interest

The authors declare that they have no conflicts of interest.

References

[1] X. Z. Lu, Y. Li, and L. P. Ye, *Theory and Design Method for Progressive Collapse Prevention of Concrete Structures*, China Architecture & Building Press, Beijing, China, 2011.

[2] M. Sasani, M. Bazan, and S. Sagiroglu, "Experimental and analytical progressive collapse evaluation of actual reinforced concrete structure," *ACI Structural Journal*, vol. 104, no. 6, pp. 731–739, 2007.

[3] L. Kwasniewski, "Nonlinear dynamic simulations of progressive collapse for a multistory building," *Engineering Structures*, vol. 32, no. 5, pp. 1223–1235, 2010.

[4] P. X. Dat and T. K. Hai, "Membrane actions of RC slabs in mitigating progressive collapse of building structures," *Engineering Structures*, vol. 55, pp. 107–115, 2013.

[5] United States General Services Administration (GSA), *Progressive Collapse Analysis and Design Guidelines for New Federal Office Buildings and Major Modernization Projects*, United States General Services Administration (GSA), Washington, DC, USA, 2010.

[6] Department of Defense (DoD), *Unified Facilities Criteria (UFC): Design of Structures to Resist Progressive Collapse*, Department of Defense, Washington, DC, USA, 2010.

[7] China Engineering Construction Standardization Association (CECS), "Code for anti-collapse design of building structures," CECS 392:2014, China Engineering Construction Standardization Association (CECS), Beijing, China, 2014.

[8] W.-J. Yi, Q.-F. He, Y. Xiao, and S. K. Kunnath, "Experimental study on progressive collapse-resistant behavior of reinforced concrete frame structures," *ACI Structural Journal*, vol. 105, no. 4, pp. 433–439, 2008.

[9] S. Li, S. Shan, C. Zhai, and L. Xie, "Experimental and numerical study on progressive collapse process of RC frames with full-height infill walls," *Engineering Failure Analysis*, vol. 59, pp. 57–68, 2016.

[10] S.-J. Wang, F.-S. Liu, and Z.-D. Xu, "Experimental and theoretical analyses on entire course of vertical progressive collapse of spatial RC frame structures," *Engineering Mechanics*, vol. 32, no. 5, pp. 162–177, 2015.

[11] L. M. Zhang and X. L. Liu, "Some issues in the collapse analysis of frame structures," *Journal of Shang Hai Jiao Tong University*, vol. 35, no. 10, pp. 1578–1582, 2003.

[12] A. G. Vlassis, B. A. Izzuddin, A. Y. Elghazouli, and D. A. Nethercot, "Progressive collapse of multi-storey buildings due to failed floor impact," *Engineering Structures*, vol. 31, no. 7, pp. 1522–1534, 2009.

[13] Y. Li, X. Lu, H. Guan, and P. Ren, "Numerical investigation of progressive collapse resistance of reinforced concrete frames subject to column removals from different stories," *Advances in Structural Engineering*, vol. 19, no. 2, pp. 314–326, 2016.

[14] W.-D. Wang, J.-X. Wang, and X.-Y. Zhou, "Nonlinear dynamic progressive collapse analysis of composite frames with concrete-filled steel tubular columns based on fiber model," *Engineering Mechanics*, vol. 31, no. 9, pp. 142–151, 2014.

[15] Ministry of Housing and Urban-Rural Development of the People's Republic of China (MOHURD), "Code for design of concrete structures," GB 50010-2010, Ministry of Housing and Urban-Rural Development of the People's Republic of China (MOHURD), Beijing, China, 2010.

[16] Ministry of Housing and Urban-Rural Development of the People's Republic of China (MOHURD), "Code for seismic design of buildings," GB 50011-2010, Ministry of Housing and Urban-Rural Development of the People's Republic of China (MOHURD), Beijing, China, 2010.

[17] T. Kabeyasawa, H. Shiohara, S. Otani et al., "Analysis of the full-scale seven-story reinforced concrete test structure," *Journal of the Faculty of Engineering, University of Tokyo*, vol. 84, pp. 203–239, 1982.

[18] K. Kolozvari and J. W. Wallace, "Practical nonlinear modeling of reinforced concrete structural walls," *ASCE Journal of Structural Engineering*, vol. 142, no. 12, 2016.

[19] F. C. Filippou and A. Issa, "Nonlinear analysis of reinforced concrete frames under cyclic load reversals," EERC Report 88/12, Earthquake Engineering Research Center, Berkeley, Calif, USA, 1988.

[20] M. Talaat and K. M. Mosalam, "Modeling progressive collapse in reinforced concrete buildings using direct element removal," *Earthquake Engineering and Structural Dynamics*, vol. 38, no. 5, pp. 609–634, 2009.

[21] M. H. Scott and G. L. Fenves, "Krylov subspace accelerated newton algorithm: application to dynamic progressive collapse simulation of frames," *Journal of Structural Engineering*, vol. 136, no. 5, pp. 473–480, 2010.

[22] H. M. Zhang, *Study on the Performance-Based Seismic Design Method for Shear Wall Structures*, Tongji University, Shanghai, China, 2007.

[23] T. A. Tran and J. W. Wallace, "Cyclic testing of moderate-aspect-ratio reinforced concrete structural walls," *ACI Structural Journal*, vol. 112, no. 6, pp. 653–665, 2015.

[24] A. Dazio, K. Beyer, and H. Bachmann, "Quasi-static cyclic tests and plastic hinge analysis of RC structural walls," *Engineering Structures*, vol. 31, no. 7, pp. 1556–1571, 2009.

[25] R. Burgueño, X. Liu, and E. M. Hines, "Web crushing capacity of high-strength concrete structural walls: experimental study," *ACI Structural Journal*, vol. 111, no. 2, pp. 235–246, 2014.

[26] P. Ren, Y. Li, X. Lu, H. Guan, and Y. Zhou, "Experimental investigation of progressive collapse resistance of one-way reinforced concrete beam-slab substructures under a middle-column-removal scenario," *Engineering Structures*, vol. 118, pp. 28–40, 2016.

[27] G. E. Wolfgram, *Experimental modelling and analysis of three one-tenth-scale reinforced concrete frame-wall structures [Ph.D. thesis]*, University of Illinois at Urbana-Champaign, Champaign, Ill, USA, 1984.

[28] Y. Bao and S. K. Kunnath, "Simplified progressive collapse simulation of RC frame-wall structures," *Engineering Structures*, vol. 32, no. 10, pp. 3153–3162, 2010.

[29] P. Ren, Y. Li, H. Guan et al., "Progressive collapse resistance of two typical high-rise RC frame shear wall structures," *Journal of Performance of Constructed Facilities*, vol. 29, no. 3, Article ID 04014087, pp. 1–9, 2015.

[30] Y. Li, X. Lu, H. Guan, and L. Ye, "An improved tie force method for progressive collapse resistance design of reinforced concrete frame structures," *Engineering Structures*, vol. 33, no. 10, pp. 2931–2942, 2011.

[31] X. Lu, L. Xie, H. Guan, Y. Huang, and X. Lu, "A shear wall element for nonlinear seismic analysis of super-tall buildings using OpenSees," *Finite Elements in Analysis and Design*, vol. 98, pp. 14–25, 2015.

[32] S. Gerasimidis and J. Sideri, "A new partial-distributed damage method for progressive collapse analysis of steel frames," *Journal of Constructional Steel Research*, vol. 119, pp. 233–245, 2016.

[33] S. Gerasimidis, G. Deodatis, T. Kontoroupi, and M. Ettouney, "Loss-of-stability induced progressive collapse modes in 3D steel moment frames," *Structure and Infrastructure Engineering*, vol. 11, no. 3, pp. 334–344, 2015.

Research Article

Integration of Geometrical and Material Nonlinear Energy Sink with Piezoelectric Material Energy Harvester

Ye-Wei Zhang,[1,2] Chuang Wang,[1] Bin Yuan,[1] and Bo Fang[1]

[1]*Faculty of Aerospace Engineering, Shenyang Aerospace University, Shenyang 110136, China*
[2]*State Key Laboratory of Structural Analysis for Industrial Equipment, Dalian University of Technology, Dalian 116024, China*

Correspondence should be addressed to Ye-Wei Zhang; zhangyewei1218@126.com

This paper presents a novel design by integrating geometrical and material nonlinear energy sink (NES) with a piezoelectric-based vibration energy harvester under shock excitation, which can realize vibration control and energy harvesting. The nonlinear spring and hysteresis behavior of the NES could reflect geometrical and material nonlinearity, respectively. Two configurations of the piezoelectric device, including the piezoelectric element embedded between the NES mass and the single-degree-of-freedom system or ground, are utilised to examine the energy dissipated by damper and hysteresis behavior of NES and the energy harvested by the piezoelectric element. Similar numerical research methods of Runge-Kutta algorithm are used to investigate the two configurations. The energy transaction measure (ETM) is adopted to examine the instantaneous energy transaction between the primary and the NES-piezoelectricity system. And it demonstrates that the dissipated and harvested energy transaction is transferred from the primary system to the NES-piezoelectricity system and the instantaneous transaction of mechanical energy occupies a major part of the energy of transaction. Both figurations could realize vibration control efficiently.

1. Introduction

A nonlinear energy sink (NES) is a simple single or multi-degrees of freedom (MDOF) system, and it can dissipate primary system energy and realize vibration control through the use of a damper and a nonlinear stiffness spring. Extensive studies have investigated some methods to reveal the capability of NES and passively control the system [1–4]. Zhang et al. analysed the effectiveness of NES connected to an axially moving string and proved that NES can effectively suppress the vibration of the axially moving string with transverse wind loadings [5]. Starosvetsky and Gendelman studied a two-DOF system with NES in the resonance and proved that simultaneous targeted energy transfer from linear oscillator to a NES is feasible [6]. Yang et al. conducted a numerical study on a pipe-NES system and found that the system can efficiently transfer and dissipate the vibration energy generated by fluid movement in the pipe [7]. Luongo and Zulli considered a general, nonlinear, multi-DOF structure attached to a nonlinear oscillator with small

mass and damping, and a mixed multiple scale/harmonic balance method was proposed to obtain differential equations describing the slow- and fast-flow dynamics of the entire structure [8]. Zhang et al. analysed the influence of flexible solar arrays on the passive multistrut vibration isolation platform of control moment gyroscopes for a satellite and discussed the reasonable parameters of flexible solar arrays [9]. Fang et al. presented an approach by integrating NES with giant magnetostrictive material (GMM) to realize vibration mitigation and energy harvesting. Parametric optimization was made to check how the values of NES mass, stiffness, and damper affect the performance of the integration of a NES and a GMM harvester [10]. Ebrahimzade et al. studied the performance of linear passive vibration absorbers and non-linear passive vibration absorbers or nonlinear energy sink (NES) on the stability properties and nonlinear behaviors of an aeroelastic model [11].

The energy of vibration dissipated by a NES damper could be very large in several cases that make energy harvesting economically efficient. Given that a piezoelectric material can

convert mechanical vibration into electrical energy with a simple structure, piezoelectric energy harvesting is considered as a self-power source in wireless sensor network systems [12]. Jacquelin et al. designed a piezoelectric harvester to harvest impact energy and discovered the influence of several mechanical parameters on harvesting output energy in order to optimize its performance [13]. Renno et al. presented a study of the effects of damping and electromechanical coupling on the power optimality of vibration energy harvesting. It is shown that mechanical dampers have an effect on optimal frequency ratios and optimal harvested power [14]. NES can absorb and dissipate energy through targeted energy transfers (TET) so that NES coupled with piezoelectric element could realize vibration control and energy harvesting. Ahmadabadi and Khadem utilised two configurations composed of NES and a piezoelectric element for vibration mitigation of a free-free beam subjected to shock excitation [15], and the NES they mentioned did not possess material nonlinearity which could realize vibration mitigation. Zhang et al. presented a piezoelectric energy harvesting device based on NES to achieve simultaneous broadband energy harvesting. The study shows that the apparatus has similar characteristics as NES as follows: 1:1 resonance, targeted energy transfer, and so forth [16].

In most cases, the actual behaviors of structures are not linear; these structures can present nonlinear behaviors in general and nonsmooth or hysteresis ones in particular (e.g., hysteresis behavior of magnetorheological fluid dampers and shape-memory alloys) [17]. The nonlinear and hysteresis behaviors of structures need to be studied to thoroughly understand the real responses of structures under external excitations. The Bouc-Wen model was proposed to describe the complex nonlinear characteristics of hysteretic systems [18, 19]. Ikhouane et al. performed an analytical study on how the parameters of the Bouc-Wen model influence the shape of the hysteresis loop, and some specific features of the hysteresis loop are defined formally [20]. Charalampakis comprehensively examined the response and dissipated energy of the Bouc-Wen model. New analytical and numerical solutions were derived through a generic model formulation without any parameter constraints [21]. Lamarque and Savadkoohi investigated time multiscale energy exchange between a main system which is of Bouc-Wen family models of hysteresis and a cubic NES, and application of the coupled NES in passive control of a main system with hysteresis behavior was demonstrated [22]. Savadkoohi et al. presented a general methodology to deal with time evolutionary energy exchanges between two oscillators with dual nonlinearities: a NES with smooth nonlinear geometrical (cubic) and nonsmooth hysteresis (Bouc-Wen) behaviors [23]. Based on the geometrical NES with material nonlinearity and the configurations composed of NES and a piezoelectric element [15], the research is made as follows.

The present study investigates a system comprised of geometrical NES with hysteresis behavior reflecting material nonlinearity and a piezoelectricity-based vibration energy harvester, which is attached to the single-degree-of-freedom primary system under shock excitation. Two configurations of the piezoelectric device, including the piezoelectric
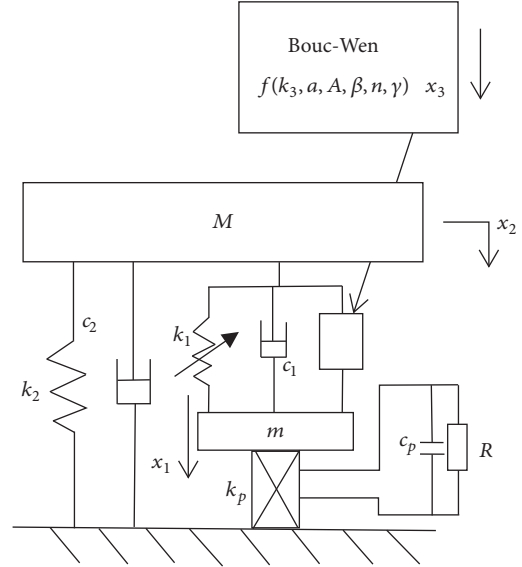

Figure 1: The single-degree-of-freedom system with the NES-piezoelectricity system: configuration 1.
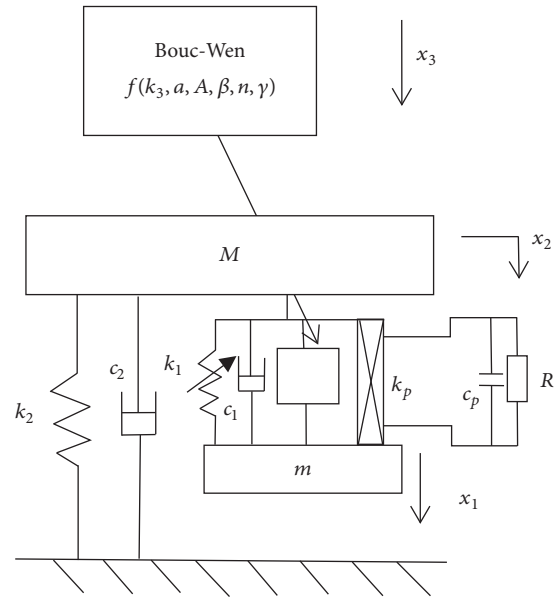

Figure 2: The single-degree-of-freedom system with NES-piezoelectricity system: configuration 2.

element embedded between the NES mass and the structure or ground, are studied through similar methods. The energy transaction measure (ETM) is adopted to study the instantaneous energy transaction between the primary and the NES-piezoelectricity system.

2. Configuration Models

Figures 1 and 2 show the primary hysteresis system containing NES and a piezoelectric element. Figure 1 shows that the piezoelectric element is in the inset between the NES mass

and ground. Figure 2 shows that the piezoelectric element is embedded between the NES mass and the primary system.

Mass M is subjected to an external shock load, $F(t)$ [15], which can be expressed in the following form:

$$F(t) = A_1 \cdot H\left(\frac{T}{8} - t\right) \cdot \sin\left(\frac{2\pi t}{T}\right), \tag{1}$$

where $A_1 = 8 \times 10^3$, H means Heaviside function, $T = 0.5/\pi$. The dynamic equations of motion of the two configurations are given in the following forms.

Configuration 1

$$m\ddot{x}_1 + c_1(\dot{x}_1 - \dot{x}_2) + k_1(x_1 - x_2)^3 + ak_3(x_1 - x_2)$$
$$+ (1-a)k_3(x_3 - x_2) + k_p x_1 + \theta V = 0,$$

$$M\ddot{x}_2 + c_1(\dot{x}_2 - \dot{x}_1) + k_1(x_2 - x_1)^3 + c_2\dot{x}_2$$
$$+ ak_3(x_2 - x_1) + (1-a)k_3(x_2 - x_3) \tag{2}$$
$$+ k_2 x_2 = F(t),$$

$$\dot{x}_3 - A\dot{x}_1 + \beta|\dot{x}_1||x_3|^{n-1}x_3 + \gamma\dot{x}_1|x_3|^n = 0,$$

$$c_p\dot{V} + \frac{V}{R} - \theta\dot{x}_1 = 0.$$

Configuration 2

$$m\ddot{x}_1 + c_1(\dot{x}_1 - \dot{x}_2) + k_1(x_1 - x_2)^3 + ak_3(x_1 - x_2)$$
$$+ (1-a)k_3(x_3 - x_2) + k_p(x_1 - x_2) + \theta V = 0,$$

$$M\ddot{x}_2 + c_1(\dot{x}_2 - \dot{x}_1) + k_1(x_2 - x_1)^3 + c_2\dot{x}_2$$
$$+ ak_3(x_2 - x_1) + (1-a)k_3(x_2 - x_3) + k_2 x_2 \tag{3}$$
$$+ k_p(x_2 - x_1) - \theta V = F(t),$$

$$\dot{x}_3 - A\dot{x}_1 + \beta|\dot{x}_1||x_3|^{n-1}x_3 + \gamma\dot{x}_1|x_3|^n = 0,$$

$$c_p\dot{V} + \frac{V}{R} - \theta(\dot{x}_1 - \dot{x}_2) = 0,$$

where M and m are the rigid mass and NES mass, respectively; x_1, x_2, and x_3 are the displacements of the NES mass, the rigid mass, and the internal variable of the hysteresis model, respectively, which are all relative to the ground; c_1 and c_2 are the linear damping coefficients; k_2 is the linear spring stiffness; k_1 is the cubic nonlinear spring stiffness; k_p and c_p are the linear equivalent stiffness and clamped capacitance of the piezoelectric element, respectively; R is the external resistance; V is the voltage across the electrodes of the piezoelectric element; and θ is the electromechanical coupling coefficient. The hysteresis behavior is assumed to be of Bouc-Wen type, $f(a, k_3, A, \beta, n, \gamma)$, with the following characteristics: x_3 is the internal variable of the hysteresis model, k_2 is the initial linear stiffness, the postyield stiffness is K_p, $a = K_p/k_2$ is the ratio of the postyield stiffness (K_p) to

the initial stiffness, $A, \beta > 0$, and γ and n are dimensionless Bouc-Wen parameters controlling the model behavior.

The parameters of the system are $m = 7\,\text{kg}$, $M = 60\,\text{kg}$, $k_2 = 2.1346 * 10^6\,\text{N/m}$, and $c_2 = 10\,\text{Ns/m}$ [10]. The parameters of the piezoelectric device are as follows: $k_p = 10^3\,\text{N/m}$, $R = 8.2 * 10^5\,\Omega$, $c_p = 10^{(-8)}\,\text{F}$, and $\theta = 0.002\,\text{C/m}^2$ [24]. The parameters of the hysteresis model are as follows: $k_3 = 5000\,\text{N/m}$, $A = 1$, $a = 0.5$, $\beta = 0.3\,\text{m}^{-2}$, $\gamma = 0.7\,\text{m}^{-2}$, and $n = 1$ [25]. In the following numerical simulations, the initial values are given for a better energy harvesting performance: x_1, x_2, x_3, and the time derivative of x_2 and x_3 are zero, while the time derivative of x_1 equals 0.4 m/s.

3. Methodologies and Simulations

Runge-Kutta algorithm (ode45 function of Matlab) [26, 27] is used to investigate the nonlinear energy dissipated by the NES damper and hysteresis behavior and harvested by the piezoelectric device. The final calculation results must satisfy the relation provided in (2) and (3) to ensure that the calculation of the model is sufficiently accurate.

$$E_{\text{out}}(t) = \left[\frac{1}{2}m\dot{x}_1^2 + \frac{1}{2}M\dot{x}_2^2\right] + \left[\frac{1}{4}k_1(x_1 - x_2)^4\right.$$
$$+ \frac{1}{2}k_2 x_2^2 + \frac{1}{2}k_p w^2 + \frac{1}{2}c_p V^2 + \frac{1}{2}ak_3(x_1 - x_2)^2\right]$$
$$+ \left[\int_0^t c_1(\dot{x}_1 - \dot{x}_2)^2 dt + \int_0^t c_2\dot{x}_2^2 dt \right. \tag{4}$$
$$\left. + E_{\text{dissipation,hysteretic}}(t)\right] + E_{\text{harvest}}(t),$$

$$E_{\text{in}}(t) = \int_0^t F(\tau)\dot{x}_2(\tau)d\tau, \tag{5}$$

$$E_{\text{harvest}}(t) = \int_0^t \frac{V^2}{R}dt. \tag{6}$$

Equation (7) derives from (5) and (6) as follows:

$$\eta_{\text{harvest,piezo}}(t) = \frac{E_{\text{harvest}}(t)}{E_{\text{in}}(t)} \times 100, \tag{7}$$

where $E_{\text{in}}(t)$ and $E_{\text{out}}(t)$ are the input and output energy up to time t, $E_{\text{harvest}}(t)$ is the harvested energy by the piezoelectric device, $\eta_{\text{harvest,piezo}}(t)$ is percentage of the transient excitation energy dissipated by the piezoelectric device, and w is the piezoelectric element displacement and defined by

$$w = x_1 \quad \text{for configuration 1,}$$
$$w = x_1 - x_2 \quad \text{for configuration 2.} \tag{8}$$

The influence of spring stiffness and damper of NES on the percentage of harvested energy by the piezoelectric device is described by Figure 3.

In Figure 3, different values of the spring stiffness and the damper of NES are considered for both configurations, namely, $k_1 \in [10, 10^9]$ and $c_1 \in [10, 170]$. In the region of $k_1 \in$
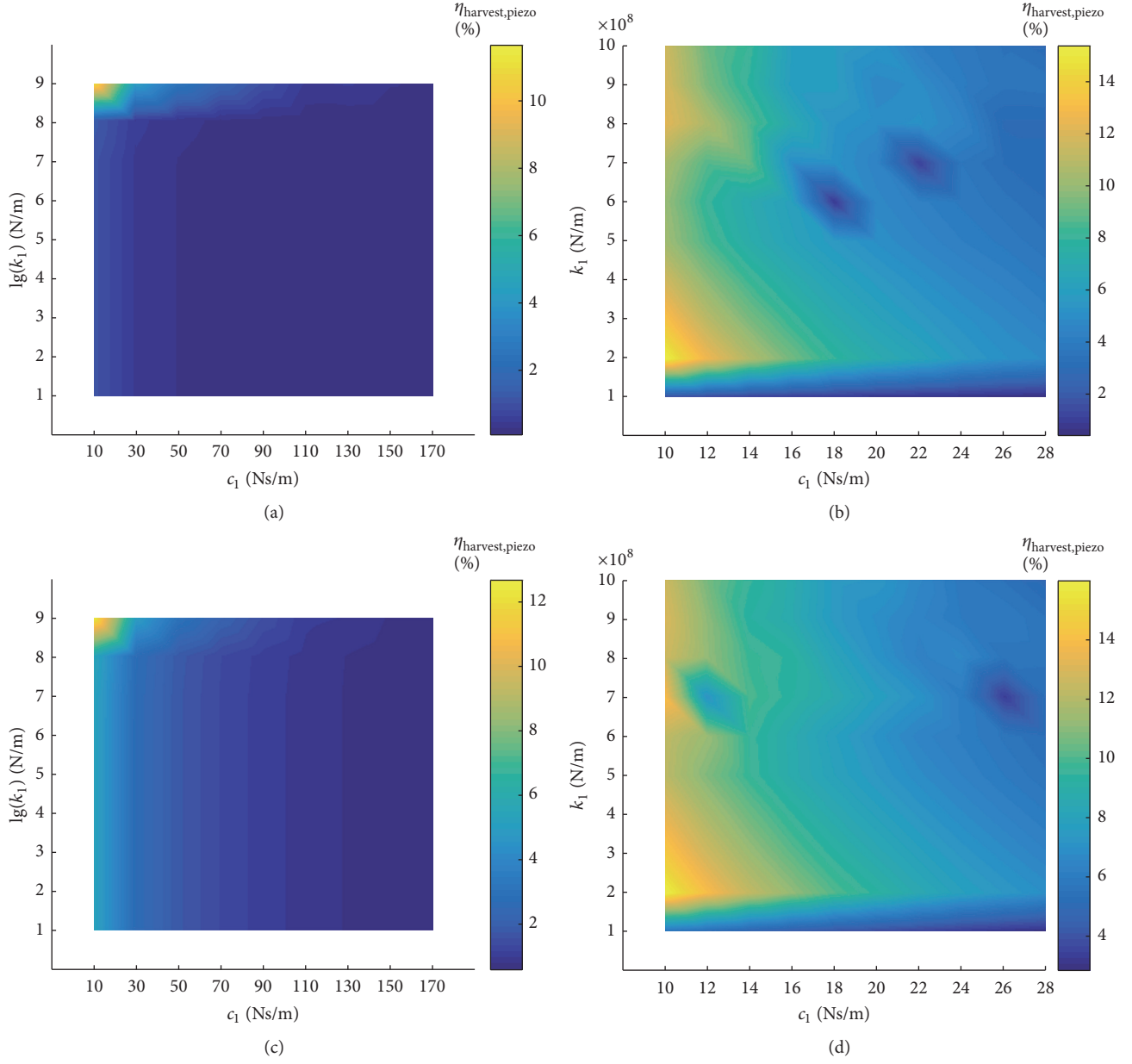
(a)

(b)

(c)

(d)

FIGURE 3: (a) The percentage of energy harvested by the piezoelectric device and (b) its enlargement of configuration 1. (c) The percentage of energy harvested by the piezoelectric device and (d) its enlargement of configuration 2.

$[10^8, 10^9]$ and $c_1 \in [10, 20]$, $\eta_{\text{harvest,piezo}}$ is obviously higher than others. The spring stiffness k_1 has no effect on $\eta_{\text{harvest,piezo}}$ except for the distinct boundary when k_1 is about 10^8 N/m, while the damper c_1 is positively correlated with $\eta_{\text{harvest,piezo}}$ in both configurations.

Input energy is dissipated by the NES damper and the hysteresis behavior of the Bouc-Wen model and harvested by the piezoelectric device. The percentage of the transient excitation energy dissipated by the NES damper ($\eta_{\text{damp,NES}}$) and hysteresis behavior ($\eta_{\text{dissipation,hysteretic}}$) and harvested by the piezoelectric device ($\eta_{\text{harvest,piezo}}$) is expressed in (9), (11), and (7), respectively. In consideration of improving energy

harvesting, the NES damper was selected with a relative small parameter, namely, $c_1 = 10$ Ns/m.

$$\eta_{\text{damp,NES}}(t) = \frac{\int_0^t c_1 \left[\dot{x}_1(\tau) - \dot{x}_2(\tau) \right] d\tau}{E_{\text{in}}} \times 100. \quad (9)$$

From (4), the equation below could be derived:

$$E_{\text{dissipation,hysteretic}}(t) = E_{\text{in}}(t) - \left[\frac{1}{2} m \dot{x}_1^2 + \frac{1}{2} M \dot{x}_2^2 \right]$$

$$- \left[\frac{1}{4} k_1 (x_1 - x_2)^4 + \frac{1}{2} k_2 x_2^2 + \frac{1}{2} k_p w^2 + \frac{1}{2} c_p V^2 \right]$$
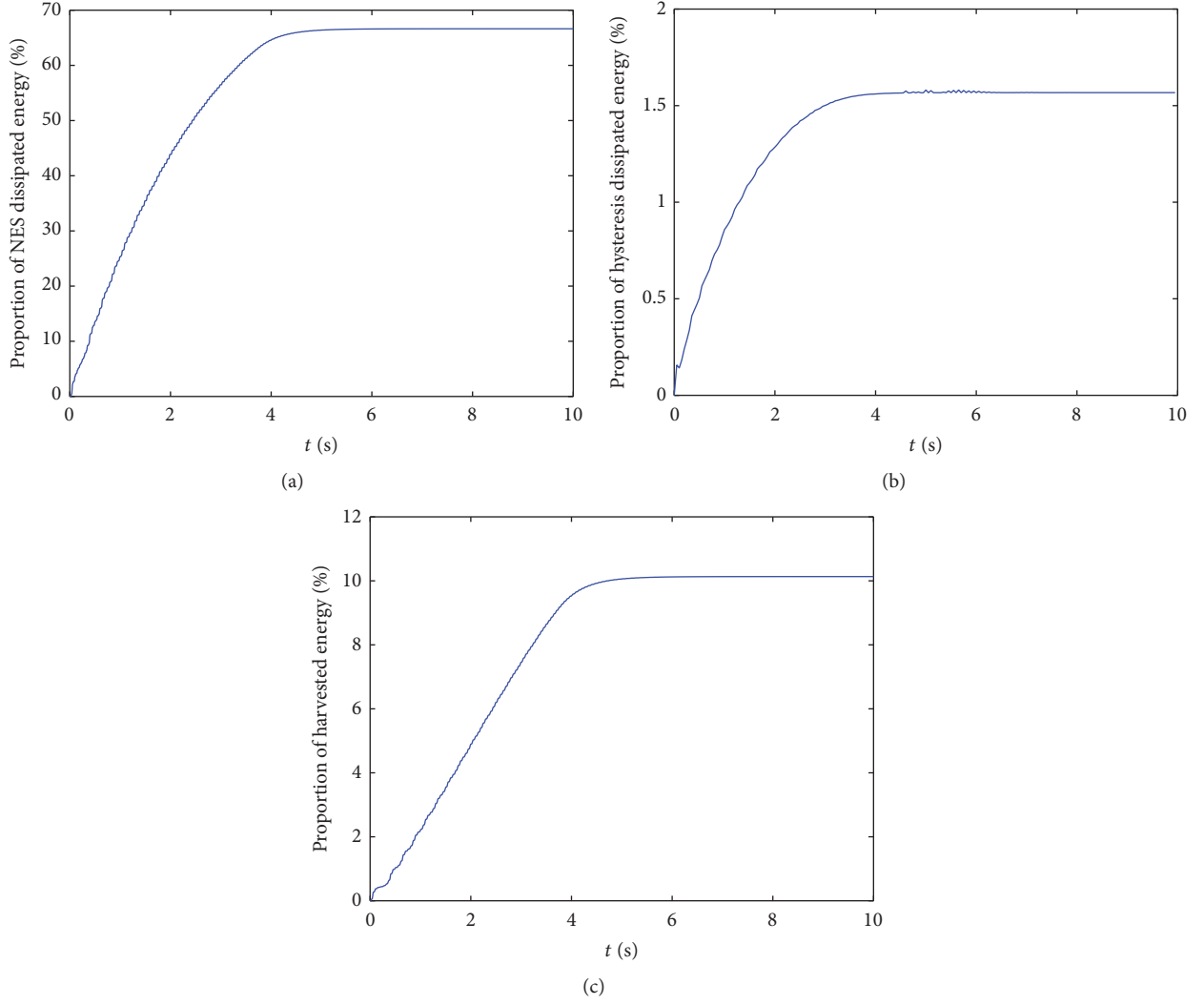
(a)

(b)

(c)

FIGURE 4: Configuration 1: (a) the percentage of energy dissipated by the NES damper; (b) the percentage of energy dissipated by the hysteresis behavior; (c) the percentage of energy harvested by the piezoelectric device.

$$+ \frac{1}{2}ak_3 (x_1 - x_2)^2 \right] - \left[\int_0^t c_1 (\dot{x}_1 - \dot{x}_2)^2 \, dt$$

$$+ \int_0^t c_2 \dot{x}_2^2 \, dt \right] - E_{\text{harvest}} (t) ,$$

(10)

$$\eta_{\text{dissipation,hysteretic}} (t) = \frac{E_{\text{dissipation,hysteretic}}}{E_{\text{in}}} \times 100.$$ (11)

Figures 4 and 5(a)–5(c) show the percentage of the captured energy dissipated by the NES damper and hysteresis behavior and harvested by the piezoelectric device, respectively. The curves in Figures 4 and 5(b) are fitted so that the tendency of energy dissipated by hysteresis behavior could be analysed better. Figures 4 and 5 show that

the system vibration ceased in 4th second approximately. The captured shock energy dissipated by the NES damper and hysteresis behavior and harvested by the piezoelectric element amounts to about 66.63%, 10.13%, and 1.57% for configuration 1, respectively, while it is 64.28%, 12.10%, and 3.17% for configuration 2. This phenomenon illustrates that most of the vibratory energy is dissipated by the NES damper and harvested by the piezoelectric material, and a small part of the energy is dissipated by the hysteresis behavior. The values of dissipated and harvested energy by NES-piezoelectric system of the two configurations are quite close. If both configurations are feasible, configuration 2 is given the priority to be adopted because of the higher energy harvesting.

The expression of instantaneous energy is presented below to show the energy change in the NES-piezoelectricity systems under external excitation.
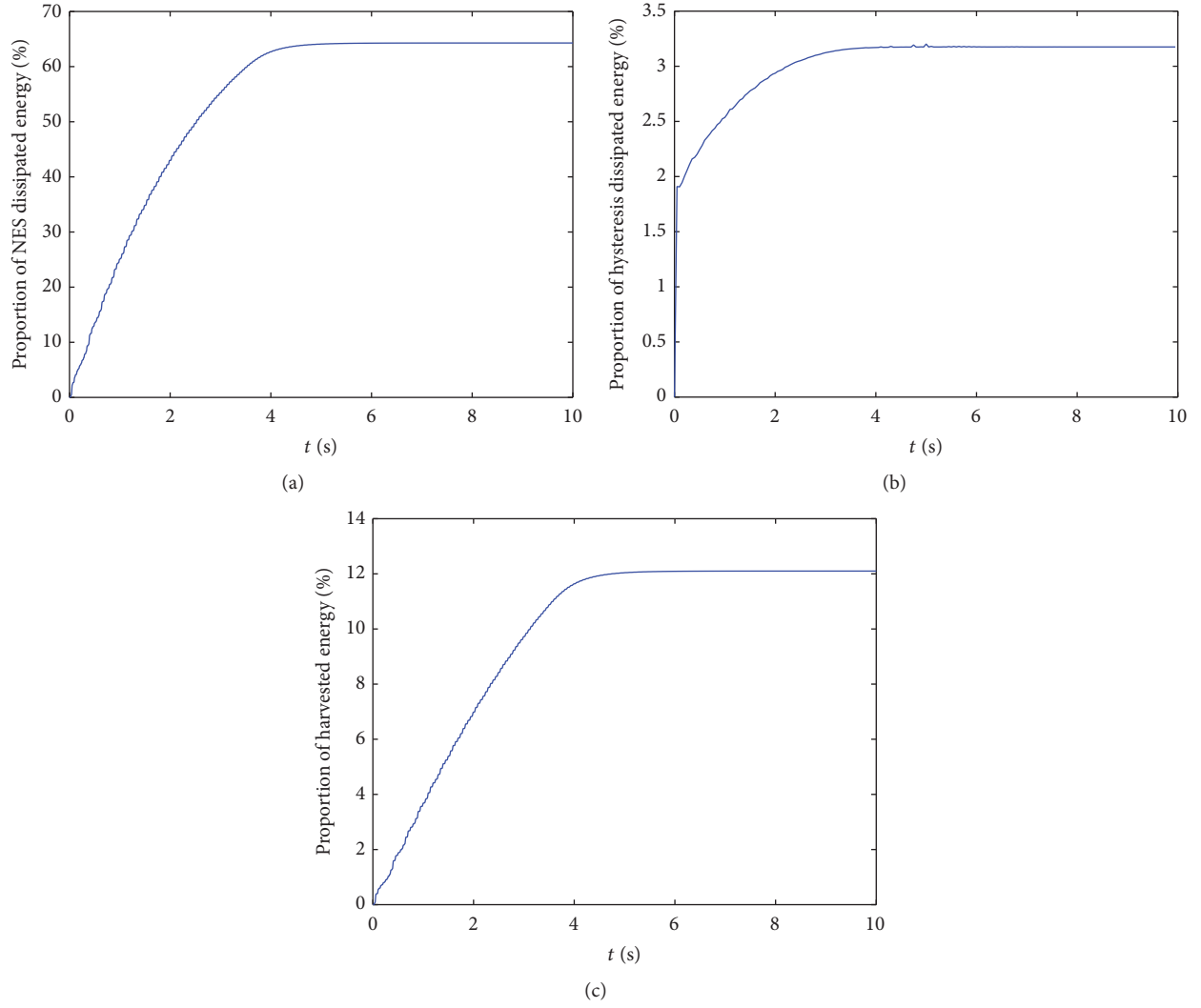
(a)

(b)

(c)

FIGURE 5: Configuration 2: (a) the percentage of energy dissipated by the NES damper; (b) the percentage of energy dissipated by the hysteresis behavior; (c) the percentage of energy harvested by the piezoelectric device.

$$
\begin{aligned}
\eta_{\text{NES,piezo,hysteretic}}(t) &= \frac{E_{\text{kinetic}}(t) + E_{\text{potential}}(t) + E_{\text{potential,hysteretic}}(t)}{E_{\text{in}}} \\
&= \frac{(1/2)\, m\dot{x}_1^{\,2}(t) + (1/4)\, k_1 \left[x_1(t) - x_2(t)\right]^4 + (1/2)\, k_p \left[x_1(t) - x_2(t)\right]^2 + (1/2)\, ak_3 \left(x_1 - x_2\right)^2}{\int_0^t F(\tau)\, \dot{x}_2(\tau)\, d\tau},
\end{aligned}
\tag{12}
$$

where $E_{\text{kinetic}}(t)$ is the instantaneous kinetic energy, $E_{\text{potential}}(t)$ is the instantaneous elastic potential energy included in NES and the piezoelectric element, and $E_{\text{potential,hysteretic}}(t)$ is the instantaneous elastic potential energy of the Bouc-Wen model. For both configurations, Figure 6 shows variation of the percentage of the instantaneous input energy captured in the NES-piezoelectricity

system with different spring stiffness of NES as time goes on. The value of spring stiffness has no obvious correlation with the proportion of instantaneous input energy. And the instantaneous mechanical energy approaches 0 as time passes.

The energy transaction measure (ETM) tremendously contributes to investigating the energy exchange [28], so it
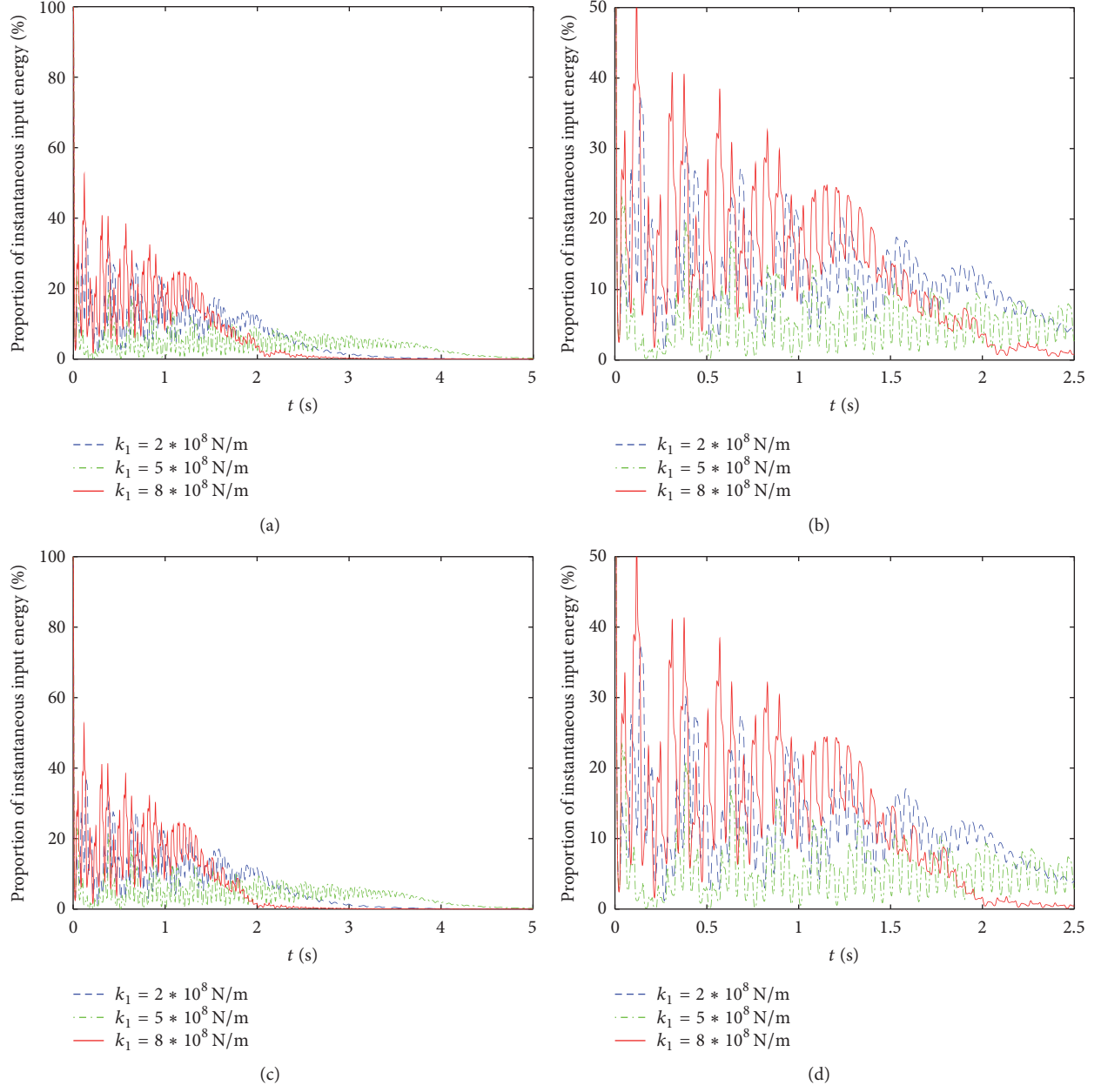
FIGURE 6: (a) The proportion of instantaneous input energy and (b) its enlargement of configuration 1; (c) the proportion of instantaneous input energy and (d) its enlargement of configuration 2.

is adopted to study the instantaneous energy transaction between the primary and NES-piezoelectricity system in this paper. ETM, E_{Trans}, between the two subsystems is defined in

$$
\begin{aligned}
E_{\text{Trans}} = {} & \Delta E_{\text{kinetic,NES}} + \Delta E_{\text{potential,NES}} + \Delta E_{\text{damp,NES}} \\
& + \Delta E_{\text{potential,hysteretic}} + \Delta E_{\text{dissipation,hysteretic}} \\
& + \Delta E_{\text{potential,piezo}} + \Delta E_{\text{harvest,piezo}},
\end{aligned}
\tag{13}
$$

where Δ represents the corresponding energy difference value among the subsystems. For instant, with time t, $E_{\text{kinetic,NES}}(t) = (1/2)m\dot{x}_1^{\,2}(t)$ is the kinetic energy in the NES;

$E_{\text{potential,NES}} = (1/4)k_1[x_1(t) - x_2(t)]^4$ is the elastic potential energy in NES; $E_{\text{damp,NES}} = \int_0^t c_1[\dot{x}_1(\tau) - \dot{x}_2(\tau)]^2 d\tau$ is the dissipated energy up to time t by NES, while $E_{\text{potential,hysteretic}} = (1/2)ak_3[x_1(t) - x_2(t)]^2$ is the elastic potential energy of hysteresis behavior; $E_{\text{potential,piezo}} = (1/2)k_p[x_1(t) - x_2(t)]^2$ is the elastic potential energy in the piezoelectric device. ETM is favourable to the identification of the transient energy inflow or outflow between the primary and NES-piezoelectricity system. Positive ETM values indicate that the transient energy is transferred from the primary system to the NES-piezoelectricity system. Negative ETM values that indicate transient energy are transferred from

(a)

— Kinetic energy of NES
— Potential energy of NES

(b)

— Potential energy of hysteresis behavior
— Potential energy of piezoelectric device

(c)

— Dissipated energy of NES
— Dissipated energy of hysteresis behavior
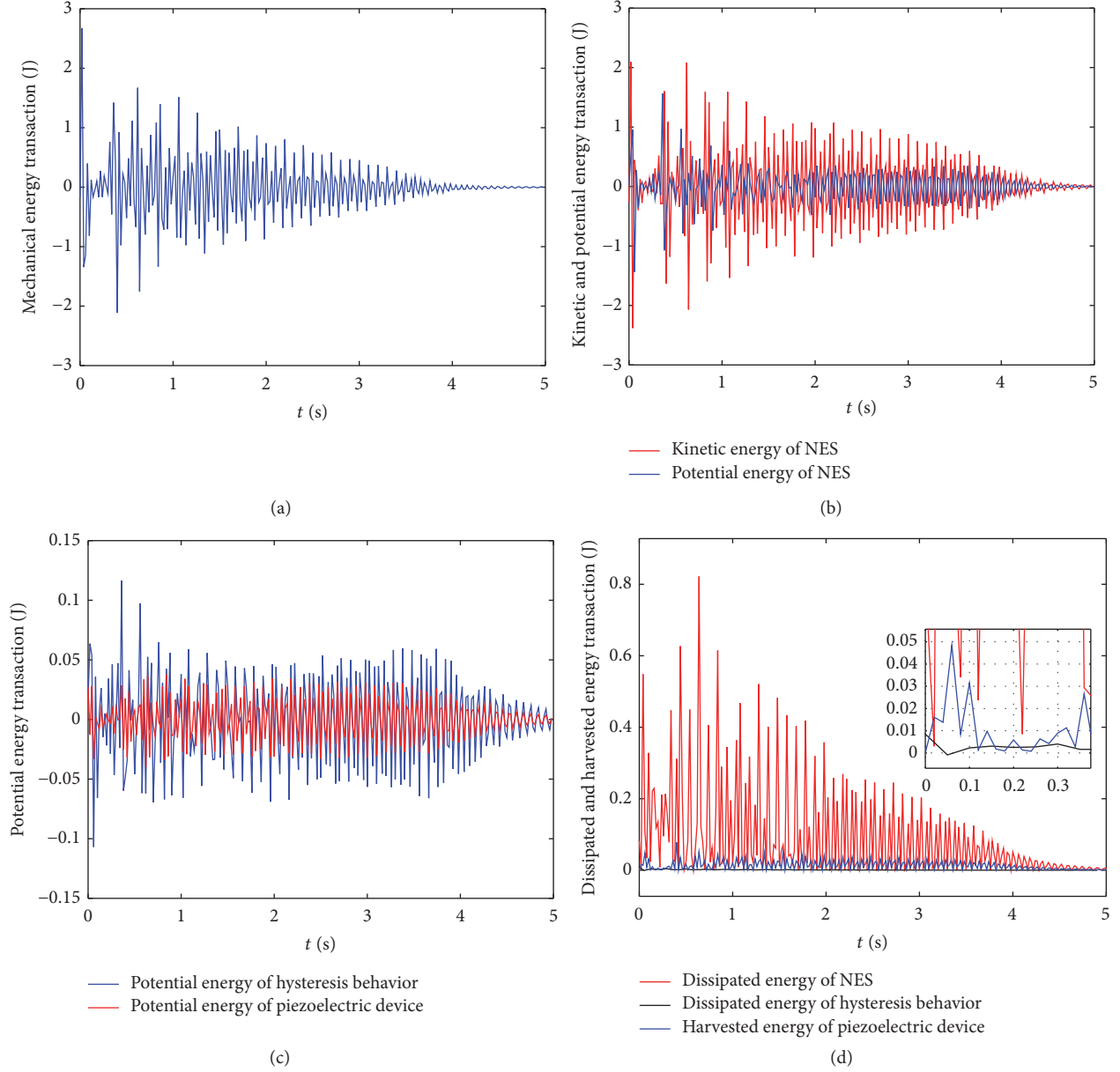— Harvested energy of piezoelectric device

(d)

FIGURE 7: Configuration 1: (a) mechanical energy transaction in the NES-piezoelectricity system; (b) kinetic and potential energy transaction of NES; (c) potential energy transaction of hysteresis behavior and piezoelectric device; (d) dissipated and harvested energy transaction in the NES-piezoelectricity system.

the NES-piezoelectricity system to the primary system. For configuration 1, Figure 7(a) presents the mechanical energy transaction in the NES-piezoelectricity system, equal $\Delta E_{\text{kinetic,NES}} + \Delta E_{\text{potential,NES}} + \Delta E_{\text{potential,hysteretic}} + \Delta E_{\text{potential,piezo}}$. Figure 7(b) depicts the kinetic and potential energy transactions of NES, namely, $\Delta E_{\text{kinetic,NES}}$ and $\Delta E_{\text{potential,NES}}$, respectively. Figure 7(c) illustrates the potential energy transaction of the hysteresis behavior and piezoelectric device, namely, $\Delta E_{\text{potential,hysteretic}}$ and $\Delta E_{\text{potential,piezo}}$, respectively. Figure 7(d) depicts the dissipated and harvested energy transactions in the NES-piezoelectricity system, namely, $\Delta E_{\text{damp,NES}}$, $\Delta E_{\text{dissipation,hysteretic}}$, and $\Delta E_{\text{harvest,piezo}}$.

For configuration 2, Figure 8(a) presents the mechanical energy transaction in the NES-piezoelectricity system. Figure 8(b) depicts the kinetic and potential energy transaction of NES. Figure 8(c) illustrates the potential energy transaction of the hysteresis behavior and piezoelectric device. Figure 8(d) depicts the dissipated and harvested energy transactions in the NES-piezoelectricity system. Figures 7 and 8 illustrate that the energy in the primary structure and NES-piezoelectricity system is flowing back and forth, highlighting that the dissipated and harvested energy transaction between the primary structure and NES-piezoelectricity system is positive and the instantaneous transaction of mechanical

(a)

Kinetic energy of NES
Potential energy of NES

(b)

Potential energy of hysteresis behavior
Potential energy of piezoelectric device

(c)

Dissipated energy of NES
Dissipated energy of hysteresis behavior
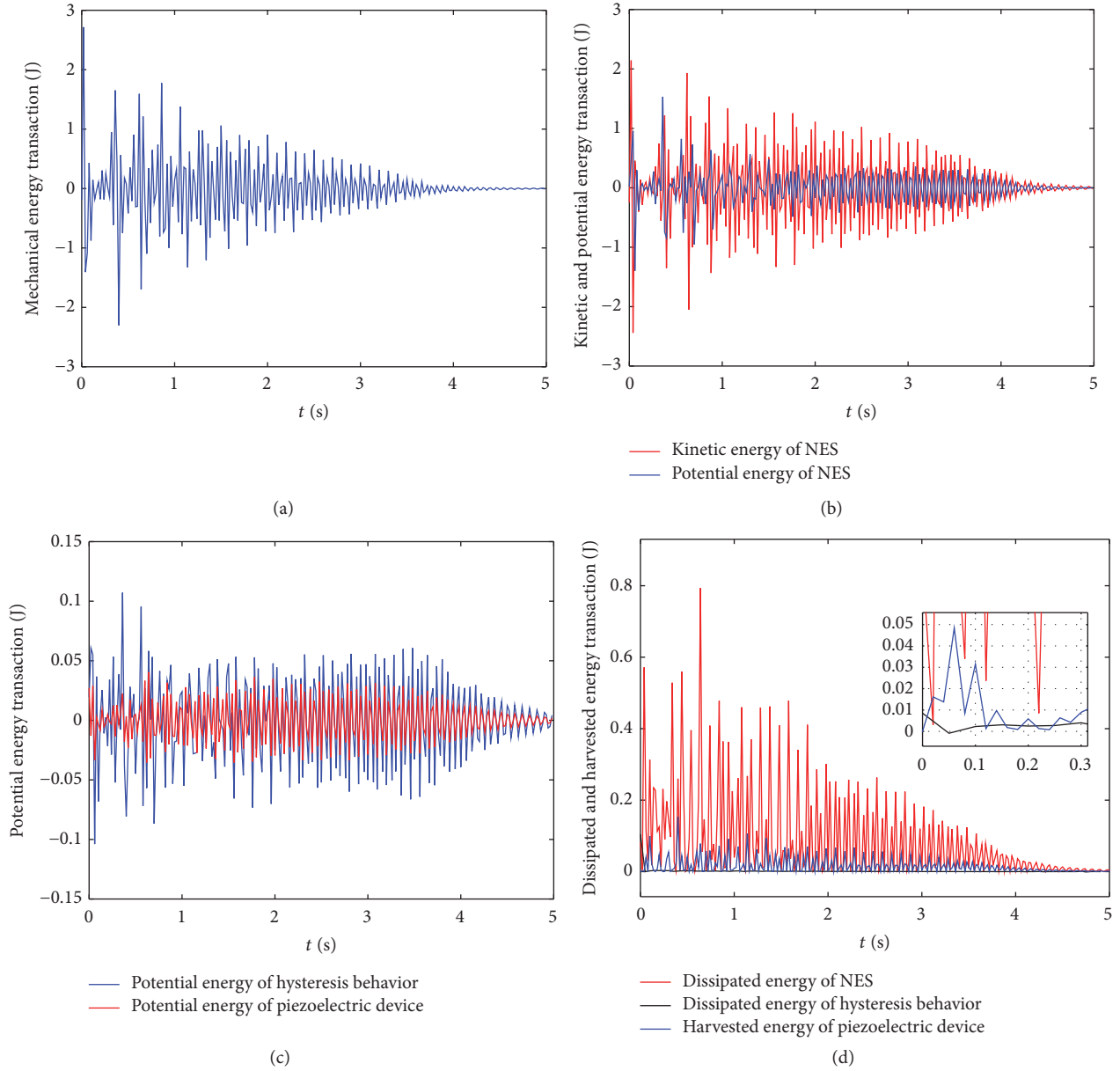Harvested energy of piezoelectric device

(d)

FIGURE 8: Configuration 1: (a) mechanical energy transaction in the NES-piezoelectricity system; (b) kinetic and potential energy transaction of NES; (c) potential energy transaction of hysteresis behavior and piezoelectric device; (d) dissipated and harvested energy transaction in the NES-piezoelectricity system.

energy between them is more significant than that of dissipated and harvested energy in both configurations.

Comparison of the transient response (the displacement of M) of the primary system with and without NES-piezoelectricity system in both configuration 1 and configuration 2 indicates that the system can contribute to vibration control. For the two configurations, the process and effect of vibration control are similar, the amplitude of M with NES-piezoelectricity system is little bigger than that without it in the first 2 seconds approximately, and after that the amplitude of M with NES-piezoelectricity system rapidly becomes much smaller than that without the system.

The response of primary structure with NES-piezoelectricity system approaches 0 at 4 seconds (Figure 9).

4. Conclusions

This study investigated a novel design for a system integrating NES including hysteresis behavior and an essential, strongly cubic, nonlinear stiffness with a piezoelectric-based vibration energy harvester under shock excitation to realize vibration mitigation and energy harvesting. Two piezoelectric device configurations, including the piezoelectric element embedded between the NES mass and the structure or ground,
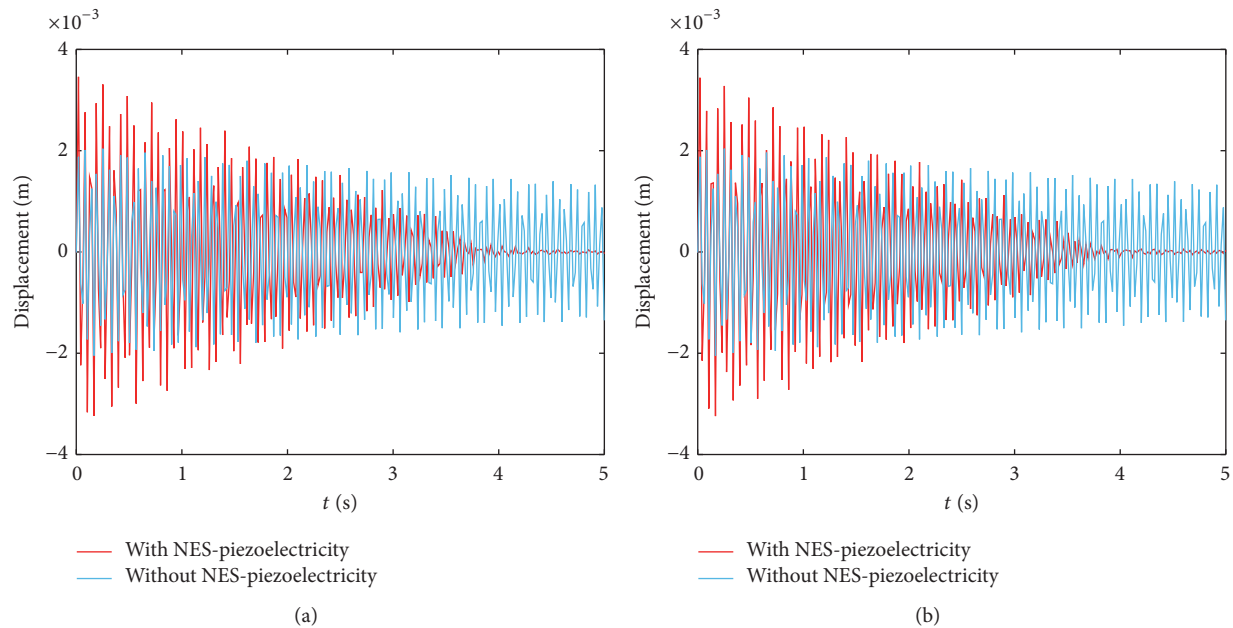
FIGURE 9: Comparing the transient response of the primary system with NES-piezoelectricity system and without it of (a) configuration 1 and (b) configuration 2.

were studied through a similar numerical research method. Initially, a big part of shock energy was captured by the NES-piezoelectricity system in the form of mechanical energy. Over time, the captured shock energy was dissipated by the NES damper and the hysteresis behavior of the Bouc-Wen model and harvested by the piezoelectric device. Finally, more than half of the input energy is dissipated by the damper of NES while the energy harvested by the piezoelectric element and dissipated by hysteresis behavior is relatively small. The dissipated and harvested energy by NES-piezoelectric system of the two configurations is slightly different. ETM was applied to examine the instantaneous energy transaction between the primary and NES-piezoelectricity system. The instantaneous transaction of mechanical energy in the NES-piezoelectricity system was more significant than that of dissipated and harvested energy. The NES-piezoelectricity system could realize vibration control of the primary structure and its displacement approaches to zero rapidly in both configurations.

Conflicts of Interest

The authors declare that they have no conflicts of interest.

Acknowledgments

References

[1] A. F. Vakakis, "Shock isolation through the use of nonlinear energy sinks," *Journal of Vibration and Control*, vol. 9, no. 1-2, pp. 79–93, 2003.

[2] M. Kani, S. E. Khadem, M. H. Pashaei, and M. Dardel, "Vibration control of a nonlinear beam with a nonlinear energy sink," *Nonlinear Dynamics*, vol. 83, no. 1, pp. 1–22, 2016.

[3] O. V. Gendelman, "Transition of energy to a nonlinear localized mode in a highly asymmetric system of two oscillators," *Nonlinear Dynamics*, vol. 25, no. 1–3, pp. 237–253, 2001.

[4] A. F. Vakakis, O. V. Gendelman, L. A. Bergman, D. M. McFarland, G. Kerschen, and Y. S. Lee, *Nonlinear Trageted Energy Transfer in Mechanical and Structural Systems*, Springer, Berlin, Germany, 2008.

[5] Y.-W. Zhang, J. Zang, T.-Z. Yang, B. Fang, and X. Wen, "Vibration suppression of an axially moving string with transverse wind loadings by a nonlinear energy sink," *Mathematical Problems in Engineering*, vol. 2013, Article ID 348042, 7 pages, 2013.

[6] Y. Starosvetsky and O. V. Gendelman, "Interaction of nonlinear energy sink with a two degrees of freedom linear system: internal resonance," *Journal of Sound and Vibration*, vol. 329, no. 10, pp. 1836–1852, 2010.

[7] T.-Z. Yang, X.-D. Yang, Y. Li, and B. Fang, "Passive and adaptive vibration suppression of pipes conveying fluid with variable velocity," *Journal of Vibration and Control*, vol. 20, no. 9, pp. 1293–1300, 2014.

[8] A. Luongo and D. Zulli, "Dynamic analysis of externally excited NES-controlled systems via a mixed Multiple Scale/Harmonic Balance algorithm," *Nonlinear Dynamics*, vol. 70, no. 3, pp. 2049–2061, 2012.

[9] Y. Zhang, J.-R. Zhang, and S.-J. Xu, "Influence of flexible solar arrays on vibration isolation platform of control moment

gyroscopes," *Acta Mechanica Sinica*, vol. 28, no. 5, pp. 1479–1487, 2012.

[10] Z. Fang, Y. Zhang, X. Li, H. Ding, and L. Chen, "Integration of a nonlinear energy sink and a giant magnetostrictive energy harvester," *Journal of Sound and Vibration*, vol. 391, pp. 35–49, 2017.

[11] N. Ebrahimzade, M. Dardel, and R. Shafaghat, "Performance comparison of linear and nonlinear vibration absorbers in aeroelastic characteristics of a wing model," *Nonlinear Dynamics*, vol. 86, no. 2, pp. 1075–1094, 2016.

[12] H. A. Sodano, D. J. Inman, and G. Park, "A review of power harvesting from vibration using piezoelectric materials," *Shock and Vibration Digest*, vol. 36, no. 3, pp. 197–205, 2004.

[13] E. Jacquelin, S. Adhikari, and M. I. Friswell, "A piezoelectric device for impact energy harvesting," *Smart Materials and Structures*, vol. 20, no. 10, pp. 1–12, 2011.

[14] J. M. Renno, J. R. Farmer, and D. J. Inman, "Effects of system parameters and damping on an optimal vibration-based energy harvester," in *Proceedings of the AIAA/ASME/ASCE/AHS/ASC Structures, Structural Dynamics, and Materials Conference*, vol. 4, AIAA, 2007, 2007-2361.

[15] Z. N. Ahmadabadi and S. E. Khadem, "Nonlinear vibration control and energy harvesting of a beam using a nonlinear energy sink and a piezoelectric device," *Journal of Sound and Vibration*, vol. 333, no. 19, pp. 4444–4457, 2014.

[16] Y. Zhang, L. Tang, and K. Liu, "Piezoelectric energy harvesting with a nonlinear energy sink," *Journal of Intelligent Material Systems and Structures*, vol. 28, no. 3, pp. 307–322, 2017.

[17] J. Awrejcewicz, L. Dzyubak, and C.-H. Lamarque, "Modelling of hysteresis using Masing-Bouc-Wen's framework and search of conditions for the chaotic responses," *Communications in Nonlinear Science and Numerical Simulation*, vol. 13, no. 5, pp. 939–958, 2008.

[18] R. Bouc, "Forced vibration of mechanical systems with hysteresis," in *Proceedings of the 4th Conference on Nonlinear Oscillations*, Prague, Czech Republic, 1967.

[19] Y. K. Wen, "Method for random vibration of hysteresis systems," *ASCE Journal of Engineering Mechanics*, vol. 102, no. 2, pp. 249–263, 1976.

[20] F. Ikhouane, J. E. Hurtado, and J. Rodellar, "Variation of the hysteresis loop with the Bouc-Wen model parameters," *Nonlinear Dynamics*, vol. 48, no. 4, pp. 361–380, 2007.

[21] A. E. Charalampakis, "The response and dissipated energy of Bouc-Wen hysteretic model revisited," *Archive of Applied Mechanics*, vol. 85, no. 9-10, pp. 1209–1223, 2015.

[22] C.-H. Lamarque and A. T. Savadkoohi, "Dynamical behavior of a Bouc-Wen type oscillator coupled to a nonlinear energy sink," *Meccanica*, vol. 49, no. 8, pp. 1917–1928, 2014.

[23] A. T. Savadkoohi, C.-H. Lamarque, and M. V. Contessa, "Trapping vibratory energy of main linear structures by coupling light systems with geometrical and material non-linearities," *International Journal of Non-Linear Mechanics*, vol. 80, pp. 3–13, 2016.

[24] L. Q. Chen and T. C. Yuan, "Nonlinear oscillation of a circular plate energy harvester," in *Proceedings of the 26th International Congress of Theoretical and Applied Mechanics*, Montrèal, Canada, August 2016.

[25] H.-G. Li and G. Meng, "Nonlinear dynamics of a SDOF oscillator with Bouc-Wen hysteresis," *Chaos, Solitons and Fractals*, vol. 34, no. 2, pp. 337–343, 2007.

[26] H. Ding and J. W. Zu, "Effect of one-way clutch on the nonlinear vibration of belt-drive systems with a continuous belt model," *Journal of Sound and Vibration*, vol. 332, no. 24, pp. 6472–6487, 2013.

[27] H. Ding and J. W. Zu, "Steady-state responses of pulley-belt systems with a one-way clutch and belt bending stiffness," *Journal of Vibration and Acoustics, Transactions of the ASME*, vol. 136, no. 4, Article ID 041006, 2014.

[28] F. Georgiades, A. F. Vakakis, and G. Kerschen, "Broadband passive targeted energy pumping from a linear dispersive rod to a lightweight essentially non-linear end attachment," *International Journal of Non-Linear Mechanics*, vol. 42, no. 5, pp. 773–788, 2007.

Research Article

Characteristics of Rainfall in Wind Field of a Downburst and Its Effects on Motion of High-Voltage Transmission Line

Chao Zhou,[1,2] **Li Li,**[1] **and Yibing Liu**[1,2]

[1]*School of Energy Power and Mechanical Engineering, North China Electric Power University, Beijing 102206, China*
[2]*Key Laboratory of Condition Monitoring and Control for Power Plant Equipment Ministry of Education,*
 North China Electric Power University, Beijing 102206, China

Correspondence should be addressed to Chao Zhou; zhouchao@ncepu.edu.cn

Despite most weather-related failures of high-voltage transmission lines (HVTLs) being attributed to the downbursts accompanied by heavy rainfall, research works mainly focused on the behaviors of the high-voltage transmission tower-line structures under dry downburst winds. This paper thus presents a preliminary study to discuss the characteristics of rainfall in the downbursts and their effects on responses of HVTLs. Based on Vicroy model, the velocities of raindrops and their loads and pressure ratios of downburst wind-driven rain and only downburst wind on the surface of HVTLs per unit length are obtained. A downburst wind-rain induced vibration model is established to calculate the effects of the rainfall intensity and wind velocities on the motions of HVTLs. To verify the feasibility and accuracy of the model, the model is applied to evaluate responses of HVTLs with measured aerodynamic coefficients. The responses of HVTLs from the evaluated (the model) and the field observation results are compared. The results indicated that the model is feasible and can capture main features of the rainfall acting on HVTLs in the downbursts. Furthermore, the effects of rainfall cannot be neglected, and more attention should be paid to the wet downbursts and their effects on aerodynamic property of HVTLs.

1. Introduction

A downburst is created by a column of sinking air that, after hitting ground level, spreads out in all directions and is capable of producing transmission line damage. 83% of the downbursts observed during the project of joint airport weather study are dry, while 64% of the downbursts identified during northern Illinois meteorological research, in the Chicago area, are wet [1]. The downbursts induced damage is similar to but distinguished from those caused by boundary layer strong winds or tornadoes [2]. It is reported that high intensity winds in the form of the downbursts or tornadoes are responsible for more than 80% of the weather-related failures of transmission lines [3]. There is a plan to have the ultra-high-voltage transmission tower-line systems across the southwest regions of China, where downbursts with high amounts of rainfall often occur. However, very few procedures in the design codes and manuals of practice

were related to the estimation of the forces of downbursts on transmission tower-line structures, especially the downbursts with high amounts of rainfall.

Many studies have been thus conducted to find out the failure mechanism behind this type of the high-voltage transmission line damage and the measures to mitigate such structural failures. Savory et al. [4] studied the failure mechanism of a self-supported transmission tower under wind fields of downbursts and tornadoes. By assuming that loads of the conductors on the self-supported transmission tower are negligible, it is found that the tower failures only occurred in case of tornadoes, while no damage was associated with the downbursts. Shehata et al. [5] developed a finite element model to predict the structural performance of transmission towers as part of a transmission line system under downburst loading. The result showed that peak forces in transmission tower members are sensitive to the downburst location, and the peak value of the axial forces associated with the

downburst exceeds those due to normal wind load by a percentage ranging between 9.0% and 304%. Aboshosha and Damatty [6] developed a new technique to analyze responses of multispan conductors under high intensity wind events, in the form of tornadoes and downbursts. The solution was the first semiclosed form for a multispan conductor under nonuniform loads in both in-plane and out-of-plane directions, and computing speed of technique was approximately 185 times faster than the nonlinear finite element method. Liang et al. [7] carried out wind tunnel tests to measure the displacements, acceleration, and strains of a full aeroelastic model of a transmission tower-line structure. The result indicated that the coupled effects of the towers and the conductor on the responses of the tower, as well as the across-wind vibration of the tower, must be considered in the wind-resistant design of electrical transmission towers. Eguchi et al. [8] developed a new type of electric wire for overhead transmission lines to reduce the drag force under typhoon conditions. By wind tunnel experiments, it is found that the free shear layer oscillation at 70° was the key to the separation point shift, and the flow fluctuation generated by the oscillation was the seed of the large eddy which collides with the wire surfaces. Kikuchi et al. [9] mounted a watering grid upwind on the wind tunnel test section to measure the drag coefficients in typhoon-weather conditions with heavy rainfalls (8, 10, 16, 25, and 40 mm per 10 min). The experimental results from the wind tunnel unveiled that the influence of heavy rainfall was not negligible on the new-design wire, which showed about 20% of increase in the drag coefficient in the cross-flow condition. Li et al. [10] established two kinds of typical aeroelastic models of transmission towers to measure the dynamic responses of the transmission towers under wind-induced and rain-wind induced actions. The result showed that vibration responses by rain-wind actions were larger than those of by wind actions, and the rain loads of strong rainstorms acting on the transmission tower cannot be neglected. Fu et al. [11] carried out a single raindrop impinging experiment with self-made piezoelectric transducer to measure the rain load and then developed a numerical method to calculate the transmission tower subjected to wind and rain loads which was conducted. The results showed that the maximum root-mean-square acceleration induced by rain load relative to the wind load can reach 22.4% at the basic wind velocity of 5 m/s and rain intensity of 200 mm/h. Wei et al. [12] established a short-term reliability model to evaluate failure probability of the IEEE-79 system under impact of strong wind and rain loads. The result showed that rain loads had obvious effects on the reliability indices of system loads. Zhou et al. [13, 14] established a rain-wind induced model to investigate the effects of wind, raindrop, and time-varying mass on dynamic response of high-voltage transmission lines. The results indicated that the largest amplitude of the high-voltage conductors only occurred within a certain range of wind velocities, and possible reasons of which might be the variable aerodynamic damping ratio.

Although many attempts have been made to discuss the behaviors of the transmission tower-line structures in the dry downburst winds, very few efforts are paid to the characteristics of rainfall in the wind fields of downbursts and its effects on the motions of high-voltage conductors. This paper thus presents a preliminary analytical study. Based on the Vicroy model of a downburst, as well as raindrops' velocities and its loads, the pressure of a downburst wind-rain rain acting on the surface of the conductor per unit length is calculated. Furthermore, a downburst wind-rain induced vibration model is developed to describe the effects of the rainfall intensity and wind velocities on the motions of the high-voltage transmission lines.

2. Theoretical Analysis of Raindrops in Wind Field of a Downburst

Downburst-driven rain or driving rain has a horizontal velocity component, and its intensity often is very large. Typically, researchers attributed the structure collapses to strong winds, while the effects of rainfall on the responses of the transmission tower-line structures are ignored in design for long-term studies. To clarify the behaviors of raindrops in the wind fields of the downbursts and their effects on the motion of high-voltage conductors, raindrops' velocities and their loads on the high-voltage conductors per unit length in the wind field of downbursts must be evaluated firstly.

2.1. Velocities of Raindrops in a Wind Field of Downburst. As a preliminary theoretical study, the vertical velocity profile of a downburst, in this paper, is expressed by Vicroy model [15] as follows:

$$V(y) = 1.22 \times \left(e^{-0.15 y/y_{max}} - e^{-3.2175 y/y_{max}}\right) \times V_{max}, \quad (1)$$

where y is height and y_{max} is the height of which the maximum velocity occurs, respectively; V_{max} is the maximum wind velocity in the vertical wind profile.

Assume that mean wind velocity of downburst at any height can be factorized as the product of the vertical profile and a time function [16] as follows:

$$\overline{U}(y,t) = V(y) \times f(t), \quad (2)$$

where t is time and $f(t)$ is a time function, and the maximum value is 1.

By assuming that the time function is $f(t) = 1$, the mean wind velocity of downburst over the height has the maximum value at any time. Let $V_{max} = 80$ m/s [16] and $y_{max} = 80$; the profiles of Vicroy model and the Boundary Layer Davenport model (the mean velocity is fitted with a power-exponent related to the terrain roughness, equal to 0.16 in this study) are plotted in Figure 1. It should be noted that Vicroy's model of $V_{max} = 80$ m/s and $y_{max} = 80$ m, to some extent, is huge. The reason why we selected Vicroy's model of $V_{max} = 80$ m/s and $y_{max} = 80$ is that the planned ultra-high-voltage transmission tower-line system is compatible with both high-rise and large-span structural features in China, which is very sensitive to downburst wind and Vicroy's model maybe more suitable to it. By comparing the two curves, it can be easily found that the vertical velocity profile of Vicroy model is obviously distinct with that of the Boundary Layer Davenport model.
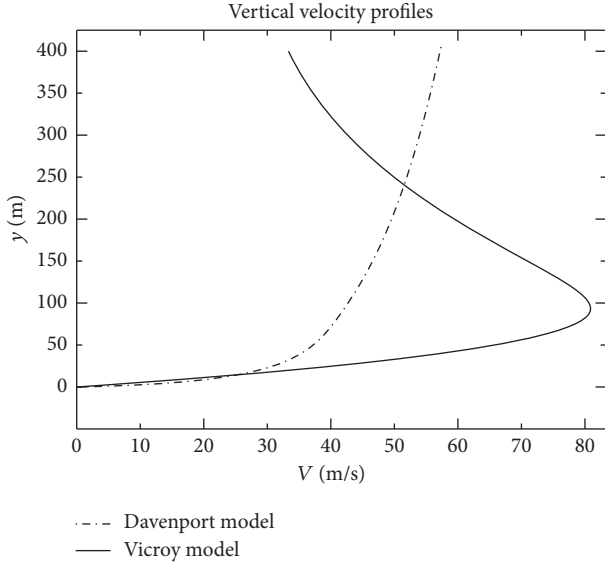
FIGURE 1: Vertical profiles of Vicroy model and Davenport model.

C: downburst center
P: observing point

FIGURE 2: Vector combination of radial and translation wind velocities.

At a certain height, the horizontal wind velocity of downburst could be, approximately, the vector sum of the radial impinging jet velocity and the storm translation velocity [17]. The radial velocity profile of horizontal downburst wind, at some height, can be represented as

$$
V_y(R)
$$
$$
= \begin{cases} V_y(R)_{\max} \times \left(\dfrac{R}{R_b} \right) & (0 \le R < R_b) \\ V_y(R)_{\max} \times \exp\left(-\left[\dfrac{(R - R_b)}{R_r} \right]^2 \right) & (R \ge R_b), \end{cases} \tag{3}
$$

where $V_y(R)_{\max}$ is the maximum horizontal velocity in the profile; R is radial distance from the downburst center; R_b is radial distance of which the maximum horizontal velocity occurs; R_r is a radial length scale.

It is assumed that the storm translates towards the line to simplify the analysis. However, it also noted that this may not represent the worst case scenario but gives an indication about the response of the high-voltage conductor. The combined wind velocity will flow around an observing point of the high-voltage conductor as the downburst passed by, which could be the vector sum of radial velocity and the downburst translation velocity. As shown in Figure 2, the downburst center is assumed to move forward along the translational track with velocity v_t, and the coordinate system is fixed to the downburst center. Thus, the wind velocity of downburst at the observing point of the high-voltage conductor can be expressed as follows:

$$
v_c(t) = V_y(R) + v_t(t). \tag{4}
$$

Wind velocity of a downburst at any height and any time is the sum of the mean wind velocity and fluctuating wind velocity as follows:

$$
U(y,t) = \overline{U}(y,t) + u(y,t). \tag{5}
$$

The wind load of a downburst can be calculated as

$$
F_{\text{wind}}(t) = \frac{\mu A' U^2(y,t)}{1.6}, \tag{6}
$$

where A' is the windward projected area of the conductor; μ' is the shape coefficient, and is 1.0 for the conductor.

Let x and z denote the two directions of horizontal plane; y denotes the vertical direction; the velocities of raindrops in wind field of the downburst can be expressed as [18]

$$
m'\frac{d^2 x}{dt^2} = \pi \mu \lambda \left(U_x - \frac{dx}{dt} \right) \frac{C_D R_e}{4},
$$
$$
m'\frac{d^2 y}{dt^2} = \pi \mu \lambda \left(U_y - \frac{dy}{dt} \right) \frac{C_D R_e}{4} - m' g \left(1 - \frac{\rho}{\rho_w} \right), \tag{7}
$$
$$
m'\frac{d^2 z}{dt^2} = \pi \mu \lambda \left(U_z - \frac{dz}{dt} \right) \frac{C_D R_e}{4},
$$

$$
R_e
$$
$$
= \frac{2\rho}{\mu} \sqrt{ \left(U_x - \frac{dx}{dt} \right)^2 + \left(U_y - \frac{dy}{dt} \right)^2 + \left(U_z - \frac{dz}{dt} \right)^2 }, \tag{8}
$$

where m' is the raindrop mass; μ is the air viscosity; U_x, U_y, and U_z are the wind velocity component in x, y, and z directions, respectively; R_e is the Reynolds number; C_D is the drag coefficient on the raindrop; λ is the raindrop radius; ρ is the air density; ρ_w is the water density.

Most raindrops in the wind fields of downburst begin to fall at a height of more than 20 m from the high-voltage conductor. Falling velocity, when the raindrops reach the

observing point of the high-voltage conductor, can be taken as terminal velocity of raindrops [19]. Thus, the vertical velocity of a raindrop with radius λ can be expressed as

$$U_v(\lambda) = 9.5 \left\{ 1 - \exp\left[-(1.13\lambda)^{1.147}\right] \right\}. \tag{9}$$

2.2. Loads of Raindrops Acting on the High-Voltage Conductor per Unit Length. A large number of observations show that the raindrop sizes in the horizontal planes obey a negative exponential distribution, which can be expressed by the Marshall-Palmer exponential size distribution as follows [20]:

$$n(\lambda) = n_0 \exp(-\Lambda\lambda), \tag{10}$$

where $n_0 = 8 \times 10^3$ (m^3·mm) for any rainfall intensity; $\Lambda = 4.1 I^{-0.21}$ is the slope factor; I is the rainfall intensity.

The velocities of raindrops become zero very quickly when the raindrops impinge on the high-voltage conductors, which obey Newton's Second Law as follows:

$$\int_0^\tau f(t) + \int_{U_i}^0 \sigma \, d\delta = 0 \quad (i = h, v), \tag{11}$$

where $\tau = \lambda/U_i$ is the time interval of impinging; $\sigma = 4\pi\lambda^3\rho_w/3$ is mass of a single raindrop.

The impact forces of a single raindrop on a high-voltage conductor can be calculated as

$$\chi_i(\tau) = \frac{4\rho_w\pi\lambda^3 U_i(y,t)}{3\tau} \quad (i = h, v). \tag{12}$$

Therefore, the rain load acting on a high-voltage conductor for any rainfall intensity can be obtained as

$$F_i = \frac{\chi_i(\tau)}{(Ab\alpha)} \quad (i = h, v), \tag{13}$$

where $A = \pi\lambda^2$ is action area; b is the section-width of the high-voltage conductor; $\alpha = (4\pi\lambda^3/3) \cdot n$ is rainfall intensity factor; $n = \int_{\lambda_1}^{\lambda_2} n(\lambda)d\lambda$.

Appling A and α into (13) leads to

$$F_i = \frac{16n\rho_w\pi\lambda^3 U_i^2(y,t)b}{9} \quad (i = h, v). \tag{14}$$

3. Model of Downburst Wind-Rain Induced Vibration and Experimental Test

3.1. Downburst Wind-Rain Induced Vibration Model of the High-Voltage Conductor. A uniform inclined cylinder is used to represent a high-voltage conductor segment, the inclination of the cylinder is denoted by angle α, and yaw angle of the cylinder to a downburst wind is defined by angle β (Figure 3). Since the cylinder is not perpendicular to the direction of the downburst wind velocity $U(y,t)$, the component of the downburst wind velocity perpendicular to the cylinder $U'(y,t)$ is needed to be found by the following equation:

$$U'(y,t) = U(y,t) \sqrt{\sin^2\beta + \cos^2\beta \sin\alpha^2}. \tag{15}$$

Accordingly, the attack angle of the downburst wind component $U'(y,t)$ is

$$\vartheta = \arcsin\left(\frac{\cos\beta \sin\alpha}{\sqrt{\sin^2\beta + \cos^2\beta \sin\alpha^2}} \right). \tag{16}$$

The raindrops which hit the cylinder may stay on the surface of the cylinder for a while, and the raindrops which stayed may form rivulets and oscillate around the surface of the high-voltage conductors. Extensive wind-rain-tunnel tests for vibration of stay cables in cable-stayed bridges have been conducted. It is found that the formed rivulet and its oscillation changed the cable original cross-section and resulted in excessive cable vibrations [21]. Furthermore, different positions were observed for the lower rivulet while keeping the upper rivulet at 40°, no changes in the amplitude were observed, and a conclusion was drawn that the lower rivulet plays a negligible role on the oscillation [22]. To simplify the analysis in the section, only the effects of the upper rivulet are considered whereas the lower rivulet is neglected.

When the cylinder moves in the positive direction y and z, two virtual flows with velocity $-\dot{y}$ and $-\dot{z}$ in the opposite direction will be induced. The upper rivulet will move on the tangential direction with the velocity of $r\dot{\gamma}$, r is the radius of the cylinder, and the relative wind velocity to the cylinder with moving rivulet is

$$U_{\text{rel}} = \sqrt{\left(U'(y,t)\sin\vartheta - \dot{y} - r\dot{\gamma}\sin\gamma\right)^2 + \left(U'(y,t)\cos\vartheta - \dot{z} - r\dot{\gamma}\cos\gamma\right)^2}. \tag{17}$$

As shown in Figure 3, the angle between the relative wind velocity $U_{\text{rel}}(y,t)$ and the horizontal axis, ϕ can be expressed as

$$\phi = \arctan\left(\frac{U'(y,t)\sin\vartheta - \dot{y} - r\dot{\gamma}\sin\gamma}{U'(y,t)\cos\vartheta - \dot{z} - r\dot{\gamma}\cos\gamma} \right). \tag{18}$$

On the basis of the theoretical and experimental instability studies of the cables of cable-stayed bridges [23], it

is obtained that $r\dot{\gamma}/U'(y,t) \ll 1$, $\dot{y}/U'(y,t) \ll 1$, and $\dot{z}/U'(y,t) \ll 1$. Thus, if the angle $U'(y,t)$ and φ are limited to a certain range, (18) can be reduced as

$$\phi = \frac{U'(y,t)\sin\vartheta - \dot{y} - r\dot{\gamma}\sin\gamma}{U'(y,t)\cos\vartheta}. \tag{19}$$
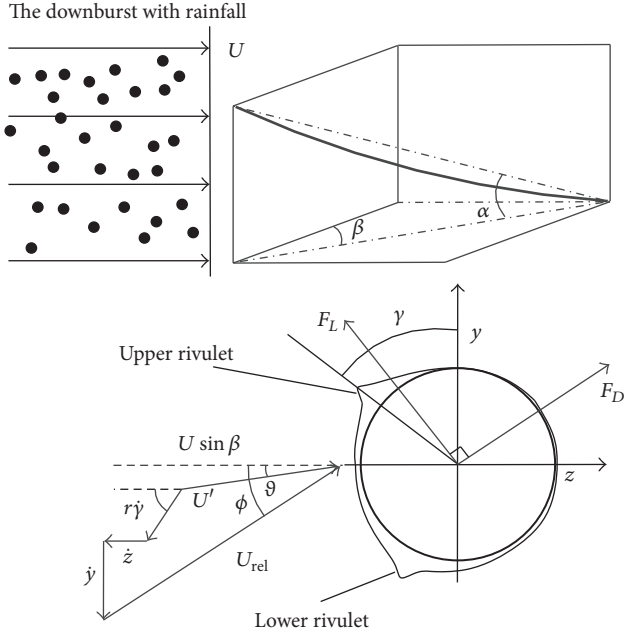
FIGURE 3: Schematic of rainfall acting on the high-voltage conductor with the downburst wind.

The drag force F_D is indicated in the direction of the relative wind velocity $U_{rel}(y, t)$, whereas the lift force F_L is perpendicular to F_D in the anticlockwise direction.

$$F_D = \rho r U_{rel}^2 C_D(\varphi),$$
$$F_L = \rho r U_{rel}^2 C_L(\varphi), \tag{20}$$

where φ is the relative attack angle and $\varphi = \phi - \gamma + 90$; C_D is the drag coefficient and C_L is the lift coefficient, respectively.

To simplify the analysis, structural damping of the cylinder is viscous, and the mass is uniformly distributed. Based on the above discussion, the motion equation of the cylinder can be written as

$$m\ddot{z} + c\dot{z} + kz = \rho r U_{rel}^2 \left(C_D \cos \phi - C_L \sin \phi \right)$$
$$- \frac{16 n \rho_w \pi \lambda^3 \left(U_h(y, t) \sin \theta - \dot{z} \right)^2 b}{9},$$
$$m\ddot{y} + c\dot{y} + ky = \rho r U_{rel}^2 \left(C_D \sin \phi + C_L \cos \phi \right)$$
$$- \frac{16 n \rho_w \pi \lambda^3 \left(U_v(y, t) - \dot{y} \right)^2 b}{9}, \tag{21}$$

where m is the mass of the cylinder per unit length; c is structural damping; k is stiffness.

3.2. Experimental Test. To clarify the aerodynamic characteristics of rainfall in the wind fields of downbursts and the responses of the high-voltage conductors, a series of experimental tests need to be carried out with different rainfall rates and downburst wind velocities. The phenomena of instability vibration of the high-voltage conductor in the wind field of downbursts are very complex. To simplify the

experimental test, some presuppositions are proposed as follows:

(1) The downburst center C is assumed to be fixed, and the downburst translation v_t is combined in the wind velocity vector v_c;

(2) Radial distance R between the observing point and the downburst center is assumed far enough, and the wind field of the downbursts is smooth relatively;

(3) Effects of electric fields and space charges on the upper rivulet are not considered;

(4) Raindrops are assumed uniformly distributed in the wind fields of downbursts.

The experimental test is conducted in a self-designed small-sized open-circuit tunnel, as shown in Figure 4. The original working section is 1.3 m (width) × 1.3 m (height), and maximum wind velocity 50 m/s. Limited by field, no attached contraction section is mounted on the tunnel, and the uniformity of mean wind velocity of the present testing section is not comparable to that of conventional boundary layer wind tunnel. The velocity and turbulence intensity profiles at the test section are similar to the boundary layer profiles, but the variations in the wind velocity and turbulence are approximately 9% and 7%, respectively. As the diameter of 40 mm is typically used with ±660 kV/800 kV UHV DC transmission lines, such as JL/G3A-1000/45-72/7 (diameter of 42.08), JL/G3A-900/40-72/7 (diameter of 39.9), and JL/G2A-900/75-84/7 (diameter of 40.6), the test model of the aluminum steel conductor in this study is defined to have a length of 1.8 m and a diameter of 40 mm. The rain-simulating unit of the experimental test includes a water sink and two sets of rain-simulation device. Rain-simulation device consists of a submersible pump, a control valve, a water pipe, and a sprinkler with FULLJET spray nozzles (inch sizes of 1/8, 2/8, and 3/8). The main parameters of the rain-wind tunnel test are shown in Table 1.

As shown in Figure 5, the two vertical rectangle-shaped supported frames are specially designed for the test model which is suspended by springs. Each supported frame contains two pairs of springs orthogonal to each other. The spring system is designed to catch the in-plane and out-of-plane motions of test model. By adjusting parameters of the spring system, natural frequencies can be changed and controlled accordingly. Both of the supported frames can be easily adjusted to any height in the vertical-plane to match the required inclination angle α of the test model or adjusted to any positions in the horizontal plane to match the required wind yaw angle β of the test model. At both ends of the test model, two sets of accelerometers are mounted to measure the response signals. Three sets of pressure tap rings are arranged at the longitudinal locations and perpendicular to the axis of test model. Each set of the tap rings consists of 16 taps circumferentially, and the time-varying surface pressure on all taps gives an instantaneous sectional fluid force within the tap ring section. A large number of tubes attached to the pressure taps have obvious effects on the motions of the test model. In the study, the oscillations of the test model are measured using accelerometers before sticking the pressure

TABLE 1: Parameters of the rain-wind tunnel test.

Wind velocity U (m/s)	Rainfall intensity (mm/h)	Yaw angle (°)	Test model	Turbulence intensity
$U < 6$	0		1.8 m (Length)	
$6 \leq U \leq 10$	2.5	$0°$	40 mm (Diameter)	7%
$10 < U \leq 18$	8	$30°$	0.2% (damping	
$U > 18$	16		ratio)	

(a)

(b)
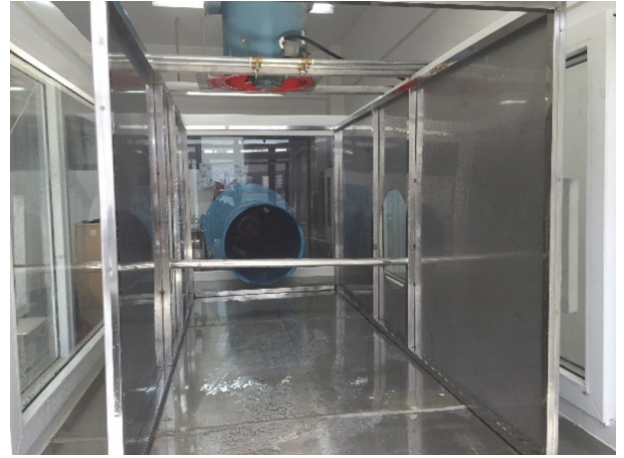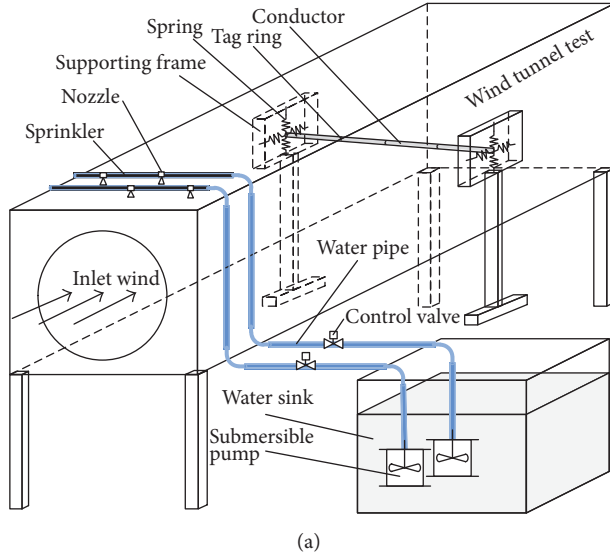
FIGURE 4: Experimental set-up of rain-wind tunnel test: (a) schematic of rain-wind experimental set-up and (b) photograph of rain-wind tunnel test with spray nozzles.

taps on the surface of the test model. The structural damping ratio is 0.2% for the case with zero wind velocity. As droplets hit the pressure tabs could lead to an obvious change in pressure, the data processing must exclude this type data.

At first, the drag and lift coefficients with the fixed test model segment are measured, and then the dynamic motions of the test model segment with the supporting of springs are obtained else. The lift and drag coefficients of the test model versus attack angle φ, at a yaw angle of $30°$, vary with different values of the rainfall intensities (Figure 6). At the rainfall rates of 8 mm/h and 16 mm/h, it is seen that when φ is near $69°$ the derivative of lift coefficients have a sudden change from a positive value to a negative one whereas the derivative of drag coefficients has a sudden change from a positive value to a negative one. This is because the rivulets are sufficient to form within the rainfall rates of 8 mm/h and 16 mm/h and the wind velocity of about 10 m/s. Moreover, the upper rivulet reaches critical angle that causes the boundary layer to trip, thus influencing the separation points of the test model on the upper side. At the rainfall rate of 2.5 mm/h, when $\varphi \approx 69°$ the derivative of lift coefficient gets a negative value whereas the derivative of drag coefficient almost has no change. The reason why the derivative of drag coefficient at the rainfall rate of 2.5 mm/h differs from those at the rainfall rates of 8 mm/h and 16 mm/h is that the rainfall rate of 2.5 mm/h is insufficient

to form the rivulets. Furthermore, the drag coefficients drop sharply and the lift coefficients with negative slopes occur once φ is close to angle of $122°$ at the rainfall rates of 2.5 mm/h, 8 mm/h, and 16 mm/h. This is because, when $\varphi \approx 122°$, the wind velocity is about 40 m/s and $R_e \approx 2 \times 10^5$ which is very close to the critical Reynolds number range [24]. With further increasing of attack angle φ ($\varphi > 122°$), both the lift and the drag coefficients stay more or less constant at the rainfall rates of 2.5 mm/h, 8 mm/h, and 16 mm/h. In order to compare with the no rainfall condition, the lift and drag coefficients of the test model at the rainfall rate of 0 mm/h are introduced in this study else. From the comparison of these curves, it can be found that when φ is about $69°$, the derivative of lift coefficient within the rainfall condition of 0 mm/h is nearly constant which is distinctly different from those within the rainfall conditions of 8 mm/h and 16 mm/h. Moreover, the derivative of lift coefficient gets a negative value while the derivative of drag coefficient almost remains unchanged. The possible reason why the lift and drag coefficients of no rainfall (0 mm/h) are different from those of the rainfall condition (2.5 mm/h, 8 mm/h, and 16 mm/h) is maybe the decrease in the surface roughness of the test model due to rainfall.

See the upper rivulet equilibrium position γ versus wind velocity U at the rainfall rates of 8 mm/h and 16 mm/h in Figure 7. When $U < 6$ m/s, there is no rivulet occurring
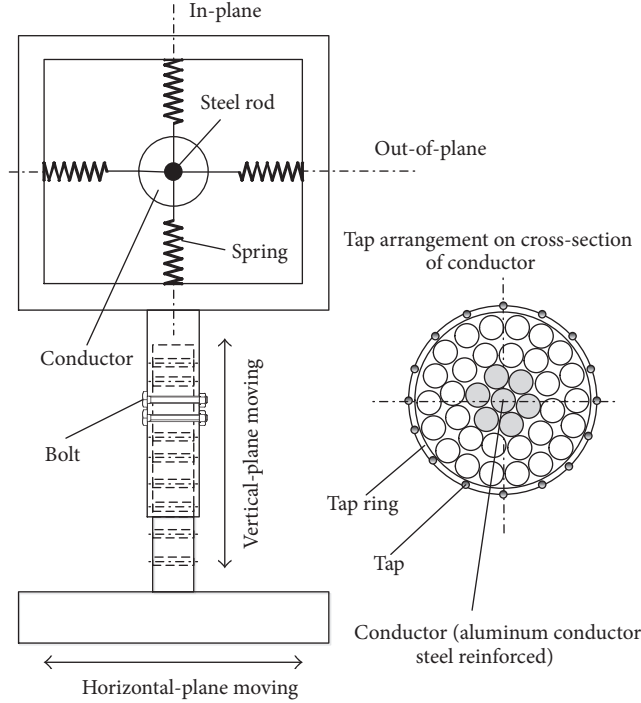
FIGURE 5: Schematic of vertical rectangle-shaped supported frame and taps arrangement on cross-section of the test model.
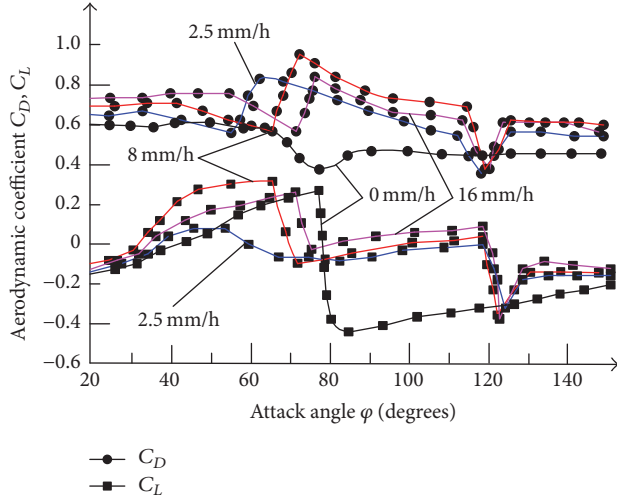

FIGURE 6: Aerodynamic coefficients versus attack angle of φ (when $\beta = 30°$).

on the surface of test model. When $7\,\text{m/s} \leq U \leq 10\,\text{m/s}$, the upper rivulet is formed and oscillates around itself at an equilibrium position of $15° \leq \gamma \leq 25°$ ($\varphi \approx 69°$) which is the separation point on the upper side of the test model. With further increasing of wind velocity, when $10\,\text{m/s} \leq U \leq 18\,\text{m/s}$, the upper rivulet equilibrium position remains almost constant. Furthermore, when $U > 18\,\text{m/s}$, the strong wind has a deteriorating trend on the rivulets and the upper rivulets are no longer there.
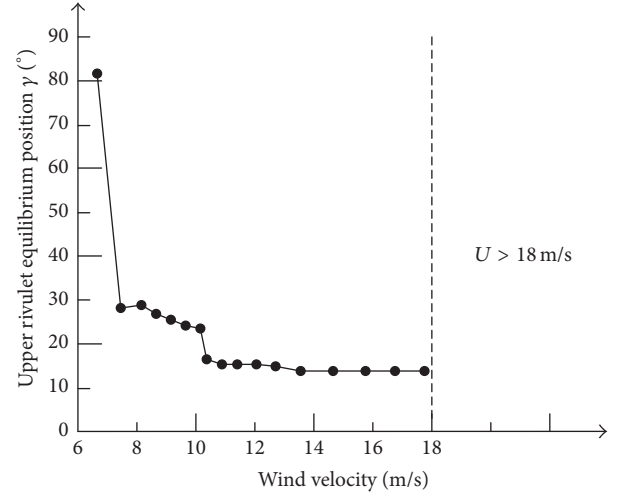
FIGURE 7: Upper rivulet equilibrium position γ versus wind velocity U.

4. Numerical Studies

To know the characteristics of rainfall in the wind fields of downbursts and their effects on dynamic responses of the high-voltage conductors, ±800 kV high-voltage transmission tower-line structures are taken as an example to carry out numerical studies in this section. The main structural parameters of the typical transmission tower-lines structures are shown in Table 2.

It is easy to find that the range of these typical towers' height is about 190 m~250 m and the span range of the tower-lines is 500 m~2100 m. Accordingly, the observing point of the high-voltage conductors may occur at any height (18 m~250 m) and any radial distance from the downburst center. Thus, it is necessary to calculate characteristics of rainfall in the wind fields of a downburst and the effects of the rainfall rates, the velocity profiles, and the rivulets on the motions of the high-voltage conductors.

4.1. Raindrop Velocity in the Wind Field of a Downburst. To simplify the analysis, we assume that the raindrops are uniformly distributed in the wind field of downbursts, which impact on the observing point of the high-voltage conductor with a yaw angle. Raindrop radius generally varies from 0.25 mm to 2.5 mm, which obeys the Marshall-Palmer exponential size distribution. In this section, 6 discrete radiuses are used to express the whole continuous distributed radius of rainfall as shown in Table 3.

Commonly accepted assumption of the raindrops' velocities in horizontal direction equal to wind velocity in boundary wind field is no longer appropriate for a nonuniform, sharper variable wind field of the downburst with the height. In this study, the observing point of the high-voltage conductor is selected at the radial distance of R_b where the maximum horizontal velocity occurs, and U_y is described by the vertical profile of Vicroy model $V(y)$. U_x and U_z are the functions of the horizontal wind velocity of downburst $V_y(R)$ and the downburst translation v_t.

TABLE 2: Main structural parameters of the typical tower-lines structures.

No	(1)	(2)	(3)	(4)
L (m)	2580	3401	2718	1985
Sp (m)	500-1580-500	840-1750-856	509-1733-476	518-2052-415
T (m)	191	201	201	246
Su (kN)	6×420	6×420	6×420	6×550
St (kN)	6×550	6×550	6×550	6×550
M (m)	18	18	18	18
D (mm)/(kg/m)	39.58/4.1	39.58/4.1	39.58/4.1	39.58/4.1

Note. L: length between two strain towers; Sp: span; T: tower height; Su: suspension insulator string; St: strain insulator string; M: minimum clearance; D: diameter/mass per unit length.

TABLE 3: The distributed radiuses of rainfall.

D_r (mm)	R_r (mm)	V_v (m/s)
0.25	0~0.35	1.96
0.5	0.35~0.75	3.85
1.0	0.75~1.25	6.49
1.5	1.25~1.75	7.98
2.0	1.75~2.25	8.76
2.5	2.25~3.0	9.15

Note. D_r: distributed radius; R_r: range of radius; V_v: vertical velocity.

TABLE 4: The raindrop's loads at different heights.

Load (N)	Radius (mm)					
	0.25	0.5	1.0	1.5	2.0	2.5
Height of 5 m	0.01	0.02	0.09	0.30	0.56	0.73
Height of 20 m	0.24	0.92	4.08	7.60	16.12	20.48
Height of 35 m	0.78	2.07	11.14	26.05	48.47	50.11
Height of 50 m	1.16	1.98	16.71	41.66	64.48	73.93
Height of 65 m	1.38	4.95	21.26	42.48	79.52	99.13
Height of 80 m	1.57	5.75	25.75	42.78	100.75	102.76
Height of 90 m	0.89	2.54	7.66	8.81	13.94	7.96
Height of 100 m	0.67	1.89	5.36	5.82	6.83	4.55
Height of 110 m	0.44	1.11	2.77	2.51	2.52	0.88

Figure 8 shows the profile of Vicroy model $V_r(y)$, obtained by using (4). By the iterative computing with (7), the horizontal velocity of the raindrop can be calculated from its trajectory. Because R_e is the function of λ, the trajectory will be different for raindrop radius. Accordingly, the horizontal velocity of the raindrops will vary with different radius at a certain height. It is seen that at the near height y of 80 m, the horizontal velocities of the raindrops have a sudden change from the values lower than that of downburst wind to the values larger than the velocity of downburst wind. The reason for this sudden change can be explained by the fact that the horizontal velocity of the downburst wind increases with the decreasing of the height ($y > 80$ m); the momentum of the raindrop in the former height must be smaller than that in the current height as the raindrop falls downwards. Moreover, once the raindrops fall down lower than the height of 80 m, the horizontal velocity of the downburst wind decreases with the decreasing of the height and the momentum of the raindrop in the former height must be larger than that in the current height.

4.2. Horizontal Loads of Raindrops and Pressures of Wind-Driven Rain Acting on the High-Voltage Conductor per Unit Length. The terminal velocities of raindrops, in boundary layer wind field, are usually taken as vertical velocities of the raindrops when close to transmission tower-line system. However, the horizontal loads of raindrops in the wind fields of a downburst are very complex, which are related to the raindrop sizes, radial distances, and heights. To know the raindrop's horizontal loads, 6 sets of loads of raindrops are created to represent the whole continuous loads of raindrops. Based on (12), the load of raindrop with different heights is obtained, at the radial distances of R_b (shown in Table 4).

By the comparison of these data, it can find out that the horizontal load of a raindrop increases with the increasing of the height ($0 \text{ m} < y \leq 80 \text{ m}$), whereas the horizontal load of a raindrop decreases with the increasing of the height ($y > 80$ m). The reason why the horizontal load has such a change is that the peak wind velocity of a downburst occurs at the range of $y \approx 80$ m, but out of this range the wind velocity of a downburst drops rapidly. Furthermore, at the same height, the larger the radius is, the more impact the load has.

Based on (14), the pressures of wind-driven rain acting on windward facade of the conductor per unit length with different values of the rainfall intensity (8 mm/h, 16 mm/h, and 32 mm/h) are calculated (Figure 9). By the comparison of these curves, it can be found that the pressure of wind-driven rain acting on windward facade of the conductor increases almost linearly with the increasing of the wind velocity. Furthermore, the higher the rainfall rates, the more the pressure of wind-driven rain acting on the windward facade of the conductor. These results can be explained by the fact that the velocity of raindrops is determined by the wind velocity, and the total mass of raindrops in per unit volume increases with the increasing of the rainfall intensity.

Based on (4) and (14), the ratio of the downburst wind-rain pressure to the downburst wind pressure on the windward facade of the conductor is calculated, with the wind velocity of the downburst (Figure 10). P_w is the pressure of the downburst wind-driven rain and P_r is the pressure of the downburst wind, respectively. By the comparison of these
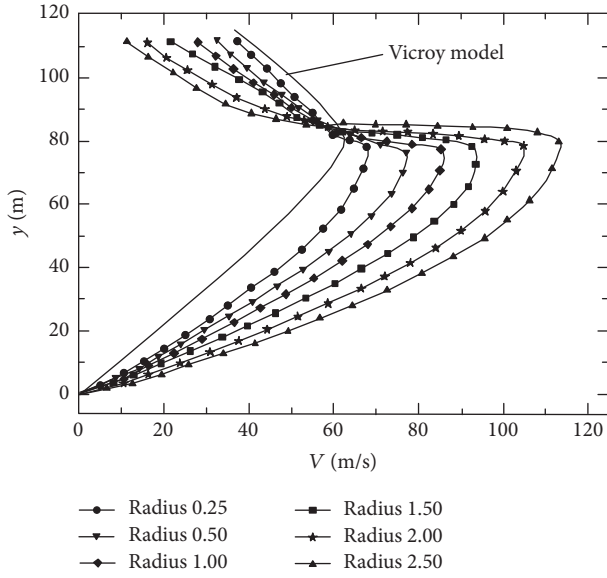
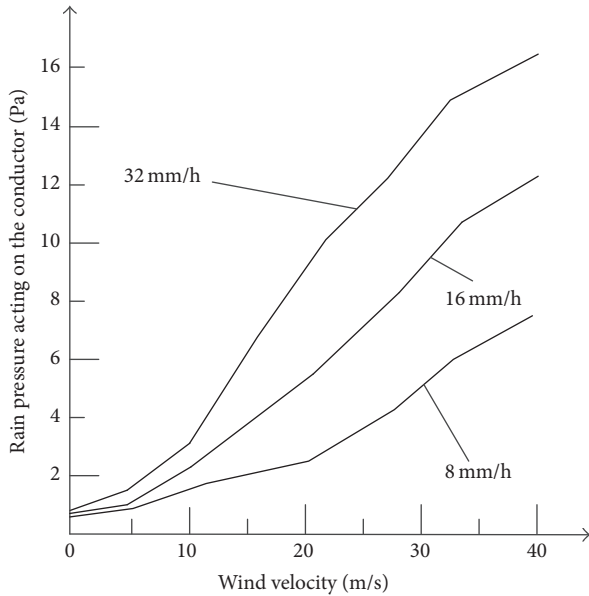FIGURE 8: Horizontal velocity of raindrop with different radius.

FIGURE 9: Rain-pressure on windward facade of the conductor versus wind velocity.

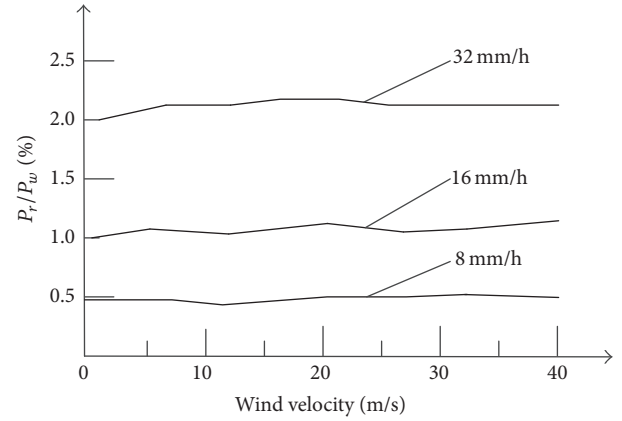
FIGURE 10: Ratio of the rain-pressure to the wind pressure on windward facade of the conductor.

4.3. Effect of Rainfall Density on Motion of the High-Voltage Conductor. The downburst often occurs suddenly and moves randomly; for those typical tower-lines structures, it may encounter with the high-voltage conductors at any heights or at any radical distances. To simplify the analysis, only the effects of rainfall density on the motions of the high-voltage conductors are discussed. It should be noted that the load variation in space due to the wind field and/or rainfall is very complex, and the dynamic behavior of the high-voltage conductors could be exaggerated enormously when neglecting the variation in space (full correlated load). The key parameters of the transmission lines are defined as follows: the diameter is 39.58 mm, the mass per unit length 4.1 kg/m, the elasticity coefficient 96.8 kN/mm^2, the tension force 160 kN, structural damping ratio 0.2%, and air density 1.25 kg/m^3. The original natural frequency and damping ratio of the high-voltage conductor are measured to be 0.98 Hz and 0.2%, respectively.

For the purposes of comparison, the span is defined to be 450 m. The drag coefficient and lift coefficient in (21) with respect to φ are fitted by the first three terms of Taylor's series. The span is discretized by the finite element method [14] and then be applied to (21) with the central difference algorithm. By calculation, in-plane vibration amplitudes of the conductor versus wind velocity and out-of-plane vibration amplitudes of the conductor versus wind velocity are obtained, as shown in Figures 11 and 12, respectively.

At the rainfall rates of 8 mm/h and 16 mm/h, the in-plane vibration amplitudes of the conductor get peak values for the wind velocity of 10 m/s whereas the in-plane vibration amplitude of the conductor just has a little increase for the rainfall rate of 2.5 mm/h. These results can be explained that the rainfall is sufficient to form the upper rivulet for 8 mm/h and 16 mm/h but insufficient to form the upper rivulet for 2.5 mm/h and 0 mm/h, and the wind velocity of 10 m/s is the critical velocity at which the rain-wind vibrations often occur. By comparing with the numerical results reported in wind effects on structures [24], it has relatively high vibration amplitude by 14%. This difference may be due to the different values of elastic elasticity coefficient and the
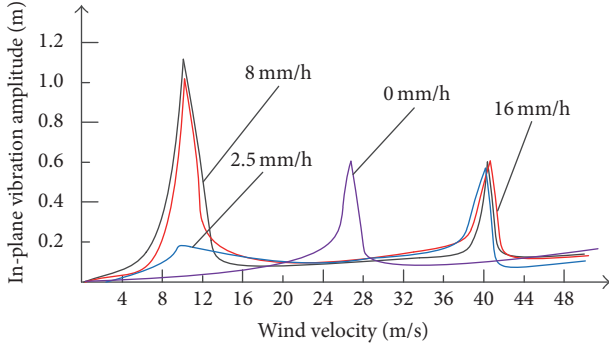
curves, it can be found that the ratio of the rain-pressure to the wind pressure on the windward facade of the high-voltage conductor is approximately constant with the increasing of the wind velocity, but it has different ratios with different rainfall rates (0.5% at rainfall rate of 8 mm/h, 1.1% at rainfall rate of 32 mm/h, and 2.2% at rainfall rate of 32 mm/h). The reason why the ratio of the downburst wind-rain pressure and the downburst wind pressure on windward facade of the conductor is almost constant is that the velocities of raindrops are proportional to the wind velocity. Accordingly, the rainfall pressure on the high-voltage conductor in the downburst condition is not very significant.

FIGURE 11: In-plane vibration amplitude of the conductor versus wind velocity.

FIGURE 12: Out-of-plane vibration amplitude of the conductor versus wind velocity.

impinging loads of raindrops. When wind velocity is at the range of 40 m/s, the in-plane vibration amplitudes of the conductor get larger values for the rainfall rates of 2.5 mm/h, 8 mm/h, and 16 mm/h else. This result is in good agreement with the field measurements at the wind velocity of 30 m/s $\leq$ U < 42 m/s [25]. At the rainfall rate of 0 mm/h, however, the conductor gets the largest in-plane vibrations when wind velocity is 26 m/s. This difference can be explained that the critical Reynolds number range of the dry conductor (at the rainfall rate of 0 mm/h) is lower than that of wet conductor (at the rainfall rates of 2.5 mm/h, 8 mm/h, and 16 mm/h).

At the rainfall rates of 8 mm/h and 16 mm/h, the out-of-plane vibration amplitudes of the conductor increase with the increasing of wind velocity and get maximum values at the critical wind velocity of 10 m/s. However, for the rainfall rate of 2.5 mm/h, the in-plane vibration amplitude only has a little increase with the increasing of wind velocity. These results can be explained that the rainfall is sufficient to form the upper rivulet for 8 mm/h and 16 mm/h, while it is insufficient to form the upper rivulet for the rainfall rate of 2.5 mm/h. After having a sudden change, the out-of-plane vibration amplitudes of the conductor increase with the increasing of wind velocity up to 19 m/s. With the further increasing of wind velocity, the out-of-plane vibration amplitudes of the conductor are nearly constant. Moreover, at the critical velocity of 40 m/s, there are sharp drops of the out-of-plane vibration amplitudes occurring. These results can be explained that when the wind velocity is at the range of 40 m/s, $R_e \approx 2 \times 10^5$ which is close to the critical Reynolds number range. At the rainfall rate of 0 mm/h, the out-of-plane vibration of the conductor increases with the increasing of wind velocity up to 15 m/s. With the further increasing of wind velocity, the amplitude vibration nearly keeps constant whereas a sharp drop occurs at the critical wind velocity of 26 m/s. This result can be explained by the fact that the drag coefficient increases with the increasing of wind velocity (U < 15 m/s), whereas it no longer increases within the wind velocity range of 15 m/s $\leq U$ < 26 m/s and suddenly drops at the critical wind velocity of 26 m/s.

Calculated results that both in-plane and out-of-plane vibrations of the conductors are basically consistent with simulated results [26], an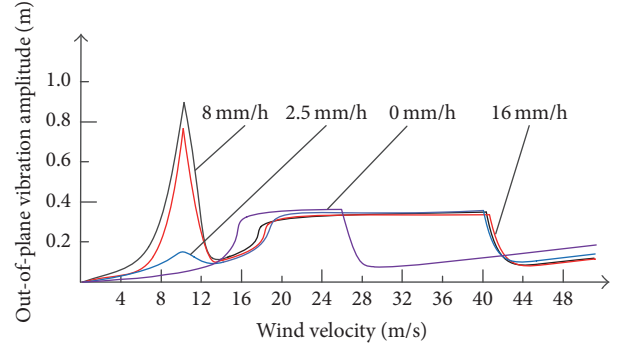d the only difference is the relatively high amplitude of vibration about 2%. This difference can be explained by fact that the radius and mass per unit length of the conductor in this study are larger than that applied in the previous study, even though the span is equal.

5. Conclusions

A preliminary research is carried out in this paper, to discuss the characteristics of rainfall in the wind field of the downburst and its effects on the motions of high-voltage transmission lines. Based on Vicroy model, the loads of raindrops and the pressures of wind-driven rain on the high-voltage conductor are calculated firstly. A downburst wind-rain induced vibration model is then proposed to calculate the effects of rainfall intensity on the motions of high-voltage conductors and verified by the comparison with the field measurements lastly.

(1) The raindrop velocity in the wind field of a downburst is obviously different from that of the boundary layer wind field;

(2) The horizontal load of a raindrop increases with the increasing of height (0 m < $y \leq$ 80 m), whereas it will decreases with the increasing of height (y > 80 m);

(3) The rainfall pressure on the high-voltage conductor, under a downburst condition, is not very significant;

(4) When wind velocity is at the range of 10 m/s, for 8 mm/h, and 16 mm/h, rainfall sufficient to form the upper rivulet and rain-wind vibration often occurs;

(5) When wind velocity is at the range of 40 m/s, the in-plane vibration amplitudes of the conductor get larger values for the rainfall rates of 2.5 mm/h, 8 mm/h, and 16 mm/h.

In this paper, a preliminary analysis about the effects of rainfall on a single high-voltage conductor under the downburst conditions is studied. A downburst often occurs suddenly and moves randomly; it may encounter the high-voltage conductors at any heights or at any radical distances. Therefore, the future studies should further focus on the multiconductor and the whole of high transmission tower-line structures to clarify some phenomena observed from the field measurements or simulated wind tunnel tests.

Competing Interests

The authors declare that there is no conflict of interests regarding the publication of this paper.

Acknowledgments

References

[1] T. T. Fujita, *The Downburst: Microburst and Macroburst, Report of Projects NIMROD and JAWS*, University of Chicago, 1985.

[2] A. Y. Shehata and A. A. El Damatty, "Behaviour of guyed transmission line structures under downburst wind loading," *Wind and Structures*, vol. 10, no. 3, pp. 249–268, 2007.

[3] D. Dempsey and H. B. White, "Winds wreak havoc on lines," *Transmission and Distribution World*, vol. 48, no. 6, pp. 32–42, 1996.

[4] E. Savory, G. A. R. Parke, M. Zeinoddini, N. Toy, and P. Disney, "Modelling of tornado and microburst-induced wind loading and failure of a lattice transmission tower," *Engineering Structures*, vol. 23, no. 4, pp. 365–375, 2001.

[5] A. Y. Shehata, A. A. El Damatty, and E. Savory, "Finite element modeling of transmission line under downburst wind loading," *Finite Elements in Analysis and Design*, vol. 42, no. 1, pp. 71–89, 2005.

[6] H. Aboshosha and A. E. Damatty, "Effective technique to analyze transmission line conductors under high intensity winds," *Wind and Structures*, vol. 18, no. 3, pp. 235–252, 2014.

[7] S. Liang, L. Zou, D. Wang, and H. Cao, "Investigation on wind tunnel tests of a full aeroelastic model of electrical transmission tower-line system," *Engineering Structures*, vol. 85, pp. 63–72, 2015.

[8] Y. Eguchi, N. Kikuchi, K. Kawabata, T. Yukino, and Y. Ishikubo, "Drag reduction mechanism and aerodynamic characteristics of a newly developed overhead electric wire," *Journal of Wind Engineering and Industrial Aerodynamics*, vol. 90, no. 4-5, pp. 293–304, 2002.

[9] N. Kikuchi, Y. Matsuzaki, T. Yukino, and H. Ishida, "Aerodynamic drag of new-design electric power wire in a heavy rainfall and wind," *Journal of Wind Engineering and Industrial Aerodynamics*, vol. 91, no. 1-2, pp. 41–51, 2003.

[10] H.-N. Li, S.-Y. Tang, and T.-H. Yi, "Wind-rain-induced vibration test and analytical method of high-voltage transmission tower," *Structural Engineering and Mechanics*, vol. 48, no. 4, pp. 435–453, 2013.

[11] X. Fu, H.-N. Li, and Y. B. Yang, "Calculation of rain load based on single raindrop impinging experiment and applications," *Journal of Wind Engineering and Industrial Aerodynamics*, vol. 147, pp. 85–94, 2015.

[12] Y. Wei, Q. Yang, X. Xiong, J. Wang, and S. Weng, "Short-term reliability evaluation of transmission system under strong wind and rain," *Journal of Power and Energy Engineering*, vol. 2, no. 4, pp. 665–672, 2014.

[13] C. Zhou, Y.-P. Liu, and Y.-W. Song, "Mechanism and modeling of rain-wind induced in-plane vibration on high-voltage transmission line," *Journal of Mechanical Science and Technology*, vol. 28, no. 4, pp. 1175–1180, 2014.

[14] C. Zhou, Y. B. Liu, and X. M. Rui, "Mechanism and characteristic of rain-induced vibration on high-voltage transmission line," *Journal of Mechanical Science and Technology*, vol. 26, no. 8, pp. 2505–2510, 2012.

[15] M. R. Hjelmfelt, "Structure and life cycle of microburst outflows observed in Colorado," *Journal of Applied Meteorology*, vol. 27, no. 8, pp. 900–927, 1988.

[16] L. Chen and C. W. Letchford, "A deterministic-stochastic hybrid model of downbursts and its impact on a cantilevered structure," *Engineering Structures*, vol. 26, no. 5, pp. 619–629, 2004.

[17] J. D. Holmes and S. E. Oliver, "An empirical model of a downburst," *Engineering Structures*, vol. 22, no. 9, pp. 1167–1172, 2000.

[18] E. C. C. Choi, "Numerical modelling of gust effect on wind-driven rain," *Journal of Wind Engineering and Industrial Aerodynamics*, vol. 72, no. 1-3, pp. 107–116, 1997.

[19] Y. Mualem and S. Assouline, "Mathematical model for rain drop distribution and rainfall kinetic energy," *Transactions of the American Society of Agricultural Engineers*, vol. 29, no. 2, pp. 494–500, 1986.

[20] J. S. Marshall and W. M. Palmer, "The distribution of raindrops with size," *Journal of Meteorology*, vol. 5, no. 4, pp. 165–166, 1948.

[21] H. Yamaguchi, "Analytical study on growth mechanism of rain vibration of cables," *Journal of Wind Engineering and Industrial Aerodynamics*, vol. 33, no. 1-2, pp. 73–80, 1990.

[22] A. Bosdogianni and D. Olivari, "Wind-and rain-induced oscillations of cables of stayed bridges," *Journal of Wind Engineering and Industrial Aerodynamics*, vol. 64, no. 2-3, pp. 171–185, 1996.

[23] M. Gu and L. Huang, "Theoretical and experimental studies on the aerodynamic instability of a two-dimensional circular cylinder with a moving attachment," *Journal of Fluids and Structures*, vol. 24, no. 2, pp. 200–211, 2008.

[24] E. Simiu and R. H. Scanlan, *Wind Effects on Structures: Fundaments and Applications to Design*, John Wiley & Sons, New York, NY, USA, 1996.

[25] C. Zhou and Y. Liu, "Analytical model of rain-wind induced vibration of high-voltage transmission line," *Advances in Mechanical Engineering*, vol. 2014, Article ID 638653, 9 pages, 2014.

[26] Q. Xie, Y. Zhang, and J. Li, "Investigation on tower collapses of 500 kV Renshang 5237 transmission line caused by downburst," *Power System Technology*, vol. 30, no. 10, pp. 59–64, 2006.

Research Article

Vibration Control of Tower Structure with Multiple Cardan Gyroscopes

Haoxiang He,[1,2] Xin Xie,[1] and Wentao Wang[1]

[1]*Beijing Key Laboratory of Earthquake Engineering and Structure Retrofit, Beijing University of Technology, Beijing 100124, China*
[2]*Beijing Collaborative Innovation Center for Metropolitan Transportation, Beijing 100124, China*

Correspondence should be addressed to Haoxiang He; hhx7856@163.com

Tower structure is sensitive to hurricane and earthquake, and it is easy to generate large deflection and dynamic response. The multiple cardan gyroscope has two rotational degrees of freedom, which can generate strong moments to constrain the two horizontal orthogonal deflections if the rotor operates in high speeds, so the structural dynamic responses can be decreased. Hence, the method of dynamic control of the tower structure under wind load and earthquake action is proposed by using the multiple cardan gyroscopes as the dampers. The dynamic mechanism and the fixed axis principle of the multiple cardan gyroscope are introduced, and the dynamic equation of the gyroscope is established. The damping mechanism of the gyroscope is also described. For the tower structure equipped with the multiple cardan gyroscope dampers, the multidimensional control equation considering torsion effect is established, and the equivalent state space equation is presented. Taking a TV Tower with a number of gyroscope dampers as an analysis example, the structural dynamic responses and damping performance under fluctuating wind loads and earthquake action is studied. The results show that the multiple cardan gyroscope dampers with suitable parameters can effectively decrease the structural vibration in horizontal directions and torsional direction.

1. Introduction

Tower structure is a type of slender and lofty structure, whose altitude is much larger than its width, often by a significant margin. Since the cross section of tower structure is relatively smaller, the lateral load plays an important role on the structural dynamic responses [1, 2]. Because the form of tower structure is tall and beautiful, it is widely used in the field of communication facilities, power facilities, chemical engineering, and so forth. Compared with the common building structure, the horizontal stiffness of tower structure is weak, so it is sensitive to hurricane and earthquake, and it is easy to generate large static deflection and dynamic response [3]. Therefore, the research on the dynamic characteristics and vibration control of tower structure has been increasingly emphasized.

In order to realize the hazard protection of structure, the tower structures should have enough capacities to dissipate energy. The dynamic performance of the traditional tower is improved by enhancing the design parameter such as stiffness and ductility, but the structure designed by normal methods still has not enough ability during strong earthquakes. Therefore, the traditional design methods have been improved by new technology such as damping control or shock absorbers. There are various means to realize the structural damping control. As one of the most effective tool of passive structural vibration control technologies, seismic isolation enables the building structure to survive a potentially devastating seismic impact through isolation bearings with large damping and flexibility [4, 5]. Based on the mechanism of tuned vibration control, the tuned mass damper is usually installed on the top of the structure to reduce the amplitude of mechanical vibrations [6, 7]. In some frame building structures, the energy dissipation braces which connect the two consecutive layers of building and incorporating suitable devices are purposely designed to dissipate a large amount of energy [8]. With the same features and functions, the fluid viscous damper and the metallic damper are also used in various structures [9, 10].

Due to the fact that the tower structure is prone to overturn if the isolation bearings are installed on the base, the seismic isolation technology is not the best option [11]. Because of the limited space, large dampers are not suitable for installation in the tower structure. The current devices mainly used in the vibration control of tower structures include viscous damper, tuned mass damper, and tuned liquid damper. The mechanism of these vibration reduction devices is definite, and it can achieve certain effect of vibration control through optimization analysis and standard production and installation. The tower structure vibration is mainly based on the first-order mode, so the optimal control position is usually on the top. However, the top location of the tower is flexible and internal space is limited, and the actual applicability of tuned damper is usually difficult to achieve owing to the huge volume of the damper [12]. To solve the above problems, it is necessary to be develop new type of the damping devices to effectively protect the safety of the tower structure in other ways.

Gyroscope is a kind of mechanical device to judge and keep directions, which is designed based on the theory of conservation of angular momentum [13]. The gyroscope is mainly composed of gyro rotor, rotation shaft, frame, and other accessories. When the gyro rotor on the axial center rotates at high speed, the inertia force and the resistance force will be produced, and the rotation axis of the gyro rotor points to a fixed direction, this property is known as fixed axis [13–15]. Gyroscope is widely applied in aerospace, microelectronics, and mechanical control, and the effect is notable, especially when the active control scheme is adopted [16–18]. If the gyroscopes are installed on the building structure, it is apparent that the gyroscopes will generate restoring force and flexural moment to keep the initial direction when the structures vibrate under external dynamic actions, and the gyroscopes play the role of damper and the control effect will be obvious if the gyro rotor rotates in higher speed.

Wang and Liu [19] have proposed the method of using the single degree of freedom gyroscope to control the structure random vibration, but this method is simple and cannot realize the multidirection vibration reduction. Moon et al. [20] have investigated the effectiveness of the gyroscope system for active seismic protection of flexible structures employing LQG control algorithms, and the simulation results show that gyroscope system has the possibility of reducing the vibration. However, only the simple building structure and active control is studied in above research, it is necessary to intensively study the performance of gyroscope damper for vibration reduction on tower structures or high-rise structures, and the passive control effect should also be verified.

In view of the characteristics of the gyroscope and previous research results, multiple cardan gyroscope is introduced as a new damper to reduce the bidirectional horizontal vibration. When the structure is subjected to wind or strong earthquake, the internal rotor damper can rotate at high speed, the fixed axis gyro can provide the reverse moment to decrease the two horizontal deflection of the structure, so the overall damper will dissipate the external dynamic energy, and then the safety of the structure is improved.
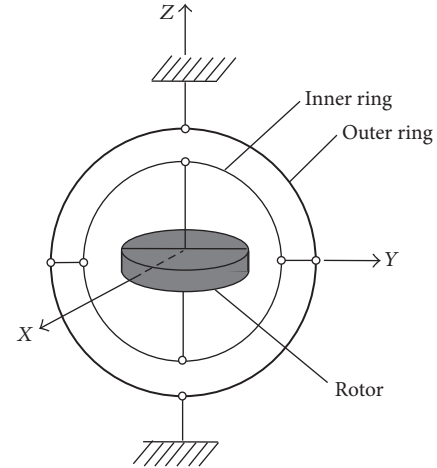
(a) Prototype and composition of gyroscope
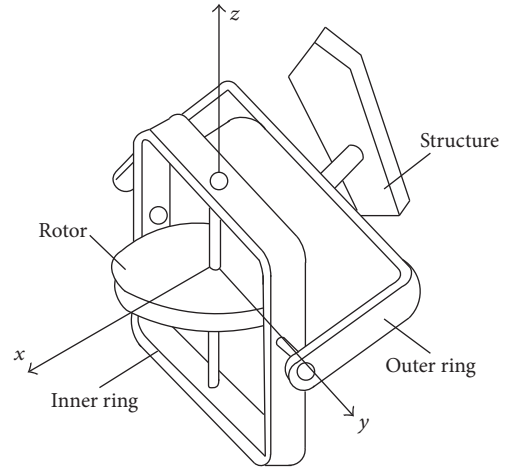
(b) gyroscope damper

FIGURE 1: Composition diagram of multiple cardan gyroscope.

In this paper, the mechanics principle of the multiple cardan gyroscope, that is, gyroscope with two DOFs, is introduced, and the dynamic control equations of the structure with the multiple cardan gyroscopes are established. The vibration reduction effect of the multiple cardan gyroscope damper on tower structure is studied. The results show that the reasonably arranged gyro dampers can effectively reduce the horizontal and torsional responses of the tower structure when it is subjected to wind and earthquake.

2. Gimbal Gyroscope Mechanics and Gyroscope Damper

The multiple cardan gyroscope mainly comprises a gimbal bracket and a rotor, as shown in Figure 1. The gimbal bracket is composed of an outer ring and an inner ring, and it is the mechanical device used for supporting the gyroscope rotor. The outer ring is installed on the supporter or the structure, and the inner ring is installed on the outer ring, and the rotor or other supporting bodies are arranged on the inner ring.

The rotary axis of the outer ring, the inner ring, and the rotor is delivered at a point O, namely, the center of the gimbal bracket support. The outer ring, inner ring, and rotor around their axis of rotation angle α, β, and ψ are cardan angle, and the outer ring, inner ring, and the rotor are, respectively, the physical coordinate systems e^1, e^2, and e^3. The e^2 is usually called the LecA coordinate system. It is the principal axis of the inner ring and the axis symmetric rotor but does not participate in the high-speed rotation of the rotor; therefore, e^2 is often used as the reference coordinate system on the dynamic calculation.

From the above basic knowledge, it is clear that the two-degree-of-freedom gyroscope mainly consists of three rigid bodies. The first one is the external ring with one-rotational-degree-of-freedom, the motion can be represented by a generalized angle coordinate which rotates around the outer ring. The second rigid body is the internal ring with two rotational degrees of freedom, and its movement can be described by two generalized coordinates which rotate around the external ring axis and the internal ring axis, respectively. The third rigid body is the rotor with three-rotational-degree-of-freedom, the corresponding motion can be represented by three generalized coordinates that rotates around the rotation axis, external ring axis, and the internal ring axis, respectively.

According to the property of fixed axis, a multiple cardan gyroscope can be used as a damper to control the structural deflection and dissipate energy. Thus, the cardan gyroscope damper consists of a gyro outer ring which can rotate around the horizontal axis of structure and a gyro inner ring rotates around the horizontal axis which is orthogonal to the above-mentioned horizontal axis, the gyro rotor which rotates by the electric power and the electric motor. There are one internal ring and one external ring, so the gyroscope in the damper has two rotational degrees of freedom. Hence, the gyro device can rotate in a certain angular velocity steadily under dynamic action, trying to keep its axis relative to the inertial space azimuth invariant properties, and the resistance moment can be generated in order to counteract the two types of horizontal displacement, which can decrease the structural horizontal displacement or deflection. The construction diagram of the cardan gyroscope damper is shown in Figure 1.

In order to investigate the effectiveness of the gyroscope damper in the vibration reduction, the dynamic equation should be established and the dynamic analysis can be carried out. In view of this demand, the gyroscope mechanics are firstly introduced and discussed.

For a multiple cardan gyroscope, the inertial reference system is set as e^0, and the principal axis coordinate system of the outer ring, the inner ring, and the rotor is set as e^1, e^2, and e^3, respectively; then the rotary shafts of the outer ring, the inner ring, and the rotor are expressed as e_1^1, e_2^2, and e_3^3, respectively. Due to the fact that the rotor is an axial symmetry, the symmetry axis is coincident with e_3^3 or e_3^2, which is called the polar axis of the gyroscope. The rotational angular velocity of each component can be expressed with cardan angle; that is, for the outer ring, $\omega_1 = \dot{\alpha} e_1^1$, for the
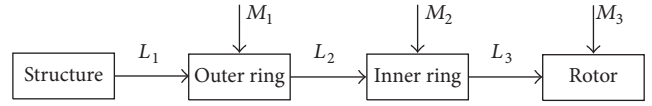

FIGURE 2: Composition diagram of multiple cardan gyroscope.

inner ring, $\omega_2 = \dot{\alpha} e_1^1 + \dot{\beta} e_2^2$, and for the rotor, $\omega_3 = \dot{\alpha} e_1^1 + \dot{\beta} e_2^2 + \dot{\varphi} e_3^2$.

The axis principal inertia moment of each component relative to the support center O is as follows: for the outer ring it is A_1, B_1, and C_1; for the inner ring it is A_2, B_2, and C_2; for the rotor it is A_3, B_3, and C_3.

As shown in Figure 2, the resultant moment relative to point O on each component is as follows: for the outer ring, the value is $M_1 + L_1 - L_3$; for the inner ring, the value is $M_2 + L_2 - L_2$; for the rotor, the value is $M_3 + L_3$.

According to the moment of momentum theorem, the dynamic equations when the rotor, the inner ring-rotor, and the outer ring-inner ring-rotor rotate around the rotary axis of the rotor, the inner ring, and the outer ring, respectively, are given by

$$C_3 \frac{d}{dt} (\dot{\varphi} + \dot{\alpha} \sin \beta) = M_{33} + L_{23}, \tag{1}$$

$$(B_2 + A_3) \ddot{\beta} + (A_2 + A_3 - C_2) \dot{\alpha}^2 \cos \beta \sin \beta - C_3 (\dot{\varphi} + \dot{\alpha} \sin \beta) \dot{\alpha} \cos \beta = M_{22} + M_{32} + L_{23}, \tag{2}$$

$$\frac{d}{dt} \left\{ \left[A_1 + C_2 + (A_2 + A_3 - C_2) \cos^2 \beta \right] \dot{\alpha} \right. \\ \left. + C_3 (\dot{\varphi} + \dot{\alpha} \sin \beta) \sin \beta \right\} = M_{11} + (M_{21} + M_{31}) \\ \cdot \cos \beta + (M_{23} + M_{33}) \sin \beta + L_{11}, \tag{3}$$

where M_{1j} ($j = 1, 2, 3$) and L_{1j} ($j = 1, 2, 3$) are the projection of M_1 and L_1 on e^1, and M_{2j}, M_{3j}, L_{2j}, and L_{3j} are the projection of M_2, M_3, L_2, and L_3 on e^2, respectively.

After the termination of the rotor drive, there are two kinds of steady-state motion, which are, respectively, corresponding to the two different constraint conditions of the driving motor, namely, the ideal constraint and the constant speed constraint. The driving moment of the former is balanced with the damping torque and the resultant force moment is zero; the latter maintains a constant speed of the rotor relative to the inner ring.

For the ideal constraint condition, the right item of (1) is zero, so the new equation can be obtained by the first integral method as

$$\dot{\varphi} + \dot{\alpha} \sin \beta = \omega_0, \tag{4}$$

in which the integral constant ω_0 is the steady value of the absolute speed of the rotor.

Substituting (4) into (2) and (3), the steady-state motion equation can be derived as follows:

$$\frac{d}{dt}\left[I\left(\beta\right)\dot{\alpha}+H_0\sin\beta\right]=M_1, \tag{5}$$

$$B\beta-\frac{1}{2}\dot{I}\left(\beta\right)\dot{\alpha}^2-H_0\dot{\alpha}\cos\beta=M_2, \tag{6}$$

where $I(\beta)=A_1+A_2+A_3+K\sin^2\beta$, $K=C_2-A_2-A_3$, $B=B_2+A_2$, $H_0=C_3\omega_0$, $M_1=M_{11}+(M_{21}+M_{31})\cos\beta+(M_{13}+M_{23})\sin\beta+L_{11}$, and $M_2=M_{22}+M_{32}+L_{22}$.

For constant speed constraints, a similar result can also be got, only the definition of K is modified as $K=C_2+C_3-A_2-A_3$.

Due to the stability of the high-speed rotating gyroscope, the rotational angular velocity of the universal may be written as

$$I\left(\beta\right)\ddot{\alpha}+\left(H_0\cos\beta\right)\dot{\beta}=M_1, \tag{7}$$

$$B\ddot{\beta}-\left(H_0\cos\beta\right)\dot{\alpha}=M_2. \tag{8}$$

If the deflection angle of outer ring α and the deflection angle of the inner ring β keep in a stable position α_0 and β_0, respectively, and the deviation values and the derivatives higher than the second can be ignored, (7) and (8) can be changed into a linear equation group

$$A\ddot{\alpha}+H\dot{\beta}=M_1, \tag{9}$$

$$B\ddot{\beta}-H\dot{\alpha}=M_2 \tag{10}$$

in which A and H are defined as $A=A_1+A_2+A_3+K\sin^2\beta_0$ and $H=H_0\cos\beta_0$.

If the rotor speed is very high and the moment of force changes slowly, the two-order derivatives $\ddot{\alpha}$ and $\ddot{\beta}$ can be omitted and (9) and (10) can be simplified as a first-order linear differential equation.

For the actual gyroscope damper, the principal moments of inertia of the outer ring, the inner ring, and the rotor which rotate the coordinate system of the base x-, y-, and z-axis are, respectively, J_{x0}, J_{y0}, J_{z0}, J_{x1}, J_{y1}, J_{z1}, J_{xR}, J_{yR}, and J_{zR}. When the rotor rotates with absolute high speed ω_0, the gyro angular momentum constant $H_0=J_zR_{\omega0}$, which means the rotor steady-state value of absolute angular momentum. Set α and β as the corner of outer frame and internal frame, according to the theory of moment of momentum, based on (9) and (10), the steady-state dynamic equation of gyroscope under ideal constraints is

$$\left[J_{x0}+J_{z1}+J_{zR}+\left(J_{x1}+J_{xR}-J_{z1}-J_{zR}\right)\cos^2\beta\right]\ddot{\alpha}$$
$$+\left(H_0\cos\beta\right)\dot{\beta}=M_x, \tag{11}$$

$$\left(J_{y1}+J_{xR}\right)\ddot{\beta}-\left(H_0\cos\beta\right)\dot{\alpha}=M_y. \tag{12}$$

When the outer frame and inner framework rotate at a certain rotating angular velocity, (11) and (12) can be simplified as

$$\left(H_0\cos\beta\right)\dot{\beta}=M_x, \tag{13}$$

$$-\left(H_0\cos\beta\right)\dot{\alpha}=M_y. \tag{14}$$

According to the above derivation and the characteristic of motion equations, it is clear that greater moment will be produced by increasing the rotational speed and the moments of inertia of the inner ring and the outer ring. If the rotational speeds of the outer ring and the inner ring increase, the effective resistance moment will increase and the displacement is reduced more dramatically according to the property of fixed axis of gyroscope. As the moments of inertia of the rings are related to the mass and the radius of gyration, the damping effect can be effectively enhanced if the mass and the radius of gyration increase. Since the radius of gyration is not easy to set to a larger value, the actual optimum values for control effect mainly include the rotational speed and the mass of the outer ring and the inner ring. The fixed axial moment provides the external force for structure to rebound to the initial equilibrium state and reduce the structural deformation. In addition, in the case of the total mass is constant, the torque value can be significantly enhanced only by increasing the gyro plane size or the rotation speed. Hence, the gyro damper is particularly suitable for installing on the top of the tower structure since it has larger outer space.

3. Dynamic Model of Structure with Gyroscope Dampers

In order to study the damping effect of the structure equipped with multiple cardan gyroscopes, the actual tower structure can be equivalent to a multidegree-of-freedom system with multiple lumped mass. It assumes that the gyro dampers are installed on the multipositions of the tower structure which has n equivalent lumped mass and the motion in two horizontal directions and around the vertical axis can be controlled. The dynamic equation of the structure system under multidimensional earthquake is given by

$$\mathbf{M\ddot{U}}+\mathbf{C\dot{U}}+\mathbf{KU}=-\mathbf{M\ddot{U}}_g\left(t\right)+\mathbf{F}\left(t\right) \tag{15}$$

in which, $\mathbf{M}$, $\mathbf{C}$, and $\mathbf{K}$ are the global mass matrix, the global damping matrix, and the global stiffness matrix of the dynamic system, respectively, and the dimension of all the matrix is all $3n\times 3n$. $\mathbf{U}=[\mathbf{U}_x,\mathbf{U}_y,\mathbf{U}_\theta]^T=\{u_{x1},\ldots,u_{xn},u_{y1},\ldots,u_{yn},u_{\theta1},\ldots,u_{\theta n}\}^T$, which is the displacement vector of the 3D structure system. x, y, and z represent one horizontal direction and the other orthogonal horizontal directions and the vertical direction. $\mathbf{\ddot{U}}_g(t)=[\mathbf{\ddot{U}}_{xg}(t),\mathbf{\ddot{U}}_{yg}(t),\mathbf{\ddot{\Phi}}_{\theta g}(t)]^T$, which is the dynamic loading or acceleration excitation. $\mathbf{F}(t)=\{0,\ldots,F_x(t),0,\ldots,F_y(t),0,\ldots,0\}^T$, which is the equivalent concentrated force of the moment of the multiple cardan gyroscopes, and the applied positions are the same as the locations of the gyro dampers.

Because the coupling damping matrix of the tower structure and the gyro dampers is not orthogonal, and it belongs to the nonclassical damping, so (13) cannot be decoupled directly by the real modal transformation method and the time history analysis cannot be carried out. To solve the above problems, the state space method can be adopted and the higher order ordinary differential equation of the

system can be transformed into one first-order differential equation in the composition of state variables by introducing adequate state vectors. First, the variable $\ddot{\mathbf{U}}_{ge}(t) = (\mathbf{I} - \mathbf{F}(t)/\mathbf{M}\ddot{\mathbf{U}}_g(t))\ddot{\mathbf{U}}_g(t)$ is defined, in which $\mathbf{I}$ is unit matrix. Hence, (15) can be rewritten as

$$\mathbf{M}\ddot{\mathbf{U}} + \mathbf{C}\dot{\mathbf{U}} + \mathbf{K}\mathbf{U} = -\mathbf{M}\ddot{\mathbf{U}}_{ge}(t). \tag{16}$$

Expressing $\mathbf{X} = \{\mathbf{U} \ \dot{\mathbf{U}}\}^T$ and $\{\mathbf{Y}\} = \{\mathbf{U} \ \ddot{\mathbf{U}}\}^T$ as the state vector of the system, then (14) can be rewritten as the state space equations as the following form:

$$\dot{\mathbf{X}} = \mathbf{A}\mathbf{X} + \mathbf{B}\ddot{\mathbf{U}}_{ge}(\mathbf{t}),$$
$$\mathbf{Y} = \mathbf{C}\mathbf{X} + \mathbf{D}\ddot{\mathbf{U}}_{ge}(\mathbf{t}), \tag{17}$$

where $\mathbf{A} = \begin{bmatrix} \mathbf{0} & \mathbf{I} \\ -\mathbf{M}^{-1}\mathbf{K} & -\mathbf{M}^{-1}\mathbf{C} \end{bmatrix}$, $\mathbf{C} = \begin{bmatrix} \mathbf{I} & \mathbf{0} \\ -\mathbf{M}^{-1}\mathbf{K} & -\mathbf{M}^{-1}\mathbf{C} \end{bmatrix}$, $\mathbf{B} = \mathbf{D} = \begin{bmatrix} \mathbf{0} \\ -\mathbf{I} \end{bmatrix}$.

In accordance with this method, after obtaining the acceleration excitation vector, the coupling dynamic response of the tower structure and the gyroscope dampers can be obtained by solving the system space state equation.

In addition, it is necessary to point out that the torsional wave of the ground motion should be used in (17), but only the horizontal components and the vertical component can be obtained in traditional ground motion database. The following method can be used to transform the existing translational ground motions into torsional component [21, 22], and the specific procedure is as follows: (1) decompose the earthquake translational acceleration waves into two plane motions $u_1(t)$ and $u_2(t)$ and one vertical movement $u_3(t)$; (2) fast Fourier transform is applied to $u_3(t)$ and $u_2(t)$ which obtain the Fourier spectrum of $U_3(\omega)$ and $U_2(\omega)$; for the given apparent wave velocity c, the Fourier spectrum of the rotational components $\Phi_2(\omega)$和 $\Phi_3(\omega)$ can be calculated according to $\Phi_3(\omega) = i\omega U_2(\omega)/2c$ and $\Phi_2(\omega) = -i\omega U_3(\omega)/c$; (3) the inverse Fourier transform is performed on $\Phi_2(\omega)$ and $\Phi_3(\omega)$; then the acceleration waves of rotational components are obtained by selecting the real parts. The apparent velocity value c can be determined according to the following formula: $c = v/\sin\theta$, where v is the body wave propagation velocity and the incident angle θ is the incident angle of the seismic wave on the ground surface. Taking into account that θ is random variables, the value can be determined according to the statistical average of related seismic records by the harmonic method in the frequency domain.

4. Numerical Example

To verify the multidimensional vibration damping effect of the tower structure with multiple cardan gyroscopes, a steel structure TV Tower is chosen as an analysis example. As shown in Figure 3, the total height of the television tower is 168 m, and the main body of the tower is Pentagon space truss structure. The tower body includes the parts of the antenna section, the tower body, and the turret. The site type is soft rock and the seismic fortification intensity is 7.0. The landform of wind environment around the steel tower is the
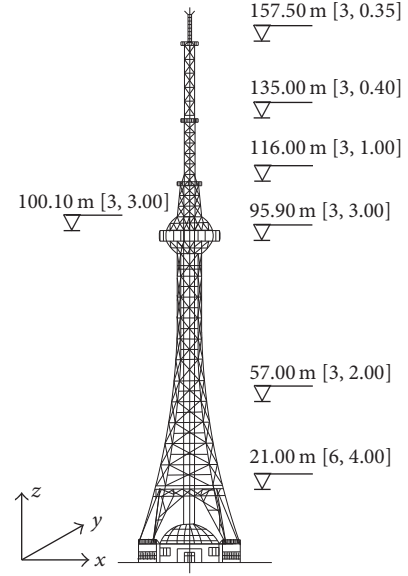

Figure 3: Scheme of TV Tower and location of the gimbal gyroscopes.

terrain B. At the standard height 20 m, the maximum wind pressure is $0.55\,\text{kN/m}^2$ which corresponds to the average 10 min time interval if the 100-year return period is assumed.

Because there are numerous elements and joints on the TV Tower, it is complex to establish the full entity model and carry out time analysis, the system is simplified by the whole truss method which considers the structural joints as hinged joints, and the weight of each element is condensed at the corresponding joints. Then the structural system is analyzed in the space coordinate system so as to accurately represent the mechanics characteristics of the steel tower. Finally, the TV Tower is simplified as a bending shear structure with multidegree of freedom and there are 43 lumped mass nodes. The first 4 order natural periods of the calculated structure are 1.96 s, 0.95 s, 0.38 s, and 0.25 s, respectively.

If the tower structure is subjected to wind load, it is assumed that the dynamic response of the tower is mainly caused by the crosswind vibration; therefore, the dynamic control in both horizontal directions under cross wind load is studied. In the simulation of fluctuating wind speed, the most widely used Davenport spectrum is selected as the standard spectrum. Considering the vertical correlation, the harmonic superposition method is used to simulate the speed history of fluctuating wind, and the wind pressure of the joints at different height can be converted according to the actual structural frontal areas. The typical velocity histories of fluctuating wind in different locations are shown in Figure 4, and the corresponding wind force histories of different sections are shown in Figure 5. The results show that the simulation data can represent the random characteristics of wind.

The multiple cardan gyroscope dampers are installed in different parts of the tower; the installation position and the elevation are shown in Figure 3. In the same elevation, the dampers are arranged evenly and symmetrically. In Figure 3,
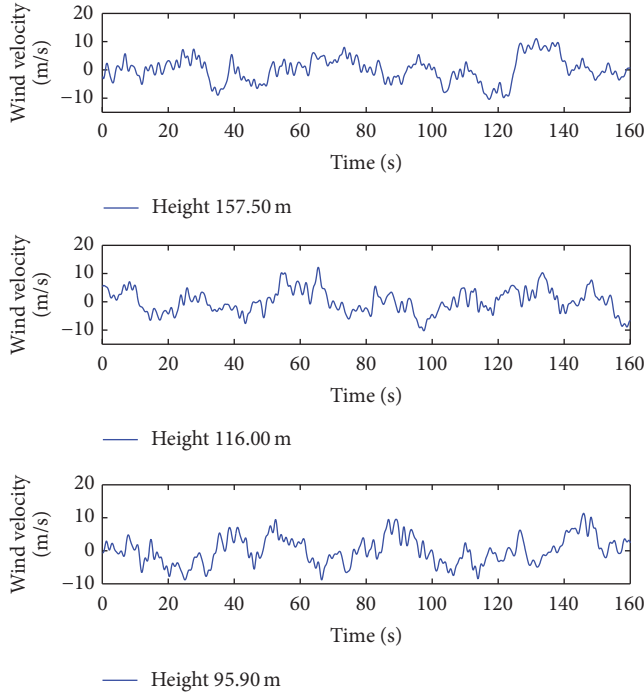
Figure 4: Velocity histories of fluctuating wind in x direction.
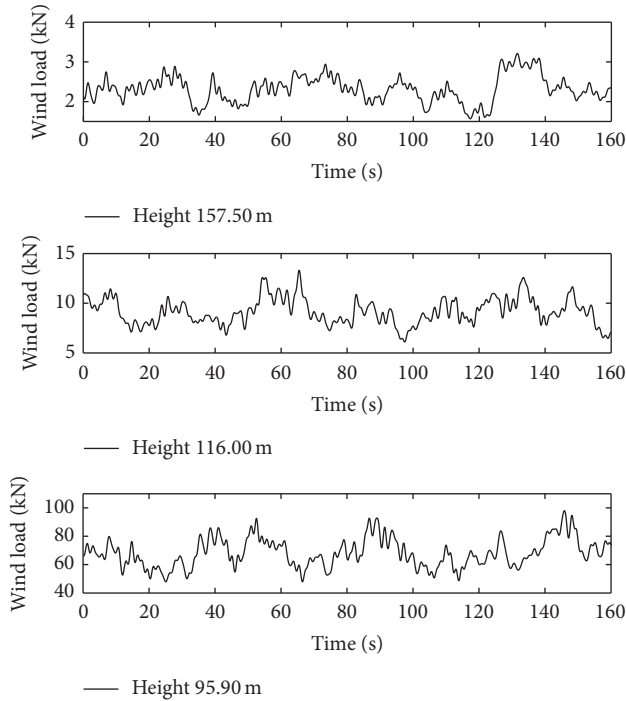
Figure 5: Wind force histories in x direction.

Figure 6: Control curves of the tower turret under wind load.

the first item in the square bracket is the number of dampers in the equivalent horizontal direction, and the second item is the diameter of the rotor in each damper. The vertical thickness of the rotor can be smaller so as to save space, and the value is set as 0.1 m in this study. The mass of each multiple cardan gyroscope damper is 100 kg.

According to (13) and (14), the rotation speed of the inner ring and the outer ring significantly influence the control moment of the gyroscope. Limited to actual conditions, the rotation speed of the outer ring is restricted to 0.20 rad/s and the control effect of the tower turret with different rotation speeds of the inner ring is analyzed, and the results are in Figure 6. It is obvious that the dynamic responses can be more significantly reduced with the speedup of rotor. Therefore, the structure control is realized by controlling the rotation speed of the inner ring.

According to the actual electric force provided by the power, it is assumed that each gyro rotor speed around the inner ring and the outer ring is 100 rad/s and 0.20 rad/s, respectively, driven by the synchronous motor. According to (17), the coupling dynamic equation is established, and the wind loads are used as the input to calculate the multidimensional dynamic responses of the TV Tower before and after the installation of the gyro dampers, and the damping effect is analyzed. Taking into account that there are constraint components in the transverse direction on the TV Tower, the transmission range of the moment provided by the gyro dampers is limited, so the length of the equivalent mass section installed with dampers is assumed as the effective arm of the gyro moment.

The comparison results of the dynamic responses of the turret (the height is 100.10 m) and the tower top (the height is 157.50 m) are shown in Figures 7 and 8, respectively. It can be seen that the structural displacement and acceleration are all reduced to a certain extent after the installation of gyro dampers, and the damping effect of the gyro dampers is preeminent. The acceleration power spectral density of the tower turret and the tower top is shown in Figure 9. It can be seen that the amplitude of all the frequencies is reduced, so the system is stable for frequency control.

The contrast results of the global displacement before and after control are shown in Figure 10; it is evident that gyro
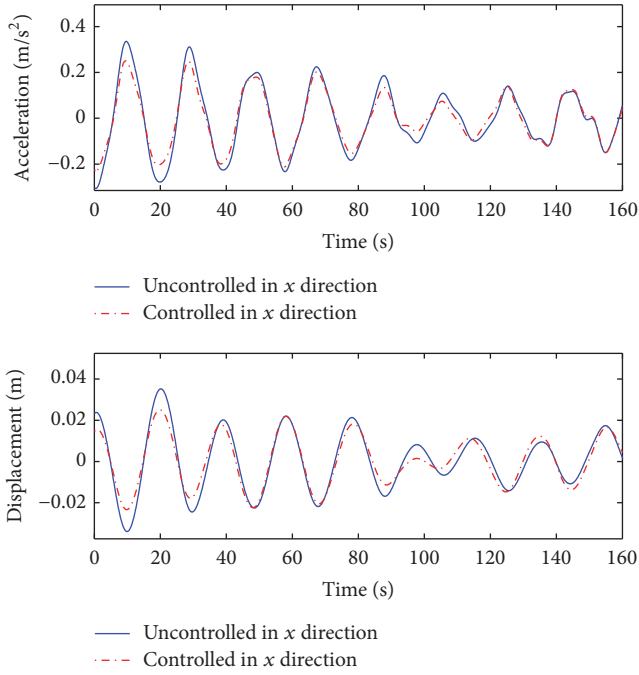
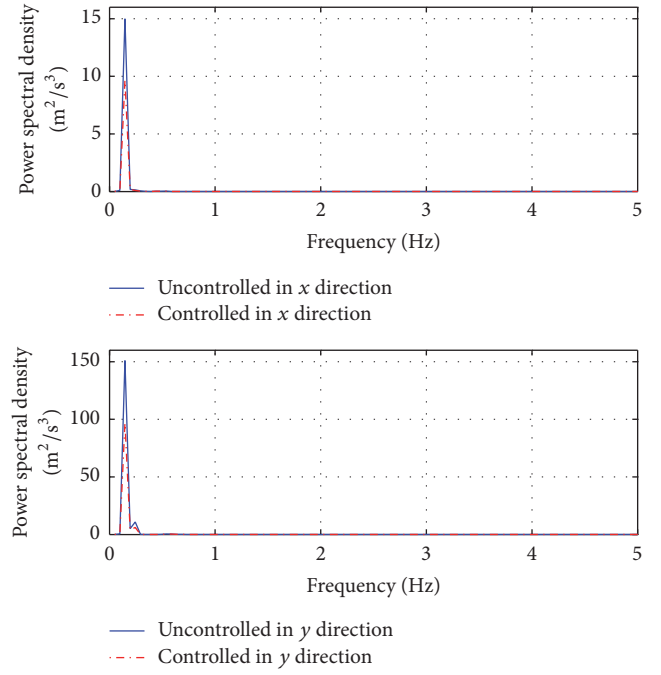FIGURE 7: Dynamic responses of the tower turret under wind load.

FIGURE 8: Dynamic responses of the tower top under wind load.

FIGURE 9: Power spectral density of acceleration responses.

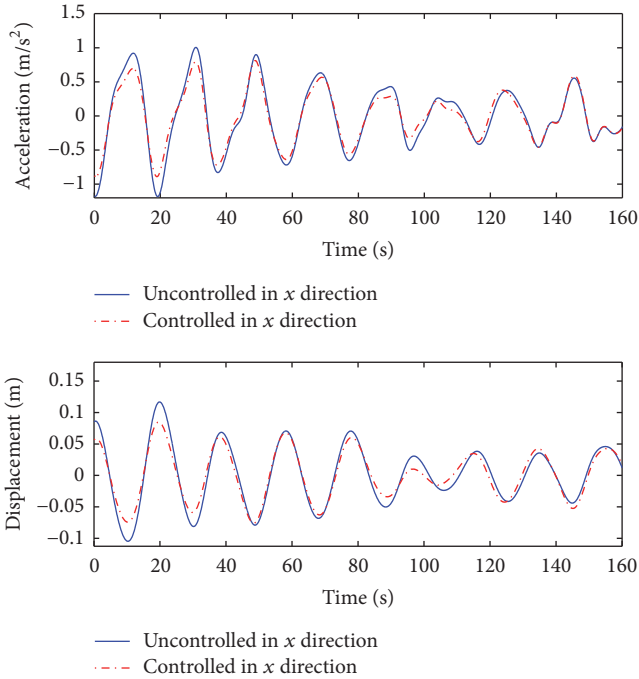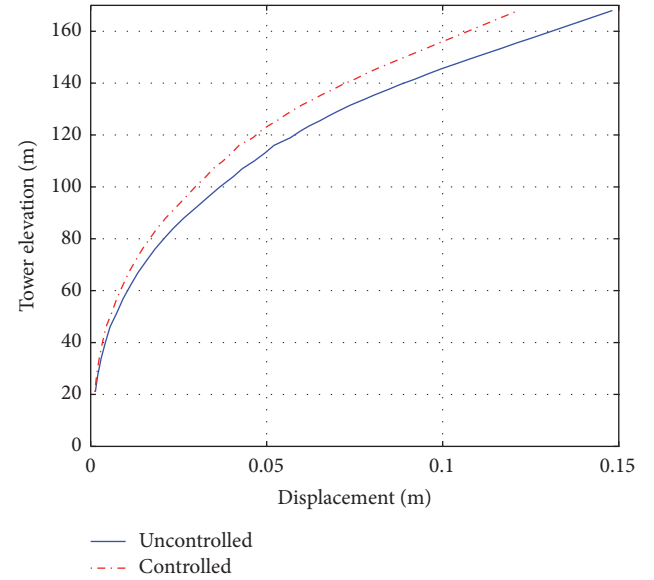FIGURE 10: Displacement control result of total tower under wind load.

dampers can effectively decrease the structural displacement under wind load, especially the top displacement of the tower.

Compared with the effect of wind load, the damping effect of the tower structure under earthquake deserves more attention. Considering the site condition and geological circumstances, El Centro waves are used as the ground motion input because these ground motion records were collected from hard soil and the predominant periods are close to the structural periods. The maximum acceleration amplitude of El Centro wave is 3.417 m/s^2. The rotational wave is computed according to the transformation method, as mentioned above. The corresponding excitations in different directions are shown in Figure 11.

It is assumed that each gyro rotor speed around the inner circle and the outer circle is 120 rad/s and 0.30 rad/s,
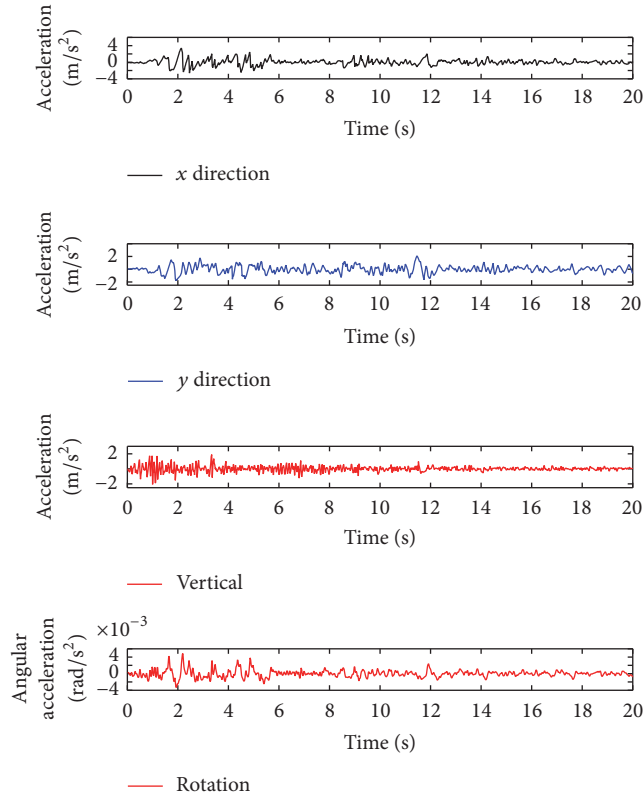
FIGURE 11: El Centro earthquake waves in different directions.

respectively, driven by the synchronous motor. The multidimensional seismic responses and the damping effect of the TV Tower with the multiple cardan gyroscope dampers are calculated.

When the structure is subjected to El Centro waves, the typical acceleration and displacement of the tower turret in x direction and y direction are shown in Figures 12 and 13, respectively. The corresponding results of the tower top are shown in Figures 14 and 15, respectively.

The acceleration power spectral density of the tower turret and tower top is shown in Figures 16 and 17, respectively. It can be seen that the amplitude of all the vast majority of frequencies is reduced, so the system is also stable for frequency control under earthquake.

The torsional response of the tower top under earthquake is shown in Figure 18. It can be seen that the structural responses including displacement, acceleration, and torsion angle are all reduced to some extent, so the control strategy using multiple cardan gyroscope dampers is feasible and effective.

Due to the fact that high frequency components of the ground motion are rich and the speed of the gyro rotor is fast, the acceleration of some parts of the structure such as tower turret will change dramatically and alternately if the dampers are installed. Nevertheless, this kind of mutation is instantaneous and the amplitude is small, and the global damping effect is acceptable.

The damping effect of the global displacement of the tower is shown in Figure 19. All the above results shows that
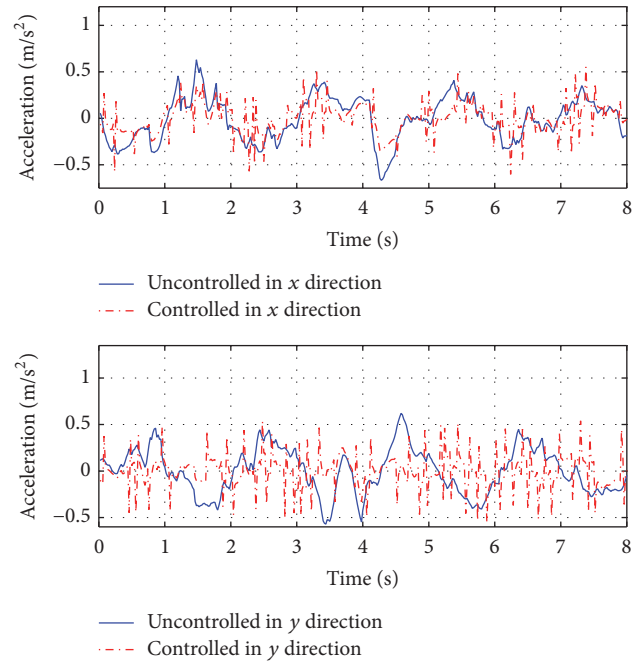
FIGURE 12: Acceleration responses of the tower turret under earthquake.
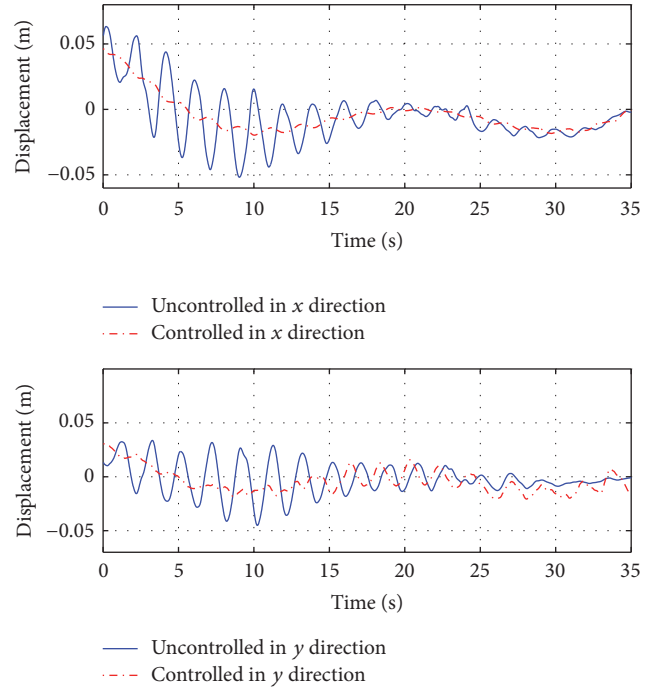
FIGURE 13: Displacement responses of the tower turret under earthquake.

the gyroscope dampers can obviously reduce the dynamic responses of the tower structure under earthquake, if the dampers are evenly distributed in order to harmonize the overall deformation of the structure.
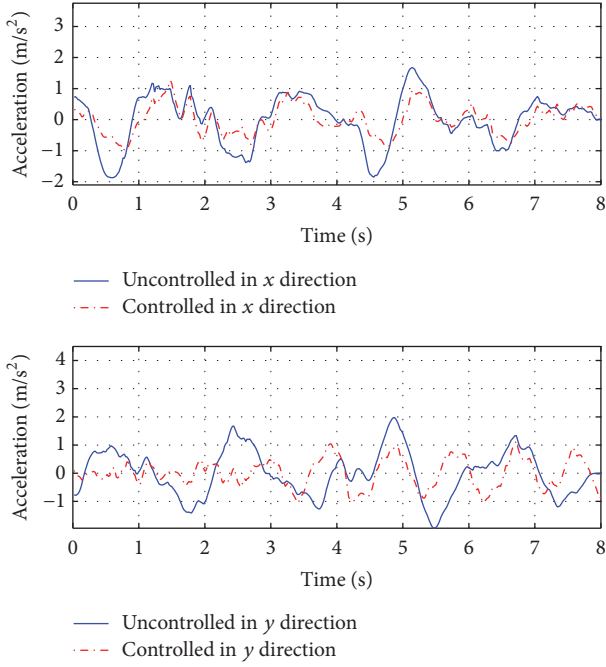
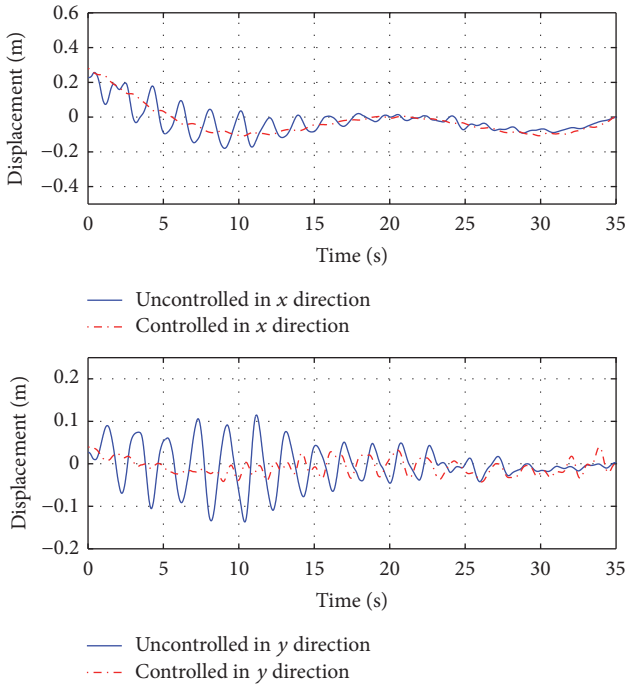FIGURE 14: Acceleration responses of the tower top under earthquake.

FIGURE 15: Displacement responses of the tower top under earthquake.
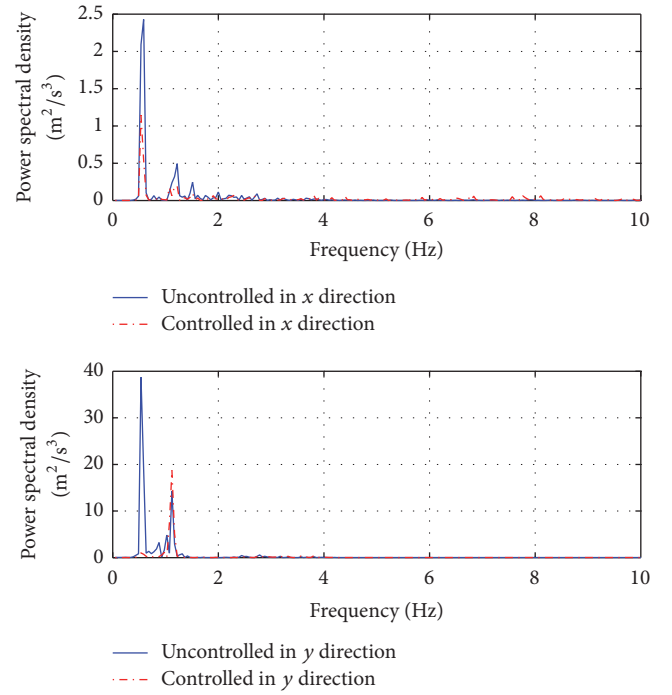

FIGURE 16: Acceleration power spectral density of the tower turret.
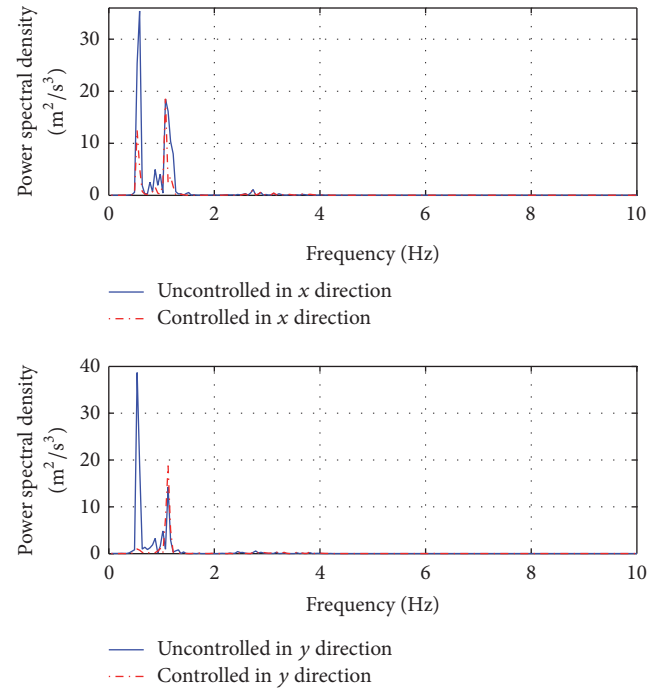
FIGURE 17: Acceleration power spectral density of the tower top.

5. Conclusion

In this study, the method of reducing the dynamic response of the tower structure under wind load and earthquake action is studied by using the multiple cardan gyroscopes as the dampers. The mechanism and the characteristics of the fixed axis of the multiple cardan gyroscope are described, and the dynamic equation of the gyroscope is established. The mechanism that the gyroscope damper controls the structural responses according to its mechanical characteristics is also described. The construction of the multiple cardan gyroscope damper is simple; it does not need large mass and strong
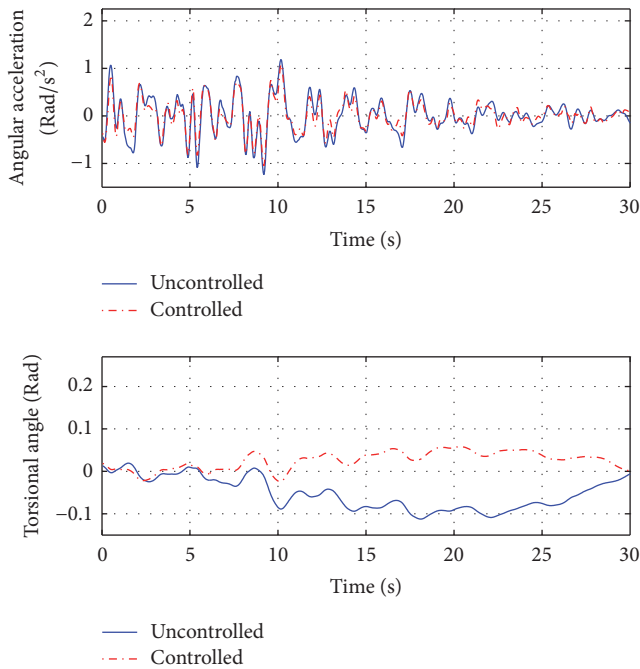
FIGURE 18: Torsional response of the tower top under earthquake.
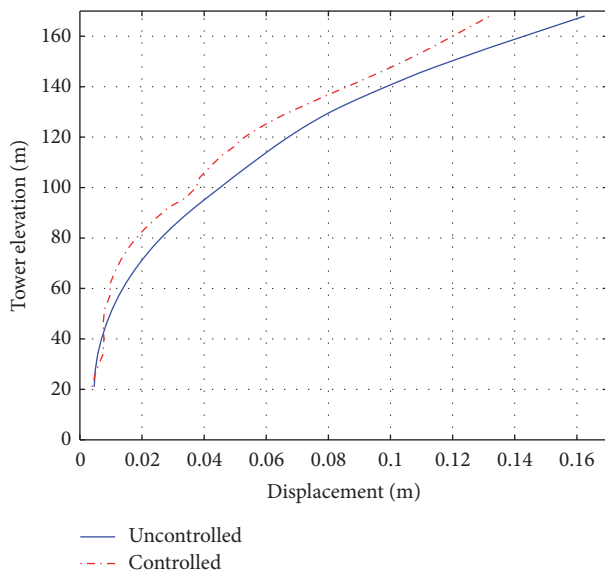
FIGURE 19: Displacement control result of total tower under earthquake.

stiffness and does not occupy too much internal space in the structure. A multidimensional control dynamic equation considering the effect of torsion is established, and the corresponding state space equation is also established, so the nonclassical damping matrix can be decoupled. A steel tower is taken as an example, and the damping effect when the structure is subjected to wind load and earthquake action is studied.

The dynamic simulation results verify that the moments provided by the multiple cardan gyroscopes can significantly decrease the structural dynamic responses, and the vibration in the horizontal directions and torsional direction is effectively controlled. Because the damping capacity of the gyroscope damper is mainly related to the rotating speed of rotor around the inner ring and the outer ring, the high power frequency conversion motor is required to realize the control effect of the large tower structure, so it is necessary to research and develop powerful electrical equipment. In addition, the optimal placement position of the gyroscope dampers, the semiactive control strategy, and the optimal rotation speed of the rotor also need further studies.

Competing Interests

The authors declare that there is no conflict of interests regarding the publication of this paper.

Acknowledgments

References

[1] Y. X. Jiang, J. C. Yue, and L. M. Ye, "Static and dynamic analysis of intake tower structure," *Applied Mechanics and Materials*, vol. 444-445, pp. 912–915, 2014.

[2] C. L. Gong, H. Liu, and J. Zhang, "Study on dynamic properties of the intake tower with finite element method," *Applied Mechanics and Materials*, vol. 501–504, no. 3, pp. 1888–1891, 2014.

[3] A. Goyal and A. K. Chopra, "Hydrodynamic and foundation interaction effects in dynamics of intake towers: earthquake responses," *Journal of Structural Engineering*, vol. 115, no. 6, pp. 1386–1395, 1989.

[4] J. M. Kelly and D. Konstantinidis, *Mechanics of Rubber Bearings for Seismic and Vibration Isolation*, John Wiley & Sons, New York, NY, USA, 2011.

[5] A. A. Markou, G. Oliveto, and A. Athanasiou, "Response simulation of hybrid base isolation systems under earthquake excitation," *Soil Dynamics and Earthquake Engineering*, vol. 84, no. 2, pp. 120–133, 2016.

[6] E. Matta and A. De Stefano, "Robust design of mass-uncertain rolling-pendulum TMDs for the seismic protection of buildings," *Mechanical Systems and Signal Processing*, vol. 23, no. 1, pp. 127–147, 2009.

[7] V. B. Patil and R. S. Jangid, "Optimum multiple tuned mass dampers for the wind excited benchmark building," *Journal of Civil Engineering and Management*, vol. 17, no. 4, pp. 540–557, 2011.

[8] A. Vulcano and F. Mazza, "Comparative study of seismic performance of frames using different dissipative braces," in *Proceedings of the 12th World Conference on Earthquake Engineering*, Auckland, New Zealand, February 2000.

[9] C.-C. Chou and Y.-C. Chen, "Development of steel dual-core self-centering braces: quasi-static cyclic tests and finite element analyses," *Earthquake Spectra*, vol. 31, no. 1, pp. 247–272, 2015.

[10] Z. Zhou, X. T. He, J. Wu, C. L. Wang, and S. P. Meng, "Development of a novel self-centering buckling-restrained brace with BFRP composite tendons," *Steel and Composite Structures*, vol. 16, no. 5, pp. 491–506, 2014.

[11] J. Sanchez, A. Masroor, G. Mosqueda, and K. Ryan, "Static and dynamic stability of elastomeric bearings for seismic protection of buildings," *Journal of Structural Engineering*, vol. 139, no. 1, pp. 1149–1159, 2013.

[12] N. Hoang, Y. Fujino, and P. Warnitchai, "Optimal tuned mass damper for seismic applications and practical design formulas," *Engineering Structures*, vol. 30, no. 3, pp. 707–715, 2008.

[13] T. R. Kane and D. A. Levinson, *Dynamics Theory and Application*, McGraw-Hill Series in Mechanical Engineering, 1985.

[14] A. H. P. Morgado, "On the determination of inertial and gyroscopic forces in multibody systems," *International Applied Mechanics*, vol. 35, no. 12, pp. 1293–1300, 1999.

[15] G. M. T. D'Eleuterio and P. C. Hughes, "Dynamics of gyroelastic spacecraft," *Journal of Guidance, Control, and Dynamics*, vol. 10, no. 4, pp. 401–405, 1987.

[16] Q. Hu, Y. Jia, and S. Xu, "Adaptive suppression of linear structural vibration using control moment gyroscopes," *Journal of Guidance, Control, and Dynamics*, vol. 37, no. 3, pp. 990–996, 2014.

[17] N.-C. Tsai and C.-Y. Sue, "Experimental analysis and characterization of electrostatic-drive tri-axis micro-gyroscope," *Sensors and Actuators A: Physical*, vol. 158, no. 2, pp. 231–239, 2010.

[18] J.-F. Shi and C. J. Damaren, "Control law for active structural damping using a control moment gyro," *Journal of Guidance, Control, and Dynamics*, vol. 28, no. 3, pp. 550–553, 2005.

[19] Z. H. Wang and D. R. Liu, "The vibration-proof research under the wind load of random in the high-rise structure in tower," *Journal of Shenyang Architectural and Civil Engineering Institute*, vol. 21, no. 5, pp. 460–463, 2005.

[20] Y. J. Moon, S. W. Cho, J. G. Park, and I. W. Lee, "Control Performance of Gyroscope System in Active Vibration Control," Sdvc.kaist.ac.kr, 2005.

[21] S. J. Sun and G. X. Chen, "Synthesis method for estimation of rotation components of ground motion," *Journal of Seismology*, vol. 18, no. 1, pp. 19–24, 1988.

[22] J. J. Wang and J. R. Jiang, "Estimation of response spectrum for rotational ground motions," *Earthquake Engineering and Engineering Vibration*, vol. 13, no. 3, pp. 7–16, 1993.

Research Article

Dynamic Analysis of a Rotor-Bearing-SFD System with the Bearing Inner Race Defect

Junhong Zhang,[1,2] Xin Lu,[1] Jiewei Lin,[1] Liang Ma,[1,2] and Jun Wang[2]

[1]*State Key Laboratory of Engines, Tianjin University, Tianjin 300072, China*
[2]*Department of Mechanical Engineering, Tianjin University Renai College, Tianjin 301636, China*

Correspondence should be addressed to Jiewei Lin; linjiewei@tju.edu.cn and Liang Ma; mliang@tju.edu.cn

In this paper, the dynamic behavior of a rotor-bearing-SFD system with the inner race defect of bearing is investigated. The contact force between the rolling element and the race is calculated in Hertzian contact and elastohydrodynamic lubrication condition. The supporting force of the SFD is simulated by integrating the pressure distribution derived from Reynolds's equation. The equations of motion of the rotor-bearing-SFD system are derived and solved using the fourth-order Runge-Kutta method. The dynamic behavior and the fault characteristics are analyzed with two configurations of the SFD: (1) mounted on the unfaulted bearing and (2) mounted on the faulty bearing. According to the analysis of time-frequency diagram, waterfall plot, and spectral diagram, the results show that the characteristics of inner race defects on bearing frequencies are related to the characteristic multiple frequency of the inner race defect and the fundamental frequency. The speed and defect width have different influence on the distribution and amplitude of frequency. The SFD can enhance the system stability under the bearing fault but the enhancement decreases with the increasing speed. Meanwhile, the beneficial effect of the SFD varies according to the mounted position in the rotor system.

1. Introduction

Bearings are most widely used in rotating machinery as one of the most critical components. However, for the complex running condition of rotating machinery, bearings easily fail. According to research, over 40% failures are due to bearing defects among failures of motors [1]. Bearing faults may cause unstable vibration of rotor system which leads to serious economic and increase the downtime [2, 3]. Therefore, it is essential to understand the dynamic and intrinsic transient characteristics of vibration caused by bearing faults.

Bearing faults can be divided into distributed defects and localized defects [4, 5]. The localized defects, also called single-points defects, include the cracks, pits on the surface of the inner race, outer race, and ball race. The distributed defects include surface roughness, waviness, misalignment races, and off-size rolling elements. In order to study the dynamic characteristics of ball bearing, Kankar et al. [6] developed a model of localized defects on a ball bearing and employed the Fast Fourier Transformation (FFT) and the

Poincare maps to analyze the defects of bearing components. Arslan and Aktürk [7] developed a shaft-bearing model and analyzed the characteristics of bearing defects in frequency and time domains; the frequency characteristics of fault were studied. Patil et al. [8] used the time domain and the power spectrum to study the frequency and acceleration of vibration components of ball bearings and discussed the effects of the defects size and locations.

According to the recent research, the vibration signals are nonstationary and time-varying with the effect of speed changing and the nonlinear characteristics of the rotor system caused by faults. To well extract the transient characteristics from signal data, many signal denoising methods have been developed [9], such as time-domain method, band-pass filtering, frequency-domain threshold, empirical mode decomposition (EMD), wavelet transform (WT), time-frequency analysis (TFA), manifold learning, and matching pursuit. However, there are still some issues that remained to be studied among these denoising methods. In these methods, time-frequency analysis can reflect the change of signal

characteristics with time and is widely used in faults diagnosis [10]. Ding and He [9] proposed a novel transient signal reconstruction method for bearing fault features extraction and find this method is effective to verify faults characteristics of bearing fault. Liu et al. [11] used a novel fault detection method to study the impact time-frequency dictionary and faulty features of roller bearing defects.

In order to reduce the nonlinear vibration, rotors are often supported by ball bearings with squeeze film dampers (SFD) in many applications [12]. SFD can be designed through introducing a centralized spring and filling the clearance with lubrication oil. In a SFD mounted rotor-bearing system, the bearing can be held in its position statically by the supporting fluid pressure. Meanwhile, the critical speed of the rotor system as well as the stability is able to be controlled by adjusting the SFD parameters. Many scholars focused on the dynamic characteristics of the rotor system affected by SFD [13–15]. Previous work on SFD on a two-disk rotor system with misalignment and the effects of SFD was discussed [16].

However, although various available models represent the dynamics characteristics of rolling element bearings, there is no universal and detailed platform for the whole system [17]. There also need the intensive study of the bearing fault laws about the faults parameters to understand the nature of the fault and the occurrence and development of the fault, so as to timely and accurate to all kinds of anomalies or failure of the emergence and development of the trend to make judgments.

On the basis of previous work [16], this paper developed a model of bearing which considered both Hertz contact and elastohydrodynamic lubrication. This model was focused on studying the fault characteristics of the rotor system caused by inner race defects. The waterfall map, time-frequency map, and spectral diagram were introduced to analyze the dynamic and signal characteristics of inner race defects, studying the law of the frequency characteristics changing with defect parameters. In the end, the effects of SFD to the dynamic characteristics of faults rotor system were discussed.

2. Model of the Rotor-Bearing-SFD System

2.1. SFD Model.
The schematic of the SFD used in this paper is shown in Figure 1. The instantaneous pressure distribution p_s can be calculated using the Reynolds equations [18]:

$$\frac{1}{R_s^2}\frac{\partial}{\partial\theta}\left(h_s^3\frac{\partial p_s}{\partial\theta}\right) + h_s^3\frac{\partial^2 p_s}{\partial x^2} = -12\mu_s\Omega\frac{\partial h_s}{\partial\theta} + 12\mu_s\frac{\partial h_s}{\partial t}. \quad (1)$$

In order to solve the Reynolds equation, the Sommerfeld transformation was introduced [19]; after integrating twice p_s can be written as

$$p_s = \frac{6\mu_s\left(\varepsilon_s\Omega\sin\theta + \dot{\varepsilon}_s\cos\theta\right)\left(x^2 - l_s^2/4\right)}{c_s^2\left(1 + \varepsilon_s\cos\theta\right)^3} \\ + \left(p_{s,2} - p_{s,1}\right)\frac{x}{l_s} + \frac{1}{2}\left(p_{s,2} + p_{s,1}\right), \quad (2)$$

where $h_s = c_s(1 + \varepsilon_s\cos\theta)$, μ_s is the oil viscosity, Ω is the precession angular velocity of the journal, c_s is the radial
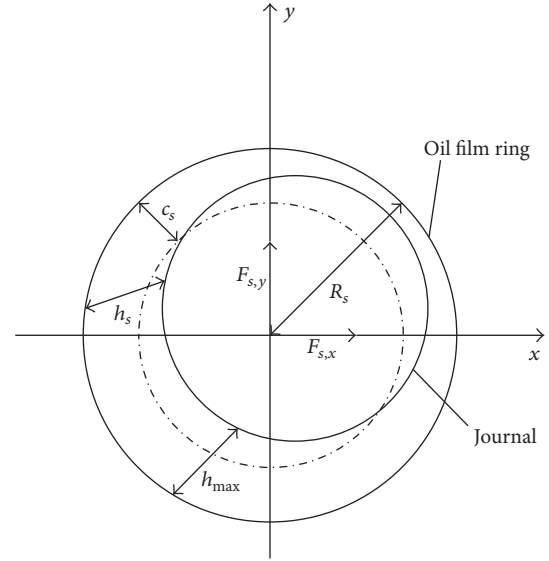

FIGURE 1: Model of the SFD.

clearance of the SFD, and ε_s is the eccentric ratio of the bearing and given as $\varepsilon_s = \sqrt{x^2 + y^2}/c_s$, $p_{s,1}$ and $p_{s,2}$ are the SFD boundary pressures, and l_s is the bearing width.

According to the Reynolds boundary condition, $p_{s,1}$ and $p_{s,2}$ are assumed equal to 0; the supporting force of the oil film can be obtained as [19]

$$F_{s,y} \\ = -\frac{\mu_s R_s l_s^3}{c_s^2\sqrt{y^2 + x^2}}\left[y\left(\dot{\varepsilon}_s I_1 + \varepsilon_s\Omega I_2\right) - x\left(\dot{\varepsilon}_s I_2 + \varepsilon_s\Omega I_3\right)\right],$$

$$F_{s,x} \qquad\qquad\qquad\qquad\qquad\qquad\qquad (3) \\ = -\frac{\mu_s R_s l_s^3}{c_s^2\sqrt{y^2 + x^2}}\left[x\left(\dot{\varepsilon}_s I_1 + \varepsilon_s\Omega I_2\right) + y\left(\dot{\varepsilon}_s I_2 + \varepsilon_s\Omega I_3\right)\right],$$

where R_s is radius of SFD, I_1, I_2, and I_3 are classic Sommerfeld integral equations; they can be written as

$$I_1 = \int_{\theta_1}^{\theta_1+\pi}\frac{\cos^2\theta}{\left(1 + \varepsilon_s\cos\theta\right)^3}d\theta,$$

$$I_2 = \int_{\theta_1}^{\theta_1+\pi}\frac{\sin\theta\cos\theta}{\left(1 + \varepsilon_s\cos\theta\right)^3}d\theta, \qquad (4)$$

$$I_3 = \int_{\theta_1}^{\theta_1+\pi}\frac{\sin^2\theta}{\left(1 + \varepsilon_s\cos\theta\right)^3}d\theta.$$

2.2. Ball Bearing Model with Faults

2.2.1. Ball Bearing Model.
The sketch of the ball bearing is shown in Figure 2. For the bearing model ignoring the effect of the lubrication oil, the load distribution of the bearing can be determined based on the Hertzian contact
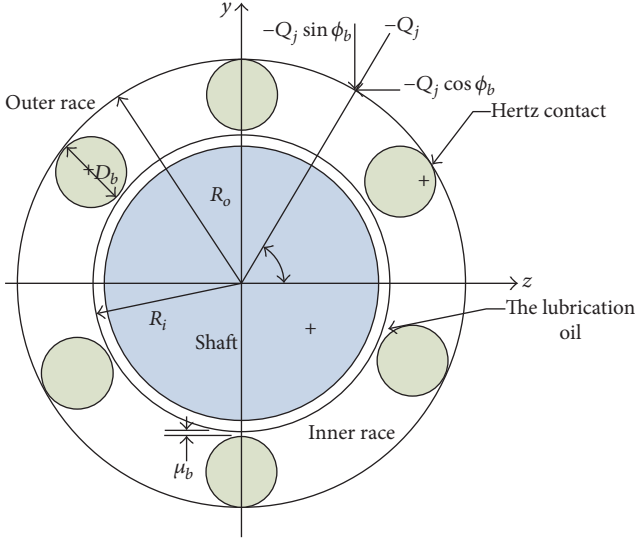
FIGURE 2: Schematic diagram of the ball bearing.

theory [20, 21]. Due to the working condition of the rotor system, the centrifugal forces of the rolling elements should be considered. The model of ball bearing can be developed by following assumptions:

(1) The outer rings are connected rigidly to the support and inner rings are fixed rigidly to the shaft.

(2) The inner race, ball, and outer race move in the plane of bearing only.

(3) The temperature of bearing is stable when the bearing is in operation.

According to Harris' work [22], the contact stiffness of the ball bearing can be calculated as follows:

$$
k_{b,j}^{H} = \frac{\partial Q_{b,j}^{i}}{\partial \delta_{b,j}} = \frac{3}{2} Q_{b,j}^{i}{}^{1/3} \left[k_{c,j}^{i}{}^{-2/3} \right.
$$
$$
+ k_{c,j}^{o}{}^{-2/3} \left(1 + \frac{F_{b,c}}{Q_{b,j}^{i}} \right)^{2/3}
$$
$$
\left. - k_{c,j}^{o}{}^{-2/3} \left(1 + \frac{F_{b,c}}{Q_{b,j}^{i}} \right)^{-1/3} Q_{b,j}^{i}{}^{-1} \right]^{-1},
$$
(5)

where Q_b is the load of ball, k_c is the contact deformation coefficient of the ball, and $F_{b,c}$ is the centrifugal force of the ball. The subscript "j" refers to the ball number, and the superscripts "i" and "o" refer to the inner and outer races, respectively.

Regarding the point contact, the oil film thickness equation proposed by Sarangi et al. [21] is appropriate for the ball bearing:

$$
H_b = 2.69 U^{0.67} G^{0.53} W^{-0.067} \left[1 - 0.61 \exp\left(-0.73 e_b\right) \right], \quad (6)
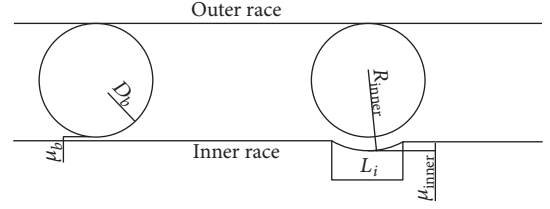$$

FIGURE 3: The Inner race defect of the ball.

where $U = \mu_b u / 2E' R_b$ is a nondimensional velocity, $G = \alpha E'$ is a nondimensional material parameter, $W = Q_b / E' R_b^2$ is a nondimensional load parameter, e_b is the ellipticity of the rolling element, μ_b is the dynamic viscosity, u is the linear velocity, $E' = E/(1-\nu^2)$ is the equivalent Young's modulus, ν is the Poisson's ratio, and α is the pressure-viscosity coefficient.

Then the oil film stiffness between the rolling element and the inner race can be calculated as

$$
k_{EHL}^{i} = \frac{\partial Q_j}{\partial H_b^i} = \left(\frac{\partial H_b^i}{\partial Q_j} \right)^{-1} = -\frac{1}{0.18023}
$$
$$
\cdot \overline{U}^{-0.67} \overline{G}^{-0.53} Q_j^{1.067} E'^{-0.067} R_b^{i}{}^{-1.134} \left(1 \right.
$$
$$
\left. - 0.61 e^{-0.73 K_{eli}} \right)^{-1}.
$$
(7)

The oil film stiffness between the rolling element and the outer race, k_{EHL}^{o}, can be calculated in the same way. Thus, the total oil film stiffness of the bearing can be obtained:

$$
k_{b,j}^{E} = \left(\frac{1}{k_{EHL}^{i}} + \frac{1}{k_{EHL}^{o}} \right)^{-1}. \quad (8)
$$

The global stiffness of the rolling element can be obtained:

$$
k_{b,j} = \left(\frac{1}{k_{b,j}^{H}} + \frac{1}{k_{b,j}^{E}} \right)^{-1}. \quad (9)
$$

Accordingly, the radial contact load of a rolling element can be calculated as

$$
Q_{b,j}^{i} = k_{b,j} \cdot \delta_{b,j}. \quad (10)
$$

Then the supporting forces of the ball bearing in the y- and x-directions are given as

$$
F_{b,y} = -Q_b \frac{y}{\delta_b},
$$
$$
F_{b,x} = -Q_b \frac{x}{\delta_b}.
$$
(11)

2.2.2. Bearing Model with Inner Race Defect. When defect occurred on inner race of bearing, Figure 2 was transferred into Figure 3 in detail. The displacement of the ith rolling element can be calculated as [6]

$$
r_j = x \cos \theta_j + y \sin \theta_j - \mu_b - \mu_{inner}, \quad (12)
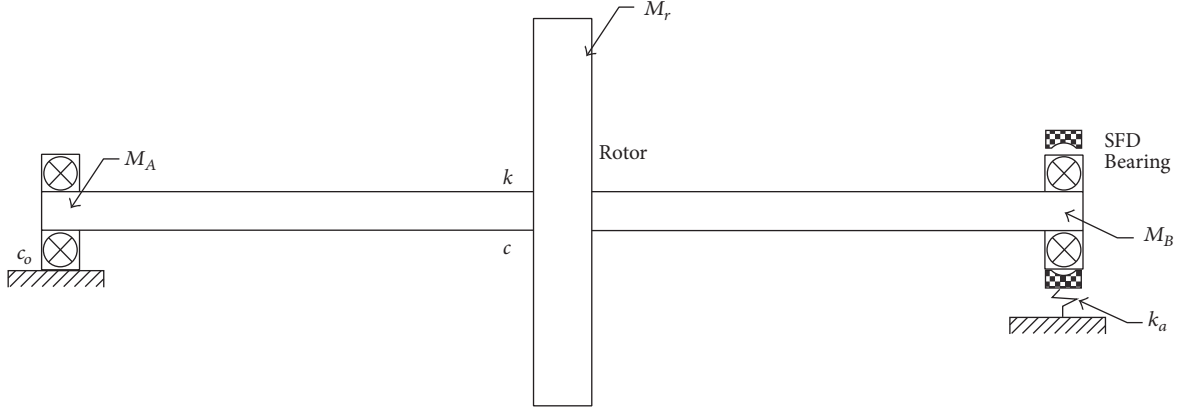$$

FIGURE 4: The model of the rotor-bearing-SFD system.

where μ_{inner} is the additional displacement of the rolling element due to the inner race defect which is given as

$$\mu_{\text{inner}} = R_{\text{inner}} - \sqrt{R_{\text{inner}}{}^2 - \left(\frac{L_i}{2}\right)^2}, \tag{13}$$

where D_b is the radius of the rolling element and L_i is the width of the defect on inner race.

The contact angle, θ_i, of the ith rolling element and the defect angle, Φ_i, are given as

$$\theta_j = \frac{2\pi}{N}(t-1) + \omega_{\text{cage}}t, \tag{14}$$

$$\Phi_j = \arcsin\frac{L_i}{2R_{\text{inner}}}, \tag{15}$$

where N is the number of the rolling element, ω_{cage} is the angular velocity of the cage, and R_{inner} is the radius of the defect.

$$\omega_{\text{cage}} = \omega_{\text{rotor}}\frac{r}{R+r}, \tag{16}$$

where R and r are the radiuses of the outer and the inner races, respectively.

Substituting Eq. (12)–(15), the additional displacement of the rolling element, μ_{inner}, per cycle can be obtained:

μ_{inner}

$$= \begin{cases} R_{\text{inner}} - \sqrt{R_{\text{inner}}{}^2 - \left(\frac{L_i}{2}\right)^2} & 0 < \text{mod}\left(\frac{\theta_j}{2\pi}\right) - \theta_{\text{inner}} < \Phi_j \\ 0 & \text{otherwise.} \end{cases} \tag{17}$$

2.3. Rotor System Model. The rotor-bearing-SFD system is developed based on the Jeffcott rotor (shown in Figure 4) in which the ball bearing B (on the right end) has the inner race defect and the SFD is mounted on one bearing at a time (e.g., the SFD was mounted on bearing B in Figure 4, and in this paper, the SFD mounted both A and B were discussed). The model is established based on the following assumptions:

(1) The movements of the rotor in axial and torsional directions are negligible.

(2) Each lumped mass point has four degrees of freedom including two translations and two rotations.

(3) The mass of spindle is lumped at the location of two bearings and the rotor mass is lumped at a point at the middle of the rotor.

The equations of motion of the dynamic system are derived as

$$\begin{aligned} & m_r\ddot{x}_r + c\dot{x}_r + k(x_r - x_A) + k(x_r - x_B) \\ & \quad = m_r e\omega^2\cos\theta, \\ & m_r\ddot{y}_r + c\dot{y}_r + k(y_r - y_A) + k(y_r - y_B) \\ & \quad = m_r e\omega^2\sin\theta - mg, \\ & m_A\ddot{x}_A + c_o\dot{x}_A + k(x_A - x_r) = F_{A(b,x)}, \\ & m_A\ddot{y}_A + c_o\dot{y}_A + k(y_A - y_r) = F_{A(b,y)} - m_Ag, \\ & m_B\ddot{x}_B + c_o\dot{x}_B + k(x_B - x_r) = F_{B(b,x)}, \\ & m_B\ddot{y}_B + c_o\dot{y}_B + k(y_B - y_r) = F_{B(b,y)} - m_Bg, \\ & m_s\ddot{x}_s + k_ax_s = F_{s,x} - F_{B(b,x)}, \\ & m_s\ddot{y}_s + k_ay_s = F_{s,y} - F_{B(b,y)} - m_sg, \end{aligned} \tag{18}$$

where m_r, m_A, and m_B are the lumped masses of the rotor at the disk and the bearing positions respectively, c and c_o are viscous damping factors of the disk and the bearing, respectively, k is the stiffness of the shaft, $F_{A(b,x)}$, $F_{A(b,y)}$, $F_{B(b,x)}$, and $F_{B(b,y)}$ are the supporting forces of the bearings in the x- and y-directions, m_s is the lumped mass of the bearing outer race, k_a is the supporting stiffness of the SFD, and $F_{s,x}$ and $F_{s,y}$ are the supporting forces of the SFD in the x- and y-directions.

2.4. Numerical Method and Simulation Parameters. In the paper, the differential equations of motion are solved by the Runge-Kutta method. The time step of the iterative procedure is $\Delta t = 1 \times 10^{-5}$ s. The time-varying data corresponding to
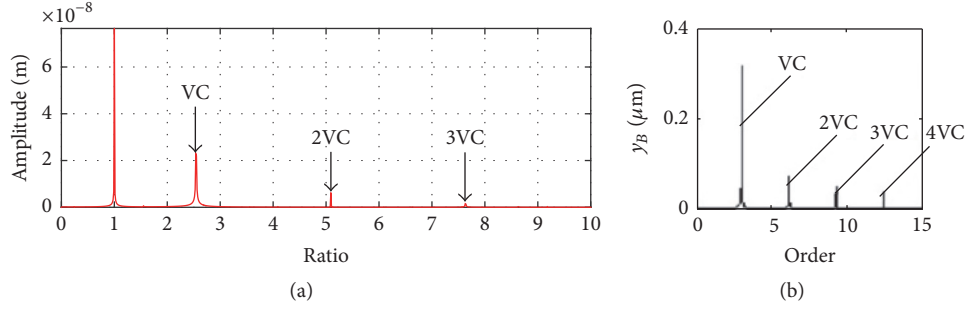
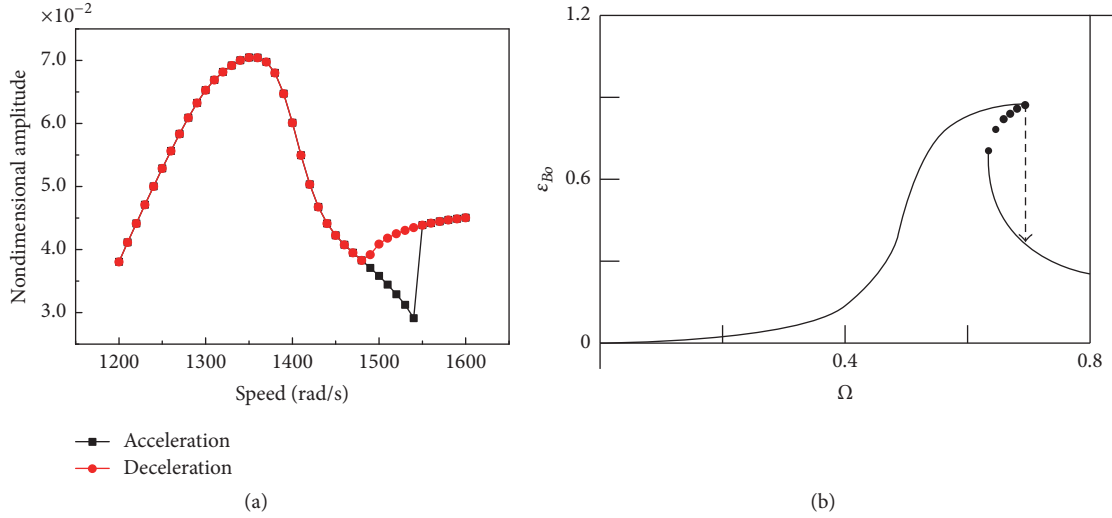FIGURE 5: Rotor response of frequency spectrum (a) in this paper (b) in [11].

FIGURE 6: Steady state responses of rotor in this paper (a) in this paper (b) in [22].

the first 500 periods generated by the numerical integration is deliberately excluded in order to discard the transient solutions. The parameters of the system are shown as follows:

Parameters of the System

d_m: 47e − 3 m

D_b: 8.731e − 3 m

m_r: 15 kg

m_A: 1 kg

m_B: 1 kg

c: 1500 N ∗ s/m

c_o: 2100 N ∗ s/m

k_a: 2e6 N/m

k: 2.5e7 N/m

μ_s: 0.02 Pa ∗ S

c_s: 8e − 5 m

l_s: 11e − 3 m

R_s: 0.03 m

3. Results and Discussion

3.1. Model Validation

3.1.1. Bearing Model. In [12], a ball bearing dynamic model was established by Zhou et al. In order to validate the ball bearing dynamic model the simulation results of the model should be compared with the results of [12] on the same computation conditions. In this paper, the response of the rotor is shown in Figure 5; it is easy to find the VC frequency and 2, 3 VC frequency which represents the ball passage frequency. The same conclusion was found in [12]; therefore, the model established in this paper is further validated.

3.1.2. SFD Model. In [23], the dynamic model of an unbalanced rotor supported on SFD without ball bearing was established by Zhu et al.; analytical method and numerical integration method were employed to obtain the responses of the rotor system. In order to validate the ball bearing dynamic model, the simulation results of the model should be compared with the results of [23] on the same computation conditions. It is shown in Figure 6 that the rotor system has multiple solutions in the region of (1480, 1550) rad/s. The same phenomenon of multiple solution was found in [23].
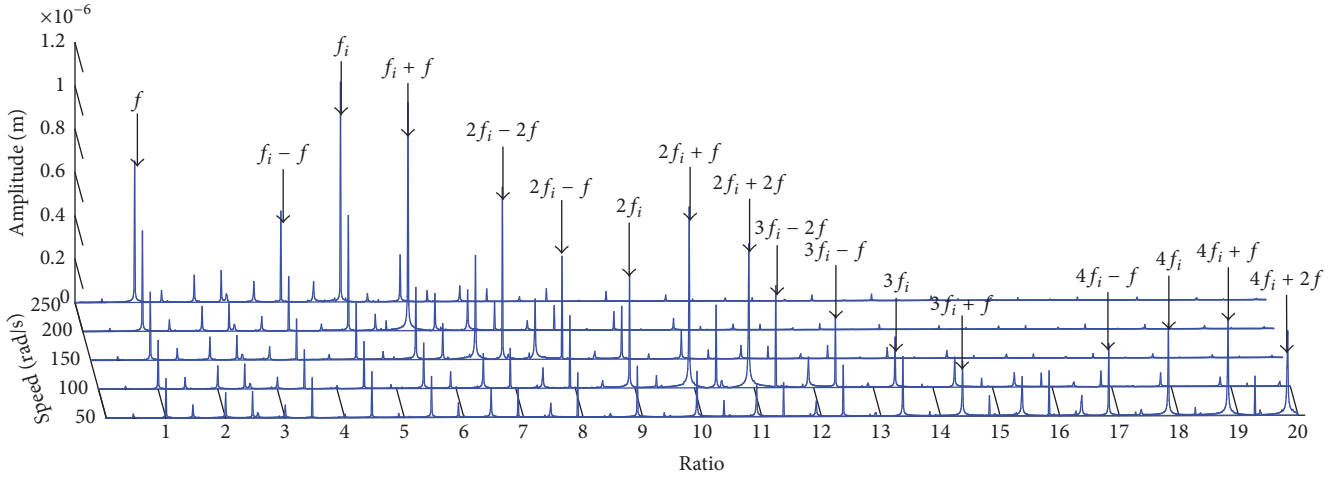
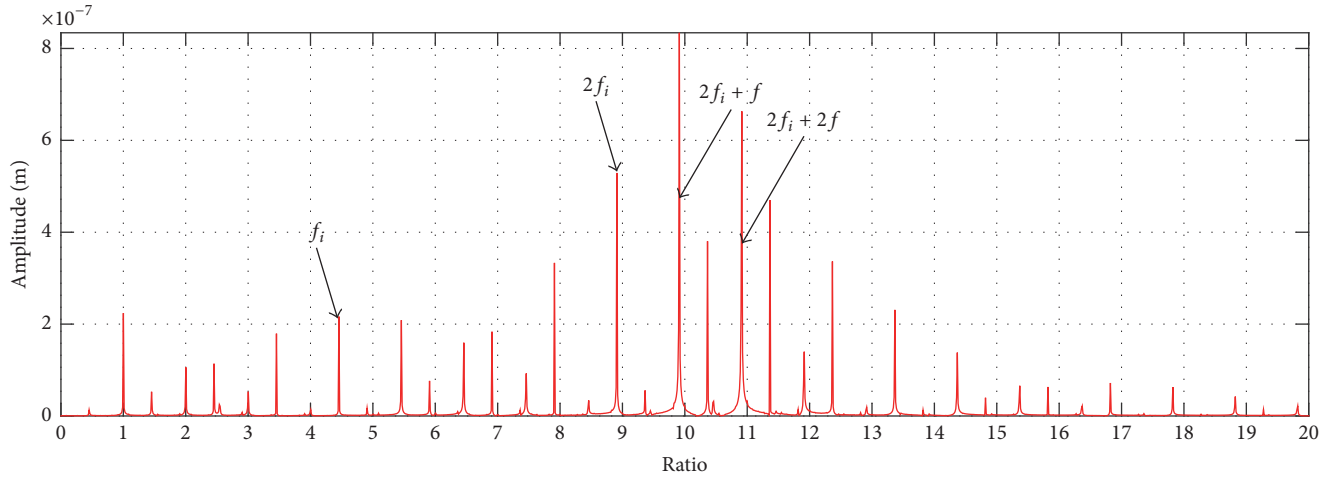FIGURE 7: Waterfall plot of inner race defect bearing system with speed at width $1e-3$ m.

FIGURE 8: The spectral diagrams of the fault system with bearing inner race defect at $\omega = 100$ rad/s and width $1e-3$ m.

By using this method, the model established in this paper is validated.

3.2. Effects of Inner Race Defect

3.2.1. Effects of Rotating Speed. For a ball bearing, the characteristic frequency of the inner race defect f_i can be calculated as

$$f_i = \frac{N}{2}\left(1 + \frac{D_b}{D_m}\right) \cdot f, \tag{19}$$

where D_b is the diameter of the rolling element, D_m is the pitch diameter of the bearing, N is the number of the rolling elements, and f is the rotating frequency of the rotor.

In order to study the fault characteristics of the bearing inner race defect, the waterfall plot of the faulted rotor system in the range of (50, 250) rad/s was shown in Figure 7. When the speed is at 50 rad/s, the maximum frequency is $4f_i + f$ ($4.5e-7$ m), the maximum frequency became f_i ($1.01e-6$ m)

at 250 rad/s, and it can be found that, with the increasing of speed, the amplitude of high frequencies higher than 10x fundamental frequency decreased obviously, the maximum frequency moved to low frequency, and the amplitude of the maximum frequency had great increasing.

From Figure 8, when the speed is at 100 rad/s, many multiple frequency components appear due to the inner race defect, in which the dominant peaks at $2f_i$, $2f_i + f$ and $2f_i + 2f$ are much higher than that at the fundamental frequency. In addition, the amplitudes at $3f_i - f$ and $2f_i - f$ are also greater than that at the fundamental frequency. Among the frequency components, the maximum amplitude at $2f_i + f$ (8.1×10^{-7} m) is nearly four times that at the fundamental frequency. Besides, the sideband frequencies centering on f_i and its multiple frequencies with an interval f (e.g., $2f_i - f$, $2f_i + f$) can be found in the faulted rotor system.

At 150 rad/s case, in Figure 9 for the faulted system, three dominant frequency components can be found which are $2f_i - 2f$, $f_i + 2f$, and $2f_i - f$. The maximum amplitude is nearly $7.9e-7$ m at $2f_i - 2f$ which is far higher than

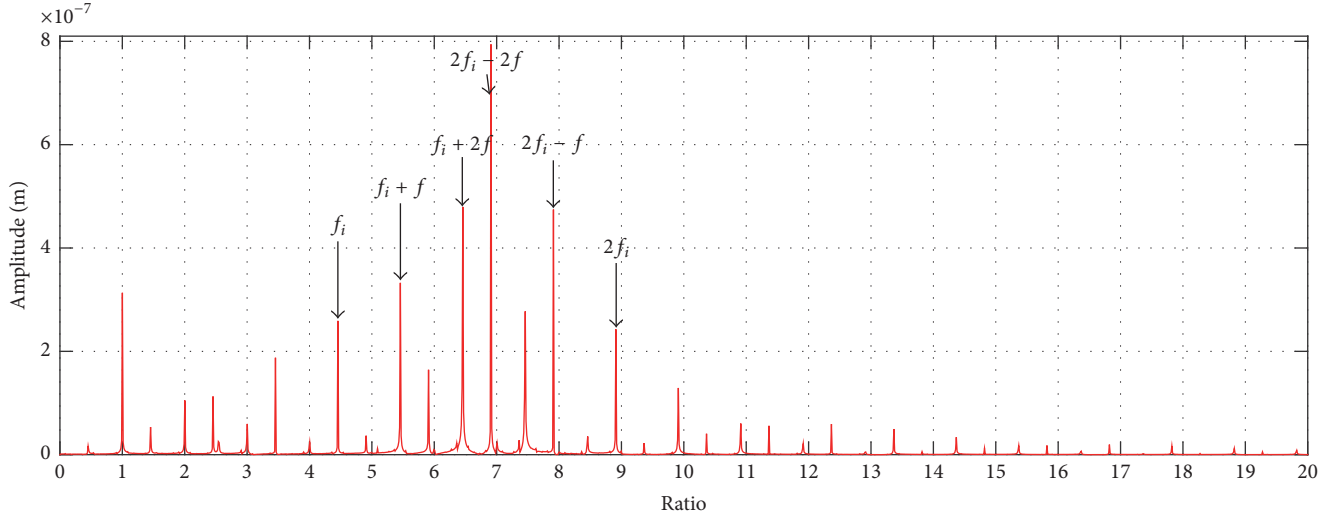FIGURE 9: The spectral diagrams of the fault system with bearing inner race defect at $\omega = 150$ rad/s and width $1e - 3$ m.
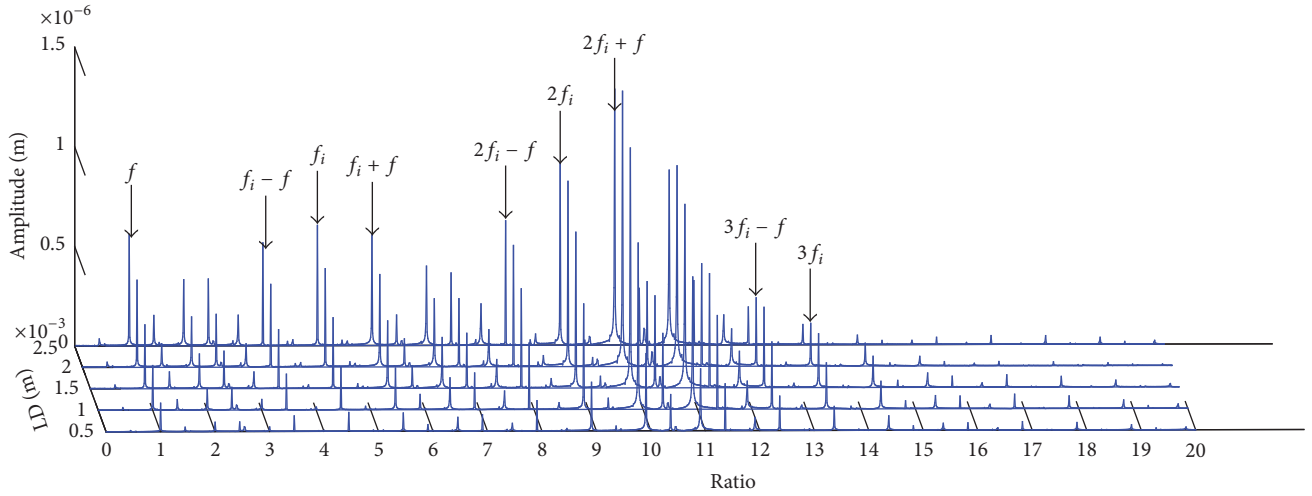

FIGURE 10: Waterfall plot of inner race defect bearing system with width of defect at 100 rad/s.

the fundamental frequency. Similar to the 100 rad/s case, sideband frequencies from f_i to $2f_i$ can be found. Comparing to the faulted system at 100 rad/s, the amplitudes at the sideband frequencies increased while that centering at $2f_i$ decreased.

By analyzing these pictures, it can be concluded that the fault characteristics of the bearing inner race defect are significant at a lower rotating speed of the rotor system. With increasing speed, the significance of the bearing fault characteristic becomes much lower due to the amplitude of the fundamental frequency increases greatly, while that of the fault characteristic frequencies only has a very slight increment.

3.2.2. Effects of Defects Width.
From Figure 10, it is found that the maximum frequency is $2f_i + f$ no matter how width changed, with the increasing of width in range of ($0.5e - 3$ m,

$2e-3$ m), the amplitude of $2f_i+f$ is increased from $3.87e-7$ m to $1.381e - 6$ m, with a little decrease when width at $2.5e - 3$ m. The sideband besides f_i has great increasing while it, besides $3f_i$, has no obvious changing. From Figure 11, the same phenomenon is found, only the maximum frequency is $2f_i - 2f$, and it increased from $3.67e - 7$ m (at $0.5e - 3$ m) to $1.569e - 6$ m (at $2.5e - 3$ m). From Figures 10 and 11, it can be found that the width of defect has great influence to the amplitude of frequency. With the increasing of width, the amplitude has great change. But the width has no obvious effect to the distribution of frequency.

3.3. Effects of SFD

3.3.1. SFD Mounted on Bearing A.
To study the effect of the SFD on the dynamic behavior of the rotor system with bearing fault, the SFD is mounted on one of the two bearings
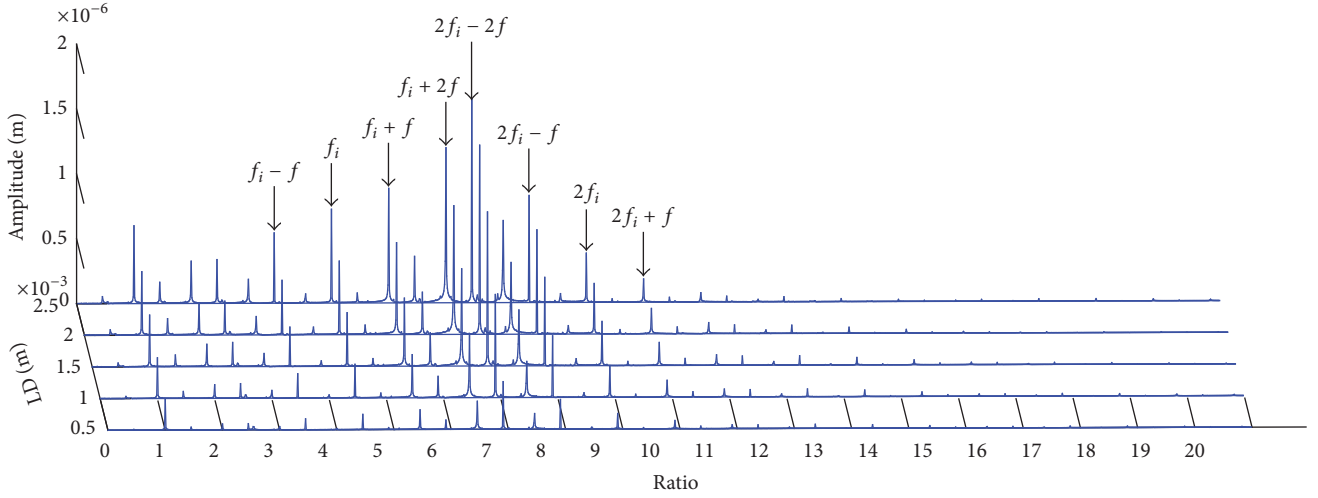
Figure 11: Waterfall plot of inner race defect bearing system with width of defect at 150 rad/s.
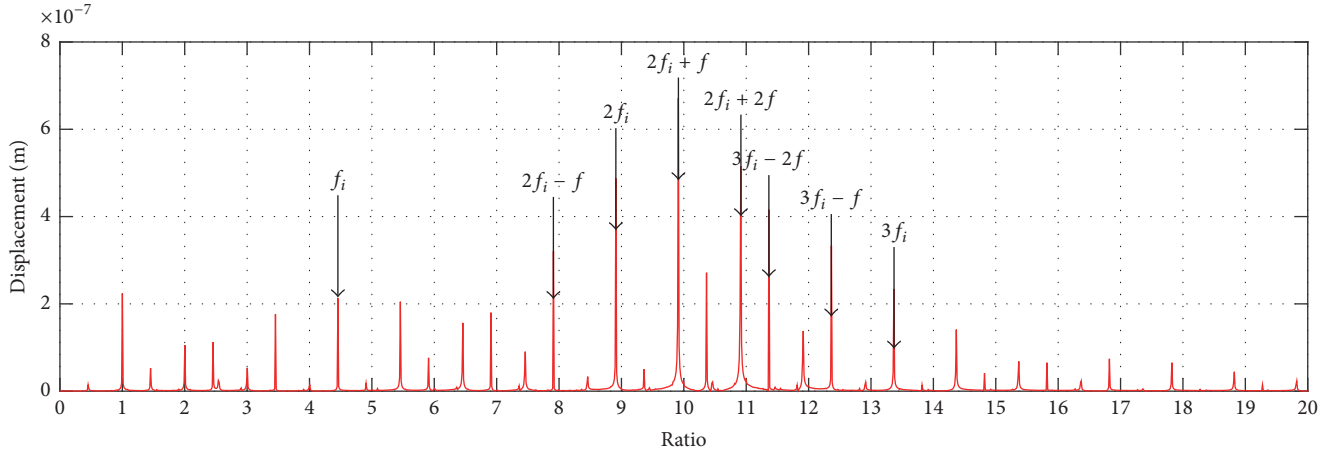

Figure 12: The spectral diagrams of the faulted system with SFD mounted on the normal bearing at $\omega = 100$ rad/s and width $= 1e - 3$ m.

at a time. The spectral diagrams of the faulted system with the SFD mounted on the normal bearing at the speed of 100 rad/s, 150 rad/s are shown in Figures 12 and 13.

Comparing with the system without SFD (Figure 8), it can be found that the amplitude of the fundamental frequency does not change, while the amplitudes at the fault characteristic frequencies and the sideband frequencies are decreased. For instance, the amplitude at $2f_i + f$ decreased from 8.1×10^{-7} m to 6.7×10^{-7} m, that at $2f_i$ decreased from 5.3×10^{-7} m to 4.8×10^{-7} m, and that at $2f_i + 2f$ decreased from 6.6×10^{-7} m to 5.3×10^{-7} m, while the maximum frequency still locates at $2f_i + f$ the same as the system without SFD. It can be seen that the introduction of the SFD on the normal bearing does not have much effect on the frequency characteristics of the rotor system at low speed.

3.3.2. SFD Mounted on Bearing B.
Figures 13–15 are the spectral diagrams of the rotor system with the SFD mounted on the fault bearing at 100 rad/s and 150 rad/s, respectively.

It can be seen that the amplitude at the fundamental frequency declines from 2.2×10^{-7} m (shown in Figure 7(b)) to 1.5×10^{-7} m (shown in Figure 13) when the rotating speed is 100 rad/s. The amplitudes at the fault characteristic frequencies also decrease a lot, such as from 8.1×10^{-7} m to 1.52×10^{-7} m at $2f_i + f$, from 5.3×10^{-7} m to 1.9×10^{-7} m at $2f_i$, and from 6.6×10^{-7} m to 6.5×10^{-8} m at $2f_i + 2f$. In addition, dominant frequency shifts to $2f_i$.

At 150 rad/s case, the amplitude of the fundamental frequency of the system with the SFD mounted on the faulted bearing does not change much comparing with that without the SFD. However, the amplitudes at fault characteristic frequencies decrease significantly due to the adoption of the SFD (from 1.04×10^{-6} m to 1.02×10^{-7} m at $f_i + f$ and from 5.3×10^{-7} m to 2.01×10^{-7} m at f_i). Apart from that, the amplitudes at fault characteristic frequencies are even smaller than that of the fundamental frequency which may be a considerable influence on system response caused by the SFD mounted on the faulted bearing. It is found that the
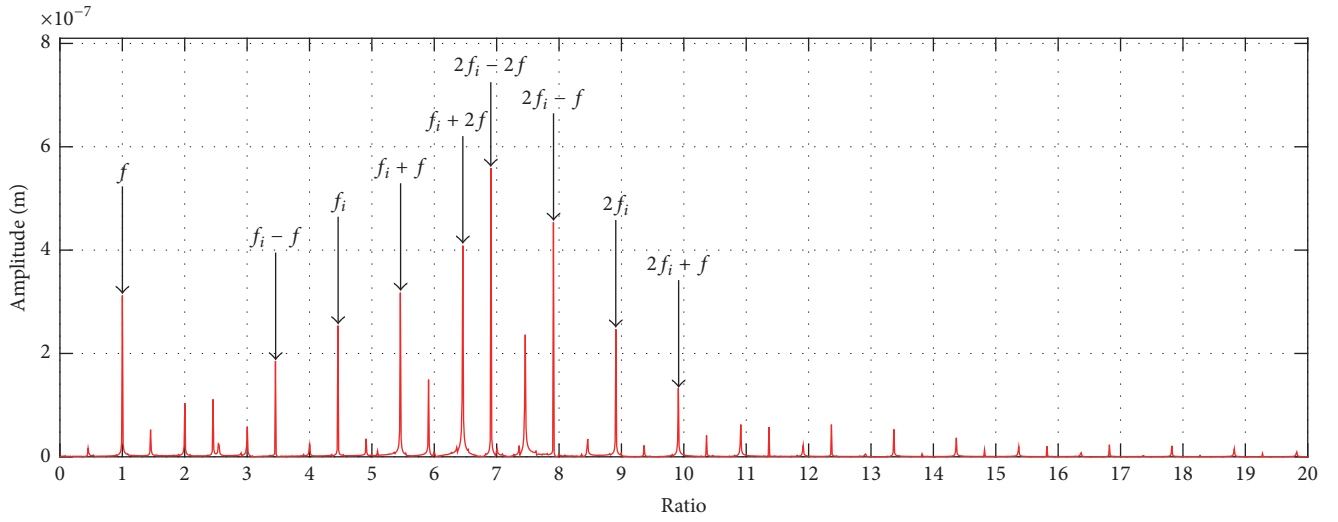
Figure 13: The spectral diagrams of the faulted system with SFD mounted on the normal bearing at $\omega = 150$ rad/s and width $= 1e - 3$ m.
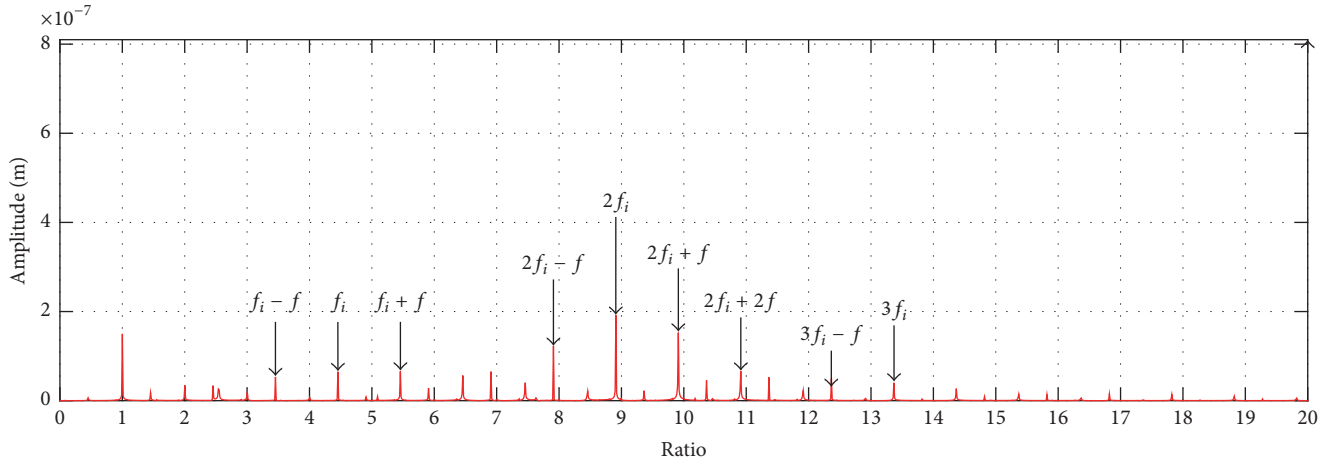

Figure 14: The spectral diagram of the faulted system with SFD mounted on the faulted bearing at $\omega = 100$ rad/s.
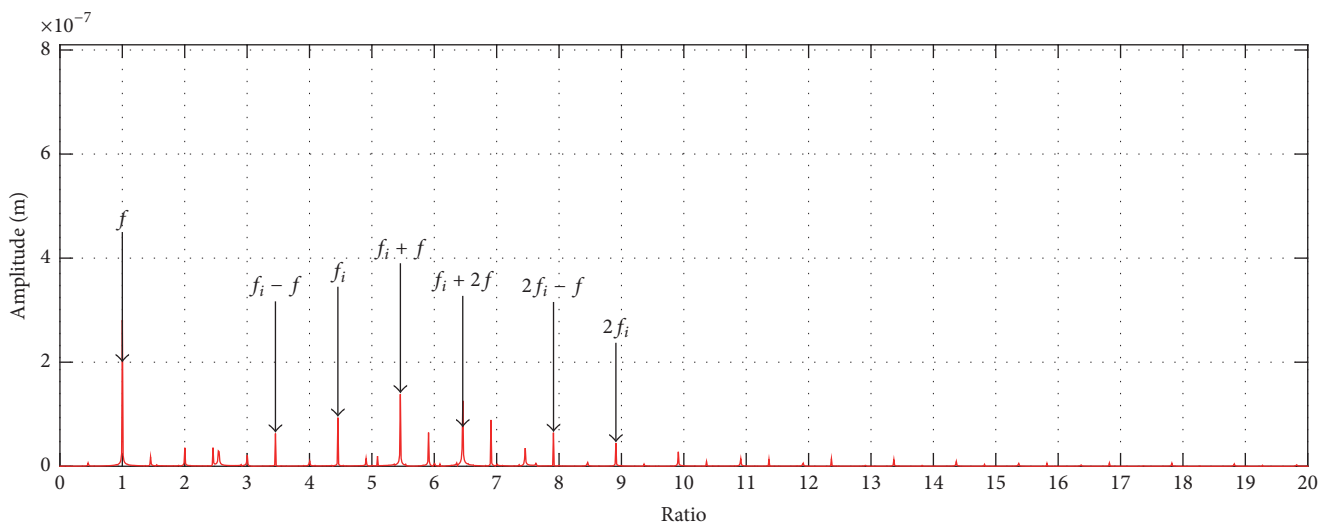

Figure 15: The spectral diagram of the faulted system with SFD mounted on the faulted bearing at $\omega = 150$ rad/s.
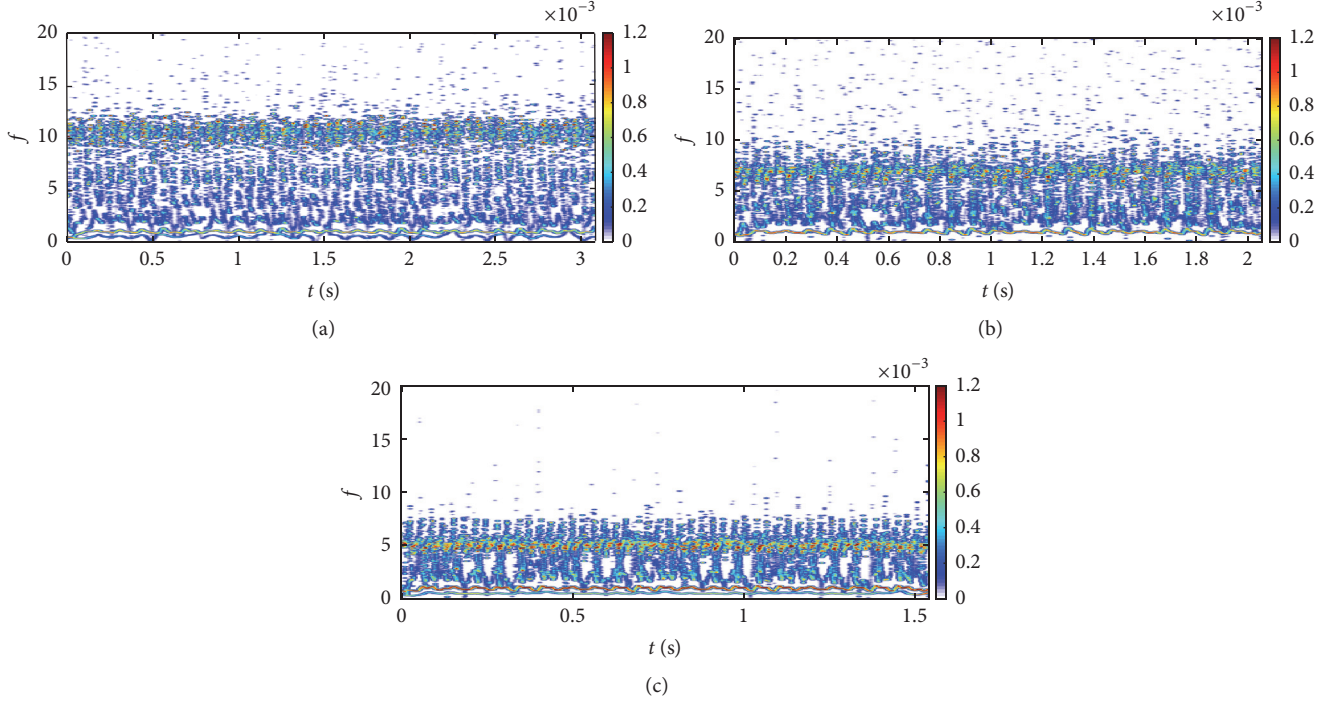
(a)

(b)

(c)

FIGURE 16: Time-frequency diagrams of the faulted system at (a) 100 rad/s, (b) 150 rad/s, and (c) 200 rad/s.

stability of the rotor system is enhanced due to the fact that fault characteristics are suppressed a lot by the SFD on the faults side compared to the normal side.

3.4. Time-Frequency Analysis

3.4.1. For Effect of Faults Characteristics. Time-frequency diagrams of the faulted rotor system at different rotating speeds are shown in Figure 16. It is found that the energy of the signal concentrates around the 10x fundamental frequency, which is close to the peak at the $2f_i + f$ frequency in the spectral diagram. The signal of the bearing fault performs as impacts in the high frequency range without any patterns, while the signal of the fundamental frequency is continuous in the same frequency range. Figure 16(b) indicates that the system energy centralizes at the fundamental frequency and between 5 and 10x fundamental frequency, and in Figure 16(c) the energy centralizes at 5x fundamental frequency. The amplitude of the max energy has a little change with the speed increasing.

The time-frequency diagrams of the faulted rotor system at different defect width were shown in Figures 16 and 17. With the increasing of defects width, the distribution of signal energy changed a little, and the characteristic of the signal is changeless, but the amplitude of energy increased a lot with width increasing.

3.4.2. For Effect of SFD. Time-frequency diagrams of the faulted rotor system with the SFD mounted on bearing A

(normal bearing) are shown in Figure 18. It can be seen that the rotor signal in high frequency range is still remittent, while the distribution of the signal energy is much looser with some components moving to the higher frequency at 100 rad/s. With the speed increased to 200 rad/s, the signal energy moves to 5x fundamental frequency ($f_i + f$ in the spectral diagram), and the energy in high frequency is reduced. Thus the system signal energy does not show apparent changes when the SFD is mounted on the normal bearing side. Comparing to Figure 16, the energy of the signal has no obvious decreasing.

Time-frequency diagrams of the rotor system with the SFD mounted on the bearing B (faulted bearing) are shown in Figure 19. At low rotating speed, the energy of the signal decreases sharply especially at the frequency higher than 10x fundamental frequency ($2f_i + f$ in the spectral diagram). As the speed increased to 200 rad/s, the energy of signal shifts to the fundamental frequency and that of the fault signal at high frequency reduces a lot.

4. Conclusions

(1) The characteristics of inner race defects on bearing can be concluded that there are all kinds of frequencies on the spectral diagram from low frequency to high frequency. Most of these frequencies are related to the characteristic multiple frequency of the inner race defect and the fundamental frequency. The signal of the bearing fault performs as impacts in the high frequency range without any patterns.
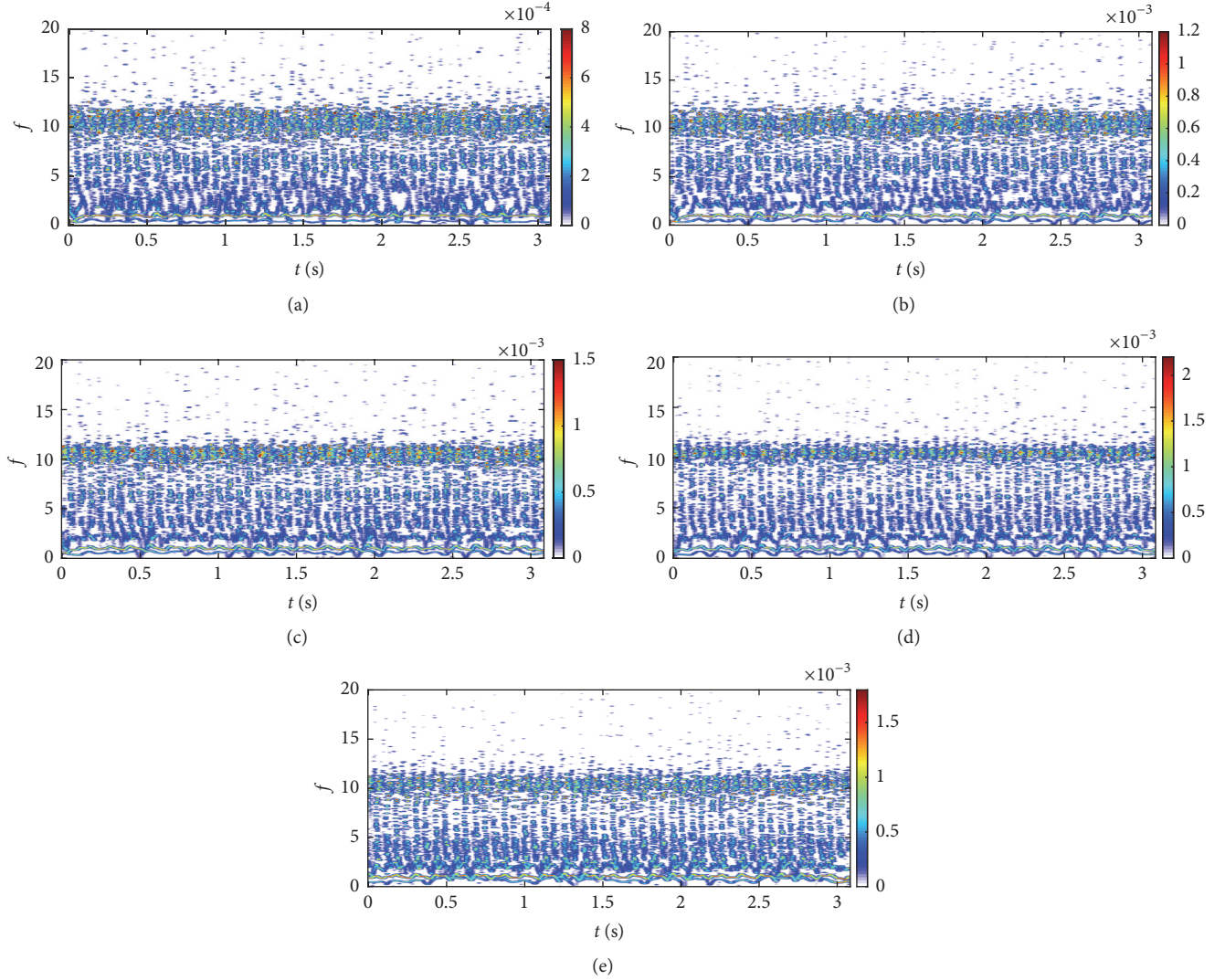
FIGURE 17: Time-frequency diagrams of the faulted system at 100 rad/s with different defect width: (a) $0.5e-3$ m; (b) $1e-3$ m; (c) $1.5e-3$ m; (d) $2e-3$ m; (e) $2.5e-3$ m.

(2) The rotating speed and defect width had an obvious influence on the characteristics of inner race bearing. With the increasing of speed, the distribution of frequencies moves to the low frequency, and the amplitude of low frequency has great increasing, while the amplitude of the signal increases a little. With the increasing of the defect width, the amplitude of frequency and signal has great increasing while the distribution changes a little.

(3) The beneficial effect of the SFD strongly depends on the position of the SFD mounted. The vibration magnitudes of the rotor system show a slight decrease when the SFD is mounted on the unfaulted bearing while it is reduced significantly with the SFD mounted on the faulted bearing.

Comparing with the existing methods of analysis on bearing defects, this analysis of this paper is focused on studying the characteristics of frequency distribution and explored the laws where the frequencies changed with the length of bearing defects and speed. This paper also explored the effects of SFD to the bearing inner race defect frequencies.

Competing Interests

The authors declare that there is no conflict of interests regarding the publication of this paper.
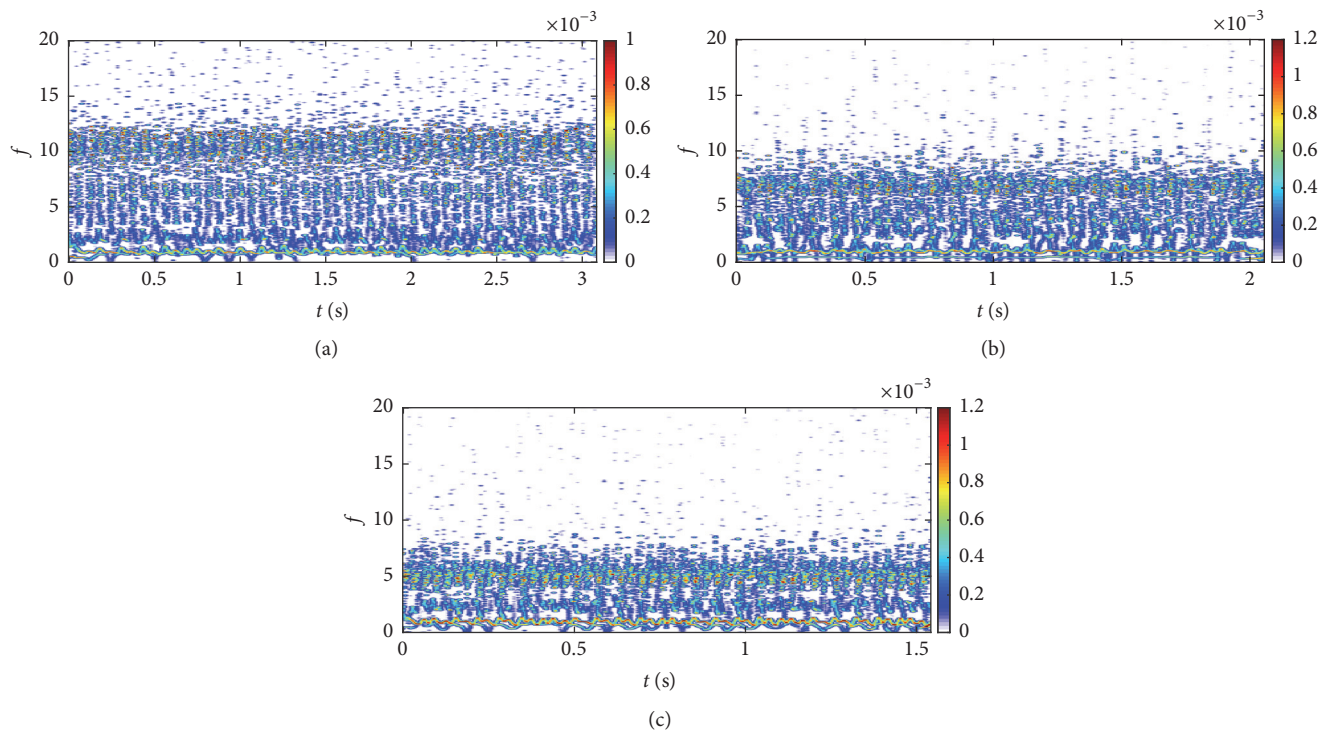
Acknowledgments

(a)

(b)

(c)

FIGURE 18: The time-frequency diagrams of the system with the SFD mounted on the normal bearing at (a) 100 rad/s and (b) 150 rad/s and (c) 200 rad/s.
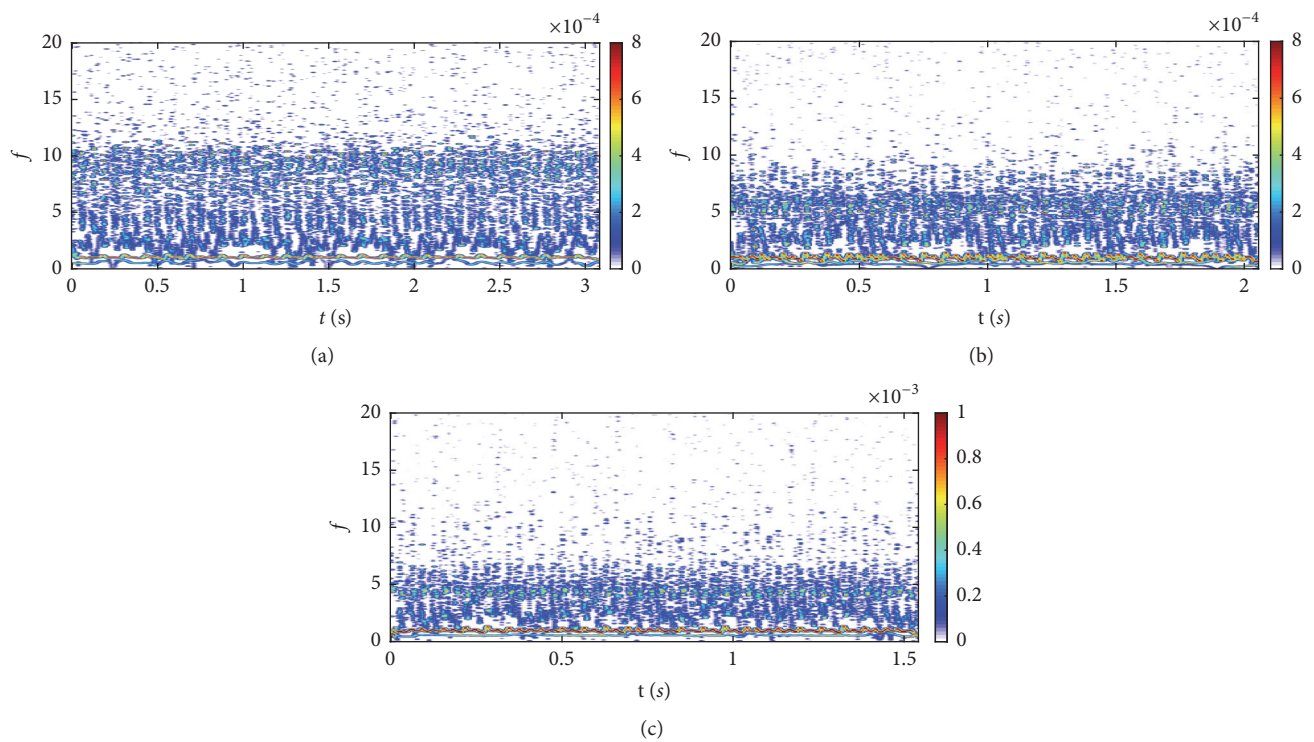

(a)

(b)

(c)

FIGURE 19: The time-frequency diagram of the system with the SFD mounted on the faulted bearing at (a) 100 rad/s and (c) 150 rad/s and (c) 200 rad/s.

References

[1] V. C. M. N. Leite, J. G. Borges Da Silva, G. F. C. Veloso et al., "Detection of localized bearing faults in induction machines by spectral kurtosis and envelope analysis of stator current," *IEEE Transactions on Industrial Electronics*, vol. 62, no. 3, pp. 1855–1865, 2015.

[2] A. K. S. Jardine, D. Lin, and D. Banjevic, "A review on machinery diagnostics and prognostics implementing condition-based maintenance," *Mechanical Systems and Signal Processing*, vol. 20, no. 7, pp. 1483–1510, 2006.

[3] X. Ding and Q. He, "Time-frequency manifold sparse reconstruction: a novel method for bearing fault feature extraction," *Mechanical Systems and Signal Processing*, vol. 80, pp. 392–413, 2016.

[4] W. Zhou, T. G. Habetler, and R. G. Harley, "Bearing fault detection via stator current noise cancellation and statistical control," *IEEE Transactions on Industrial Electronics*, vol. 55, no. 12, pp. 4260–4269, 2008.

[5] L. Frosini and E. Bassi, "Stator current and motor efficiency as indicators for different types of bearing faults in induction motors," *IEEE Transactions on Industrial Electronics*, vol. 57, no. 1, pp. 244–251, 2010.

[6] P. K. Kankar, S. C. Sharma, and S. P. Harsha, "Vibration based performance prediction of ball bearings caused by localized defects," *Nonlinear Dynamics*, vol. 69, no. 3, pp. 847–875, 2012.

[7] H. Arslan and N. Aktürk, "An investigation of rolling element vibrations caused by local defects," *Journal of Tribology*, vol. 130, no. 4, Article ID 041101, 2008.

[8] M. S. Patil, J. Mathew, P. K. Rajendrakumar, and S. Desai, "A theoretical model to predict the effect of localized defect on vibrations associated with ball bearing," *International Journal of Mechanical Sciences*, vol. 52, no. 9, pp. 1193–1201, 2010.

[9] X. Ding and Q. He, "Time–frequency manifold sparse reconstruction: a novel method for bearing fault feature extraction," *Mechanical Systems and Signal Processing*, vol. 80, pp. 392–413, 2016.

[10] H. Ma, T. Yu, Q. Han, Y. Zhang, B. Wen, and C. Xuelian, "Time-frequency features of two types of coupled rub-impact faults in rotor systems," *Journal of Sound and Vibration*, vol. 321, no. 3–5, pp. 1109–1128, 2009.

[11] R. Liu, B. Yang, X. Zhang, S. Wang, and X. Chen, "Time-frequency atoms-driven support vector machine method for bearings incipient fault diagnosis," *Mechanical Systems and Signal Processing*, vol. 75, pp. 345–370, 2016.

[12] H.-L. Zhou, G.-H. Luo, G. Chen, and F. Wang, "Analysis of the nonlinear dynamic response of a rotor supported on ball bearings with floating-ring squeeze film dampers," *Mechanism and Machine Theory*, vol. 59, pp. 65–77, 2013.

[13] C.-W. Chang-Jian, "Non-linear dynamic analysis of a HSFD mounted gear-bearing system," *Nonlinear Dynamics*, vol. 62, no. 1-2, pp. 333–347, 2010.

[14] H.-L. Zhou, G.-Q. Feng, G.-H. Luo, Y.-T. Ai, and D. Sun, "The dynamic characteristics of a rotor supported on ball bearings with different floating ring squeeze film dampers," *Mechanism and Machine Theory*, vol. 80, pp. 200–213, 2014.

[15] J. I. Inayat-Hussain, "Bifurcations in the response of a flexible rotor in squeeze-film dampers with retainer springs," *Chaos, Solitons & Fractals*, vol. 39, no. 2, pp. 519–532, 2009.

[16] L. Ma, J. Zhang, J. Lin, J. Wang, and X. Lu, "Dynamic characteristics analysis of a misaligned rotor-bearing system with squeeze film dampers," *Journal of Zhejiang University-SCIENCE A*, vol. 17, no. 8, pp. 614–631, 2016.

[17] M. Nakhaeinejad and M. D. Bryant, "Dynamic modeling of rolling element bearings with surface contact defects using bond graphs," *Journal of Tribology*, vol. 133, no. 1, Article ID 011102, 2011.

[18] K. H. Groves and P. Bonello, "Improved identification of squeeze-film damper models for aeroengine vibration analysis," *Tribology International*, vol. 43, no. 9, pp. 1639–1649, 2010.

[19] C. J. Maday, "The foundation of the Sommerfeld transformation," *Journal of Tribology*, vol. 124, no. 3, pp. 645–646, 2002.

[20] M. Sarangi, B. C. Majumdar, and A. S. Sekhar, "Stiffness and damping characteristics of lubricated ball bearings considering the surface roughness effect. Part 1: theoretical formulation," *Proceedings of the Institution of Mechanical Engineers, Part J: Journal of Engineering Tribology*, vol. 218, no. 6, pp. 529–538, 2004.

[21] M. Sarangi, B. C. Majumdar, and A. S. Sekhar, "Stiffness and damping characteristics of lubricated ball bearings considering the surface roughness effect. Part 2. Numerical results and application," *Proceedings of the Institution of Mechanical Engineers Part J: Journal of Engineering Tribology*, vol. 218, no. 6, pp. 539–547, 2004.

[22] Harris, *Rolling Bearing Analysis*, John Wiley & Sons, New York, NY, USA, 1991.

[23] C. S. Zhu, D. A. Robb, and D. J. Ewins, "Analysis of the multiple-solution response of a flexible rotor supported on non-linear squeeze film dampers," *Journal of Sound and Vibration*, vol. 252, no. 3, pp. 389–408, 2002.